Innovative materials chemistry strategies for engineered-enhanced thermomaterials for barocaloric and related solid-state refrigeration

Javier García Ben

Doctoral Thesis UDC | 2023

Directors:

Profa. María Antonia Señarís Rodríguez

Dr. Juan Manuel Bermúdez García

Universidade da Coruña

Departamento de Química, Facultade de Ciencias

Centro Interdisciplinar de Química y Biología (CICA)

Programa de doctorado regulado por el RD 99/2011:

Química Fundamental y Medioambiental

Memoria presentada en el Facultad de Ciencias de la Universidade da Coruña por Javier García Ben para optar al Grado de Doctor en Química por la Universidade da Coruña.

A Coruña, octubre 2023

Doctorando

Javier García Ben

Directores

María Antonia Señarís Rodríguez

Juan Manuel Bermúdez García

UNIVERSIDADE DA CORUÑA

Profa. María Antonia Señarís Rodríguez, Catedrática de Química Inorgánica, y Dr. Juan Manuel Bermúdez García, contratado Ramón y Cajal, pertenecientes al Departamento de Química (Área de Química Inorgánica) y al Centro Interdisciplinar de Química y Biología (CICA) de la Universidade da Coruña (UDC).

Hacen constar:

Que la presente memoria titulada "*Innovative materials chemistry strategies for engineered-enhanced thermomaterials for barocaloric and related solid-state refrigeration*" ha sido realizada bajo su dirección por el Graduado en Química Javier García Ben y, habiendo sido concluida, autorizan su presentación para optar al Grado de Doctor en Química con mención de Doctor Internacional.

A Coruña, octubre 2023

Profa. María Antonia Señarís Rodríguez

Dr. Juan Manuel Bermúdez García

PhD Thesis presented in the Faculty of Sciences of the University of A Coruña by Javier García Ben.

A Coruña, October 2023

Court of this *PhD Thesis*

Vogal Secretary President

This *PhD Thesis* was elaborated within the ***Official PhD Program of Environmental and Fundamental Chemistry*** in the ***QUIMOLMAT*** research group between the Faculty of Science and the Biology and Chemistry Interdisciplinar Centre (**CICA**) of the University of A Coruña (**UDC**).

This *PhD Thesis* was funded by **Predoctoral Xunta de Galicia Fellowship** (ED481A 2020/030) and the financial support from the projects MAT2017-86453-R and PID2021-122532OB-I00 funded by MCIN/AEI/10.13039/501100011033/ and by **FEDER** *Una manera de hacer Europa*, the project PDC2021-121076-I00 funded by MCIN/AEI/10.13039/ 501100011033 and by the **European Union** *Next GenerationEU/PRTR* and the projects *Development of research strategic actions UDC I+D+i 2021-2022: CICA-Disrupting Projects 2021SEM-A3 (NanoCool)*, ED431G/09 and ED431C 2022/39 funded by **Xunta de Galicia**. During this *PhD Thesis* there were collaborations with *Nanochem* research group of the International Iberian Nanotechnology Laboratory (INL) of Braga, Portugal during a 3-months research stay funded by **IACOBUS Program**, with *Phillips Group* of the Queen Mary University of London (QMUL), United Kingdom during another 3-months research stay funded by **Xunta de Galicia**, and with *Tomoyuki Mochida Group* of the Kobe University of Kobe, Japan during 1.5-months research stay funded by scholarships for predoctoral stays of **Inditex-UDC 2022**.

‘No Gods or Kings, only Man’

Andrew Ryan - 2007

Aknowledgements / Agradecimientos

La presente *Tesis Doctoral* ha sido financiada por un contrato predoctoral de la **Xunta de Galicia** (modalidad A del año 2020, con el código ED481A-2020/030). Además, este trabajo de investigación ha sido financiado por el **Ministerio de Economía y Competitividad (MINECO)** y por el **Fondo Europeo de Desarrollo Regional (EU-FEDER)**, (proyectos MAT2017-86453-R, PDC2021-121076-I00 y PID2021-122532OB-I00) y la **Xunta de Galicia** (proyectos Development of research strategic actions UDC I+D+i 2021-2022: CICA-Disrupting Projects 2021SEM-A3 (NanoCool), ED431G/09 y ED431C 2022/39).

Asimismo, durante esta *Tesis Doctoral* se han efectuado diversas estancias de investigación en el extranjero gracias a la financiación del programa **IACOBUS** para la realización de una estancia de 3 meses en el *International Iberian Nanotechnology Laboratory*, INL (Braga, Portugal), a la **Xunta de Galicia** para la realización de una estancia de 3 meses en la *Queen Mary University of London*, QMUL (Londres, Reino Unido) y a las ayudas para estancias predoctorales **Inditex-UDC 2022** para la realización de una estancia de 1.5 meses en Kobe Daigaku (Kobe, Japón).

Por otra parte, durante la realización de este trabajo de investigación he tenido el placer de haber trabajado y colaborado con numerosos investigadores a los cuales me gustaría dedicarles este pequeño espacio para agradecer todas las experiencias y enseñanzas que me han otorgado.

Para empezar, quiero dar las gracias a mis directores, la **Profa. María Antonia Señarís Rodríguez** y el **Dr. Juan Manuel Bermúdez García**, así como al **Dr. Manuel Sánchez Andújar** y a la **Dra. Socorro Castro García**, investigadores del grupo de UDCSólidos del Centro Interdisciplinar de Biología y Química (CICA) de la Universidade da Coruña (UDC). Siempre me habéis brindado todo el apoyo y ayuda que he necesitado, incluso antes de comenzar esta aventura hace ya cuatro años. Os estaré eternamente agradecido por la excelente acogida que he tenido en este grupo.

Por supuesto agradecer a los actuales doctorandos del grupo, con los que he compartido muchas horas en el laboratorio. Deseo que su experiencia en este grupo sea tan buena como ha sido para mí la mía, además de darles mucho ánimo a los cuatro con su carrera científica. Quería agradecer en especial a el **Dr. Jorge Salgado**, el cual no ha sido solo un compañero de trabajo, sino que también un muy buen amigo y siempre me ha ayudado y enseñado todo lo que necesitaba, sobre todo cuando llegué a esta ciudad por primera vez.

Me gustaría agradecer también a los investigadores con los que he tenido el placer de trabajar y compartir esta experiencia:

A todos mis compañeros del CICA por los buenos momentos que hemos compartido a lo largo de estos cuatro años.

Al **Dr. Jorge López** y el resto de los investigadores del grupo de '*Propiedades Térmicas y Reológicas de Materiales*' de la UDC los cuales siempre han tenido sus puertas abiertas para mis innumerables visitas.

Al **Dr. Alberto García** que desde Estocolmo me ha brindado todo su apoyo y me ha proporcionado toda la ayuda que necesitaba en las numerosas colaboraciones que hemos tenido.

Al **Dr. Bruno Alonso** de la Universidad de Montpellier por su excelente trabajo y profesionalidad, con el cuál espero poder volver a colaborar en el futuro.

I also want to thank **Dr. Julian Walker** and **Dr. Charles McMonagle** for the exhaustive time spent in the synchrotron, where your company and expertise made it wonderful experience.

I would like to extend my thanks to **Dr. Yury V. Kolen'ko**, **Dra. Laura Salonen**, **Dra. Liliana Sousa**, and the rest of 'Nanochemistry Research Group' at INL for all their support and help that they bring me during my 3-months research stay.

Moreover, I wish to express my appreciation to **Dr. Anthony Phillips** and **Dr. Richard Dixey** for my great experience during my stay in QMUL.

Finally, I'd like to express my gratitude to **Prof. Tomoyuki Mochida**, **Dr. Ryo Sumitani** and the rest of professors and students that I met during my stay in Kobe University. Despite being so far from my home, they welcomed me and made me feel at home. I am deeply grateful for how well you treated me.

Desde un punto de vista menos profesional y más personal, me gustaría agradecer a mi familia todo su apoyo, en especial a mi madre **Cristina Ben**, quien siempre me ha cuidado y quien más se ha preocupado por mí, y a mi padre **Francisco Javier García**, quien ha sido mi referente y modelo a seguir desde pequeño. También a mi madrina **Eva Ben**, que es como mi segunda madre y a mi hermana **Ana García**. Y por supuesto, gracias al resto de mi familia que siempre me ha apoyado y preocupado por mí. Y sin olvidar a mi tío **Manuel García**, que pese haberte ido este año siempre te recordaré y te agradeceré lo mucho que te interesabas por mi carrera científica.

También quería agradecer a **Leticia Montes**, quien me iba a decir que tú ibas a ser lo mejor del máster que hicimos en París.

No quiero olvidarme de **Diego Gallego** y **Lara Casal**, que, aunque la distancia nos limite, siempre os llevaré conmigo, con vosotros he vivido una de las mejores etapas de mi vida.

No hay suficientes palabras para agradecer a **Lucas Álvarez** y **Víctor Fariña**, igual que al resto del grupo de mis amigos **Hadrián Freire**, **Samuel Martínez** y **Carlos Codesido**, por todos estos momentos que hemos vivido desde aquel fatídico año que decidí meterme en una ingeniería. Para mí sois como mi propia familia.

Por último, y no por eso menos importante, a ti **María**, muchísimas gracias por tu apoyo, los ánimos que me has dado y por todo lo que hemos compartido. Sin ti esto hubiera sido imposible, me has dado energías para continuar todos los días, que sepas que una parte de este trabajo es gracias a tu ayuda, tu apoyo y la confianza que depositaste en mí. Te quiero.

Index

Abstract 1

Foreword 7

Chapter 1: Introduction 9

1.1. Current energetic, environmental and socioeconomic challenges of refrigeration 13

1.2. Present mature refrigeration technologies and most promising emerging alternatives 14

1.3. References 25

Chapter 2: Objectives 29

Chapter 3: New tools for chemistry-engineered barocaloric hybrid dicyanamide perovskites 33

3.1. Introduction to hybrid perovskites 37

3.2. Identification of new distortions and degrees of freedom in hybrid dicyanamide perovskites 41

3.3. Revisiting the tolerance factor, a useful tool for designing novel hybrid dicyanamide perovskites 51

3.4. Modulation of functional properties of hybrid dicyanamide perovskites by solid solution preparation 73

Chapter 4: New organometallic and hybrid organic-inorganic plastic crystals with enhanced barocaloric performance and simultaneous 'cold-storage' 89

4.1. Introduction to plastic crystals 93

4.2. Cyclopentadienyl organometallic-sandwich plastic crystals with ring-rotation induced barocaloric effects 97

4.3. Di-n-butylammonium tetrafluoroborate hybrid organic-inorganic material with thermal properties for multipurpose barocaloric refrigeration and 'cold-storage' 115

Chapter 5: Enhanced thermal changes through simultaneous combination of barocaloric effects and gas adsorption processes 141

5.1. Introduction to MOFs with flexible structures and solid-solid phase transitions 145

5.2. Displaying the breathing-caloric effect: a new alternative based in the combination of barocaloric effect and adsorption cooling in MOFs **149**

Chapter 6: General conclusions **171**

Annexes **175**

Annex I: Spanish summary **177**

Annex II: Crystallographic data and conventional NMR data **181**

Annex III: IP protection and scientific dissemination (patents, publications, communications) **193**

Annex IV: National and international collaborations and research visits **203**

Abstract

The present *PhD Thesis* focuses on the search of new thermomaterials (materials that have large latent heat associated to a solid-solid phase transition), specifically hybrid organic-inorganic materials, with the aim of exploring their potential use in cooling applications.

There is an urgent need to develop alternatives to current refrigeration in order to address the climate and energy challenges that our society is living in order to move towards a carbon-neutral economy with more energy-efficiency, no greenhouse gases emissions, and which relies solely on renewable energy sources. In this context, solid materials are considered attractive options to replace current technologies.

Taking this into consideration, the current *PhD Thesis* investigates three different families of hybrid organic-inorganic materials with potential applications as refrigerants in solid-state refrigeration: hybrid dicyanamide perovskites, hybrid ionic plastic crystals, and metal-organic frameworks (MOFs).

On one hand, the structural distortions of hybrid dicyanamide perovskites family were studied and explored, the tolerance factor for this family was revisited, and their first solid solution was prepared. On the other hand, three ionic plastic crystals were tested for their use in barocaloric refrigeration: $[Cp_2M][PF_6]$ (Cp = C_5H_5 and M = Fe, Co) and $[DBA][BF_4]$ (DBA = dibutylammonium). Lastly, the thermal response of a flexible MOF with a solid-solid phase transition linked to adsorption/desorption of carbon dioxide process upon the application of low pressure was measured: the MIL-53(Al) with general formula $[Al(OH)(C_8H_4O_4)]$.

It is worth noting that in addition to assessing the viability of some materials from these families as solid-state refrigerants, significant emphasis has also been placed on the search for design tools for new materials to provide guidelines that contribute to the development of solid-state refrigeration.

Resumen

La presente *Tesis Doctoral* se centra en la búsqueda de nuevos termomateriales (materiales que presentan grandes calores latentes asociados a una transición de fase sólido-sólido), en particular materiales híbridos orgánicos-inorgánicos, con el objetivo de explorar su potencial uso para aplicaciones de refrigeración.

Existe una urgente necesidad de desarrollar alternativas a la refrigeración actual para hacer frente a los desafíos climáticos y energéticos que nuestra sociedad está viviendo, con el fin de avanzar hacia una economía neutra en carbono, con mayor eficiencia energética, sin emisiones de gases de efecto invernadero y que dependa únicamente de fuentes de energía renovables. En este contexto, los materiales sólidos se consideran una opción muy atractiva para reemplazar las tecnologías actuales.

Teniendo esto en cuenta, la presente *Tesis Doctoral* investigó tres familias diferentes de materiales híbridos orgánicos-inorgánicos con gran potencial para su uso en refrigeración de estado sólido: las perovskitas híbridas de dicianamina, los cristales plásticos híbridos iónicos y las redes metal-orgánicas o MOFs.

Por una parte, en las perovskitas de dicianamina se estudiaron y buscaron las distorsiones estructurales, se reevaluó el factor de tolerancia para esta familia y se preparó su primera disolución sólida. Por otra parte, se pusieron a prueba tres cristales plásticos iónicos para su aplicación en refrigeración barocalórica, $[Cp_2M][PF_6]$ (Cp = C_5H_5 y M = Fe, Co) y $[DBA][BF_4]$ (DBA = dibutilamonio). Por último, se midió la respuesta térmica de un MOF flexible con transición de fase sólido-sólido ligada a la adsorción/desorción de dióxido de carbono tras la aplicación de pequeñas presiones: el MIL-53(Al) con fórmula general $[Al(OH)(C_8H_4O_4)]$.

Cabe a destacar que además de medir la viabilidad de algunos materiales de estas familias como refrigerantes en estado sólido, también se ha hecho gran hincapié en la búsqueda de herramientas para el diseño de nuevos materiales con el fin de mostrar directrices que ayuden al desarrollo de la refrigeración de estado sólido.

Resumo

A presente *Tese Doutoral* céntrase na busca de novos termomateriais (materiais que presentan grandes calores latentes asociados a unha transición de fase sólido-sólido), en particular materiais híbridos orgánicos-inorgánicos, co obxectivo de explorar o seu potencial uso para aplicacións de refrixeración.

Existe unha urxente necesidade de desenvolver alternativas á refrixeración actual para facer fronte aos desafíos climáticos e enerxéticos que a nosa sociedade está vivindo, co fin de avanzar cara a unha economía neutra en carbono, con maior eficiencia enerxética, sen emisións de gases de efecto invernadoiro e que dependa unicamente de fontes de enerxía renovables. Neste contexto, os materiais sólidos considéranse unha opción moi atractiva para substituír as tecnoloxías actuais.

Tendo isto en conta, a presente *Tese Doutoral* investigou tres familias diferentes de materiais híbridos orgánicos-inorgánicos con gran potencial para o seu uso en refrixeración de estado sólido: as perovskitas híbridas de dicianamina, os cristais plásticos híbridos iónicos e as redes metal-orgánicas ou MOFs.

Por unha banda, nas perovskitas de dicianamina estudáronse e buscáronse as súas distorsións estruturais, reanalizou o factor de tolerancia para esta familia e preparouse a súa primeira disolución sólida. Por outra banda, puxéronse a proba tres cristais plásticos iónicos para a súa aplicación en refrixeración barocalórica, $[Cp_2M][PF_6]$ (Cp = C_5H_5 y M = Fe, Co) y [DBA][BF_4] (DBA = dibutilamonio). Por último, mediuse a resposta térmica dun MOF flexible con transición de fase sólido-sólido ligada á adsorción/desorción de dióxido de carbono trala aplicación de pequenas presións: o MIL-53(Al) con fórmula xeral $[Al(OH)(C_8H_4O_4)]$.

Cabe a destacar que ademais de medila viabilidade de algúns materiais de estas familias como refrixerantes en estado sólido, tamén se fixo gran fincapé na busca de ferramentas para o deseño de novos materiais co fin de mostrar directrices que axuden ao desenvolvemento da refrixeración de estado sólido.

Foreword

Our society still lives an enormous dependence on non-renewable energies. The increasing demand of energy and the slow adaptation of the world into renewable alternatives are traduced in the worrying climate change that our planet is experimenting.

In this context, refrigeration is one of the driving forces of our society and is one of the primary sectors contributing to the increasing energy demand. However, refrigeration is also deeply rooted to an old technology associated to low energy efficiency and climate-related issues, such as global warming.

One arising alternative is the use of thermomaterials as refrigerants. These solid-state materials have a reversible solid-solid phase transition which can be induced by an external stimulus (temperature, pressure, electric and/or magnetic field, etc.). One of the most promising family of thermomaterials for refrigeration are those which show the solid-solid state phase transition under the application of external pressure, called barocaloric materials.

With that in mind, this *PhD Thesis* studied some these potential solid-state refrigerants, in particular the known as hybrid organic-inorganic materials. To show and discuss the work done, this *PhD Thesis* is organized in the following chapters:

Chapter 1 starts with an introduction to the energetic, environmental and socioeconomic challenges that refrigeration needs to address in order to transition to a more efficient and environmentally friendly technology, followed by a brief presentation of current refrigeration technologies (active and passive) and the most promising emergent alternatives.

Chapter 2 collects the objectives of this *PhD Thesis*.

Chapter 3 is devoted to the search of new compounds within the hybrid dicyanamide perovskite family through three key aspects: First a comprehensive study of all reported distortions observed in this family. The second one revolves around the revisit of the well-established tolerance factor for hybrid perovskites to suit the hybrid dicyanamide perovskite family. The third one involves the development of the first solid solution within the hybrid dicyanamide perovskite family ($[Pr_4N][Co_{0.5}Ni_{0.5}(dca)_3]$).

Chapter 4 studied other promising family of materials for barocaloric applications; hybrid ionic plastic crystals. This chapter is focused in the refrigeration potential of three materials of this family: $[Cp_2Fe][PF_6]$, $[Cp_2Co][PF_6]$ and $[DBA][BF_4]$ (where Cp = cyclopentadiene and DBA = n-dibutylammonium).

Chapter 5 explored a new alternative for cooling by combining solid-state barocaloric effects and adsorption cooling. For that, this chapter examined the thermal response related to the gas adsorption provoked by a solid-solid phase transition of the flexible MOF called MIL-53(Al) (with general formula [Al(bdc)(OH)], where bdc = $C_8H_4O_4$) after the application/retirement of CO_2 pressure.

Chapter 6 ends with general conclusions of the work presented.

Annex I is the Spanish summary of this *PhD Thesis*.

Annex II contains all the crystallographic data and conventional nuclear magnetic resonance (NMR) that supports the results discussed in all the chapters.

Annex III includes the IP protection and science communication (patents, publications, communications, congress participations).

Annex IV cover the national and international collaborations and research visits.

Chapter 1

Introduction

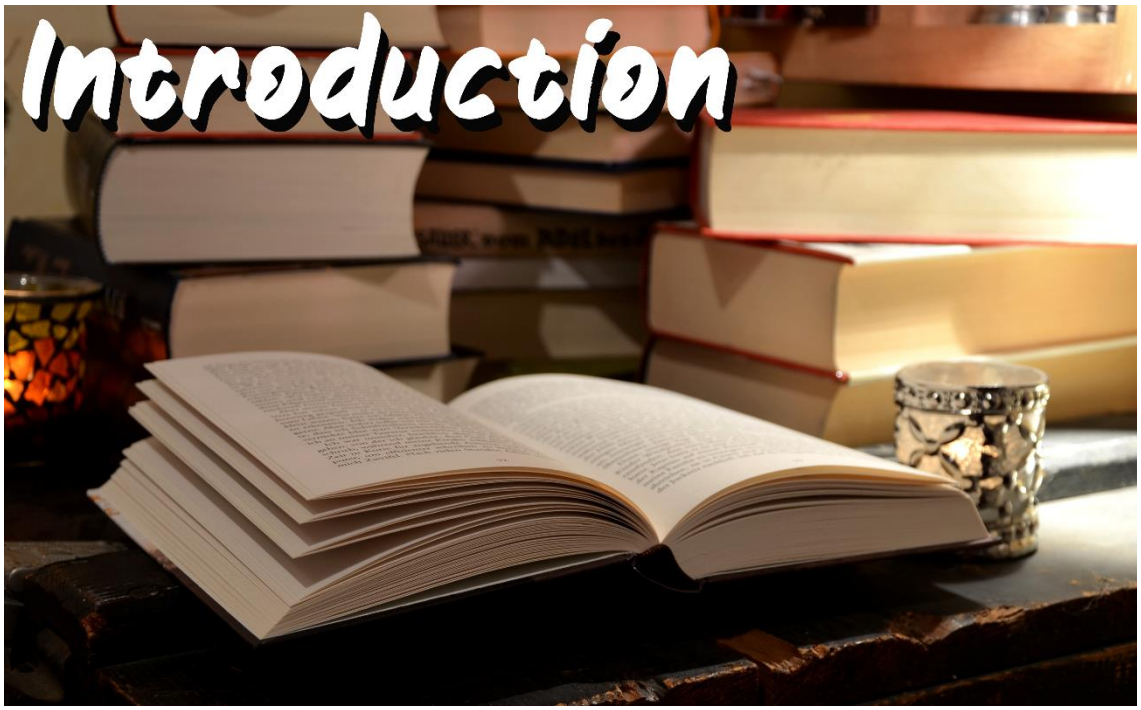

Chapter 1: Introduction

Index

1.1. Current energetic, environmental and socioeconomic challenges of refrigeration **13**

1.2. Present mature refrigeration technologies and most promising emerging alternatives **14**

1.2.1. Active refrigeration systems 14

a) Vapour compression refrigeration 15

b) Barocaloric refrigeration 17

c) Adsorption cooling 22

1.2.2. Passive refrigeration systems: ‘cold-storage’ 24

1.3. References **25**

1.1. Current energetic, environmental and socioeconomic challenges of refrigeration

Current refrigeration technologies are deeply ingrained in our society. Refrigeration is commonly associated with everyday life, such as household refrigerators, freezers, and air conditioners. However, refrigeration also has a significant impact at the industrial level (see Figure 1-1), for example:

- The cold chain is essential to the conservation of quality and safety in alimentation and drinks, where most of the products of this sector need to be refrigerated from the production to the consumption.[1,2]
- Chemical industries need refrigeration to cold down and control the temperature of some of their processes.[3]
- Cold is needed in the synthesis and transport of vaccines or some drugs, exhibiting the importance of refrigeration in the pharmaceutical and sanitary field.[4]
- In automobile, most of the vehicles have air conditioning, the use of which could increase fuel consumption by up to 20%.[5] This fact goes further in hybrid and electric vehicles, where the refrigeration of the batteries is indispensable for not losing autonomy.[6,7]
- In the case of naval industry, large vessels need to cool down the fuel to 100 K or lower before using it.[8] In addition, there are a large number of freezer vessels which need to transport merchandise at low temperature (as food or vaccines).
- For the preparation of fibres, to control the temperature and the humidity is crucial to obtain the desired properties. Actually, energetic cost destinated to refrigeration in a textile factory could rise up to 7% of the total.[9]
- In entertainment and culture sector, such as shops, mails, cinemas, stations and other venues have elevated costs in refrigeration, in particular air conditioning.[10]

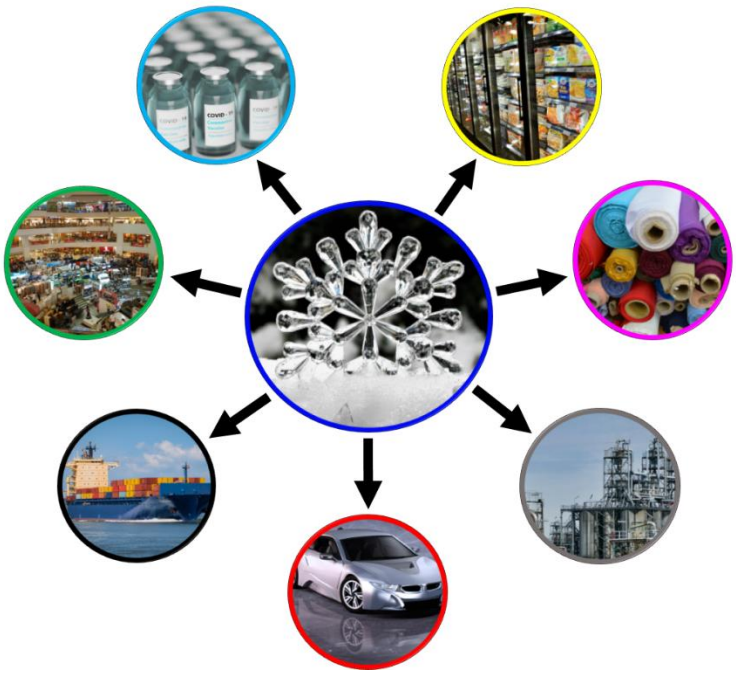

Figure 1-1. Refrigeration connected with food and drinks, chemical industries, pharmaceutic and sanitary sector, automobile, naval industry, textile and entertainment and culture.

As a result of the strong connection and extensive use of this technology in industrial, household, leisure, and medical-pharmaceutical sectors, refrigeration presents significant challenges in terms of energy consumption and environmental pollution.

According to the International Energy Agency (IEA), refrigeration technologies (such as refrigerators, freezers and HVAC —heating, ventilation and air conditioning— systems) already account for over 20% of global energy consumption.[11–13] Moreover, this enormous demand is expected to escalate in the coming years due to the alarming rise in global warming, which is projected to reach an increase of 1.5 to 2 °C by 2050.[14–16]

Furthermore, refrigeration technologies are responsible for approximately 7% of greenhouse gas emissions. They can be divided into direct and indirect emissions. On one hand, direct emissions represent around 2% of the total pollutant gases emissions and they are caused by refrigerant gases due to leaks or improper handling of refrigeration-related waste (devices, refrigerants, etc.). On the other hand, indirect emissions contribute approximately 5% of the total and they occur due to the energy consumption of these refrigeration technologies.[11,12]

This creates a vicious cycle as the expected increase in energy consumption for refrigeration in the coming decades, coupled with the emissions it generates, results in a greater need of energy for cooling, leading to further global warming.

It is worth noting the significant energy and resource wastage associated with refrigeration every year. In terms of thermal energy storage, previous studies by the International Renewable Energy Agency have reported that Europe could save 1.4 million GWh/year and avoid 400 million tons of CO_2 emissions in buildings and industrial sectors through a more extensive use of cold and heat storage.[17] Additionally, a clear example within the aforementioned sectors (Figure 1-1) is food waste. Around 46% of produced food requires refrigeration for proper preservation. However, only half of this food is adequately refrigerated, leading to a loss of around 13% of the total food production annually.[1]

Taking all this into account, the field of refrigeration faces various challenges that need to be addressed to improve the socioeconomic situation in the coming decades. It is urgent to reduce the pollution and emissions of greenhouse gases, thereby mitigating the global warming. Consequently, it is necessary to seek environmentally friendly, non-toxic, and non-hazardous refrigerants to minimize direct contamination. Moreover, refrigeration needs to focus on optimizing the energy efficiency of its systems to minimize indirect emissions. This aspect is further exacerbated by the origin of our energy, which still heavily relies on fossil fuels. The transition to renewable energy sources is still too slow, and our energy resources mostly consist of natural gas and petroleum derivatives. Unfortunately, these fossil fuels are highly polluting and depleting, leading to increase energy costs. This not only results in higher household bills but also drives up prices for food products, medicines, clothing, and other industrial processes mentioned in Figure 1-1.[12,18]

1.2. Present mature refrigeration technologies and most promising emerging alternatives

1.2.1. Active refrigeration technologies

Active cooling technology refers to systems where energy-consuming methods and devices are used to cool or maintain low temperatures in a specific environment. This technology uses mainly electronic or mechanical devices to generate and transfer cold temperatures. The most relevant examples for this *PhD Thesis* are:

a) Vapour compression refrigeration

Nowadays, vapour compression technology is strongly linked to our daily life and society. Most fridges, freezers or HVAC systems are based on this technology, which makes use of refrigerant gases, most of them toxic/flammable and/or contaminants to the environment. This technology works with compression/decompression cycles where the refrigerant gas changes to liquid and back again to gas phase. The Figure 1-2 represents a simple vapour compression cycle of a refrigerant gas. Where **1** is the compressor, which compresses the gas, forcing a phase transition to liquid. This liquid has an excess of heat which is released in the condenser (**2**), heating the environment. After that, the liquid is conducted to **3** or the expansion valve, where the refrigerant is decompressed suffering back the phase transition to the gas state. Otherwise of **2**, the gas enters in the evaporator (**4**) with a deficiency of heat, adsorbing heat from the environment and cooling it.

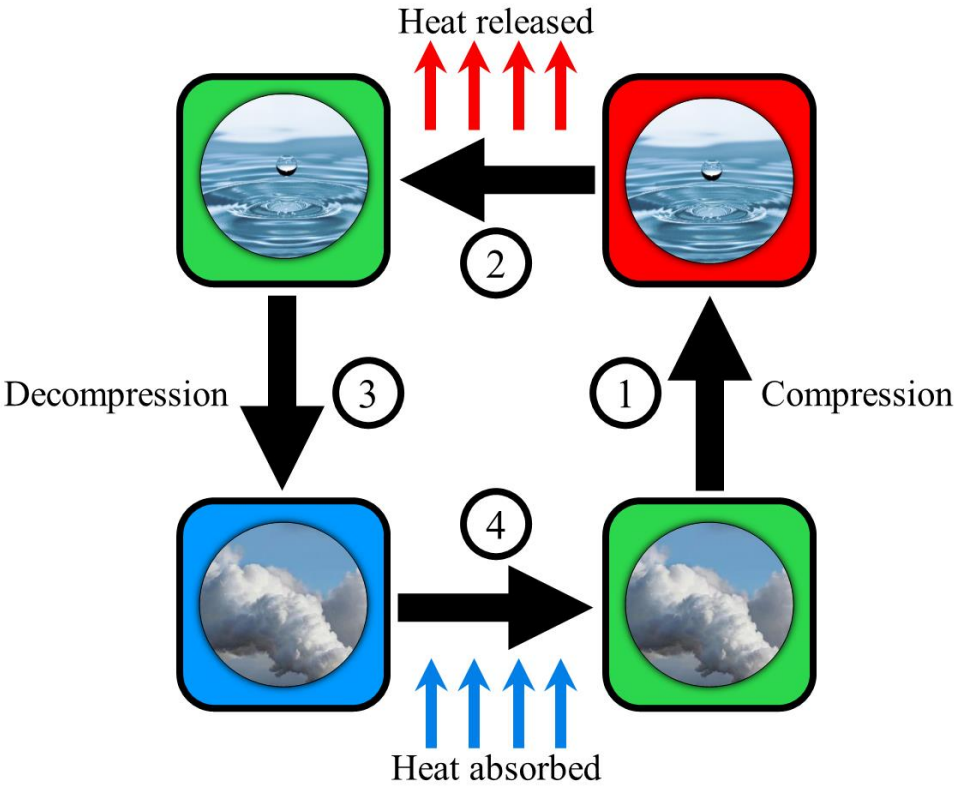

Figure 1-2. Simple vapour compression cycle for refrigeration with gases. 1: Compressor, 2: Condenser, 3: Expansion valve and 4: Evaporator.

This technology has been dominant and is the most used refrigeration technology from the invention of the first refrigeration device until nowadays. The problems and the solutions generated by this technology and its refrigerants gases, are translated into a constant evolution of the field.

The precursor of refrigeration devices based in vapour compression technology was proposed by O. Evans in 1805, where he suggested to evaporate ether under vacuum and pump the vapour into a heat extender cooling water and condensing the ether to be re-used.[19] But it was not until 1830s when J. Perkins built the first vapour compression device and in 1834 when he described the first patent using volatile fluids in order to produce the cooling or freezing and condensing them to be re-used producing zero waste.[20] After that, the refrigerant gases used in vapour compression technologies evolved and change depending on the main objectives of the era, such as efficiency,

safety, durability or ecology in the last decades. This evolution can be divided in four different generations (see Figure 1-3):

- The 1st generation (1830s – 1930s) was known as a period to test different refrigerant gases where the availability was prioritized. In this context, this generation was marked by the use of very common and cheap gases, highlighting propane (R-290), ammonia (NH_3 or R-717) and to a lesser extent carbon dioxide (CO_2 or R-744), between many others. This priority results in safety problems since most of the gases used end as toxic and/or flammable.[21–23]

- For that reason, and after some problems generated by leaks of the previous generation, the 2nd generation (1930s – 1990s) focused on safety and durability of the refrigerant gases. The first part of the generation was dominated by chlorofluorocarbons (CFCs) such as trichlorofluoromethane and dichlorodifluoromethane (R-11 and R-12, respectively). While in the second part, hydrochlorofluorocarbons (HCFCs) as chlorodifluoromethane or 2,2-dichloro-1,1,1-trifluoroethane (R-22 and R-123, respectively) grew in importance.[21,24,25]

- In the last years of the previous generation, diverse studies proved that the emission of HCFCs and more importantly CFCs were destroying the ozone layer of our planet due to their large Ozone Depletion Potential (ODP). This leads to the approval of the Montreal Protocol in 1987 in which all the participating countries committed to phase out the use of CFCs and reduce gradually the use of HCFCs with a full consumption phase out by 2030. With that in mind, CFCs disappear in the 3rd generation (1990s – 2010s) of refrigerant gases, where some of HCFCs with smaller ODP were still used, as 1,1-dichloro-1-fluoroethane (R141b), but the most relevant refrigerants in this generation were the hydrofluorocarbons (HFCs) as the 1,1,1,2-tetrafluoroethane (R134a) which nowadays is still one of the most used refrigerant gases. HFCs present several advantages such as very low operational pressure, they do not destroy the ozone layer (as CFCs or HCFCs), non-toxic, non-flammable and non-corrosive.[21]

- Finally, the current 4th generation (2010s – present) is focused on low *Global Warming Potential* (GWP) refrigerant gases. This comes from the rising temperature that our planet is suffering due to our emissions of tons of greenhouse gases to the atmosphere. It is well known that most HCFCs and HFCs have high GWP, showing up to 1000 times more GWP than CO_2. Because of that and in addition of the approval of the *Kigali Amendment* or the *F-Gas regulation* in 2014, this new generation changed the refrigerant gases to low GWP HFCs as 1,1-difluoroethane (R-152a), with GWP ~124, or hydrofluoroolefins (HFOs) as 1,1-difluoroethene or 2,3,3,3-tetrafluoroprop-1-ene (R-1132a and R1234yf, respectively), with GWP $\leq$ 1, among others.[21,26] However, most part of the industry is focusing in the return to old refrigerants. The two most arising options, which lost their protagonism few generations ago, are ammonia and carbon dioxide.[27,28] In the case of the natural refrigerant ammonia, it is an interesting alternative due to their very low GWP (< 1), high energy efficiency (high coefficient of performance, abbreviated as COP), excellent thermodynamic properties as high critical temperature (~405 K, allowing a large range of operating temperature), good heat transfer coefficients, large latent heat and vapor density, easy detection and very abundant (cheap). However, NH_3 still has the same important drawbacks which leaded to its disuse after 1st generation such as its toxicity, flammability, corrosiveness (in particular with copper) and high adiabatic exponent.[29] The other natural refrigerant, carbon dioxide appears to be the most compelling alternative and has been gaining importance in recent years. The main reason is the strengths that it presents in comparison with current HFCs:

    - Low GWP (= 1, due to CO_2 is the reference gas for the GWP values), making much less harmful for the atmosphere.

    - Higher thermal conductivity, vaporization latent heat and specific heat capacity.[30]

- Lower dynamic viscosity.[30]
- CO_2 is one of the most common chemical wastes produced by our society, which leads this gas to have a large availability and low price. In addition, HFCs are synthetic while CO_2 is a natural gas found in nature or as chemical waste. For that reason, this gas can be reused, helping the circular economy and avoiding any additional contamination from the synthesis.[31]

On the other hand, CO_2 has important drawbacks that impede the full transition to this refrigerant:

- Low COP, in other words low energy efficiency.
- CO_2 needs larger pressures to work (> 70 bar) in comparison to HFCs (< 10 bar), which is translated to the requirement of more sophisticated equipment, and more dangerous systems for the users.[32,33]
- Due to its low critical temperature (~304 K), it can be too difficult or impossible to work at higher temperatures, significantly shorting the operational temperature range of this gas.[32,33]

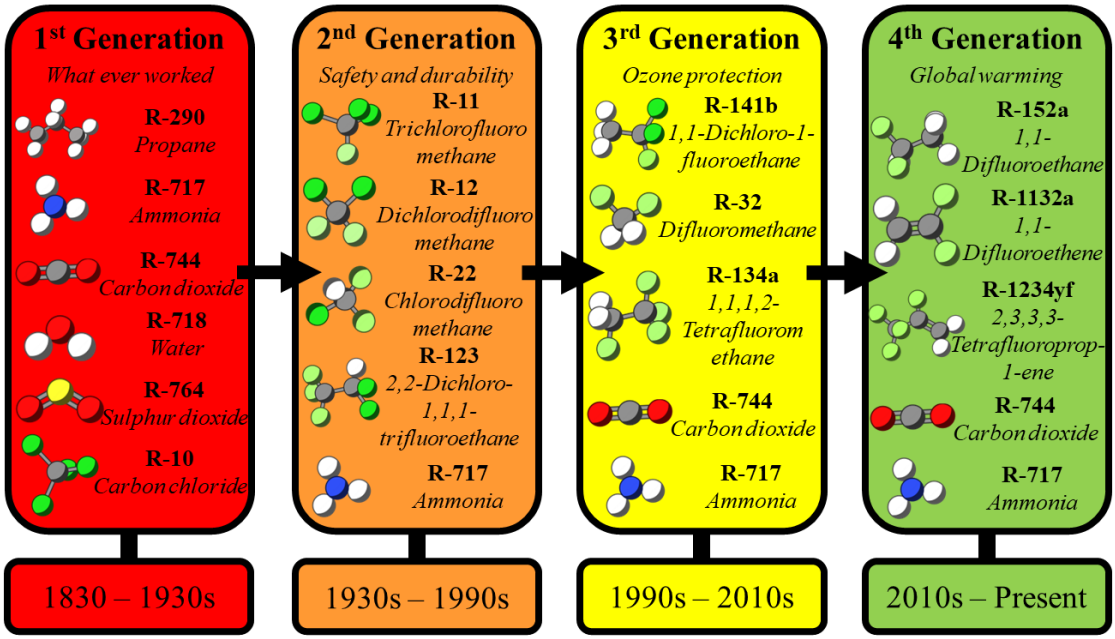

Figure 1-3. Some of the most relevant gas refrigerants of each generation for vapour compression technology. *Note*: Figure adapted from reference.[21]

b) Barocaloric refrigeration

One arising option for cooling is solid-state refrigeration which is based on thermomaterials (materials that have large latent heat associated to a solid-solid phase transition).[34] The latent heat related to the phase transitions shown by these solids involves a temperature interchange with the environment, heating (in case of exothermic transition) or cooling (in case of endothermic transition), very similar to refrigerant gases where the phase change is from liquid to gas and vice versa. The thermomaterials which present those characteristics are known as caloric materials. Interestingly, the transition of caloric materials can be induced by an external stimulus, such as temperature, magnetic and/or electric field or uniaxial/hydrostatic pressure, between others.[35,36]

One of this solid-state refrigeration alternative which arose over last years is the barocaloric refrigeration.[37–39] This cooling technology is based on the barocaloric effect, which is referred to

the temperature change that occurs when a solid-state material undergoes a reversible phase transition between two solid structures upon the application/retirement of pressure (see more details below). This system works with barocaloric materials in a manner similar to how vapour compression technology operates with refrigerant gases (see Figure 1-4):[40]

First, pressure is applied to the solid material in (**1**) which is in the initial state. This increase of pressure forces a solid-solid phase transition which involves a response of the material in terms of latent heat. This is translated into the release of heat to the environment in (**2**). After heating the environment, the pressure is reduced to the initial value in (**3**), where the material comes back to the initial state with an opposite response in terms of latent heat than before. Finally, the solid absorbs heat from the environment in (**4**), cooling it, ending at the starting phase and conditions of the material, closing the reversible cycle.[41]

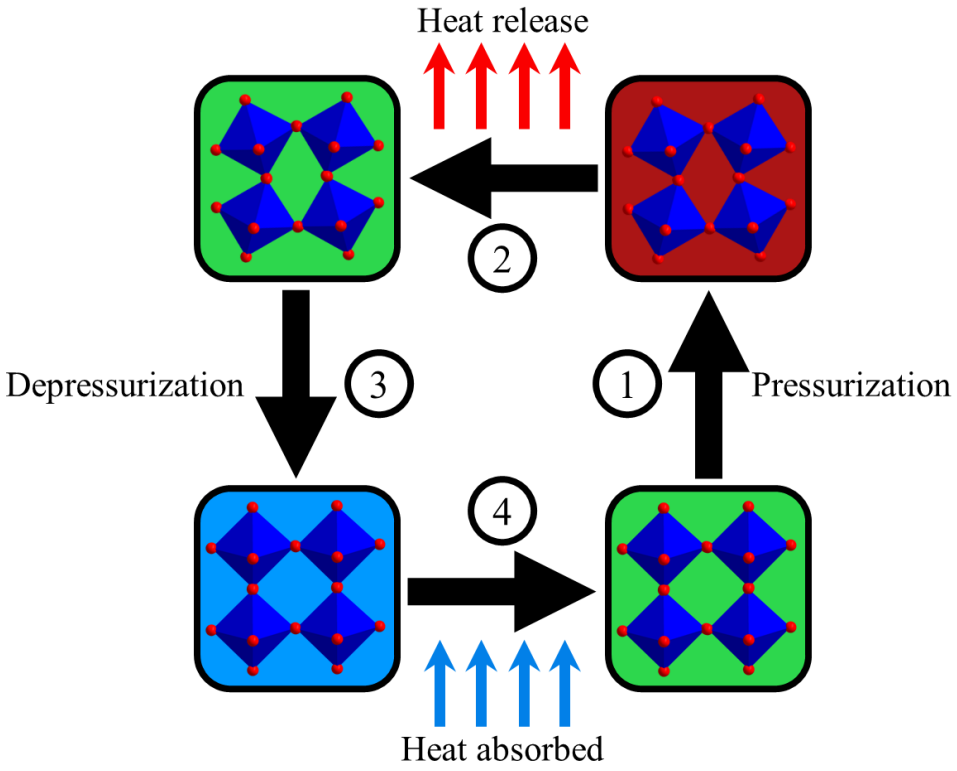

Figure 1-4. Simple pressurization/depressurization cycle of a solid-state material for heating/refrigeration.

Barocaloric refrigeration could be the substitution of well-stablish vapour compression technologies since the new technology carries out diverse advantages versus the well-stablish vapour compression:[42]

- Barocaloric refrigeration holds the potential for improving the low energy efficiency of vapour compression.
- This technology will reduce the environmental impact since barocaloric materials will not present emissions to the atmosphere. Thanks to that, they do not present ODP or GWP.
- Barocaloric refrigerants are safer than gases since they could not be toxic or flammable.
- More compact systems can be built due to the high density of the barocaloric solids in comparison with gases.

- The reparation of the barocaloric system should be simpler since the management of solids are easier than gases. Also, in case of breakdown, the refrigerant will not escape so replacement is not needed as happens in gases.
- The transportation of barocaloric refrigerants is also safer and cheaper since they do not need pressurized cylinders as gases.

Despite these numerous advantages, barocaloric refrigeration faces a significant obstacle: the majority of solids are highly insensitive to pressure, making it difficult to use them as refrigerants since they require excessively high pressures to be operated. Consequently, during the last few years, this technology has been focusing on the development and exploration of several material that do not exhibit this drawback, aiming to reduce the required operating pressure.

In this search, high sensitiveness to pressure in the materials, which can lead to lower operational pressures, is not only what barocaloric field is looking for. This field also considers various physical-chemistry and thermodynamic parameters when a solid material is analyzed as barocaloric refrigerant. These parameters will determine the potential of such materials for barocaloric applications:

- **Transition temperature (T_t)**: It is the temperature where the solid-solid phase transition occurs (see Figure 1-5a), generally this parameter is referred to the temperature at the maximum of the transition's peak in a differential scanning calorimetry (DSC), but T_t could be also defined as the onset (T_{onset}) or less usual offset (T_{offset}) (see Figure 1-5a). The desired T_t will depend on the application. It is necessary for the T_t to be as close as possible to the required temperature.
- **Thermal hysteresis:** It is the difference between the T_t in heating and in cooling (see Figure 1-5a). This is a crucial parameter for barocaloric applications: the higher thermal hysteresis, more pressure would be needed to see reversible effects. Therefore, for barocaloric applications thermal hysteresis should be as small as possible.
- **Operating pressure:** It is the pressure needed by the material to work as refrigerant. Commonly with higher pressures, the barocaloric parameters improve. Unfortunately, higher pressures involve more complicated devices, so for barocaloric applications the operating pressure should be as small as possible.
- **Barocaloric coefficient (dT/dp):** It is the sensibility of T_t to the applied pressure, in other words, how much T_t varies with pressure applied. Figure 1-5b shows a variable-pressure differential scanning calorimetry (VP-DSC) where the phase transition is displaced upon the increase of pressure. On the other hand, Figure 1-5c shows the phase diagram of a solid-state material with two phases, and how T_t increases upon the application of p, where the dT/dp is obtained as the slope of the curve. Commonly, $dT/dp > 0$, which means that T_t increases as pressure is applied. However, there are cases where the material exhibits an inverse barocaloric effect ($dT/dp < 0$), resulting in a decrease of T_t when pressure is applied.

  This parameter is essential in order to predict the behaviour of the material as barocaloric refrigerant. With the thermal hysteresis, barocaloric coefficient will enable the estimation of the pressure needed to see reversible barocaloric effects and will help to calculate the operating temperature of the material (see below). This parameter can be observed experimentally and can also be calculated theoretically by using the Clausius-Clapeyron equation (Equation 1-1):[36]

$$\frac{dT}{dp} = \frac{\Delta V}{\Delta S} \qquad \textbf{Equation 1-1}$$

  where ΔV is the volume change that exhibits the material and ΔS in the entropy change of the phase transition.

For barocaloric applications it is desirable to have barocaloric coefficients as large as possible.

- **Isobaric entropy change (ΔS_{ib}):** It is the entropy change exhibited by the phase transition of the material in isobaric conditions (see Figure 1-5d). This parameter is calculated by the integration of the isobaric curves through before and after T_t (Figure 1-5b) following the Equation 1-2:[13]

$$\Delta S_{ib} = S\left(T_f, p\right) - S\left(T_0, p\right) = \int_{T_0}^{T_f} \frac{1}{T} \frac{dQ}{dT}\left(T, p\right) dT \qquad \textbf{Equation 1-2}$$

where T_0 and T_f are the starting and ending temperature chosen by eye below and above of the transition, respectively, p is the constant pressure of each isobaric curve, p_{atm} is atmospheric pressure.

This parameter is of great importance for the barocaloric effect (see below), along with the barocaloric coefficient and thermal hysteresis. Therefore, the greater entropy change, the greater barocaloric effect, and the better the material's prospects for barocaloric applications.

It is worth noting that in order to obtain other barocaloric parameters, it is important to calculate the ΔS_{ib} taking account the specific heat capacity (C_p) contribution through Equation 1-3:[43]

$$\Delta S_{ib} = \int_{T_0}^{T_f} \frac{1}{T}\left[C_p\left(T, p_{atm}\right) + \frac{dQ}{dT}\left(T, p\right)\right] dT \qquad \textbf{Equation 1-3}$$

- **Barocaloric effect:** It is defined as the thermal response generated by a material upon the application of pressure. This effect can be given as either as an isothermal entropy change or as an adiabatic temperature change:
    - **Isothermal entropy change (ΔS_{it}):** It is the entropy change exhibited by the phase transition of the material in isothermal conditions (see Figure 1-5e). This parameter can be measured with pressure ramps under isothermal conditions (direct method) or calculated from the isobaric entropy change curves following the Equation 1-4 (quasi-direct method):[13]

$$\Delta S_{it} = \Delta S_{ib}(p \neq 1, T) - \Delta S_{ib}(p = 1, T) \qquad \textbf{Equation 1-4}$$

    - **Adiabatic reversible temperature change (ΔT_{rev}):** It is the temperature that the material can cool down or heat up and one of the most important values. This parameter defines how much the material can cool with one barocaloric cycle (see Figure 1-5f). It is calculated using the quasi-direct method and following the Equation 1-5:[43]

$$|\Delta T_{rev}(S;p_{atm}\leftrightarrow p)| = |T_C(S;p) - T_H(S;p_{atm})| \qquad \textbf{Equation 1-5}$$

    where $T_C(S;p)$ is each temperature of the cooling ΔS_{ib} at high pressure with the C_p contribution (Equation 1-3). While $T_H(S;p_{atm})$ is each temperature of the heating ΔS_{ib} at atmospheric pressure with the C_p contribution.

In barocaloric materials, the main focus is to find the largest possible barocaloric effects with minimal pressure application.

- **Operating temperature (T_{span}):** It is also a very important parameter as it will define the temperature range in which the material can work. It is calculated from the ΔS_{it} or ΔT_{rev} curves (see Figure 1-5e and 1-5f), being the difference of the temperature (axis x) from the start to the end of the curve. The larger T_{span}, the better the material for barocaloric refrigeration.

- The materials should be **non-toxic**, **non-flammable** and **non-corrosive**: The safety of the user and the cooling device is a vital requirement that the technology must meet in order to be commercially viable.

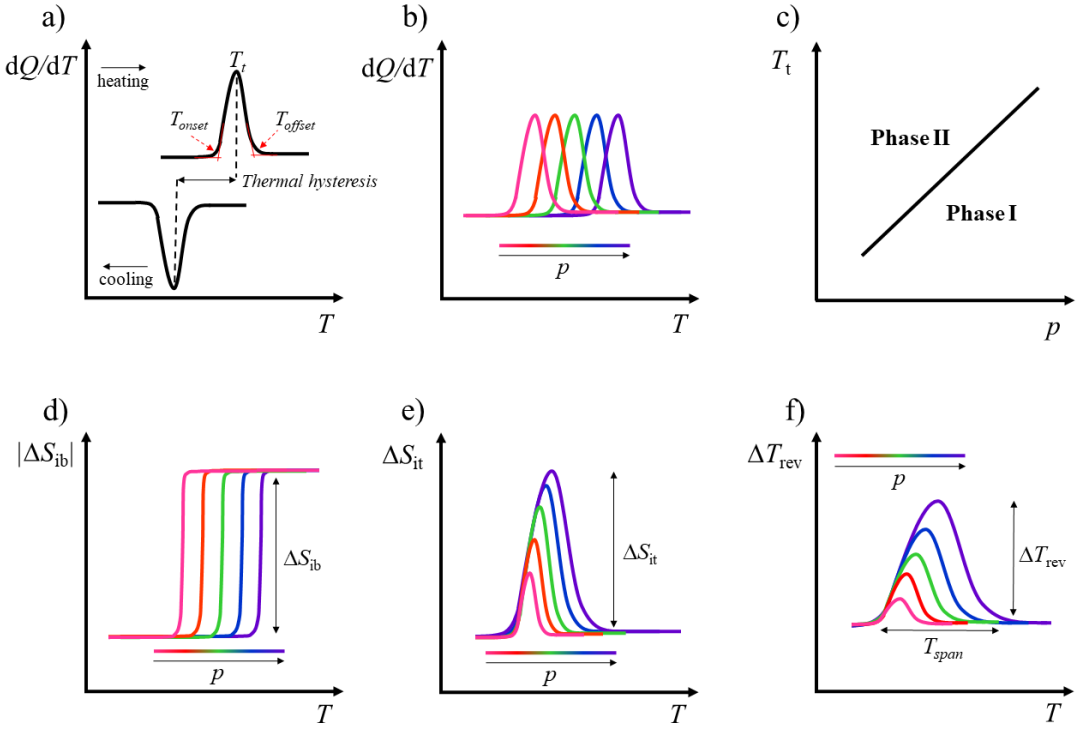

Figure 1-5. Various representations of the barocaloric parameters: a) temperature transition and thermal hysteresis, b), c) barocaloric coefficient, d) isobaric entropy change, e) isothermal entropy change and f) reversible adiabatic temperature change and operating temperature.

Since the beginning of this technology, many attempts have been made to find materials that could improve the parameters mentioned above. Thus, the first group of barocaloric materials that began to be studied was intermetallic compounds or metal alloys family. Representative examples of this family are compounds with general formulas $Gd_5(Ge_{1-x}Si_x)_4$ or $La(Fe_xSi_{1-x})_{13}$. These compounds exhibit small thermal hysteresis, which made them interesting in the field. However, due to their low dT/dp (requiring more than 1 kbar to operate) and their small barocaloric effects (ΔS_{it} ~20 J K^{-1} kg^{-1}, much lower than refrigerant gases), they turned out to be complicated to use as refrigerants.[40,44]

Another important milestone at the start of the barocaloric field was the discovery that the presence of NH_4^+ cations could enhance the thermal response by promoting the disorder transition in structures with fluorides or oxyfluorides. For example, the compound $(NH_4)_3MoO_3F_3$, reported in 2011, was the first hybrid perovskite in the barocaloric field and greatly increased the barocaloric effect compared to previous metal alloys (ΔS_{it} ~55 J K^{-1} kg^{-1}). Unfortunately, this value still remained far from refrigerant gases, and the pressure required to achieve it increased to 5 kbar.[45]

Other relevant compound to mention in the line of interest of NH_4^+ cation is the inorganic salt $(NH_4)_2SO_4$. In 2015, the inverse barocaloric coefficient of this material was reported, showing ΔS_{it} ~60 J K^{-1} kg^{-1} with the application of 1 kbar.[46]

A significant family in the field is the ionic superconductor, with the only example being AgI, described in 2017. Similarly to ammonium sulfate, this material exhibits ΔS_{it} ~64 J K^{-1} kg^{-1} with the application of slightly higher pressures, such as 2.5 kbar.[47] Both materials had significantly increased the thermal response and required lower pressures than $(NH_4)_3MoO_3F_3$. However, the

main advantage of these ionic compounds over the initial alloys is the simply and cheap synthesis. Despite all this, the barocaloric effect remains insufficient, and the working pressures are still too high to compete with refrigerant gases.

In addition, in 2017 a polymer was proposed as a barocaloric refrigerant, the natural rubber. It presented a ΔS_{it} ~21 J K^{-1} kg^{-1}, a very low value similar to some of the alloys, but with the main advantage that this effect is achieved with only the application of 0.43 kbar, less than half of the pressure required by the other mentioned materials. Additionally, another characteristic shown by natural rubber was its ability to work at very different temperature ranges (from 283 to 333 K), something unusual in the barocaloric field.[48]

An important step forward in the barocaloric field was the entry of hybrid perovskites of dicyanamide. Specifically, $[TPrA][Mn(dca)_3]$ (TPrA = tetrapropylammonium and dca = dicyanamide), which, despite not showing excessively high ΔS_{it} (~37 J K^{-1} kg^{-1}), it is the first barocaloric material capable of operating at pressures similar to vapor compression technology (p ~70 bar) due to its very low thermal hysteresis (~1 K) and its large dT/dp (~23 K $kbar^{-1}$).[13]

Continuing the search for refrigerants with high dT/dp values, in 2018, materials with spin-crossover properties entered in the field. This family is usually associated to solid-solid phase transitions with significant volume changes, as described in its first example in barocaloric field $[Fe(pzt)_6][(PF_6)_2]$ (pzt = 1-propyltetrazole). As expected, due to its high volume change, this material exhibited dT/dp ~29 K $kbar^{-1}$. Although its ΔS_{it} was not excessively high, ~46 J K^{-1} kg^{-1}, it solidified the spin-crossover materials' family as potential refrigerants for barocaloric applications.[49]

In 2019, the barocaloric effect of an organic plastic crystal known as neopentylglycol ($C_5H_{12}O_2$) was described. In contrast to the aforementioned perovskite, this material exhibited a gigantic thermal change (ΔS_{it} ~380 J K^{-1} kg^{-1}), capable of surpassing some refrigerant gases. However, its working pressures were again too high for practical applications (p ~2.5 kbar).[50]

With this in mind, the search for new barocaloric materials aims to find materials that can combine high thermal changes like neopentylglycol with reduced working pressures like $[TPrA][Mn(dca)_3]$.

c) Adsorption cooling

Adsorption cooling is an arising alternative based on the adsorption/desorption processes of gas molecules, called adsorbates, and porous solid materials, known as adsorbent. This technology shows a lot of variations depending on the adsorbates and the adsorbents used and their needs.[51,52] For that reason, despite this technology involves much more complex technology, Figure 1-6 presents a very simple process of adsorption cooling formed by two beds (the places where the adsorbent is handed in), only focused on the adsorption part (without any other addition, that are commonly find in this technology). In the adsorption bed, the porous solid material adsorbs the gas molecules producing an exothermic process which releases heat to the environment, heating it. After that, the adsorbent with the gas molecules in the pores, goes to the desorption bed in which the gas is desorbed obtaining the opposite results as in the adsorption, an endothermic process which absorbs the heat from the environment, cooling it.

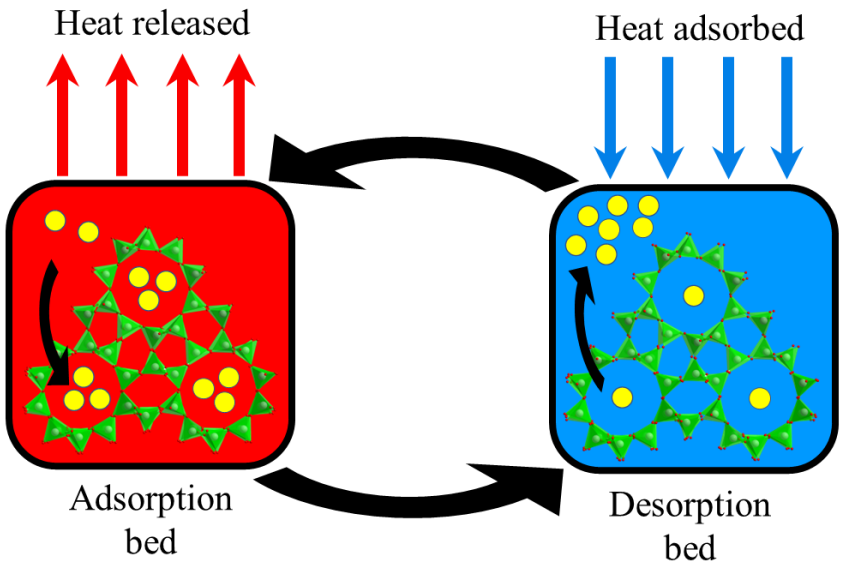

Figure 1-6. Simple adsorption cooling with only the adsorption and desorption beds. *Note*: for easier visualization, the adsorbate is placed randomly in the porous of the adsorbant.

Adsorption cooling has a wide range of possibilities, not only in the adsorbate and adsorbent, but also in the stimulus applied for the desorption such as vacuum or temperature. Increasing the temperature is an efficient manner of forcing the gas desorption and, moreover, the heat needed for that could come from renewable sources as solar, or heat waste from industry or engines.

There is large list of adsorbates, such as water,[53,54] methanol,[55] ethanol,[51] ammonia[56] and carbon dioxide,[51,52] between others. The selection of the adsorbate and the efficiency that the system will obtain is strongly linked to the adsorbent chosen. There are also many possibilities for such porous solid materials, some of them are:[51,52]

- **Activated carbons** encompass a wide range of amorphous carbonaceous materials that exhibit high porosity, providing them with a large surface area. These materials exhibit a wide diversity in terms of particle size, shape, and even functional groups on their surface, resulting in a variety of options and behaviours for adsorption applications.[57]
- **Zeolites** are microporous inorganic solids with a three-dimensional crystalline structure. They are primarily composed of aluminosilicates, although they can also contain other elements such as sodium, calcium, potassium, boron, iron and more. They possess a network of interconnected channels and cavities that form a structure with a large surface area and a regular distribution of uniformly sized pores.[58]
- **Silica gel** is a porous and granular material. It is composed of amorphous silica dioxide, which has a three-dimensional cage-like structure with interconnected pores. Due to its porous structure, it has a large surface area available to capture and retain principally water molecules.[59]

Another emerging family of porous solids for being used as adsorbents in adsorption cooling are metal-organic frameworks (MOFs). These solids are classified as porous hybrid organic-inorganic materials (HOIMs), formed by metal ions or clusters acting as joints in the MOF structure and organic linkers as secondary building blocks (SBU).[60] In addition, they can have up to 90% of empty space, exhibiting high surface areas, generating enormous porosity. This porosity results in a wide range of applications such as gas storage/separation, sensing, catalysis, drug delivery, and so on.[61] MOFs showed an extraordinary ability to adsorb an enormous variability of molecules in their pores, which in addition of the abovementioned, lead these structures as promising contenders for being adsorbents in adsorption cooling. Also, it is

significant to mention that the adsorption of gases in MOF structures is linked to a thermal change which is highly dependent on the interactions between the gas and the framework.[62]

Adsorption cooling is a promising alternative to vapour compression, but with road ahead. Finally, it is worth noting that, it shows advantages such as the possibility to use water or other non-harmful gases to the environment/users and the fact that some of the thermodynamic values are similar or even higher than some of vapour compression refrigerants. On the other hand, such devices are commonly more complex than vapour compression, and the COP is usually very low due to the thermal coupling irreversibility.[63]

1.2.2. Passive refrigeration systems: 'cold-storage'

The term "passive refrigeration" refers to refrigeration technologies that aim to achieve cooling without or with minimal energy consumption in order to improve their performance. Additionally, when passive systems does require energy, it is obtained from renewable sources in the majority of cases.[64]

Thermal energy storage (TES) is a passive technology that involves storing thermal energy for later use in heating/cooling and/or power generation applications.[65] In the particular case of using TES under room temperature, it is named 'cold-storage'.[66,67]

Cold-storage technologies use thermally-induced phase change materials (PCMs) that can absorb heat from the surroundings and store it, mainly in the form of latent heat, so they can help to cool down when the ambient temperature increases above their phase transition.[68] Most PCMs used for cold-storage applications are solid materials that undergo solid-liquid phase transitions from 20 ºC down to sub-zero Celsius.[68] These include eutectic mixtures (mixture of salts and salt/water), alcohols, hydrated salts, paraffins, fatty acids and clathrates.[65,68–70] These substances exhibit very large thermal changes, although they also present important drawbacks for devices, such as leaks of the liquid phase, incongruent melting, or mechanical strain due to large volume changes, among others.[68]

Trying to solve some of the limitations of the solid-liquid cold-storage materials, the scientific community has recently started to focus on solid-state PCMs (SS-PCMs). These thermomaterials undergo solid-solid (instead of solid to liquid) phase transitions upon change in ambient temperature.[71,72] These phase transitions have associated large thermal changes which are of interest for cooling and heating technologies. Among other advantages, these thermomaterials avoid any leak to the environment of hazardous and/or greenhouse fluids, avoid any incongruent melting and exhibit lower volume changes that would result into more compact devices and less mechanical strain of such devices.

For TES applications, the most studied SS-PCMs are typically organic polyalcohols (such as, pentaerythritol, neopentylglycol, trimethylolpropane and pentaglycerine) with plastic crystal transitions.[73,74] However, those materials work at room temperature and above, therefore, are not adequate for cold-storage applications (see Figure 1-7). For this reason, the scientific community is focusing on new SS-PCMs that exhibit thermal changes similar or greater than solid-liquid PCMs, that can operate below room temperature, and that can solve the problems mentioned before.

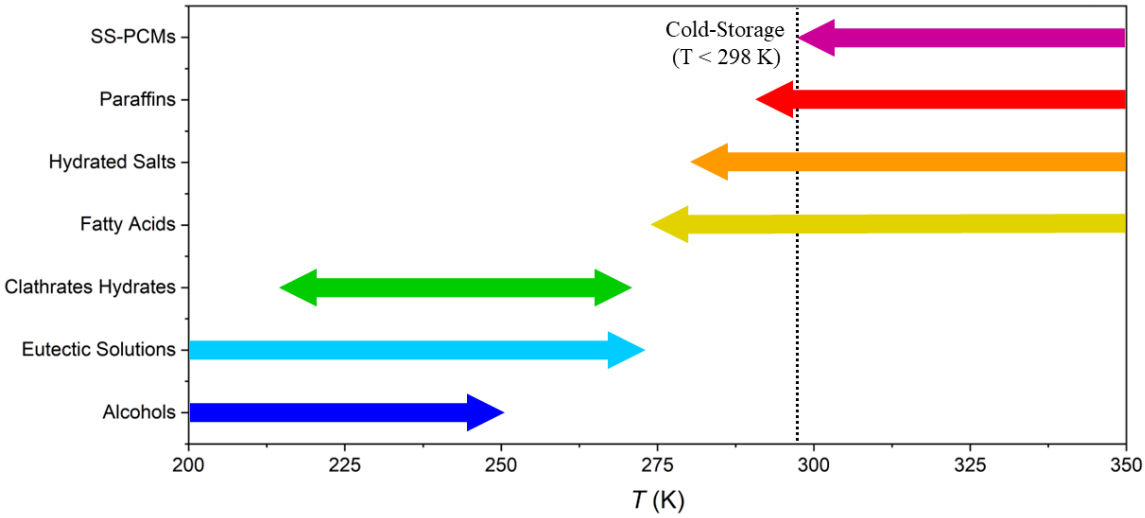

Figure 1-7. Current working temperature of the different families of PCMs. *Note:* Data obtained from the references.[71,75,76] *Note₂*: Figure adapted from reference.[76]

Among all types of thermal energy storage, PCMs are based on latent heat storage (LHS) where the material stores the thermal energy exclusively through a phase change.[77,78] To calculate the thermal energy storage capacity (E) of PCMs, factors such as mass, temperature range, heat capacity and latent heat of the phase transition are considered, following Equation 1-6:[77,79]

$$E = m\left\{\left[\int_{T_1}^{T_t} C_p^{LT}\,dT\right] + \Delta H + \left[\int_{T_t}^{T_2} C_p^{HT}\,dT\right]\right\} \qquad \textbf{Equation 1-6}$$

where m is the mass of the material or compound, T_1 is the initial temperature, T_2 is the final temperature, T_t is the temperature which the phase transition occurs, $C_{p(LT)}$ and $C_{p(HT)}$ are the specific heat capacities before and after the transitions, respectively, and ΔH is the latent heat of the phase transition.

PCMs have an important limitation as their temperature range is restricted to the phase transition. However, their enormous capacity to store thermal energy due to their latent heat makes them a highly attractive materials for 'cold-storage' systems.[80]

1.3. References

[1] "The Role of Refrigeration in Worldwide nutrition (2020), 6th Informatory Note on Refrigeration and Food," can be found under https://iifiir.org/en/fridoc/the-role-of-refrigeration-in-worldwide-nutrition-2020-142029, **2020**.

[2] G. Lorentzen, *Int. J. Refrig.* **1978**, *1*(3), 157-165.

[3] T. Lund, M. J. Skovrup, M. Holst, "Comparing energy consumption and life cycle costs of industrial size refrigeration systems," can be found under https://iifiir.org/fr/fridoc/comparaison-de-la-consommation-energetique-et-des-couts-sur-le-cycle-de-35093, **2019**.

[4] J. Wang, Y. Peng, H. Xu, Z. Cui, R. O. Williams, *AAPS PharmSciTech* **2020**, *21*, 225.

[5] Endesa, "Air conditioning: up to 1 litre per 100 km," can be found under https://www.endesa.com/en/blogs/endesa-s-blog/air-conditioning/heating-air-conditioning-car, **2019**.

[6] Y. Miao, P. Hynan, A. Von Jouanne, A. Yokochi, *Energies* **2019**, *12*, 1.

[7] Boyd, “What do EV Battery Cooling Systems do?,” can be found under https://www.boydcorp.com/industries/e-mobility/ev-battery-cooling-system.html#:~:text=Electric vehicle battery cooling plates,a heat exchanger or radiator, **2022**.

[8] K. Kim, G. Roh, W. Kim, K. Chun, *J. Mar. Sci. Eng.* **2020**, *8*(3), 183.

[9] P. Riaño, I. P. Gestal, “SOS de la industria: materias primas y energía ahogan al textil de cabecera,” can be found under https://www.modaes.com/entorno/sos-de-la-industria-materias-primas-y-energia-ahogan-al-textil-de-cabecera, **2021**.

[10] European Commission, “Re-conceptualize shopping malls from consumerism to energy conservation,” can be found under https://cordis.europa.eu/project/id/608678/reporting, **2018**.

[11] F. Birol, “The Future of Cooling Opportunities for energy- efficient air conditioning,” can be found under https://www.iea.org/reports/the-future-of-cooling, **2018**.

[12] “Renewables 2019, Analysis and forecast to 2024,” can be found under https://www.iea.org/reports/renewables-2019, **2019**.

[13] J. M. Bermúdez-García, M. Sánchez-Andújar, S. Castro-García, J. López-Beceiro, R. Artiaga, M. A. Señarís-Rodríguez, *Nat. Commun.* **2017**, *8*, 15715.

[14] NASA, “Vital Signs,” can be found under https://climate.nasa.gov/vital-signs/global-temperature/, **2022**.

[15] R. Lindsey, L. Dahlman, “Climate Change: Global Temperature,” can be found under https://www.climate.gov/news-features/understanding-climate/climate-change-global-temperature, **2023**.

[16] “Global Warming of 1.5 ºC,” can be found under https://www.ipcc.ch/sr15/, **2019**.

[17] “Thermal energy storage: Technology brief,” can be found under https://www.irena.org/publications/2013/Jan/Thermal-energy-storage, **2013**.

[18] D. Coulomb, J. Dupont, A. Pichard, “The Role of Refrigeration in the Global Economy (2015), 29th Note on Refrigeration Technologies,” can be found under https://iifiir.org/en/fridoc/the-role-of-refrigeration-in-the-global-economy-2015-138763, **2015**.

[19] O. Evans, *The Abortion OF The Young Steam Engineer’s Guide*, Philadelphia, USA, **1805**.

[20] J. Perkins, *Apparatus for Producing Ice and Cooling Fluids*, **1834**, 6662.

[21] J. M. Calm, *Int. J. Refrig.* **2008**, *31*, 1123.

[22] C. L. and P. Company, *Ice Refrig.* **1922**, *28*, 12.

[23] W. H. Carrier, R. W. Waterfill, *Refrig. Eng.* **1924**.

[24] R. C. Downing, *History of the Organic Fluorine Industry*, John Wiley And Sons, New York, USA, **1966**.

[25] R. C. Downing, *Development of Chlorofluoro-Carbon Refrigerants.*, Of, ASHRAE Transactions. American Society Heating, Refrigerating, And Air-Conditioning Engineers (ASHRAE), Atlanta, USA, **1984**.

[26] M. O. McLinden, M. L. Huber, *J. Chem. Eng. Data* **2020**, *65*, 4176.

[27] K. Zolcer Skačanová, M. Battesti, *Int. J. Refrig.* **2019**, *107*, 98.

[28] S. A. Tassou, J. S. Lewis, Y. T. Ge, A. Hadawey, I. Chaer, *Appl. Therm. Eng.* **2010**, *30*, 263.

[29] R. Ciconkov, Z. H. Ayub, *Heat Transf. Eng.* **2009**, *30*, 324.

[30] E. Bellos, C. Tzivanidis, *Energy Convers. Manag. X* **2019**, *1*, 100002.

[31] C. M. Hussain, M. S. Paulraj, S. Nuzhat, *Source Reduct. Waste Minimization* **2022**, 127, 1-22.

[32] *Emerson Clim. Technol.* **2015**, *6*

[33] R. Ciconkov, *Int. J. Refrig.* **2018**, *86*, 441.

[34] A. Kitanovski, U. Plaznik, U. Tomc, A. Poredoš, *Int. J. Refrig.* **2015**, *57*, 288.

[35] L. Caron, N. Ba Doan, L. Ranno, *J. Phys. Condens. Matter* **2017**, *29*(7), 075401.

[36] X. Moya, S. Kar-Narayan, N. D. Mathur, *Nat. Mater.* **2014**, *13*, 439.

[37] D. Boldrin, *Appl. Phys. Lett.* **2021**, *118*(17), 170502.

[38] L. Mañosa, A. Planes, *Adv. Mater.* **2017**, *29*(11), 1603607.

[39] C. Cazorla, *Appl. Phys. Rev.* **2019**, *6*, 041316.

[40] L. Mañosa, A. Planes, M. Acet, *J. Mater. Chem. A* **2013**, *1*, 4925.

[41] J. M. Bermúdez-García, *Classic molecular compounds and emergent organic-inorganic hybrid perovskites with (multi)functional properties and (multi)stimuli responsiveness* **2016**.

[42] C. Aprea, A. Greco, A. Maiorino, C. Masselli, *Energy* **2018**, *165*, 439.

[43] J. Li, M. Barrio, D. J. Dunstan, R. Dixey, X. Lou, J. L. Tamarit, A. E. Phillips, P. Lloveras, *Adv. Funct. Mater.* **2021**, *31*, 1.

[44] L. Mañosa, D. González-Alonso, A. Planes, M. Barrio, J. L. Tamarit, I. S. Titov, M. Acet, A. Bhattacharyya, S. Majumdar, *Nat. Commun.* **2011**, *2*, 1.

[45] I. N. Flerov, M. V. Gorev, A. Tressaud, N. M. Laptash, *Crystallogr. Reports* **2011**, *56*, 9.

[46] M. V. Gorev, E. A. Mikhaleva, I. N. Flerov, E. V. Bogdanov, *J. Alloys Compd.* **2019**, *806*, 1047.

[47] A. Aznar, P. Lloveras, M. Romanini, M. Barrio, J. L. Tamarit, C. Cazorla, D. Errandonea, N. D. Mathur, A. Planes, X. Moya, L. Mañosa, *Nat. Commun.* **2017**, *8*(1), 1851.

[48] E. O. Usuda, N. M. Bom, A. M. G. Carvalho, *Eur. Polym. J.* **2017**, *92*, 287.

[49] P. J. von Ranke, B. P. Alho, P. O. Ribeiro, *J. Alloys Compd.* **2018**, *749*, 556.

[50] P. Lloveras, A. Aznar, M. Barrio, P. Negrier, C. Popescu, A. Planes, L. Mañosa, E. Stern-Taulats, A. Avramenko, N. D. Mathur, X. Moya, J. L. Tamarit, *Nat. Commun.* **2019**, *10*, 1.

[51] F. Shabir, M. Sultan, T. Miyazaki, B. B. Saha, A. Askalany, I. Ali, Y. Zhou, R. Ahmad, R. R. Shamshiri, *Renew. Sustain. Energy Rev.* **2020**, *119*, 109630.

[52] A. N. Shmroukh, A. H. H. Ali, S. Ookawara, *Renew. Sustain. Energy Rev.* **2015**, *50*, 445.

[53] I. Solmuş, B. Kaftanoğlu, C. Yamali, D. Baker, *Appl. Energy* **2011**, *88*, 4206.

[54] S. Cho, J. Kim, *Energy* **1992**, *17*, 829.

[55] X. H. Li, X. H. Hou, X. Zhang, Z. X. Yuan, *Energy Convers. Manag.* **2015**, *94*, 221.

[56] M. Louajari, A. Mimet, A. Ouammi, *Appl. Energy* **2011**, *88*, 690.

[57] R. C. Bansal, M. Goyal, *Activated Carbon Adsorption*, CRC Press, Boca Raton, **2005**.

[58] B. Smit, T. L. M. Maesen, *Chem. Rev.* **2008**, *108*, 4125.

[59] K. C. Ng, H. T. Chua, C. Y. Chung, C. H. Loke, T. Kashiwagi, A. Akisawa, B. B. Saha, *Appl. Therm. Eng.* **2001**, *21*, 1631.

[60] M. Safaei, M. M. Foroughi, N. Ebrahimpoor, S. Jahani, A. Omidi, M. Khatami, *TrAC - Trends Anal. Chem.* **2019**, *118*, 401.

[61] K. Wang, Y. Li, L. H. Xie, X. Li, J. R. Li, *Chem. Soc. Rev.* **2022**, *51*, 6417.

[62] S. Bourrelly, P. L. Llewellyn, C. Serre, F. Millange, T. Loiseau, G. Férey, *J. Am. Chem. Soc.* **2005**, *127*, 13519.

[63] F. Meunier, *Clean Prod. Process.* **2001**, *3*, 0008.

[64] I. Oropeza-Perez, P. A. Østergaard, *Renew. Sustain. Energy Rev.* **2018**, *82*, 531.

[65] G. Li, Y. Hwang, R. Radermacher, *Int. J. Refrig.* **2012**, *35*, 2053.

[66] L. Cabeza, H. Mehling, *Heat and Cold Storage with PCM*, **2008**.

[67] Y. Zhao, X. Zhang, X. Xu, S. Zhang, *J. Mol. Liq.* **2020**, *319*, 114360.

[68] E. Oró, A. de Gracia, A. Castell, M. M. Farid, L. F. Cabeza, *Appl. Energy* **2012**, *99*, 513.

[69] G. Li, Y. Hwang, R. Radermacher, H. H. Chun, *Energy* **2013**, *51*, 1.

[70] X. Q. Zhai, X. L. Wang, T. Wang, R. Z. Wang, *Renew. Sustain. Energy Rev.* **2013**, *22*, 108.

[71] A. Fallahi, G. Guldentops, M. Tao, S. Granados-Focil, S. Van Dessel, *Appl. Therm. Eng.* **2017**, *127*, 1427.

[72] C. R. Raj, S. Suresh, R. R. Bhavsar, V. K. Singh, *J. Therm. Anal. Calorim.* **2020**, *139*, 3023.

[73] J. Font, J. Muntasell, J. Navarro, J.-L. Tamarit, J. Lloveras, *Sol. Energy Mater.* **1987**, *15*, 299.

[74] M. Barrio, J. Font, J. Muntasell, J. Navarro, J. L. Tamarit, *Sol. Energy Mater.* **1988**, *18*, 109.

[75] L. Yang, J. nan Huang, F. Zhou, *Energy Convers. Manag.* **2020**, *214*, 112876.

[76] "Types of Phase Change Materials," can be found under https://www.pcmproducts.net/Phase-Change-Material-Solutions.htm, **2023.**

[77] I. Sarbu, A. Dorca, *Int. J. Energy Res.* **2019**, *43*, 29.

[78] R. A. Huggins, *Energy Storage*, Springer Cham, Stanford, USA, **2016**.

[79] S. D. Sharma, K. Sagara, *Int. J. Green Energy* **2005**, *2*, 1.

[80] H. Mehling, J. Leys, C. Glorieux, J. Thoen, *SN Appl. Sci.* **2021**, *3*(2).

Chapter 2

Objectives

Chapter 2: Objectives

As was indicated in the introduction (*Chapter 1*), large thermal changes and low operational pressure, are two barocaloric parameters that are often difficult to combine. So, the main challenge of barocaloric refrigeration is to find materials with solid-solid phase transitions which could show large enough thermal changes mixed with acceptable operating pressure.

For that reason, this *PhD Thesis* have three-main objectives:

(1) ***Understanding and optimizing structure and phase transitions in hybrid dicyanamide-perovskites:*** One of the main limitations of barocaloric dicyanamide-perovskites is that they present relatively low barocaloric effects in terms of entropy changes (ΔS ~11.5 - 40 J K^{-1} kg^{-1}). To achieve this objective, an in-depth study of the hybrid dicyanamide perovskite structure will be necessary, along with the development of new chemistry strategies to obtain new promising barocaloric dicyanamide-perovskites.

(2) ***Exploring new organometallic and hybrid organic-inorganic families with plastic crystal transitions for barocaloric cooling and 'cold-storage':*** Organic plastic crystals are very well-known for their thermal energy storage capacity and, even more recently, also for presenting colossal barocaloric effects. However, both thermal properties are often mutually exclusive. Furthermore, one of the main limitations of barocaloric organic plastic crystals (mostly glycols or adamantine-derivatives) operate at very high temperatures (over 310 K) and under the application of very large pressures (over 1000 bar). This objective aims to find new families of hybrid plastic crystals which could work at lower temperatures and reduced operating pressures.

(3) ***Enhancing barocaloric effects through combination with other thermal effects*:** Barocaloric materials are postulated as a promising alternative for eco-friendly refrigeration. Nevertheless, in comparison with commercial refrigeration gases, these barocaloric materials present important drawbacks such as noticeably lower thermal changes, lower operating temperature ranges and/or higher operating pressures. The main point of this objective is to reduce or eliminate these drawbacks through the combination of barocaloric technology and other thermal effects as the used in adsorption cooling.

Chapter 3

New tools for chemistry engineered barocaloric hybrid dicyanamide perovskites

Chapter 3: New tools for chemistry engineered barocaloric hybrid dicyanamide perovskites

Index

3.1. Introduction to hybrid perovskites **37**

3.2. Identification of new distortions and degrees of freedom in hybrid dicyanamide perovskites **41**

3.2.1. Introduction 41

3.2.2. Experimental 42

3.2.3. Structural distortions 43

3.2.4. Conclusions 47

3.2.5. References 48

3.3. Revisiting the tolerance factor, a useful tool for engineering and designing novel hybrid dicyanamide perovskites **51**

3.3.1. Introduction 51

3.3.2. Experimental 54

3.3.3. Results and discussion 56

3.3.4. Conclusions 69

3.3.5. References 69

3.4. Modulation of the functional properties of hybrid dicyanamide perovskite by solid solution preparation **73**

3.4.1. Introduction 73

3.4.2. Experimental 74

3.4.3. Results and discussion 76

3.4.4. Conclusions 86

3.4.5. References 87

3.1. Introduction to hybrid perovskites

Hybrid organic-inorganic perovskites (HOIPs) show a general formula ABX_3, where A is an organic cation (in general, ammoniums or phosphoniums), B is a metal cation (commonly transition metals) and X can be halides (Cl^-, Br^- or I^-), classical inorganic anions (BF_4^-, ClO_4^- or $HPOO^-$, between others), organic anions (CN^-, $HCOO^-$, N_3^-, SCN^- or $N(CN)_2^-$) and in some cases linear complexes as dicyanometallates ($M(CN)_2^-$, where M is Ag^+ or Au^+) (see Figure 3-1).[1] This structure is based on 3D $[BX_3]^-$ networks where the anion X is six-coordinating the B-cation, forming $[BX_6]$ octahedra, and the resulting network's cavities are occupied by the A-cation which is twelve-coordinated by the anion, forming $[AX_{12}]$ cuboctahedra.[2] HOIP structure shows minimal or negligible voids, inaccessible for foreign molecules, giving the materials high stability and density (in comparison with other 3D HOIMs). However, the structure exhibits significant flexibility, making it of great interest for multiple applications. This is due to the organic components, which can move or adapt with great ease. On the other hand, this flexibility is translated in a high degree of susceptibility to distortions, such as tilting or shifting, among many others.

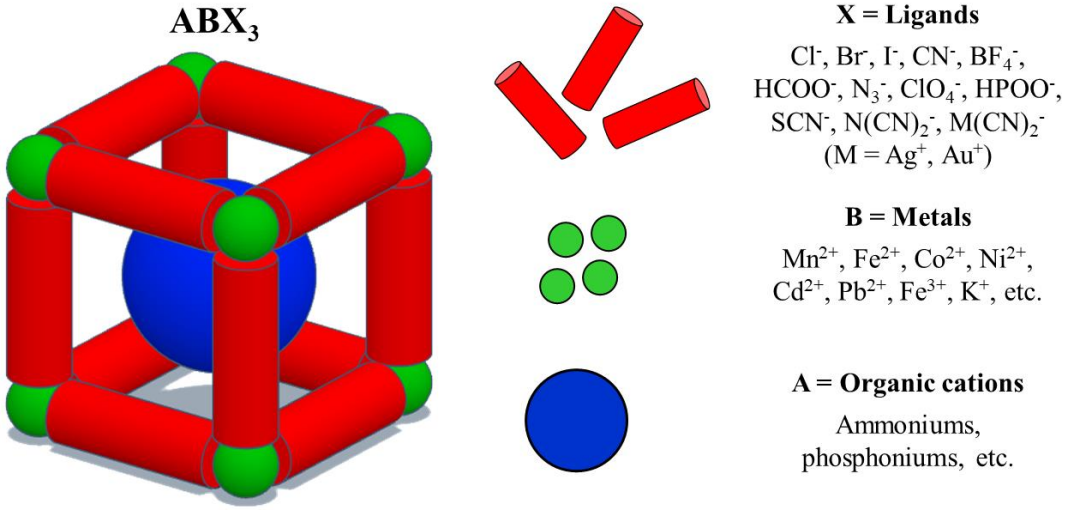

Figure 3-1. Scheme of hybrid organic-inorganic perovskites with general formula ABX_3.

Interestingly, HOIP structure allows this family to confer multifunctional properties as photovoltaic[3] and optoelectronic,[4] long-range ferroic order,[5] even type-I and type-II multiferroicity,[6,7] and very recently, and of greater interest for this *PhD Thesis*, for barocaloric purposes.[8–10]

There is a very large list of HOIPs, which can be classified in different forms. The most common classification is based on the type of anion. These anions can give to the structure various characteristics, but one of the most iconic is the cavity volume which is highly depended on the anion's length: from small chlorides (3.62 Å) allocating very small A-cations such as NH_4^+ to large dicyanometallates (9.50 Å) accommodating large A-cations as $[(Ph_3P)_2N]^+$ (see Figure 3-2).[11]

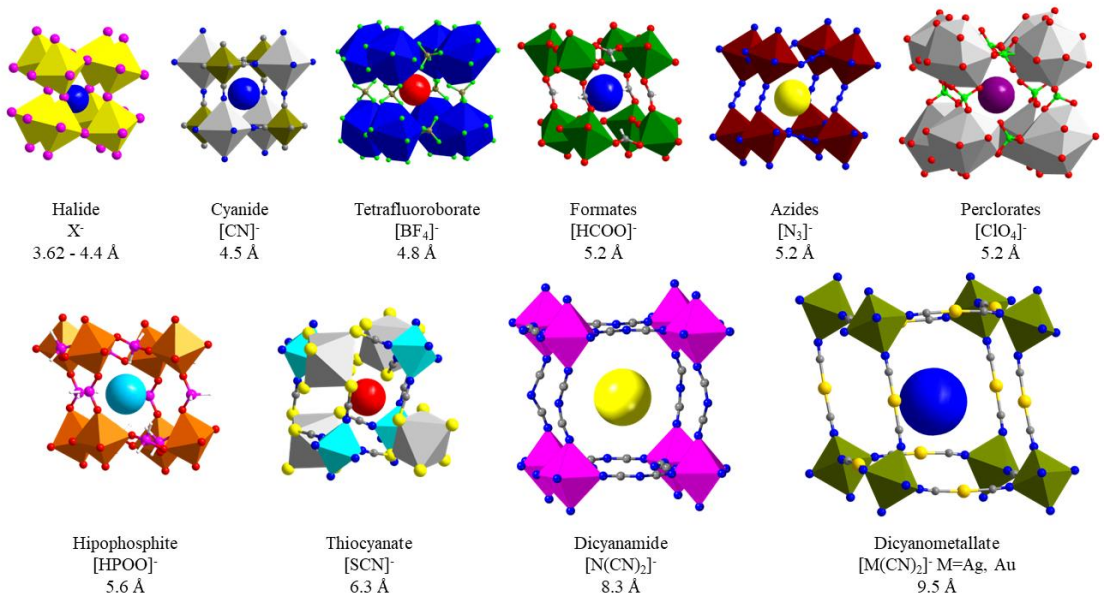

Figure 3-2. Different HOIPs with their anion's length. *Note*: Figure adapted from reference.[12]

As mentioned in *Chapter 1*, hybrid dicyanamide perovskites have tremendous potential in the field of barocaloric refrigeration. The two hybrid dicyanamide perovskites ([TPrA][M(dca)$_3$], M = Mn^{2+} and Cd^{2+}) reported in the barocaloric field exhibit significantly large barocaloric coefficients (dT/dp = 23.1 and 38.2 K bar^{-1}, respectively). This suggests that other perovskites within this family may have similar values, making them potentially attractive for barocaloric refrigeration.

With that in mind, this chapter is focused on the first objective mentioned in *Chapter 2*: to understand and to optimize the structure and phase transitions in hybrid dicyanamide perovskites. It begins with the subchapter titled '*Identification of new distortions and degrees of freedom in hybrid dicyanamide perovskites*', which aims to comprehend what makes this structure unique. Specifically, it reviews all hybrid dicyanamide perovskite structures reported, looking for their distortions. This will provide a better understanding of the desired characteristics in a hybrid dicyanamide perovskite for its application in the barocaloric field.

The next subchapter, titled '*Revisiting the tolerance factor, a useful tool for engineering and designing novel hybrid dicyanamide perovskite*' focuses on the design of new materials within this family. The tolerance factor is a highly useful tool that has long been employed for inorganic perovskites. Recently, efforts have been made to adapt it for hybrid perovskites, but this adaptation mainly targeted hybrid perovskites with short ligands such as azides and formates. However, for HOIPs with larger ligands like hybrid dicyanamide perovskites, the adaptation was not entirely reliable. Therefore, this subchapter aims to revisit and find a better way to calculate the tolerance factor for hybrid dicyanamide perovskites.

Lastly, the subchapter '*Modulation of the functional properties of hybrid dicyanamide perovskite by solid solution preparation*' explores the modulation of functional properties, including thermal and caloric properties, through the use of solid solutions.

References

[1] W. Li, Z. Wang, F. Deschler, S. Gao, R. H. Friend, A. K. Cheetham, *Nat. Rev. Mater.* **2017**, *2*, 16099.

[2] J. D. Tilley, Richard, *Perovskites: Structure-Property Relationships*, Wiley, **2016**.

[3] J. Burschka, N. Pellet, S.-J. Moon, R. Humphry-Baker, P. Gao, M. K. Nazeeruddin, M. Grätzel, *Nature* **2013**, *499*, 316.

[4] M. M. Lee, J. Teuscher, T. Miyasaka, T. N. Murakami, H. J. Snaith, *Science,* **2012**, *338*, 643.

[5] M. Sánchez-Andújar, S. Presedo, S. Yáñez-Vilar, S. Castro-García, J. Shamir, M. a Señarís-Rodríguez, *Inorg. Chem.* **2010**, *49*, 1510.

[6] B. Pato-Doldán, L. C. Gómez-Aguirre, J. M. Bermúdez-García, M. Sánchez-Andújar, A. Fondado, J. Mira, S. Castro-García, M. A. Señaris-Rodriguez, *RSC Adv.* **2013**, *3*, 22404.

[7] D. W. Fu, W. Zhang, H. L. Cai, Y. Zhang, J. Z. Ge, R. G. Xiong, S. D. Huang, T. Nakamura, *Angew. Chemie - Int. Ed.* **2011**, *50*, 11947.

[8] J. M. Bermúdez-García, M. Sánchez-Andújar, S. Castro-García, J. López-Beceiro, R. Artiaga, M. A. Señarís-Rodríguez, *Nat. Commun.* **2017**, *8*, 15715.

[9] J. M. Bermúdez-García, S. Yáñez-Vilar, A. García-Fernández, M. Sánchez-Andújar, S. Castro-García, J. López-Beceiro, R. Artiaga, M. Dilshad, X. Moya, M. A. Señarís-Rodríguez, *J. Mater. Chem. C* **2018**, *6*, 9867.

[10] J. Salgado-Beceiro, A. Nonato, R. X. Silva, A. García-Fernández, M. Sánchez-Andújar, S. Castro-García, E. Stern-Taulats, M. A. Señarís-Rodríguez, X. Moya, J. M. Bermúdez-García, *Mater. Adv.* **2020**, *1*, 3167.

[11] J. Lefebvre, D. Chartrand, D. B. Leznoff, *Polyhedron* **2007**, *26*, 2189.

[12] J. García-Ben, L. N. McHugh, T. D. Bennett, J. M. Bermúdez-García, *Coord. Chem. Rev.* **2022**, *455*, 214337.

3.2. Identification of new distortions and degrees of freedom in hybrid dicyanamide perovskites

Part of this work have been published in the review:

J. García-Ben, L. N. McHugh, T. D. Bennett, J.M. Bermúdez-García, *Coord. Chem. Rev.*, **2022**, *455*, 214337.

3.2.1. Introduction

The dca anion, $[N{\equiv}C\text{-}N\text{-}C{\equiv}N]^-$, is a very versatile ligand with one central N-amide atom and two end -C≡N cyanide groups. Since it was first used by Köhler *et al*. to obtain non-molecular solids,[1] it has been widely employed to obtain novel chemical architectures and compounds, some of which display long-range magnetic coupling between metals.[2]

This conjugated long anion displays three different N-coordination centres that can provide up to eight coordination modes with different denticity, as shown in Figure 3-3.[2] In the literature, a short nomenclature for each one of the coordination modes is often found. This nomenclature uses the symbol "μ" (which indicates coordination) followed by numbers that indicate the position where the dca ligand is linked with a given metal (where 1 and 5 indicate coordination through the N-cyanide atoms, and 3 indicates coordination through the N-amide atom). In that way, the dca ligands can be monodentate coordinating through one of the N-cyanide ends (μ_1) or through the N-amide atom (μ_3). Moreover, this anion can also act as a bidentate–bridge ligand when coordinating through the two N-cyanide ends ($\mu_{1,5}$) or through one of the N-cyanide atoms and the N-amide ($\mu_{1,3}$). And even more, in some cases, the dca ligand can present tridentate ($\mu_{1,3,5}$ or $\mu_{1,1,5}$), tetradentate ($\mu_{1,1,3,5}$) or pentadentate ($\mu_{1,1,3,5,5}$) coordination modes.

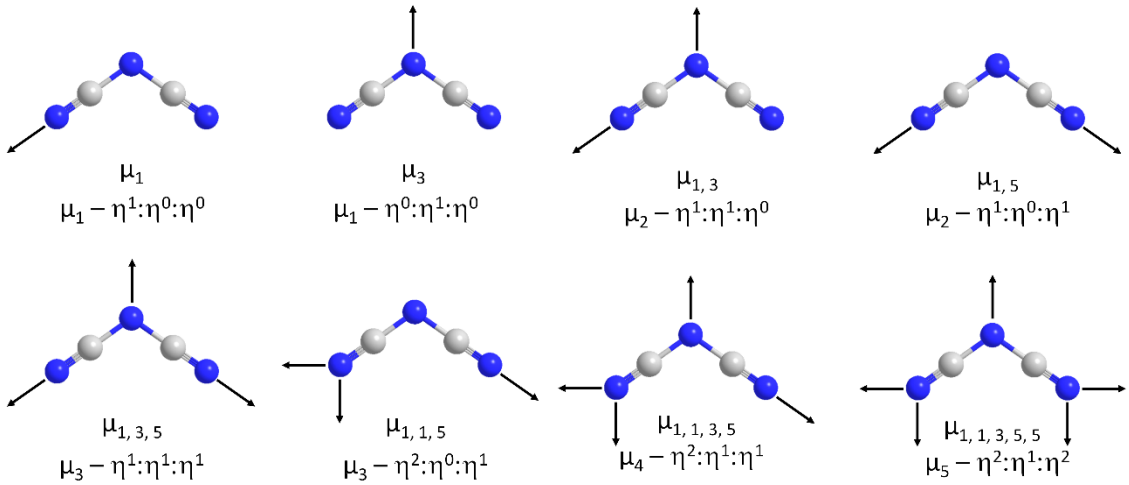

Figure 3-3. Coordination modes of the conjugated dca ($[N{\equiv}C\text{-}N\text{-}C{\equiv}N]^-$) ligand observed to date. The first nomenclature is the traditional short one (most commonly used in the literature), and the second nomenclature follows the normative IUPAC recommendations. *Note*: N-atoms are represented in blue, and C-atoms in grey.

Alternatively, and according to the IUPAC, the extended nomenclature for these coordination modes will use the symbol "μ_n" to represent the denticity of the ligand (where "n" shows the number of metals linked to the ligand) and the symbol "η^n" to indicate the hapticity of each N-

atom (where "n" shows the number of metals linked to the given N-atom).[3,4] Herein, as a matter of example, a pentadentate dca ligand can be defined as "$\mu_{1,1,3,5,5}$" in the traditional short nomenclature or "μ_5 - η^2:η^1:η^2" in the normative IUPAC nomenclature.

In what follows, it should be noted that all dicyanamide-perovskites exhibit only the $\mu_{1,5}$ (or μ_2 – η^1:η^0:η^1) coordination mode, which is also the most common mode found in most dicyanamide-containing compounds.[2]

Another remarked feature of the dca coordination modes is the bonding direction. In the literature, the $\mu_{1,5}$-dca coordination is generally represented as frontal bonding between the dca and the linked metals (Figure 3-4).[2] However, a deeper structural analysis (from the reported single crystal structures) shows that dicyanamide-perovskites present lateral dca-metal bonds related to the structural distortions (discussed further in section 3.2.3). In order to differentiate the observed lateral dca-metal bonds, this chapter adapts the nomenclature reported for formate-perovskites,[5] which identifies two types of bonding for each N-cyanide atom: *anti* and *syn* (Figure 3-4). These bonding modes are defined by studying the angle formed between the coordinated metal atom, the N-cyanide coordinating atom, and the N-amide non-coordinating atom (M−N−N). Accordingly, when the M−N−N angle is smaller than π, the bond direction is syn. Meanwhile, when this angle is larger than π, the bond direction is considered *anti*. From the different combinations of the bonding directions of both terminal N-atoms, three different possibilities are identified: *anti-anti*, *syn-syn*, and *syn-anti* (Figure 3-4).

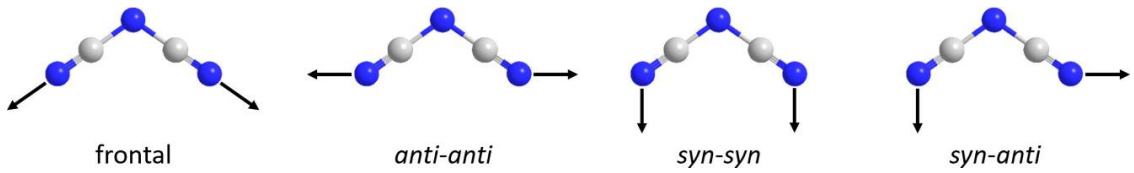

Figure 3-4. $\mu_{1,5}$-dca bond directions, namely frontal bond and lateral (*anti-anti*, *syn-syn* and *syn-anti*) bonds. *Note:* N-atoms are represented in blue, and C-atoms in grey.

In the ABX_3 dicyanamide-perovskites, these versatile dca anions occupy the X-site bridging divalent transition metal B cations (thus far only including Mn^{2+}, Fe^{2+}, Co^{2+}, Ni^{2+} and Cd^{2+}) and form $[B(dca)_6]$ octahedra. Remarkably, these dca ligands, with lengths of ~8.3 Å, are one of the longest ligands introduced to the HOIPs X-site. The resultant large pseudo-cuboctahedral cavities, in addition to the flexibility and the variety of coordination of the dca ligands, finalize a large list of different distortions.

3.2.2. Experimental

3.2.2.1. Search of hybrid dicyanamide perovskites

For the proper identification of the distortions presented by this family, all the structures reported in this family have been carefully searched. Various scientific search engines such as Google Scholar, Scopus and SciFinder, as well as different reviews of HOIPs, have been used for this purpose.[6–9]

3.2.2.2. Structure obtention

The structural files of all hybrid dicyanamide perovskites have been obtained through the Cambridge Crystallographic Data Centre (CCDC), using the codes from different scientific publications previously found.

3.2.2.3. Structure analysing

For the representation and study of all the found structures, the software Mercury[10] and Diamond[11] have been used. This study has focused primarily on the distances, angles, and crystallographic positions of the different atoms forming the structure, seeking possible transitions linked to significant changes in degrees of freedom. Finally, an attempt will be made to link these potential transitions to the thermal properties that may arise from them in order to optimize possible future searches for the barocaloric field.

3.2.3. Structural distortions

The dicyanamide-perovskites display a large variety of structural distortions, which allows the framework to adapt to vast range of different sizes and shapes of the A-cations. In that regard, this chapter has revisited the reported crystal structures of this family of HOIPs and have compiled their main structural distortions, which are summarized in Figure 3-5.[12–14]

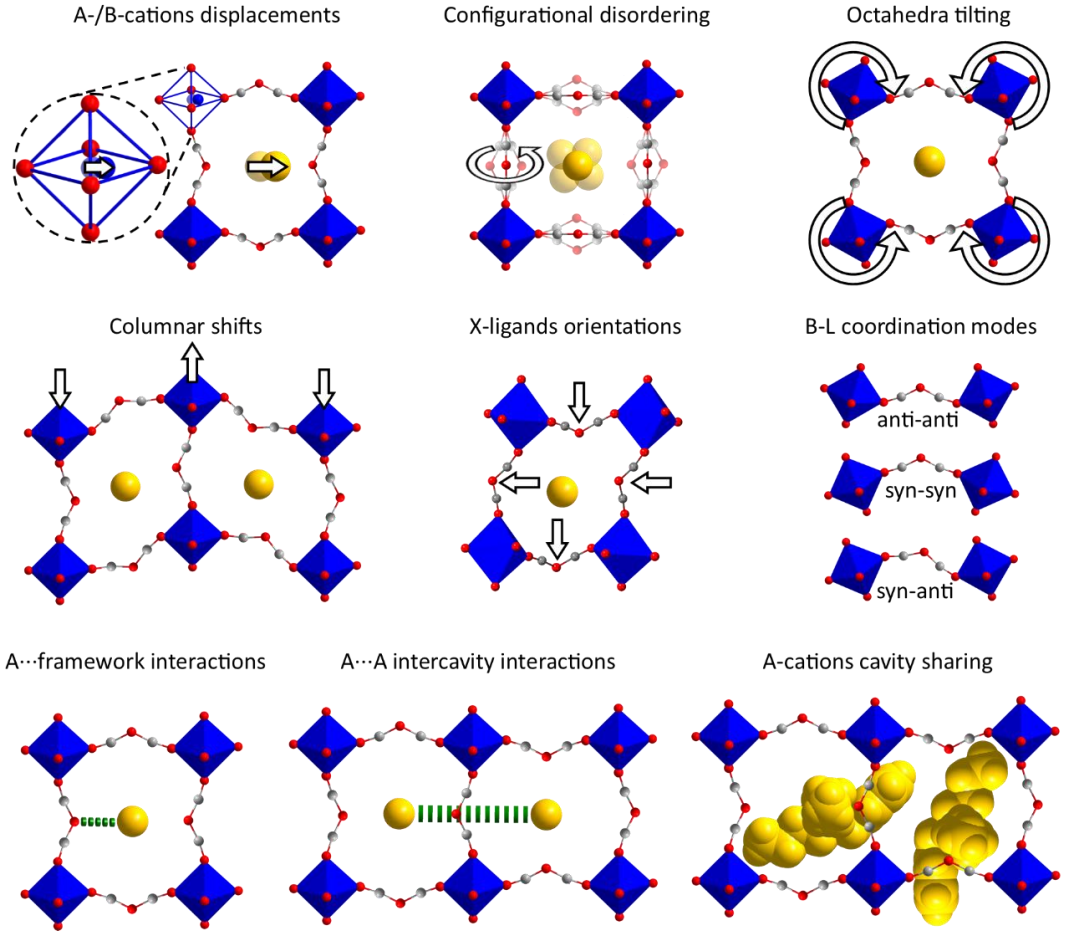

Figure 3-5. Schematics of the different structural distortions found in dicyanamide-perovskites. *Note:* the represented octahedra tilting is conventional (neighboring octahedra rotate in opposite directions). In dicyanamide-perovskites non-conventional tilting (neighboring octahedra rotate in the same directions) is also possible. The represented columnar shifts are out-of-phase (displaced in opposite directions), although in-phase shifts (displacement in the same direction) are also possible. The represented X-ligands orientation is in-phase (dca ligands oriented in the same direction), although out-of-phase orientations are also possible (as represented in all the rest of archetypical perovskite-cubes of this figure).

Some of these distortions are common to both inorganic perovskites and HOIPs (such as displacive, order-disorder and conventional octahedra tilting distortions). Meanwhile, some of them appear only in HOIPs with polyatomic X-ligands (such as non-conventional octahedra tilting, columnar shifts, different X-ligands orientations and B-X coordination modes, and interactions between the A-cation and the framework). Even more interestingly, a few of these distortions are exclusively found in dicyanamide-perovskites (such as what this chapter has called "extreme octahedra tilting" or interactions between A-cations and cavity sharing, see detailed explanations below), with some of them being described and analysed for the first time in this chapter.

Starting with the first group, and similar to what is observed for some inorganic perovskites, almost all the reported dicyanamide-perovskites can exhibit displacive distortions that may imply the A- and/or B-cations, that is, off-centre shifts of these cations from the centre of the $[AX_{12}]$ cuboctahedral cavities or the $[BX_6]$ octahedra, respectively. However, most of these displacements are antiparallel and/or randomly compensated so that they do not give rise to long-range ferroelectric order.[15,16]

Another distortion, also frequently found in inorganic and HOIPs, is the configurational disordering of the structure, which in the case of the dicyanamide-perovskites can simultaneously appear in the A-cations and X-ligands. Due to the larger number of contributing atoms that may increase the degrees of freedom of dicyanamide compounds, their resulting configurational disorder is much larger than in other perovskites. Additionally, this disorder highly increases with temperature and, in some cases, the dca ligands even act as rotors around the M-M longitudinal axis.[15,16]

The so-called columnar shifts are relatively new structural distortions that have only been observed in HOIPs. This term was introduced by A. L. Goodwin in 2016 as a new symmetry-breaking element in these materials. Columnar shifts refer to correlated displacements of columns of connected BX_6 octahedra (...-$[BX_5]$-X-$[BX_5]$-...), which can be displaced out-of-phase (in antiparallel directions) or in-phase (in the same direction).[12] In the literature, out-of-phase columnar shifts have already been reported,[12,17] and are the most commonly observed displacements.

As for structural distortions derived from octahedral tiltings, it is best to first describe the concepts of conventional and non-conventional tiltings before explaining the recently observed "extreme octahedra tilting". In this context, the first term refers to the distortions in which neighbouring octahedra rotate in opposite directions (see Figure 3-5).[18] This is the situation typically found in perovskites with monoatomic X-anions (i.e. inorganic perovskites and hybrid halide perovskites)[18], which can exclusively exhibit this type of rotation. This distortion is also found in most dicyanamide-perovskites. In addition, HOIPs containing polyatomic ligands in the X-site may also present the so-called "forbidden" or non-conventional rotations, where neighbouring octahedra rotate in the same direction. However, these distortions are very rare and, up to now, were only found in a few perovskites, where X = azide,[19,20] dicyanometallate,[21] and hyphophosphite.[22]

Traditionally, conventional tilting in oxide- and halide-perovskites can be described by the simple Glazer notation.[18] However, HOIPs show the coexistence of conventional and non-conventional tilts together with columnar shifts, which hinder the use of this simple notation to unambiguously defined tilting modes. Accordingly, HOIPs octahedral tilts are normally defined by using complex group-theoretical software, rigid unit modes (RUMs) and the corresponding irreps, although these studies are still scarce. At this point, it should be noted that a complex "tilting engineering" study is far from the scope of this chapter, and the reader can find excellent works on this topic elsewhere.[6,12,23] In the same line, this investigation into the reported structures also helped to discover another rare form of octahedra tilting, where this chapter found that the $[Et_3P(CH_2CH_2F)][Mn(dca)_3]$ perovskite (and its Cd-analogue)[24] exhibits a singularity never observed before in other HOIPs. So, since $[Et_3P(CH_2CH_2F)]^+$ is the smallest A-cation fitted in a dicyanamide-perovskite,[24,25] the framework has to largely shrink the A-cavities to accommodate

it. The framework consequently rotates the octahedra in a peculiar and unprecedented form of tilting, which in this chapter was named “extreme octahedra tilting”. This distortion consists of conventional tilts with a maximized angle of rotation of 45º, where the octahedra edges adopt a face-to-face orientation (Figure 3-6). Following this strategy, the cavity of this perovskite achieves a volume reduction of ~80% in comparison with the dicyanamide-perovskite that integrates the largest A-cation so far, namely, the $[Bu_3NBn]^+$ cation.[26]

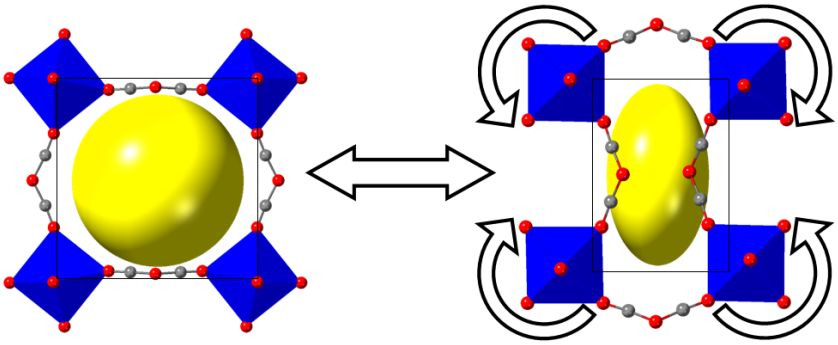

Figure 3-6. Schematics of the “extreme octahedral tilting” observed in the dicyanamide-perovskites $[Et_3(CH_2CH_2F)P][M(dca)_3]$ ($M = Mn^{2+}$, Cd^{2+}),[25,27] where the octahedra exhibit a conventional rotation with a maximized angle of 45° facing edges.

In order to illustrate the diversity of distortions that the dicyanamide-perovskites can exhibit, three compounds have been chosen as case studies (Figure 3-7). The first one is $[Pr_4N][Fe(dca)_3]$[15] (polymorph observed at 200 K), which shows out-of-phase columnar shifts along the *a*- and *b*-axes with conventional octahedra tilts perpendicular to the *ab*-plane (red arrows), which results in an out-of-phase orientation of the dca-ligands along the *a*- and *b*-axis (green arrows). The second compound, $[Et_3P(CH_2CH_2F)][Mn(dca)_3]$ (polymorph observed at 293 K),[25] exhibits in-phase columnar shifts along the [011] direction and conventional octahedral tilting perpendicular to the $(11\bar{1})$ plane (red arrows), which leads to an out-of-phase orientation of the dca ligands along the [020] and $[1\bar{2}2]$ directions (green arrows). Finally, the $[Et_3P(CH_2OCH_3)][Mn(dca)_3]$[28] (200 K polymorph) shows in-phase columnar shifts along the *c*-axis and non-conventional octahedral tilting perpendicular to the *ac*-plane (red arrows), resulting in the dca ligands being oriented in-phase along the *c*-axis and along the $[3\bar{1}2]$ direction (green arrows).

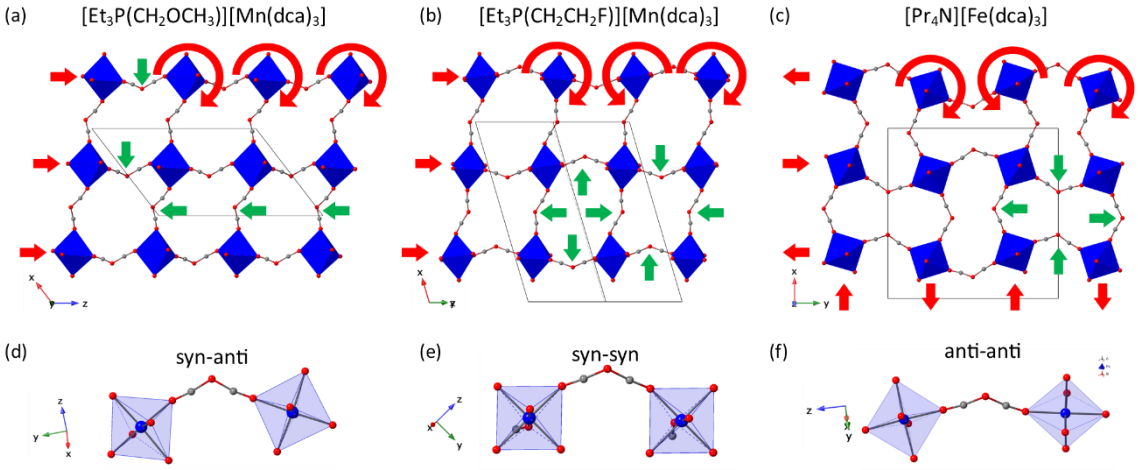

Figure 3-7. Selected structural distortions for the (a,d) $[Pr_4N][Fe(dca)_3]$[15] (b,e) $[Et_3(CH_2CH_2F)P][Mn(dca)_3]$,[25] and (c,f) $[Et_3(CH_2OCH_3)P][Mn(dca)_3]$[28]dicyanamide-perovskites. *Note:* straight red arrows represent columnar shifts, curved red arrows represent octahedral tilting, and straight green arrows represent X-ligands orientations. Unit-cells are represented by black lines.

It could therefore deduce that the combination of the columnar shifts and the octahedra tilting influences the orientation of the dca ligand when coordinated in the framework. In that regard, conventional octahedra tilting, together with in-phase or out-of-phase columnar shifts, give rise to dca ligands oriented out-of-phase. Meanwhile, non-conventional octahedra tilting together with in-phase columnar shifts induces in-phase orientation of dca ligands. Furthermore, these distortions highly affect the size and shape of the cavities and their windows. For instance, the $[Pr_4N][Fe(dca)_3]$ shows double-pentagon cavity-windows, the $[Et_3P(CH_2CH_2F)][Mn(dca)_3]$ displays both star-shaped and oval-shaped cavity-windows, and the $[Et_3P(CH_2OCH_3)][Mn(dca)_3]$ compound exhibits a mushroom-shaped cavity-window (see Figure 3-7a-c).

It should be noted that this is the first time that non-conventional octahedra tilting and in-phase columnar shifts have been identified and described for dicyanamide-perovskites, further enlarging the already rich diversity of distortions known for this family of compounds.

These three compounds can also serve as an example for the different B-X coordination modes depending on the M-N-N angle. As was explained in section 3.2.1, when the internal M-N-N angle of dca is bigger than π, this chapter denotes the coordination as an *anti* mode. On the contrary, when this angle is smaller than π, the coordination is called a *syn*-mode. As the dca ligand has two N-amide coordinating centres, there are three possible coordination modes: *anti-anti*, *syn-syn* and *syn-anti* (see Figures 3-4 and 3-7d-f). The *anti-anti* and *syn-anti* modes have already been observed in formate-perovskites,[5] however here in this chapter it is identified a *syn-syn* coordination mode in the $[Et_3P(CH_2CH_2F)][Mn(dca)_3]$ perovskite that is described for the first time in any member of the vast HOIP family.

Following more complex distortions, and as already mentioned in the case of "extreme octahedra tilting", the dicyanamide-perovskites use distortions as a strategy to accommodate A-cations. For example, for accommodating cations as large as $[Bu_3NBn]^+$, $[Et_3NBn]^+$ or $[Ph_3S]^+$,[26,29] the dicyanamide-perovskites find a solution unobserved in any other HOIP, and that more closely resemble characteristics typical of MOFs. In this case, the large A-cations can partially occupy more than one $[AX_{12}]$ cavity and, on the other side, there is a "cavity sharing" where each $[AX_{12}]$ cavity hosts two partial A-cations (see Figure 3-8).

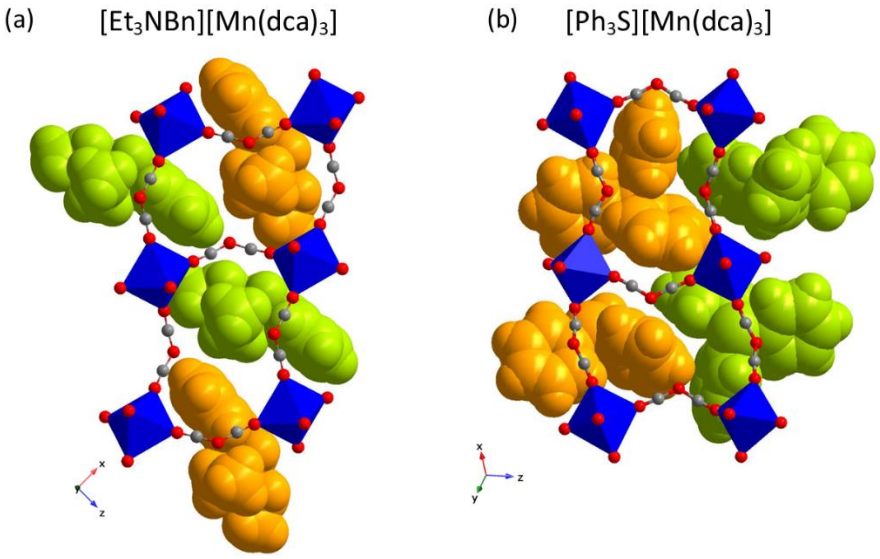

Figure 3-8. Examples of the cavity sharing of A-cations inside the same $[AX_{12}]$ cuboctahedron for the (a) $[Et_3BnN][M(dca)_3]$ (M = Mn^{2+}, Fe^{2+})[26] and (b) $[Ph_3S][Mn(dca)_3]$[29] perovskites. *Note:* A-cations sharing the same cavity are represented by different colours (green and orange) to aid visualization.

In addition, dicyanamide-perovskites can also exhibit interactions between the A-cations and the framework. Some of these interactions, such as the "A-H···X" hydrogen bonds first reported by

M.-L. Tong *et al.* in dicyanamide-perovskites,[26] are also observed in other HOIPs.[30] However, the large volume of the cuboctahedra cavities allows the presence of new supramolecular "A···A" and "A···framework" interactions, which are uncommon in HOIPs but generally found in MOFs. For instance, our deep structural study for this review reveals "intercavity interactions" of A-cations through "A-H···Cl-A" hydrogen bonds. This phenomena occurs in the $[Et_3P(CH_2CH_2Cl)][M(dca)_3]$ (M = Mn^{2+} and Cd^{2+}) perovskites,[24,25] see Figure 3-9a.

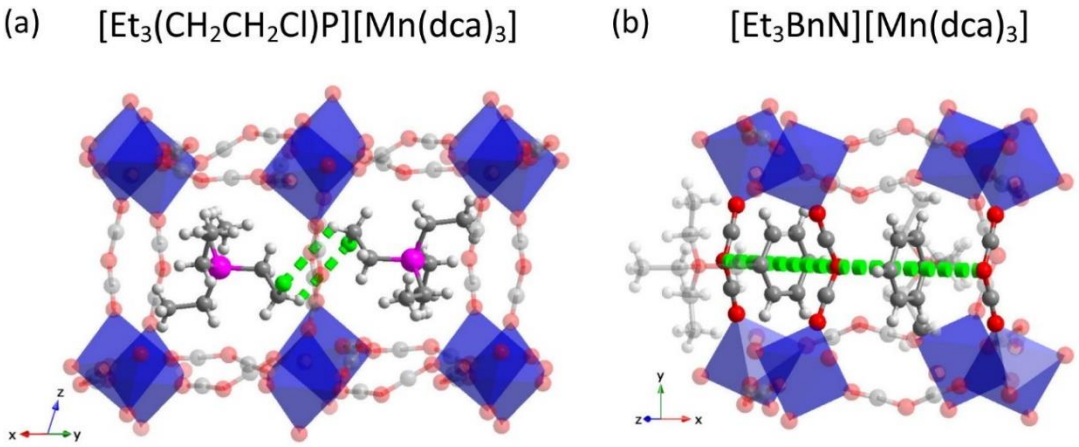

Figure 3-9. (a) Intercavity interactions of "AH···XA" hydrogen bonds observed in $[Et_3(CH_2CH_2Cl)P][M(dca)_3]$ (M = Mn^{2+} and Cd^{2+}) perovskites,[24,25] and (b) detected supramolecular π···π staking interactions between the benzyl groups of the A-cations and dca-ligands of the framework in $[Et_3BnN][M(dca)_3]$ (M = Mn^{2+}, Fe^{2+})[26] perovskites. *Note:* transparent colours are used to aid visualization of the interacting parts represented by solid colours. Green dash lines are visual guides representing the interactions.

Furthermore, in this chapter is also noticed the presence of singular "π···π" staking interactions between the dca-ligands and the aromatic rings of A-site cations, which occurs in $[Et_3NBn][M(dca)_3]$ (M = Mn^{2+}, Fe^{2+}) and $[Bu_3NBn][M(dca)_3]$ (M = Mn^{2+}, Co^{2+}) (Figure 3-9b). In view of these uncommon features, this chapter anticipate that such intermolecular interactions could give rise to new functional properties, such as charge transport or photosensitivity.

It is worth mentioning that phase transitions are strongly linked to changes in entropy (or thermal changes) based on the difference in degrees of freedom between the phases.

With this in mind, for the search of hybrid dicyanamide perovskites for barocaloric applications, it is essential to focus on structures that may exhibit solid-solid transitions involving distortions with significant changes in degrees of freedom. Among the most noteworthy distortions, the configurational disordering stand out above the rest. These are often associated with high changes in degrees of freedom, which translates to remarkable changes in entropy. Other distortions that can be estimated to have significant changes in the compound's degrees of freedom include A-cation interactions with the framework of other A-cations, extreme octahedral tilting, and cavity sharing.

3.2.4. Conclusions

When dicyanamide acts as a ligand, it exhibits a set of characteristics that give rise to numerous distortions in structures such as hybrid dicyanamide perovskites, leading to possible solid-solid phase transitions. The ligand's shape, its various coordination possibilities, and its potential interactions with the A cations of the perovskite, due to their double bonds, result in a wide range of distortions that can be involved in solid-solid transitions.

While hybrid dicyanamide perovskites may display the well-studied distortions typically found in classical inorganic perovskites, these hybrid structures present an extensive list of new distortions, some of which have not been reported previously in any HOIPs, as extreme octahedra tilting and cavity sharing.

The magnitude of the thermal changes involved in phase transitions tends to be correlated to the nature of the transition's distortion or the difference in the degrees of freedom between the phases. Considering this, and within this extensive list of distortions in the search of transitions with significant thermal changes for barocaloric applications, the most intriguing ones include configurational disorder, A-cation interactions with the framework of other A-cations, extreme octahedral tilting, or cavity sharing.

3.2.5. References

[1] A. M. Golub, H. Köhler, V. V. Skopenko, *Chemistry of Pseudohalides*, Elsevier, Oxford, **1986**.

[2] S. R. Batten, S. M. Neevillee, D. R. Turner, *Coordination Polymers - Design, Analysis and Application*, RSCPublishing, Victoria, Australia, **2009**.

[3] N. G. Connelly, T. Damhus, R. M. Hartshorn, A. T. Hutton, *NOMENCLATURE OF INORGANIC CHEMISTRY IUPAC Recommendations 2005 IUPAC Periodic Table of the Elements Fm No*, **2005**.

[4] J. Gao, K. Ye, M. He, W. W. Xiong, W. Cao, Z. Y. Lee, Y. Wang, T. Wu, F. Huo, X. Liu, Q. Zhang, *J. Solid State Chem.* **2013**, *206*, 27.

[5] L. C. Gómez-Aguirre, B. Pato-Doldán, A. Stroppa, S. Yáñez-Vilar, L. Bayarjargal, B. Winkler, S. Castro-García, J. Mira, M. Sánchez-Andújar, M. A. Senaris-Rodriguez, *Inorg. Chem.* **2015**, *54*, 2109.

[6] H. L. B. Boström, A. L. Goodwin, *Acc. Chem. Res.* **2021**, *54*, 1288.

[7] W. J. Xu, Z. Y. Du, W. X. Zhang, X. M. Chen, *CrystEngComm* **2016**, *18*, 7915.

[8] W. Li, Z. Wang, F. Deschler, S. Gao, R. H. Friend, A. K. Cheetham, *Nat. Rev. Mater.* **2017**, *2*, 16099.

[9] B. Saparov, D. B. Mitzi, *Chem. Rev.* **2016**, *116*, 4558.

[10] C. F. MacRae, I. Sovago, S. J. Cottrell, P. T. A. Galek, P. McCabe, E. Pidcock, M. Platings, G. P. Shields, J. S. Stevens, M. Towler, P. A. Wood, *J. Appl. Crystallogr.* **2020**, *53*, 226.

[11] K. Brandernburg, M. Berndt, *J. Appl. Crystallogr.* **1999**, *32*, 1028.

[12] H. L. B. Boström, J. A. Hill, A. L. Goodwin, *Phys. Chem. Chem. Phys.* **2016**, *18*, 31881.

[13] S. Ezzine Yahmed, R. Nasri, M. F. Zid, A. Driss, *Acta Crystallogr. Sect. E Struct. Reports Online* **2013**, *69*(9), 57-59.

[14] N. C. Burtch, J. Heinen, T. D. Bennett, D. Dubbeldam, M. D. Allendorf, *Adv. Mater.* **2018**, *30*, 1.

[15] J. M. Bermúdez-García, M. Sánchez-Andújar, S. Yáñez-Vilar, S. Castro-García, R. Artiaga, J. López-Beceiro, L. Botana, A. Alegría, M. A. Señarís-Rodríguez, *J. Mater. Chem. C* **2016**, *4*, 4889.

[16] J. M. Bermúdez-García, M. Sánchez-Andújar, S. Yáñez-Vilar, S. Castro-García, R. Artiaga, J. López-Beceiro, L. Botana, Á. Alegría, M. A. Señarís-Rodríguez, *Inorg.*

Chem. **2015**, *54*, 11680.

[17] J. M. Bermúdez-García, S. Yáñez-Vilar, A. García-Fernández, M. Sánchez-Andújar, S. Castro-García, J. López-Beceiro, R. Artiaga, M. Dilshad, X. Moya, M. A. Señarís-Rodríguez, *J. Mater. Chem. C* **2018**, *6*, 9867.

[18] A. M. Glazer, *Acta Crystallogr. Sect. B Struct. Crystallogr. Cryst. Chem.* **1972**, *28*, 3384.

[19] L. C. Gómez-Aguirre, B. Pato-Doldán, A. Stroppa, L.-M. Yang, T. Frauenheim, J. Mira, S. Yáñez-Vilar, R. Artiaga, S. Castro-García, M. Sánchez-Andújar, M. A. Señarís-Rodríguez, *Chem. - A Eur. J.* **2016**, *22*, 7645.

[20] Z. Y. Du, Y. P. Zhao, W. X. Zhang, H. L. Zhou, C. T. He, W. Xue, B. Y. Wang, X. M. Chen, *Chem. Commun.* **2014**, *50*, 1989.

[21] J. A. Hill, A. L. Thompson, A. L. Goodwin, *J. Am. Chem. Soc.* **2016**, *138*, 5886.

[22] Y. Wu, T. Binford, J. A. Hill, S. Shaker, J. Wang, A. K. Cheetham, *Chem. Commun.* **2018**, *54*, 3751.

[23] H. L. B. Boström, *CrystEngComm* **2020**, *22*, 961.

[24] M. M. Zhao, L. Zhou, P. P. Shi, X. Zheng, X. G. Chen, J. X. Gao, F. J. Geng, Q. Ye, D. W. Fu, *Chem. Commun.* **2018**, *54*, 13275.

[25] M. M. Zhao, L. Zhou, P. P. Shi, X. Zheng, X. G. Chen, J. X. Gao, L. He, Q. Ye, C. M. Liu, D. W. Fu, *Chem. - A Eur. J.* **2019**, *25*, 6447.

[26] M.-L. Tong, J. Ru, Y.-M. Wu, X.-M. Chen, H.-C. Chang, K. Mochizuki, S. Kitagawa, *New J. Chem.* **2003**, *27*, 779.

[27] M. M. Zhao, L. Zhou, P. P. Shi, X. Zheng, X. G. Chen, J. X. Gao, L. He, Q. Ye, C. M. Liu, D. W. Fu, *Chem. - A Eur. J.* **2019**, *25*, 6447.

[28] F. J. Geng, L. Zhou, P. P. Shi, X. L. Wang, X. Zheng, Y. Zhang, D. W. Fu, Q. Ye, *J. Mater. Chem. C* **2017**, *5*, 1529.

[29] J. A. Schlueter, J. L. Manson, K. A. Hyzer, U. Geiser, *Inorg. Chem.* **2004**, *43*, 4100.

[30] M. Sánchez-Andújar, S. Presedo, S. Yáñez-Vilar, S. Castro-García, J. Shamir, M. a Señarís-Rodríguez, *Inorg. Chem.* **2010**, *49*, 1510.

3.3. Revisiting the tolerance factor, a useful tool for designing hybrid dicyanamide perovskites

Part of this work showed and discussed here has been published in the following article:

J. García-Ben, A. García-Fernández, P. Dafonte-Rodríguez, I. Delgado-Ferreiro, U.B. Cappel, S. Castro-García, M. Sánchez-Andújar, J.M. Bermúdez-García, M.A, Señarís-Rodríguez, *J. Solid State Chem.,* **2022**, *316*, 123635.

This work belongs to the Special Issue: *Synthesis, Structure and Microstructure of novel Non-molecular Materials - Dedicated to Prof. Miguel Ángel Alario-Franco on the occasion of his 80th Birthday.*

3.3.1. Introduction

One of the foremost goals in Solid State and Materials Chemistry is the design and prediction of new solid-state materials with interesting functional properties, for the development of new technologies that allow to better face the pressing challenges of current society. But materials design is a complex and sometimes even frustrating task, resource intensive and time consuming. In that context, during the last decades, much effort has been devoted to accelerate materials discovery, such as the use of data repositories, automation with robotics and, above all, parallelisation and computational resources.[1] Also, more traditional semi-empirical rules that are extracted from experimental facts of series of compounds are still highly effective to guide the prediction and design of new materials, in particular with given crystal structures.[2] In this context, Goldschmidt's tolerance factor (t) has been successfully used during the last century to predict the stability of ABX_3 compounds,[3] specially mixed oxides, with perovskite structure, many of them with very outstanding properties (ferroelectricity, high superconductivity, magnetoresistance, etc.). As it is well-known, the tolerance factor is essentially geometrical parameter which relates the size of the cations in the A- and B-sites to that of the anions in the X-site, through Equation 3-1:

$$t = \frac{r_A + r_X}{\sqrt{2}\,(r_B + r_X)} \qquad \textbf{Equation 3-1}$$

In this model, the involved inorganic ions are considered as hard spheres with ionic radii of r_A, r_B and r_X for the A-, B- and X sites, respectively. This simple —but very effective— relationship can be used to easily predict the formation of inorganic perovskites from different combinations of A, B and X ions. For values of t ¼ [0.8–1], it is found that the selected combination will have a high probability of forming a perovskite structure. This structure is expected to display a cubic symmetry for t ¼ [0.9–1], while structural distortions —specifically the octahedra tiltings described by Glazer[4]— are expected for t ¼ [0.8–0.89]. Tolerance factors outside this range will lead to different structural topologies, such as ilmenite (for t < 0.8) or hexagonal structures (t > 1).

In 2014, Kieslich *et al.* extended the tolerance factor approach to predict the stability of the perovskite structure among members of the emergent family of dense hybrid organic-inorganic compounds with ABX_3 stoichiometry.[5-7] The resulting materials, which are known as hybrid organic-inorganic perovskites (HOIPs), integrate organic and inorganic building-blocks in the structure, namely: organic cations (normally alkylamine or alkylphosphone cations) in the A-site, metal cations in the B site and either halides or organic/inorganic polyatomic bidentate-bridging ligands in the X-site.[8] Depending on X, different families of HOIPs arise such as azide, formate, halide, thiocyanate, dicyanamide, perchlorate, hypophosphite, tetrafluoroborate or borohydride perovskites.[8-10] In the last years some of these HIOPs have attracted a lot of attention due to their

outstanding functional properties such as photovoltaic,[11,12] ferroelectric,[13] or barocaloric behaviour.[14-16]

This explains the relevance of having a powerful and simple guiding principle to predict which combination of A, B and X ions will lead to the formation of HOIPs and the great enthusiasm with which the extended tolerance factor was received by the scientific community.

In the Kieslich *et al.* proposed model to estimate such extended tolerance factor (illustrated in Figure 3-10), it is assumed that the organic A-cations are rigid spheres, independently of their real shape, with rotational freedom around their centre of mass, and with an effective radii (r_{Aeff}) equivalent to Equation 3-2:

$$r_{Aeff} = r_{mass} + r_{ion} \quad \textbf{Equation 3-2}$$

In this expression r_{mass} is calculated using single crystal X-ray diffraction data as the distance between the centre of mass and the furthest atom from this centre (excluding hydrogen atoms), and r_{ion} is the corresponding ionic radius of this furthest atom.[5] In a similar way, X-anions are treated as rigid cylinders with effective radius (r_{Xeff}) and effective height (h_{Xeff}).

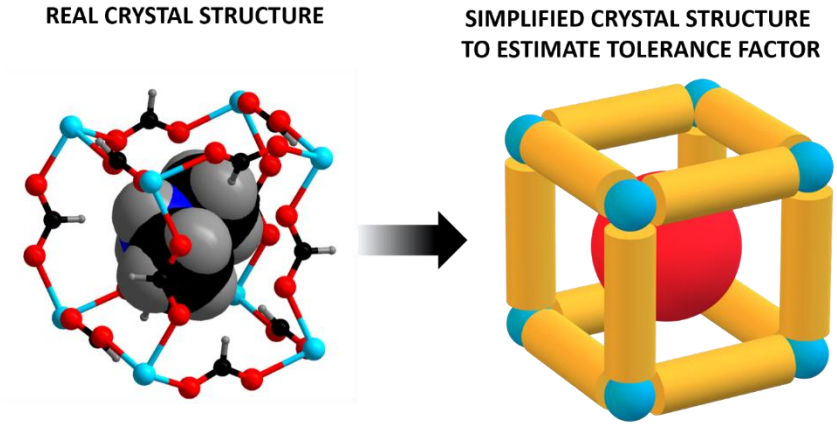

Figure 3-10. Comparison of a real hybrid perovskite with the simplified structure used to estimate its extended tolerance factor.

These parameters are then included in the extended Goldschmidt's tolerance factor for HOIPs, α, in Equation 3-3:

$$\alpha = \frac{r_{Aeff} + r_{Xeff}}{\sqrt{2}\,(r_B + 0.5\,h_{Xeff})} \quad \textbf{Equation 3-3}$$

Most interestingly, despite its simplicity, the extended tolerance factor identifies a stability window α = [0.8–1], where hybrid organic-inorganic compounds with ABX_3 stoichiometry are expected to exhibit the perovskite structure.[5]

This approach has been very successful for hybrid perovskites with short polyatomic X-anions, such as azides, formates, cyanides or borohydrides.[6] Nevertheless, it also has some limitations, especially when there is an important covalent contribution to the B-X bonds[9] or when rather large and anisotropic A cations and long X ions are present in the structure. This second problematic is found, for example, in the case of dicyanamide (dca = $[N(CN)_2]^-$) perovskites with general formula $[A][M(dca)_3]$.

In those $[A][M(dca)_3]$ HOIPs, the presence of the relatively large dca bridging ligand gives rise to perovskites with unprecedent structural degrees of freedom, that in turn allow for a large chemical diversity of polyatomic cations that can be accommodated in the A-site. As a result, this family has been expanding in the last years, and at present about 32 $[A][M(dca)_3]$ HOIPs are

already known, in which A are rather large monovalent organic cations (typically alkylammonium or alkylphosphonium cations) and M are Mn^{2+}, Fe^{2+}, Co^{2+}, Ni^{2+} and Cd^{2+} divalent metal cations.[17] It has be found that some of those dicyanamide HOIPs already show very remarkable barocaloric, ferroelastic or weak-ferromagnetic properties.[18–25] Hence, there is a marked interest in having tools, such the predictions of the stability using the extended tolerance factor, to help design and prepare new members of this promising family.

Nevertheless, and as mentioned above, the extended tolerance factor approach does not seem to be very accurate for such $[A][M(dca)_3]$ perovskites, since the calculated α values for the existing ones are in the range [0.88-1.20], which exceed the theoretical value of 1, the expected limit for perovskite structure stability. This can be mainly attributed to the simplifications assumed in the model to estimate the radius of the A–cations, which could fail for very irregularly shaped and anisotropic cations. The first difficulty already arises when trying to set their centre of mass, which is often not straightforward.

In this chapter, and with the aim of facilitating the design of new hybrid dicyanamide perovskites as well as other HOIPs containing large A-cations, it is proposed using the A-cation molecular volume as a means of calculating an effective A-ionic radius. This alternative, and still simple approach is carried out in two steps (Figure 3-11, approach 2): first, the "real" volume of the A-site cation is calculated using the CrystalExplorer 17 software;[26] second, the obtained volume is approximated to that of a sphere to calculate an effective radius for the A-cation. It should also be noted that, in this method, a free and open-access crystallographic software is using in order to expand the usefulness of the method to the wide scientific community.

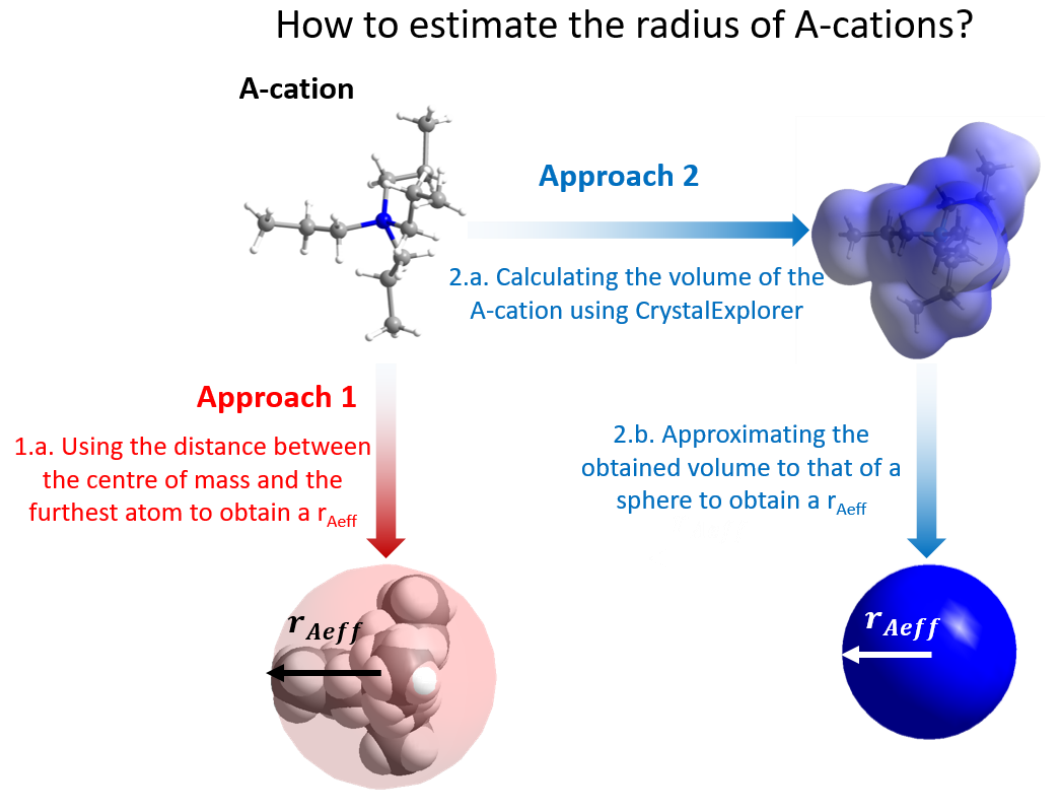

Figure 3-11. Two different approaches to estimate the radius of the A-site cations: (1) using the distance between the centre and the furthest atom, as originally proposed by Kieslich et al. (approach 1) and using the here proposed procedure (approach 2). The resulting A-sizes are represented by the red sphere (approach 1) or the blue sphere (approach 2).

The test of this method is focused on dicyanamides [A][M(dca)$_3$] with M = Mn, as Mn-dicyanamides are the series with more members known so far and whose crystal structures are available in the literature. The volumes of A-cations that can stabilize the perovskite structure and the resulting range of allowed tolerance factors is determined more precisely by analysing their crystal data. In a further step, new A-site cations were selected in order to design new [A][Mn(dca)$_3$] compounds, which were prepared and elucidated their crystal structures to confront the experimental results with the predictions resulting from this new approach.

In the course of this study, the influence of not only the size but also the shape of the molecular A-cation in the stability of the perovskite was also become aware. Therefore, this second parameter was also explored by making use of one of the large number of metrics used to quantify it: the globularity of the A-cation, which is a measure of the degree to which the surface area of a molecule differs from the surface value of a sphere with the same volume.[26]

In what follows it is presented the more relevant aspects and conclusions of these studies.

3.3.2. Experimental

3.3.2.1. Procedure used to easily calculate the effective volume and radii for A cations and recalculation of extended tolerance factors for [A][Mn(dca)$_3$] compounds.

A literature survey was carried out to search for reported crystalline hybrid Mn-dicyanamide compounds with [A][Mn(dca)$_3$] stoichiometry (either with perovskite structure or alternative ones). Until May 2022, 23 compounds were identified which satisfy such criteria and which are summarized in Table 3-1 (see section 3.3.3.1).

Starting from their available crystallographic data, the open access CrystalExplorer software[26] was used to calculate the A-cation volume enclosed by the ‘‘promolecule electron density isosurface”,[27] a molecular surface that has been shown to be very similar to other *ab initio* molecular surfaces but easier to calculate.[26,27] This software uses pre-calculated spherical atomic electron density functions and the molecular geometry to generate the promolecule electron density ($\sum_{i\in molecule}^{n} \rho_i\,(r)$ sums over the atoms belonging to the molecule, where $\rho_i\,(r)$ is are spherically averaged electron densities for each atom centered on nucleus i) and its isosurfaces.[28] For the study a promolecule isosurface of 0.002 au (~0.013 e Å^{-3}) as it typically contains more than 98 % of the electron density associated with that molecule was used.

After estimating the volume of the polyatomic A-cations by this procedure, the obtained volume was subsequently approximated to a sphere in order to calculate an effective radius for the A-site cation (see Figure 3-11, approach 2). Finally, the as-obtained ionic radius was introduced in Equation 3-3 to calculate the extended tolerance factor of the corresponding dicyanamide compounds, by assuming, as in the original approach, that the size of the X- ion remains unchanged and can be estimated in all cases by the same cylinder.

In the case of new A cations, for which no experimental data were available in the literature, the A-cation´s structure was designed, introduced it in the software Chem3D or Avogadro[39] and allowed the program to optimize bond angles and distances using the computational calculations MM2 force field energy minimization.[40,41] It is worth to note any other software with similar capabilities can also be suitable.

With such input data, the volume of the A-cation was subsequently simulated using CrystalExplorer software and the as-obtained radii was used to calculate the theoretical extended tolerance factor for the hypothetical [A][Mn(dca)$_3$] compounds containing such cations.

3.3.2.2. Calculation of globularity

The globularity of the A-site cations (G) was calculated using the Crystal Explorer 17 software as G=(S_{sp}/S_m), where S_m is the surface of the A-molecule while S_{sp} is the surface of a sphere of volume equal to that of the A-molecular volume.[42] It is worth noting that, according to this definition, G is 1.0 for a sphere, and progressively less than 1.0 as the molecular surface becomes more structured.

3.3.2.3. Synthesis of new dicyanamide compounds

Five new [A][Mn(dca)$_3$] compounds were synthesized, with A: [$R_3(CH_2X)N]^+$ (R: Et= CH_3CH_2-, Pr= $CH_3CH_2CH_2$-, X: Cl or Br) and [$Bu_4P]^+$Bu= $CH_3CH_2CH_2CH_2$-. For this purpose analytical grade Sigma-Aldrich reagents Na(dca) (96%), $(CH_3CH_2)_3N$ (≥99%), $(CH_3CH_2CH_2)_3N$ (≥98%), $[(CH_3CH_2CH_2CH_2)_4P]Br$ (98%), CH_2Cl_2 (98%), CH_2Br_2 (≥98.5%) and $Mn(NO_3)_2$ $4H_2O$ (≥97%) were used as starting materials.

In the case of the ammonium compounds, their preparation implied, as first step, the synthesis of the halides of the desired A-cations, as [$R_3(CH_2X)N]X$ ammonium salts are not commercially available.

a) Synthesis of [$R_3(CH_2X)N]X$ (R: Et, Pr, X: Cl^-, Br^-) compounds

The compounds [$R_3(CH_2X)N]X$, R: Et, Pr and X: Cl, Br were prepared by mixing R_3N in an excess of CH_2X_2 and stirring at room temperature for 72 hours. The resulting white solids were obtained by removing the solvent under reduced pressure at 343K, and the formation of the corresponding phases was corroborated with NMR, see Figures A3-1, A3-2, A3-3 and A3-4 of the *Annex II*.

[$Et_3(CH_2Cl)N]Cl$: ^{1}H NMR (300 MHz, $CDCl_3$): δ 5.67 (s, 2H), 3.63 (q, J = 7.2 Hz, 6H), 1.48 (t, J = 7.2 Hz, 9H) ppm.

[$Et_3(CH_2Br)N]Br$: ^{1}H NMR (300 MHz, $CDCl_3$): δ 5.53 (s, 2H), 3.66 (q, J = 7.2 Hz, 6H), 1.48 (t, J = 7.2 Hz, 9H) ppm.

[$Pr_3(CH_2Cl)N]Cl$: ^{1}H NMR (300 MHz, $CDCl_3$): δ 5.69 (s, 2H), 3.44 (m, J = 8.4 Hz, 6H), 1.83 (m, J = 7.2 Hz, 6H), 1.01 (t, J = 7.2 Hz, 9H) ppm.

[$Pr_3(CH_2Br)N]Br$: ^{1}H NMR (300 MHz, $CDCl_3$): δ 5.51 (s, 2H), 3.46 (m, J = 8.4 Hz, 6H), 1.81 (m, J = 7.2 Hz, 6H), 1.00 (t, J = 7.2 Hz, 9H) ppm.

b) Synthesis of [A][M(dca)$_3$] compounds.

[$R_3(CH_2X)N$][Mn(dca)$_3$] compounds, with R= Et, Pr and X = Cl, Br, were obtained by slow evaporation of the solution containing the corresponding [$R_3(CH_2X)N]X$, $Mn(NO_3)_2{\cdot}4H_2O$ and Na(dca) reagents in 1:1:3 molar proportion. The [Bu_4P][Mn(dca)$_3$] compound was also obtained by slow evaporation of the solution containing [$Bu_4P]Br$, $Mn(NO_3)_2{\cdot}4H_2O$ and Na(dca) in 1:1:3 molar proportion. In all cases, colourless crystals were obtained after a few days at room temperature.

3.3.2.4. Nuclear Magnetic Resonance (NMR)

NMR spectra were recorder on a Bruker Advance 300 MHz for 1H equipped with a dual cryoprobe. The solvent used for NMR experiments was $CDCl_3$ (98.5% ACROS Organics).

3.3.2.5. Single-crystal X-ray diffraction (SCXRD)

Single-crystal X-ray diffraction (SCXRD) experiments were carried out at 100 K, 150 K and room temperature. For that purpose, single-crystal diffraction data sets of one crystal were collected at room temperature in a Bruker D8 VENTURE Kappa X-ray diffractometer equipped with a PHOTON III detector and using monochromatic MoKα radiation (λ=0.71073 Å).

A suitable crystal was chosen and mounted on a MiTeGen MicroMount™ using Paratone® N (Hampton Research). The data integration and reduction were performed using the APEX3 v2019.1-0 (Bruker AXS, 2019) software suite. The integrations of the reflections were performed with SAINT 8.40A and the intensities collected were corrected for Lorentz and polarization effects and for absorption by semi-empirical methods on the basis of symmetry-equivalent data using SADABS 2016/2 of the suite software. The structures were solved by the dual-space algorithm implemented in SHELXT2014/5 program[43] and were refined by least squares method on SHELXL2018/3.[44]

3.3.2.6. Powder X-ray diffraction and Synchrotron powder X-ray diffraction

Powder X-ray diffraction (PXRD) patterns of the obtained polycrystalline compounds were obtained in a Siemens D-5000 diffractometer with CuK_α radiation at room temperature. Experimental PXRD patterns of the obtained compounds were compared with the simulated PXRD patterns from the crystal structure obtained from single crystal X-ray diffraction.

In addition, the Synchrotron powder X-ray diffraction (SPXRD) pattern of $[Et_3(CH_2Br)N][Mn(dca)_3]$ was recorded at the BM01 beamline of the ESRF Synchrotron (Grenoble, France) using a wavelength of 0.601 Å at room temperature. The wavelength was determined by refining the positions of six individual reflections of a NIST640D silicon standard collected with a Pilatus 2M detector. The recorded 2D patterns were integrated into a 1D powder profile. For this purpose, the sample was enclosed in a glass capillary (inner diameter ϕ = 0.5 mm) and in continuous rotation during data collection to improve powder averaging. Rietveld refinement was carried out using the program GSAS-II.[45]

3.3.3. Results and discussion

3.3.3.1. Calculation of effective volume and radii of A cations and tolerance factor for already reported [A][Mn(dca)$_3$] compounds

The volume and the effective radii of the A-cations of previously reported $[A][Mn(dca)_3]$ compounds (see Table 3-1, calculated A-site ionic radius (approach 2)) were calculated following the here proposed methodology, explained in section 3.3.2.1. With such data their extended tolerance factors were recalculated, that are plotted against the volume of the A-cation in Figure 3-15.

Table 3-1. List of A-site cations in reported crystalline hybrid Mn-dicyanamide compounds with general formula [A][Mn(dca)$_3$], and comparison of the A-ionic radius calculated when using approach 1 (Kieslich method) and the here proposed method (approach 2). *Abbreviations*: Me: methyl group (-CH_3), Et: ethyl group (-CH_2CH_3), Pr: propyl group (-$CH_2CH_2CH_3$), Bu: butyl group (-$CH_2CH_2CH_2CH_3$), Pn: pentyl group (-$CH_2CH_2CH_2CH_2CH_3$), Bn: Benzyl group (-$CH_2C_6H_5$), Ph: phenyl group (C_6H_5) and Cp: cyclopentadienyl (C_5H_5)$^-$.

ID number	A-cation	Perovskite structure	Ionic radius of A-site cations (Å)		Reference
			Approach 1	Approach 2	
1	$[Et_3(CH_2CH_2F)P]^+$	Yes	3.808	3.692	[29]
2	$[Et_3(CH_2CHCH_2)P]^+$	Yes	4.445	3.726	[23]
3	$[Et_3(CH_2OCH_3)P]^+$	Yes	4.62	3.717	[23]
4	$[Et_3(CH_2CH_2Cl)P]^+$	Yes	4.592	3.751	[29]
5	$[Et_3PrP]^+$	Yes	4.911	3.759	[23]
6	$[Pr_3MeN]^+$	Yes	4.651	3.791	[30]
7	$[Et_3BnN]^+$	Yes	5.917	3.916	[18]
8	$[Pr_4N]^+$	Yes	4.628	3.993	[31]
9	$[Pr_3(CH_3CHCH_2OH)N]^+$	Yes	4.745	4.042	[32]
10	$[Pr_3(CH_2CHOHCH_3)N]^+$	Yes	4.72	4.049	[32]
11	$[Bu_3MeN]^+$	Yes	5.868	4.080	[20]
12	$[Ph_3S]^+$	Yes	5.249	4.124	[19]
13	$[Cp^*_2Co]^+$	Yes	3.826	4.404	[33]
14	$[Cp^*_2Fe]^+$	Yes	3.975	4.450	[33]
15	$[Bu_3BnN]^+$	Yes	5.922	4.471	[18]
16	$[Me_3(CH_2CH_2Cl)N]^+$	No	4.38	3.279	[34]
17	$[Me_3(CH_2CH_2Br)N]^+$	No	4.897	3.325	[35]
18	$[Pr_3NH]^+$	No	4.636	3.279	[36]
19	$[EtPh_3P]^+$	No	5.299	4.323	[37]
20	$[Bu_4N]^+$	No	5.802	4.367	[31]
21	$[Ph_4P]^+$	No	5.286	4.504	[38]
22	$[Ph_4As]^+$	No	5.402	4.534	[38]
23	$[Pn_4N]^+$	No	7.107	4.662	[31]

Focusing in the fifteen compounds which exhibit a perovskite structure (corresponding to compounds **1** to **15** in Table 3-1, and represented as red dots in Figure 3-12), the first interesting remark is that when using this method most of their extended tolerance factors nicely range between 0.85-0.925 (highlighted with a red shadow in Figure 3-12).

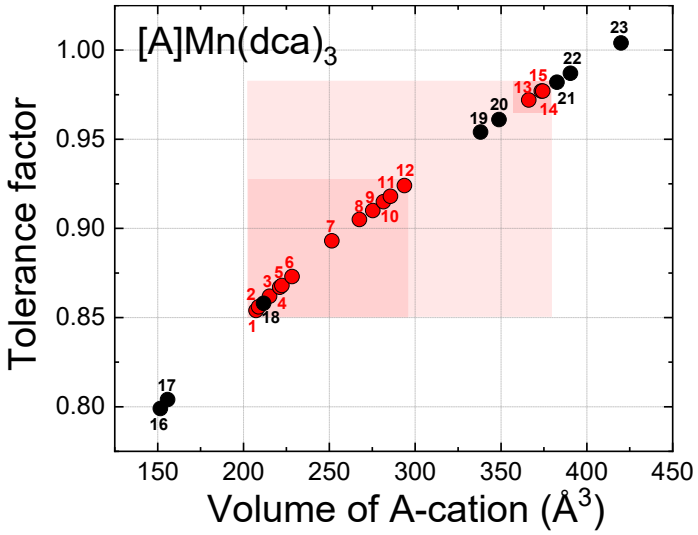

Figure 3-12. Tolerance factor versus volume of A-cation for the reported [A][Mn(dca)$_3$] compounds calculated using the here proposed method. *Note*: red dots: compounds with perovskite structure; black dots: compounds with non-perovskite structure, where the numbers correspond to the compounds listed in Table 3-1; the dark red shadowed squares indicate regions with existing examples of dicyanamide compounds with perovskite structure, and the lighter red shadow area the region where compounds with such structure might form.

Meanwhile, when using the A-site ionic radius obtained following approach 1 (see Table 3-1), most of the calculated α values are considerable higher, around 1 and above, that is, out of the stability range for perovskites, see Figure 3-13, where they are compared with the ones obtained using approach 2.

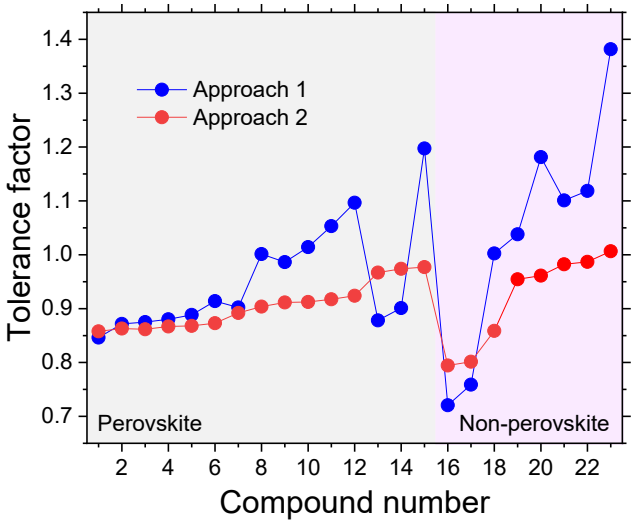

Figure 3-13. Tolerance factor of the reported [A][Mn(dca)$_3$] compounds listed in Table 3-1 of the main manuscript obtained when using the A-radius calculated by approach 1 and by approach 2. The dark grey shadowed region indicates values with existing examples of Mn-dicyanamide compounds with perovskite structure.

As it can also be seen in Figure 3-12, according to the method reported in this work, the volume of the A-cations in the compounds with perovskite structure mainly ranges between 205-295 Å^3. Additionally, there are three compounds (**13**, **14** and **15**) with perovskite structure with higher tolerance factors and volumes, α ~0.975 and V ~375 A^3, suggesting that probably there is still room to find new members of the family.

As for the lowest α value (~0.85), it corresponds to compound **1** containing the $[Et_3P(CH_2CH_2F)]^+$ A-cation with a volume of 204.62 $Å^3$. Meanwhile, the highest α value (~0.975) corresponds to the compound **15** containing $[Bu_3(CH_2C_6H_5)N]^+$ as A-cation[18] with a volume of 374.35 $Å^3$.

To try to learn more about the stability range for the perovskite structure the other eight dicyanamide compounds $[A][Mn(dca)_3]$ with a different structure took the attention. For these, the effective volume and the radii of their A-cations and their extended tolerance factors were also estimated (compounds **16** to **23** in Table 3-1, represented as black dots in Figure 3-12).

In this context, the **16** and **17** compounds with the smallest A-cation, $[Me_3(CH_2CH_2X)N]^+$ (X = Cl or Br) (cation volume 152 $Å^3$ and the smaller tolerance factors, α ~0.8), crystallize in an alternative 2D crystal structure.[34,35] As for the **18** Mn-dicyanamide, with tripropylammonium $[Pr_3NH]^+$ cation, even if its extended tolerance factor seems in principle adequate to stabilize the perovskite structure (A-cation volume = 211.68 $Å^3$ and α ~0.86), the flat molecular geometry of its A-cation is probably an important factor which favours a 2D crystal structure instead of that of the perovskite.

In the opposite extreme of Figure 3-12 is the Mn-dicyanamide numbered as **23** in Table 3-1, with the largest A-cation (the tetrapentylammonium $[Pn_4N]^+$ with a volume of 419.97 $Å^3$), compound which shows a α slightly above 1 (α = 1.004) and crystallizes in a different $LiSbO_3$ structure.[31]

Interestingly, Figure 3-12 also reveals that that compounds **19** to **22** which show high tolerance factors, but in any case, smaller than 1, and close to the value shown by compound **15**, can already crystallise in other structures. This is the case of the **21** Mn-dicyanamide with tetraphenylphosphonium[38] $[Ph_4P]^+$ with A-cation volume = 382.60 $Å^3$ and α = 0.982, and the 20 Mn-dicyanamide with tetrabutylammonium[31] $[Bu_4N]^+$ (A-cation volume = 338.85 $Å^3$ and α = 0.955,), whose reported crystal structures are 2D and triple rutile, respectively.

These findings suggest that, as in the case of inorganic perovskites, close to the tolerance factor limits more than one structural type probably compete and it is difficult to predict which one will form. It seems that in this range there are other factors that affect the stability of the perovskite structure apart from size, among them probably the shape of the A-cations.

To explore the possible role of this shape on the stability of the perovskite structure, the globularity of the A-cations present in these dicyanamide compounds was calculated.

The obtained results are depicted in Figure 3-14, where they are plotted against the tolerance factor of the corresponding $[A][Mn(dca)_3]$ compounds. Very interestingly, and as it can be seen there, there is a clear correlation not only between the tolerance factor but also the A-cation globularity and the stability of the perovskite structure. In this context, the compounds with perovskite structure, in general, contain A-cations with globularities higher than 0.75.

On the other hand, there are two groups of non-perovskite compounds: ones whose A-cations present a globularity higher than 0.75, but whose size is too small to stabilize the perovskite structure; and a second group with A-cations of adequate size, but which are strongly anisotropic and show a globularity lower than 0.75.

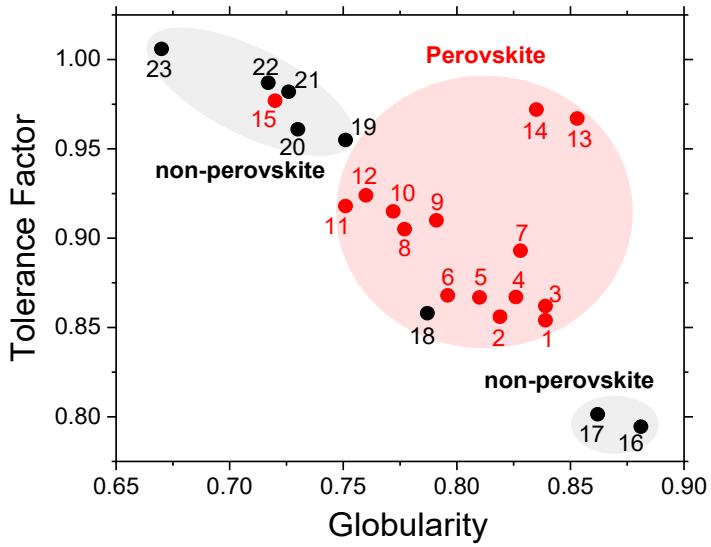

Figure 3-14. Plot of tolerance factor versus globularity for the reported [A][Mn(dca)$_3$] compounds, showing the regions where the perovskite structure is (or not) stable.

It is worth to highlight that two compounds, **15** and **18**, do not follow this trend. The first one, containing the $[Bu_3BnN]^+$ cation, exhibits a perovskite structure even if the globularity of this A-cation is lower than 0.75. It is worth noting that, as was previously reported in the 3.2 section this compound exhibits a very peculiar distortion called cavity sharing, where the long pendant groups of A cation occupy multiple cavities. Therefore, it seems that this cavity is contributing to stabilize the perovskite structure despite the low globularity value of this A-cation. Meanwhile compound **18**, with $[Pr_3NH]^+$, does not exhibit a perovskite structure, even if its tolerance factor and A-cation globularity are, in principle, adequate. It seems that the flat molecular geometry of the tripropylammonium cation, which already is responsible for a globularity value lower than that of related cations (compounds **1** and **2**) with similar volume (Figures 3-12 and 3-14), favours the stability of the 2D crystal structure rather than a 3D-perovskite.

In short, from the analysis of the crystallographic data of previously reported [A][Mn(dca)$_3$] compounds it is found that both the size and the shape of the A cations are critical factors to stabilize the perovskite structure. And that, in general, compounds with tolerance factor values ranging between 0.85-0.975 and with A-cations with G>0.75 are the ones with more probability to be perovskites.

3.3.3.2. New [A][Mn(dca)$_3$] compounds with specifically designed A-site cations to test the validity of the here proposed approach

Firstly, the phase purity of the designed compounds was checked by PXRD (see Figures 3-15, 3-16 and 3-17) in order to confirm that all the obtained compounds are single phase materials, without secondary phases present. It is worth to note that the apparent unmatching between the simulated and experimental patterns is mainly due to the presence of preferential orientations in the experimental patterns recorded using a Bragg-Brentano geometry; the temperature difference between experimental data (room temperature) and reference data (below room temperature); and probably also, as it is very often the case, disorder processes in the samples at room temperature.

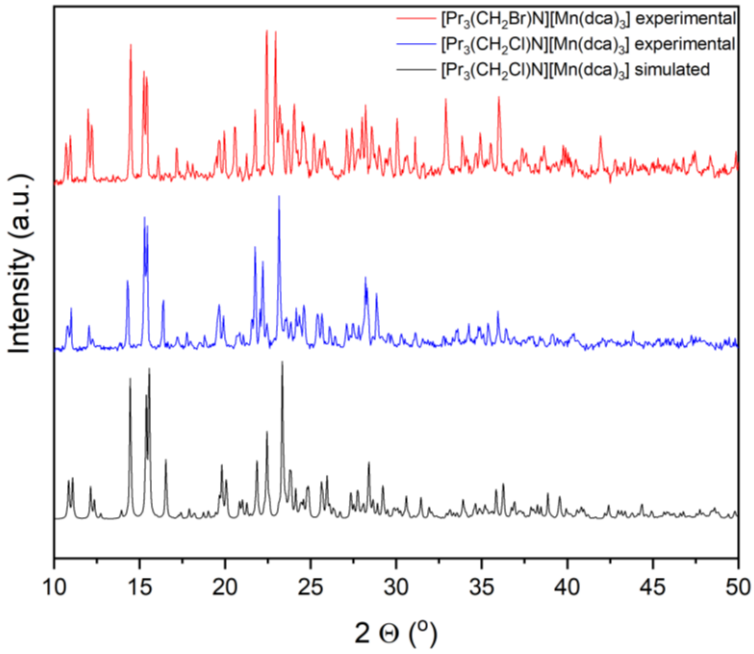

Figure 3-15. Comparison of powder X-ray diffraction patterns (λ= 1.54184 Å) of the simulated from the single-crystal structure of $[Pr_3(CH_2Cl)N][Mn(dca)_3]$ with the experimental patterns of $[Pr_3(CH_2Cl)N][Mn(dca)_3]$ and $[Pr_3(CH_2Br)N][Mn(dca)_3]$.

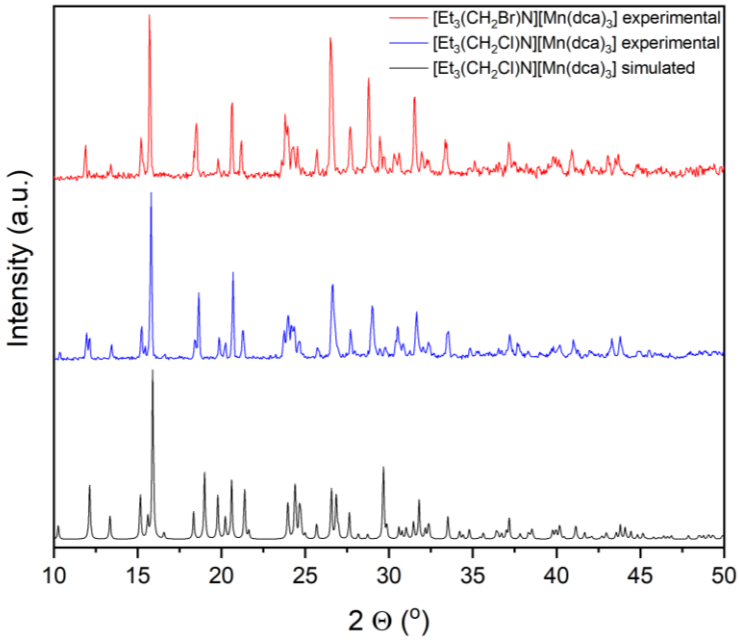

Figure 3-16. Comparison of powder X-ray diffraction patterns (λ= 1.54184 Å) of the simulated from the single-crystal structure of $[Er_3(CH_2Cl)N][Mn(dca)_3]$ with the experimental patterns of $[Et_3(CH_2Cl)N][Mn(dca)_3]$ and $[Et_3(CH_2Br)N][Mn(dca)_3]$.

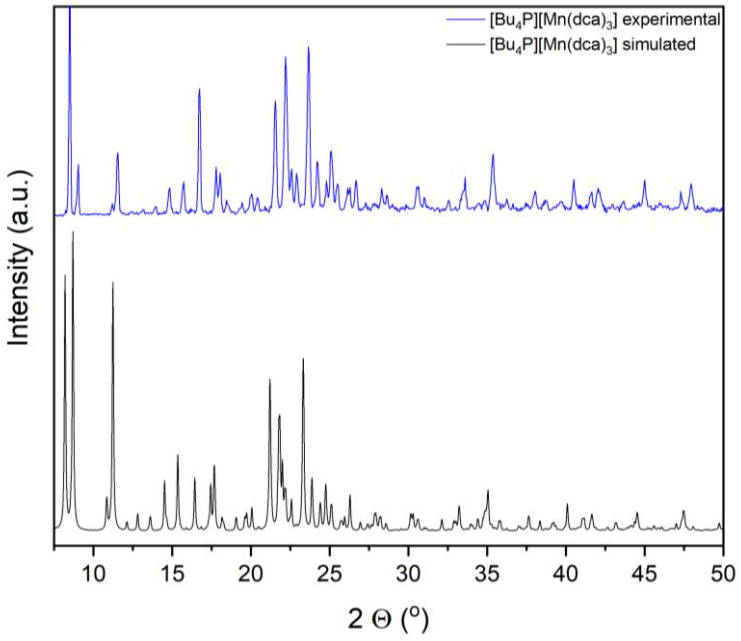

Figure 3-17. Comparison of powder X-ray diffraction patterns (λ= 1.54184 Å) of the simulated from the single-crystal structure of $[Bu_4P][Mn(dca)_3]$ with the experimental patterns of $[Bu_4P][Mn(dca)_3]$.

In order to obtain new members of this $[A][Mn(dca)_3]$ family and further refine the stability limits of the perovskite structure, possible A-site cations that can give rise to tolerance factors between ~0.8 and ~1 were looked for. For that purpose, the methodology explained in section 3.3.2.1. was followed when no structural information is available.

Their values of globularity were also had in count, looking for candidates with G≥0.70.

Finally, The quaternary ammonium cations $[R_3(CH_2X)N]^+$ (R: CH_3CH_2 (Et), $CH_3CH_2CH_2$ (Pr), X: Cl or Br) were selected, sketched in Figure 3-18 and indicated in more detail in Table 3-2, where information about their calculated volume, the extended tolerance factor of the resulting hypothetical $[A][Mn(dca)_3]$ compounds and the A-cation globularity were indicated.

Table 3-2. List of the A-site cations here designed and synthesized, with their estimated volumes (using the Chem3D software), and globularity values, together with the tolerance factors calculated for the resulting $[A][Mn(dca)_3]$ compounds.

Label	A-cation	Volume ($Å^3$)	α	Globularity
a	$[Et_3(CH_2Cl)N]^+$	187.79	0.836	0.865
b	$[Et_3(CH_2Br)N]^+$	194.23	0.842	0.863
c	$[Pr_3(CH_2Cl)N]^+$	247.97	0.889	0.796
d	$[Pr_3(CH_2Br)N]^+$	254.14	0.894	0.794
e	$[Bu_4P]^+$	361.02	0.969	0.702

According to these calculations, the $[Pr_3(CH_2X)N]^+$ (X = Cl, Br) cations (b and c in Table 3-2) would lead to $[A][Mn(dca)_3]$ dicyanamide compounds with a tolerance factor ~0.9 and A-site

globularity ~0.8, so that the perovskite structure would be clearly expected for the resulting compounds (see Figure 3-18).

On the other hand, the $[Et_3(CH_2X)N]^+$ (X = Cl, Br) cations (a and b in Table 3-2) would lead to dicyanamide compounds with a tolerance factor lower than 0.85, in principle, out of the stability range seen so far for the perovskite structure (Figure 3-18), even if with an adequate globularity value (high than 0.75).

Additionally, compound with the large A-cation $[Bu_4P]^+$ was tested in order to further explore the stability limits of the perovskite structure, with a volume of 361.02 $Å^3$, and $\alpha = 0.969$, similar to those reported for the largest A-cations with perovskite structure (see Figure 3-15), even if with smaller G ~0.7 (see Figure 3-18).

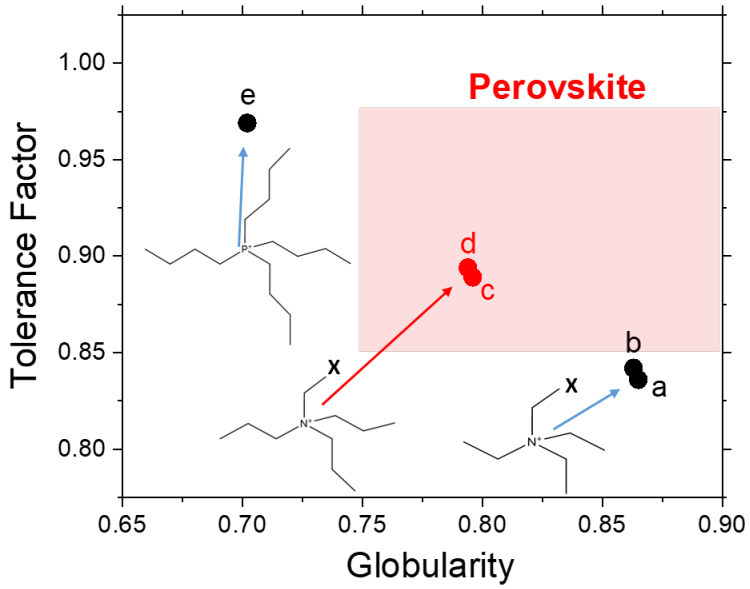

Figure 3-18. Tolerance factor versus A-site cation globularity for the here proposed new $[A][M(dca)_3]$ compounds. The circles (red and black, for perovskite and non-perovskite structures, respectively) correspond to the data for A-cations: $[Et_3(CH_2X)N]^+$ (X= Cl, Br), $[Pr_3(CH_2X)N]^+$ (X= Cl, Br) and $[Bu_4P]^+$, a-e in Table 3-2, whose molecular geometry is also sketched in the graph. The light red shadowed square indicates the region where the perovskite structure is expected to form.

3.3.3.3. Experimental structures for the here prepared new $[A][Mn(dca)_3]$ compounds

Five new compounds were prepared following the synthesis method explained in section 3.3.2.1, and their crystal structures were elucidated. Interestingly, the obtained results show that the three types of cations, namely $[Et_3(CH_2X)N]^+$, $[Pr_3(CH_2X)N]^+$ and $[Bu_4P]^+$, drive into three types of crystal structures, whose main features will be now briefly highlighted:

a) Structures of $[Pr_3(CH_2X)N][Mn(dca)_3]$ (X= Cl, Br)

As expected from these calculations, the as-synthesised crystals of $[Pr_3(CH_2Cl)N][Mn(dca)_3]$ and $[Pr_3(CH_2Br)N][Mn(dca)_3]$, compounds **c** and **d** of Table 3-2, crystallise in a perovskite structure. In both cases they show monoclinic space group $P2_1/n$, and rather similar lattice parameters, even if these are slightly larger in the compound with X = Br, associated to the larger volume of the $[Pr_3(CH_2Br)N]^+$ cation, namely a = 16.0853(4) Å, b = 16.2405(5), c = 16.4503(5) Å and β = 97.648(1) for X = Cl and a = 16.1458(11) Å b = 16.2630(13), c = 16.4926(13) (5) Å and β = 96.469(3) at 100 K, for X = Br (see more details on Table A3-1 of *Annex II*).

In both compounds, each Mn^{2+} is octahedrally coordinated to its neighbouring Mn^{2+} cations through six $\mu_{1,5}$-[dca]-bridges forming the 3D $[Mn(dca)_3]^-$ framework with the $[Pr_3(CH_2X)N]^+$ cations sitting in the pseudocuboctahedra cavities, as expected for a perovskite structure (see Figure 3-19) .

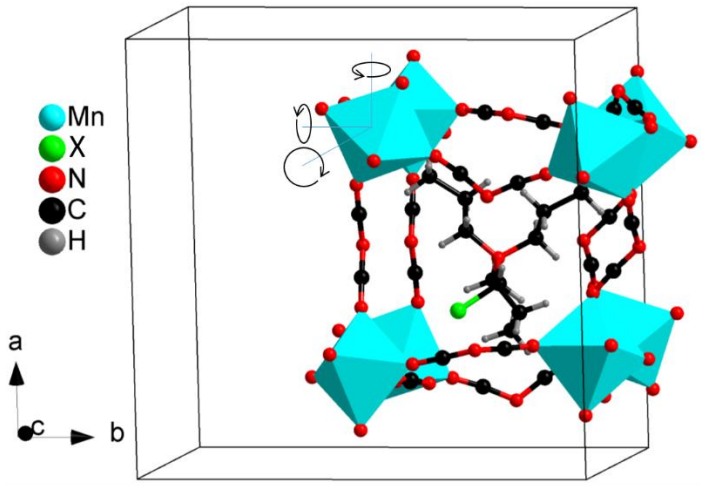

Figure 3-19. Detail of the crystal structure of $[Pr_3(CH_2X)N][Mn(dca)_3]$ (X = Cl or Br) at 100 K, showing a highly distorted $[Mn(dca)_3]^-$ framework and a cooperative octahedral tilting along the three main axis.

Interestingly, in both $[Pr_3(CH_2X)N][Mn(dca)_3]$ (X = Cl or Br) compounds the $\mu_{1,5}$-[dca]-bridges show both *syn–anti* and anti–coordination modes, depending on the crystallographic direction. Additionally, the presence of these dca ligands allow for both conventional (reported on pure inorganic perovskites) or unconventional (exclusive of hybrid perovskites)[46] $[MnN_6]$ octahedral tilts, and $[MnN_6]$ columnar shifts,[47] provoking large distortions of the 3D-perovskite framework.

In particular, the $[MnN_6]$ octahedral tilt pattern shows one in-phase and two out-of-phase tilts with the Glazer notation ($a^- b^+ c^-$). As for the columnar shifts, they are active along the three main axis, with a shifted out-of-phase relative to their immediate neighbours and are especially large along c-axis (see Figure 3-20).

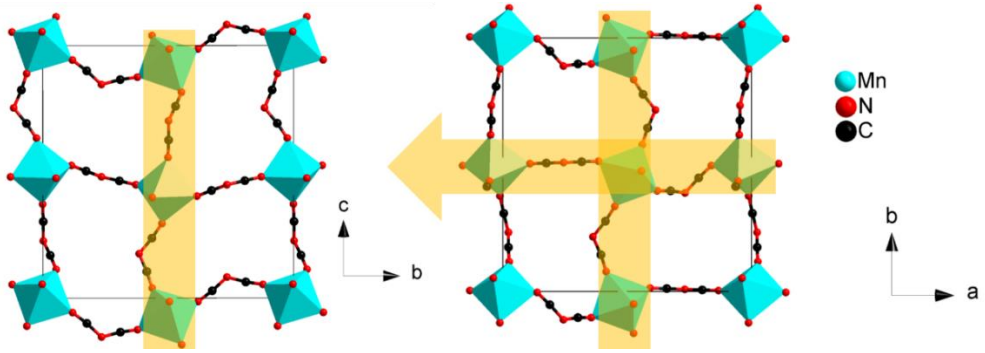

Figure 3-20. Detail of the crystal structure of $[Pr_3(CH_2X)N][Mn(dca)_3]$ showing the columnar shift along the main axis.

To further test the validity of the here proposed approximation, that very nicely predicts the formation of the perovskite structure, it was also compared the volume of the A-cations obtained from the geometrical optimization carried out with the software Chem3D with those obtained from experimental data applying approach 1 and the here proposed approach 2. As shown in Table 3-3 there is a very good agreement between the values obtained by the geometrical optimization and the volume calculated using approach 2, explained in section 3.2.1.

Meanwhile the volume calculated for the A-cations using approach 1 turns to be again higher (see Table 3-3) probably because when using such approach with irregularly shaped A-cations, empty void spaces are included as if they were part of the cation, which is not really the case, resulting in an overestimation of their size (see sketch in Figure 3-11).

On the other hand, the good matching between the first two in turn implies that the estimated volume of the A-cation using a simple software for molecular geometry optimization, that can subsequently be used to calculate the tolerance factor, can be a powerful and very simple tool to predict the formation (or not) of new [A][Mn(dca)$_3$] hybrid dicyanamide perovskites. This is especially useful when A-cations are complex and difficult to prepare.

Table 3-3. Comparison of the volume of A-cations obtained by geometrical optimization of the cations and the experimental values calculated from crystal structure data following the approach 1 and the here proposed approach 2 indicated in section 3.3.1.

A-cation	Cation volume from geometrical optimization (Å^3)	Cation volume, from crystallographic data (Å^3), approach 1	Cation volume, from crystallographic data (Å^3), approach 2
[Pr$_3$(CH$_2$Cl)N]$^+$	247.97	356.8	245.23
[Pr$_3$(CH$_2$Br)N]$^+$	254.14	381.7	251.07

b) Structures of [Et$_3$(CH$_2$X)N][Mn(dca)$_3$] (X = Cl, Br)

[Et$_3$(CH$_2$Cl)N][Mn(dca)$_3$], compound **a** in Table 3-2, crystallizes in the monoclinic *C*2/*m* space group with a=14.9722(3) Å, b=17.2255(3) Å, c=7.4663(2) Å and β =102.724(1) (see more details in Table A3-2 of *Annex II*). It contains one atom of oxygen inside its crystal assembly, suggesting that the compound is monohydrated.

Interestingly, at difference with the compounds described in the previous section 3.3.3.a), this compound does not show a perovskite structure, but a layered structure similar to the previously reported for the [Me$_3$(CH$_2$CH$_2$X)N][M(dca)$_3$] compounds with M = Mn and Cd.[34,35] It basically consists of a 2D [Mn(dca)$_3$]$^-$ anionic scaffold complemented by the [Et$_3$(CH$_2$Cl)N]$^+$ cations acting as counterions and one water molecule per formula (see Figure 3-21). Within the 2D layered [Mn(dca)$_3$]$^-$ network structure, each Mn^{2+} cation is octahedrally coordinated by six N atoms from six bridging dca ligands, and the neighbouring metal cations are linked to four Mn^{2+} cations in two different ways: by double dca-bridges to two Mn^{2+} cations (along the c-axis) and by single dca-bridges to other two Mn^{2+} cations (along the b-axis) (see details in Figure 3-22).

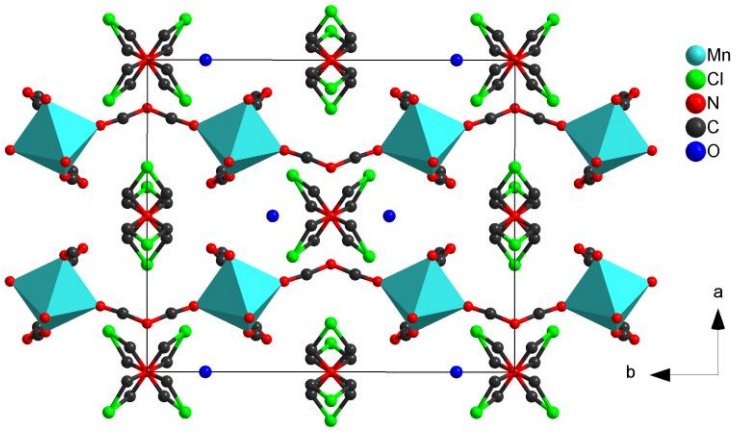

Figure 3-21. Crystal structure of [Et$_3$(CH$_2$Cl)N][Mn(dca)$_3$]·H$_2$O at 150 K.

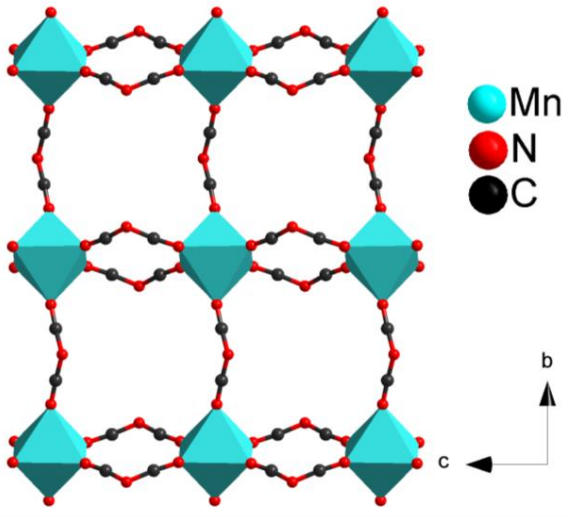

Figure 3-22. Detail of the $Mn(dca)_3^-$ layered arrangement in the crystal structure of $[Et_3(CH_2X)N][Mn(dca)_3]\cdot H_2O$.

Such 2D $Mn(dca)_3^-$ layers are stacking along the a-axis and the spaces between adjacent layers are filled with $Et_3(CH_2Cl)N^+$ cations and water molecules. Strong disorder is observed in the A-site cations, with the C and Cl atoms located at 8 and 4 different crystallographic sites, respectively, while the N-atoms sit in a single crystallographic site.

The structure of $[Et_3(CH_2Br)N][Mn(dca)_3]$, compound **b** in Table 3-2—for which single crystals could not be obtained— could be elucidated by Synchrotron X-ray powder diffraction. According to the as-obtained results (Figure 3-23), it is similar to that shown by the X=Cl compound, with slightly larger cell parameters —as expected in view of the larger volume of the $[Et_3(CH_2Br)N]^+$ cation—, namely a = 15.2521(8) Å, b = 17.2552(3) Å, c = 7.5481(3) Å and β = 100.867(2) at room temperature (see more details in Table A3-3 of *Annex II*).

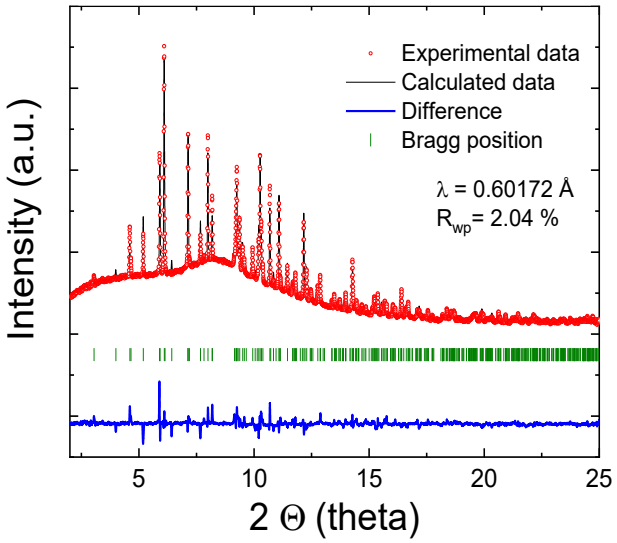

Figure 3-23. Rietveld refinement of the SPXRD pattern for $[Et_3(CH_2Br)N][Mn(dca)_3]$ at room temperature. The experimental points are represented by red circles, while calculated profile is a black full line and the blue lower line is the difference. The green markers correspond to the allowed Bragg positions.

Therefore, as none of the $[Et_3(CH_2X)N][Mn(dca)_3]$ (X = Cl, Br) compounds exhibit the perovskite structure, it is deduced that the size of the used A-cation and thus the tolerance factor of the obtained compounds are not large enough to stabilize it, even if the globularity of the $[Et_3(CH_2X)N]^+$ cation would be adequate, G>0.75

This is also an interesting result that helps to better defining the lower limit of the tolerance factor and the volume of the A-cations to stabilize the perovskite structure and confirms the power of the predictions. Thus, it is established that the minimum size of A-site cations in $[A][Mn(dca)_3]$ compounds to obtain a perovskite structure should be in the range of [195-205] $Å^3$ and the lower limit of the tolerance factor should be in the range of [0.84-0.85].

c) Structure of $[Bu_4P][Mn(dca)_3]$

$[Bu_4P][Mn(dca)_3]$, compound **e** in Table 3-2, crystallises in the orthorhombic space group $P2_12_12$ (non-centrosymmetric) with lattice parameters a = 16.268(6) Å, b = 16.323(6) Å and c = 21.550(7) Å at 295 K (see more details on Table A3-4 of *Annex II* and Figure 3-24). This compound does not show either the perovskite structure, but a framework in which each octahedrally coordinated Mn^{2+} is connected to five neighbouring Mn^{2+} cations through $\mu_{1,5}$-[dca]-bridges: to four of them through simple dca bridges and to the fifth one through two dca ligands resulting in an edge sharing configuration (see Figure 3-25).

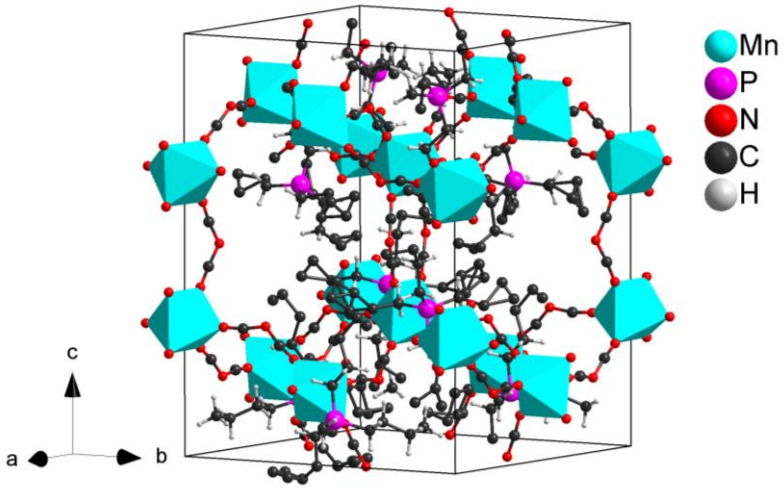

Figure 3-24. Crystal structure of $[Bu_4P][Mn(dca)_3]$ at room temperature.

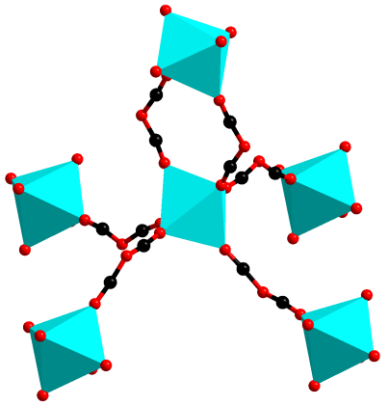

Figure 3-25. Details of the crystal structure of $[Bu_4P][Mn(dca)_3]$ showing that each octahedrally coordinated Mn^{2+} is connected to five neighbouring Mn^{2+} cations through $\mu_{1,5}$-[dca]-bridges: to four of them through simple dca bridges and to one through two dca ligands resulting in an edge sharing configuration

As shown in more detail in Figure 3-26, the arrangement of this framework can be described as formed by $[Mn_2(dca)_{10}]^{6-}$ dimers, which are comprised of two edge-sharing octahedra (connected by two bridging dca anions) and each dimer is linked to other eight neighbouring dimers by corner-sharing octahedra. This arrangement has clear reminiscences to that shown by some oxide and hybrid hexagonal perovskites. In particular, it is very similar to the structure shown by the $(DMA)PbX_3$ compounds (with DMA= dimethylammonium cation and X = Cl, Br), that exhibit a 4H-hexagonal perovskite polytype[48] (see Figure 3-24). This is a very common crystal structure observed in purely inorganic ABX_3 compounds when the A-cation is too large to be located in the cuboctahedra cavity of the perovskite structure.

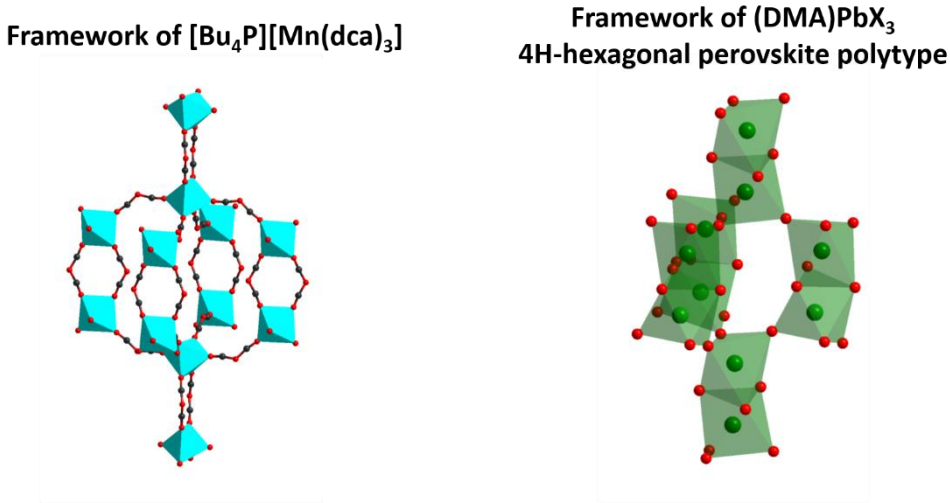

Figure 3-26. Details of the crystal structure of $[Bu_4P][Mn(dca)_3]$ showing the arrangement of the framework (on the left), compared to the 4H-hexagonal perovskite polytype of $(DMA)PbX_3$, where DMA is dimethylammonium cation and X is chloride or bromide anions (on the right).

In fact, the here presented framework creates a rather large cavity delimited by ten $[MnN_6]$ octahedra, in contrast to the eight $[MnN_6]$ present in a perovskite structure, where the very bulky $[Bu_4P]^+$ cations (which in addition show partially disorder in the C-atoms in three of the four butyl groups) can be accommodated.

It should also be pointed out that the relatively lower globularity value of this cation (G ~0.70) is also another factor playing against the stabilisation of this compound in the perovskite structure.

3.3.4. Conclusions

This work proposes an alternative method to calculate the effective volume and radii of A-cations, whether previous crystallographic data are available or not, that helps predicting the stability of perovskite structures through the tolerance factor approach. The reported methodology, which is carried out in an easy way, is especially useful when large and irregular A-cations are present, and avoids, for example the difficulty to estimate their centre of mass or overestimation of their size.

Despite the simplicity of the method, this study demonstrates that it behaves reasonably well to predict, in a first approach, the stability of [A][Mn(dca)$_3$] hybrid dicyanamide perovskites. In this context, it has established the lower and upper tolerance factor and A-site volume limits for such perovskite dicyanamides more precisely, which may help in the search for new members of this emerging family of (multi)functional multi(stimuli)-responsive materials. In particular, it is observed that in most [A][Mn(dca)$_3$] perovskites the A-cation volume lies between 200-300 Å^3 ($0.85<\alpha<0.925$), and two new members of the family falling in this range were experimentally obtained. In addition, there is probably still room to find new members of the family for A-cations with a size between 300-400 Å^3 ($0.925<\alpha<1$).

In addition, it is shown that the shape of the A-cation plays also a role in the stabilisation of the perovskite structure. In that context, a minimum globularity value G>0.75 that favours the formation of the structure is established, provided that the size of the A-cation, and thus the tolerance factor is also adequate.

In any case, there could be other factors involved that have not been considered in this simple approach, among which the liberation of pendant groups of the A-cations could also be important in some cases.

Finally, it is worth noting that the here proposed methodology, which is initially developed to facilitate the design of new hybrid dicyanamide perovskites, is not only valid for this particular family but very useful for any other hybrid perovskites and related materials.

For example, most recently Burger *et al.*[49] have reported new and very interesting perovskite-like AB_2X_6 compounds based on a $[BX_3]^-$ ReO_3-type host network ($[Mn(C_2N_3)_3]^-$), in which the divalent A^{2+} cations ($[Pr_3N(CH_2)_nNPr_3]^{2+}$ with n = 4 and 5) with separated charge centres bridge adjacent A-site cavities. To test the validity of the here proposed procedure beyond "conventional" perovskites, the volume of these two divalent organic A-cations using the CrystalExplorer software was estimated. Then the obtained volumes are divided by two, as each of the divalent cation occupies two A-sites, to subsequently approach them to that of a sphere to calculate an effective radius, according to the here explained approach 2. Very interestingly, the as-estimated tolerance factor and globularity values for these compounds turn to be: $\alpha = 0.885$, G = 0.80 when A^{2+}: $[Pr_3N(CH_2)_4NPr_3]^{2+}$; and $\alpha = 0.893$, G = 0.79 when A^{2+}: $[Pr_3N(CH_2)_5NPr_3]^{2+}$. That is both values nicely fit within the range that was defined as stable for the perovskite structure.

3.3.5. References

[1] F. T. Szczypiński, S. Bennett, K. E. Jelfs, *Chem. Sci.* **2021**, *12*, 830.

[2] C. Shi, C. H. Yu, W. Zhang, *Angew. Chemie - Int. Ed.* **2016**, *55*, 5798.

[3] V. M. Goldschmidt, *Naturwissenschaften* **1926**, *14*, 477.

[4] A. M. Glazer, *Acta Crystallogr. Sect. B Struct. Crystallogr. Cryst. Chem.* **1972**, *28*, 3384.

[5] G. Kieslich, S. Sun, A. K. Cheetham, *Chem. Sci.* **2014**, *5*, 4712.

[6] G. Kieslich, S. Sun, A. K. Cheetham, *Chem. Sci.* **2015**, *6*, 3430.

[7] S. Burger, M. G. Ehrenreich, G. Kieslich, *J. Mater. Chem. A* **2018**, *6*, 21785.

[8] W. Li, A. Stroppa, Z. Wang, S. Gao, *Hybrid Organic-Inorganic Perovskites*, Wiley, **2020**.

[9] W. Li, Z. Wang, F. Deschler, S. Gao, R. H. Friend, A. K. Cheetham, *Nat. Rev. Mater.* **2017**, *2*, 16099.

[10] H. L. B. Boström, A. L. Goodwin, *Acc. Chem. Res.* **2021**, *54*, 1288.

[11] A. Kojima, K. Teshima, Y. Shirai, T. Miyasaka, *J. Am. Chem. Soc.* **2009**, *131*, 6050.

[12] T. J. Jacobsson, *et. al.*, *Nat. Energy* **2022**, *7*, 107.

[13] H. L. B. Boström, M. S. Senn, A. L. Goodwin, *Nat. Commun.* **2018**, *9*, 2380.

[14] J. M. Bermúdez-García, M. Sánchez-Andújar, S. Castro-García, J. López-Beceiro, R. Artiaga, M. A. Señarís-Rodríguez, *Nat. Commun.* **2017**, *8*, 15715.

[15] J. M. Bermúdez-García, M. Sánchez-Andújar, M. A. Señarís-Rodríguez, *J. Phys. Chem. Lett.* **2017**, *8*, 4419.

[16] J. Salgado-Beceiro, A. Nonato, R. X. Silva, A. García-Fernández, M. Sánchez-Andújar, S. Castro-García, E. Stern-Taulats, M. A. Señarís-Rodríguez, X. Moya, J. M. Bermúdez-García, *Mater. Adv.* **2020**, *1*, 3167.

[17] J. García-Ben, L. N. McHugh, T. D. Bennett, J. M. Bermúdez-García, *Coord. Chem. Rev.* **2022**, *455*, 214337.

[18] M.-L. Tong, J. Ru, Y.-M. Wu, X.-M. Chen, H.-C. Chang, K. Mochizuki, S. Kitagawa, *New J. Chem.* **2003**, *27*, 779.

[19] J. A. Schlueter, J. L. Manson, K. A. Hyzer, U. Geiser, *Inorg. Chem.* **2004**, *43*, 4100.

[20] M. Mączka, A. Gągor, M. Ptak, D. Stefańska, L. Macalik, A. Pikul, A. Sieradzki, *Dalt. Trans.* **2019**, *48*, 13006.

[21] Z. B. Liu, L. He, P. P. Shi, Q. Ye, D. W. Fu, *J. Phys. Chem. Lett.* **2020**, *11*, 7960.

[22] J. M. Bermúdez-García, M. Sánchez-Andújar, S. Yáñez-Vilar, S. Castro-García, R. Artiaga, J. López-Beceiro, L. Botana, Á. Alegría, M. A. Señarís-Rodríguez, *Inorg. Chem.* **2015**, *54*, 11680.

[23] F. J. Geng, L. Zhou, P. P. Shi, X. L. Wang, X. Zheng, Y. Zhang, D. W. Fu, Q. Ye, *J. Mater. Chem. C* **2017**, *5*, 1529.

[24] J. M. Bermúdez-García, S. Yáñez-Vilar, A. García-Fernández, M. Sánchez-Andújar, S. Castro-García, J. López-Beceiro, R. Artiaga, M. Dilshad, X. Moya, M. A. Señarís-Rodríguez, *J. Mater. Chem. C* **2018**, *6*, 9867.

[25] M. M. Zhao, L. Zhou, P. P. Shi, X. Zheng, X. G. Chen, J. X. Gao, F. J. Geng, Q. Ye, D. W. Fu, *Chem. Commun.* **2018**, *54*, 13275.

[26] P. R. Spackman, M. J. Turner, J. J. McKinnon, S. K. Wolff, D. J. Grimwood, D. Jayatilaka, M. A. Spackman, *J. Appl. Crystallogr.* **2021**, *54*, 1006.

[27] A. S. Mitchell, M. A. Spackman, *J. Comput. Chem.* **2000**, *21*, 933.

[28] M. A. Spackman, P. R. Spackman, S. P. Thomas, *Complement. Bond. Anal.* **2021**, 329.

[29] M. Zhao, L. Zhou, P. Shi, X. Zheng, X. Chen, J. Gao, L. He, Q. Ye, C. Liu, D. Fu,

Chem. – A Eur. J. **2019**, *25*, 6447.

[30] S. Burger, S. Grover, K. T. Butler, H. L. B. Boström, R. Grau-Crespo, G. Kieslich, *Mater. Horizons* **2021**, *8*, 2444.

[31] J. a Schlueter, J. L. Manson, U. Geiser, *Inorg. Chem.* **2005**, *44*, 3194.

[32] Z. Liu, L. He, P. Shi, Q. Ye, **2020**, *11*, 19, 7960-7965.

[33] P. M. Van Der Werff, E. Martínez-Ferrero, S. R. Batten, P. Jensen, C. Ruiz-Pérez, M. Almeida, J. C. Waerenborgh, J. D. Cashion, B. Moubaraki, J. R. Galán-Mascarós, J. M. Martínez-Agudo, E. Coronado, K. S. Murray, *Dalt. Trans.* **2005**, 285.

[34] S. S. Wang, R. K. Huang, X. X. Chen, W. J. Xu, W. X. Zhang, X. M. Chen, *Cryst. Growth Des.* **2019**, *19*, 1111.

[35] S. S. Wang, X. X. Chen, B. Huang, R. K. Huang, W. X. Zhang, X. M. Chen, *CCS Chem.* **2019**, *1*, 448.

[36] Y. Huang, X. Yu, Z. Rong, Y. Ai, K. Qian, J. Yang, *Zeitschrift für Naturforsch. B* **2019**, *74*, 485.

[37] P. M. van der Werff, S. R. Batten, P. Jensen, B. Moubaraki, K. S. Murray, J. D. Cashion, *Cryst. Growth Des.* **2004**, *4*, 503.

[38] J. W. Raebiger, J. L. Manson, R. D. Sommer, U. Geiser, A. L. Rheingold, J. S. Miller, *Inorg. Chem.* **2001**, *40*, 2578.

[39] M. D. Hanwell, D. E. Curtis, D. C. Lonie, T. Vandermeersch, E. Zurek, G. R. Hutchison, *J. Cheminform.* **2012**, *4*, 17.

[40] N. L. Allinger, Y. H. Yuh, J. H. Lii, *J. Am. Chem. Soc.* **1989**, *111*, 8551.

[41] N. L. Allinger, *J. Am. Chem. Soc.* **1977**, *99*, 8127.

[42] J. J. McKinnon, A. S. Mitchell, M. A. Spackman, *Chem. - A Eur. J.* **1998**, *4*, 2136.

[43] G. M. Sheldrick, IUCr, *Acta Crystallogr. Sect. A Found. Adv.* **2015**, *71*, 3.

[44] G. M. Sheldrick, *Acta Crystallogr. Sect. C Struct. Chem.* **2015**, *71*, 3.

[45] B. H. Toby, R. B. Von Dreele, *J. Appl. Crystallogr.* **2013**, *46*, 544.

[46] S. G. Duyker, J. A. Hill, C. J. Howard, A. L. Goodwin, *J. Am. Chem. Soc.* **2016**, *138*, 11121.

[47] I. E. Collings, J. A. Hill, A. B. Cairns, R. I. Cooper, A. L. Thompson, J. E. Parker, C. C. Tang, A. L. Goodwin, *Dalt. Trans.* **2016**, *45*, 4169.

[48] A. García-Fernández, E. J. Juarez-Perez, J. M. Bermúdez-García, A. L. Llamas-Saiz, R. Artiaga, J. J. López-Beceiro, M. A. Señarís-Rodríguez, M. Sánchez-Andújar, S. Castro-García, *J. Mater. Chem. C* **2019**, *7*, 10008.

[49] S. Burger, K. Hemmer, D. C. Mayer, P. Vervoorts, D. Daisenberger, J. K. Zaręba, G. Kieslich, *Adv. Funct. Mater.* **2022**, *32*, 2205343.

3.4. Modulation of the functional properties of hybrid dicyanamide perovskites by solid solution preparation

Part of the work showed and discussed in this chapter has been published in the following article:

J. García-Ben, J. Salgado-Beceiro, I. Delgado-Ferreiro, P. Dafonte-Rodríguez, J. López Beceiro, R. Artiaga, S. Castro-García, M. Sánchez-Andújar, J.M. Bermúdez-García, M.A, Señarís-Rodríguez, *Crystals*, **2022**, *12*(6), 860.

This work belongs to the Special Issue: *Solid State Chemistry: Memorial Issue for Professor Emilio Morán*.

3.4.1. Introduction

In solid-state chemistry a well-known route to obtain new compounds and modulate their properties is forming solid solutions, a strategy widely exploited in the case of classical inorganic-perovskites, but relatively unexplored among emergent hybrid organic-inorganic perovskites (HOIPs).

From the chemical and structural point of view, it is well known that traditional inorganic perovskites are highly tolerant to partial and/or total substitution of the A, B, and X building-blocks, leading to the so-called substitutional solid solutions.[11] Over the years, this strategy has successfully allowed to modulate, tune and even introduce new functional properties in inorganic perovskites, such as high-temperature superconductivity[12] and colossal magnetoresistance.[13]

Nevertheless, studies on solid solutions in analogous hybrid perovskites are still scarce and mainly limited to those perovskites with short ligands, such as halides, formates or hypophosphites.[14,15] One example is the work of Cheetham *et al.*, that were able to obtain mixed X-site perovskites using formate and hypophosphite ligands on $[GUA][Mn(HCOO)_{3-x}(H_2POO)_x]$ (GUA=guanidinium cation).[16] Other example is the Goodwin *et al.* work, that have reported the synthesis and structural characterization of three mixed-metal formate perovskite families $[C(NH_2)_3][Cu_xM_{1-x}(HCOO)_3]$ (M = Mn, Zn, Mg). Very interestingly, these authors have reported for x = 0.5 a nanoscale segregation involving the coexistence of polar/apolar nanoregions, such as relaxor ferroelectrics.[17] In any case, this approach gives a valuable new handle for controlling the properties of hybrid perovskites, opening the door to many new possible compositions. In this context, it should be noted that the preparation of hybrid perovskite solid solutions by either cation or anion substitution remains a challenge due to several factors. On the one hand, the large differences between the sizes of some anions and others makes it difficult to obtain X-site substituted solutions.[18] On the other hand, the fact that there is more variability of cations than anions makes it difficult to find the right anion/cation combination without compromising structural stability.[18] Moreover, differences in the kinetics of crystal growth with different cations or anions can arise, with one of the structures being more favoured.[19]

In the particular case of dicyanamide-perovskites with general formula $[A][M(dca)_3]$ (dca = $(CN)_2N^-$), some interesting properties arise due the length and flexibility of the dicyanamide anion.[20] Such flexibility gives rise to pseudo-cubic cavities that can be modulable in size and shape to allocate a wide diversity of A-cations. Actually, the variability of the size of the A-cations that can form this hybrid perovskite is the largest within the HOIPs family. Moreover, those structures tolerate a large diversity of transition metal cations M in the B-site, such as Mn^{2+}, Ni^{2+}, Co^{2+}, Fe^{2+} or Cd^{2+}. Very interesting properties found in this family of hybrids, such as magnetic and dielectric properties, large pressure responsiveness and even giant barocaloric effects, are given by those structural characteristics which can be tuned by selecting different building blocks.[20–22]

However, and despite the intensive studies on the family of hybrid dicyanamide perovskites in recent years, no studies have been reported that address the use of solid solutions to tune their crystal structures and functional properties.

This work reported the preparation and structural characterization of a substitutional solid solution, with Co:Ni = 1:1 in the M position, of the previously reported[23] [TPrA][M(dca)$_3$] perovskite (TPrA = $(CH_3CH_2CH_2)_4N^+$; M = Ni^{2+}, Co^{2+}; dca = $(N(CN)_2^-$). This work also reports the variation of the dielectric, optical and thermal properties of the parent hybrid perovskites by the formation of such solid solution.

In addition, given the ability of the original hybrids to give rise to metal nanoparticle systems embedded in carbon nanotubes by controlled calcination,[27] the potential of the solid solution to also be used as a precursor for carbon nanostructures have been studied.

3.4.2. Experimental

3.4.2.1. Materials and synthesis

Commercially available $Co(NO_3)_2 \cdot 6H_2O$ (98%, Sigma-Aldrich), $Ni(NO_3)_2 \cdot 6H_2O$ (98.5%, Sigma-Aldrich), (TPrA)Br (98%, Aldrich), Na(dca) (96%, Aldrich) and absolute ethanol (Panreac) were employed.

The synthetic route followed for preparation of the [TPrA][$Co_{0.5}Ni_{0.5}$(dca)$_3$] was the slow evaporation of a mixture of all the reagents (see Figure 3-27). Four different solutions of 2 mmol of (TPrA)Br solved in 20 mL of absolute ethanol, 6 mmol of Na(dca) in 10 mL of H_2O, 1 mmol of $Co(NO_3)_2 \cdot 6H_2O$ in 5 mL of H_2O and 1 mmol of $Ni(NO_3)_2 \cdot 6H_2O$ in 5 mL of H_2O were prepared separately. Ni- and Co-solutions were mixed together; dca- and the TPrA-solutions were also mixed together; and finally, both resultant solutions were mixed in a crystallizer. After two days, small cubic purple crystals (around 1 mm) were formed, isolated by filtration and washed several times with ethanol.

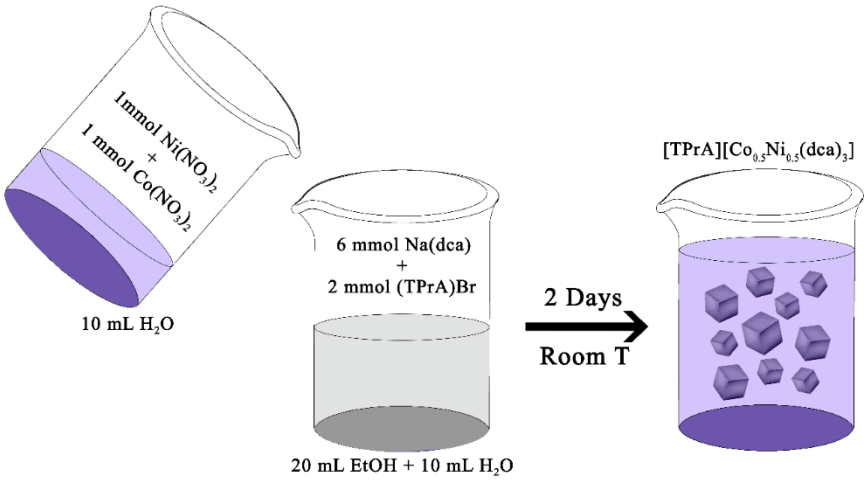

Figure 3-27. Synthesis scheme of [TPrA][$Co_{0.5}Ni_{0.5}$(dca)$_3$] by slow evaporation.

Part of the obtained product was thermally decomposed in order to check its availability to be used as precursor of metal- and carbon-nanostructures, following the method reported by J.M. Bermúdez-Garcia *et al.*[24] The sample was heated in a tubular furnace Lenton LTF 16/--/180 under nitrogen atmosphere at 5 ºC/min, from room temperature up to 900 ºC, maintaining that temperature for 1 hour and then cooling down at 10 ºC/min.

3.4.2.2. Powder X-ray diffraction (PXRD)

A Siemens D-5000 diffractometer using CuK_α radiation (λ = 1.5418 Å) was used to study the compounds by X-ray powder diffraction (XRPD) at room temperature. The PXRD pattern was refined with Le Bail method using the software GSAS-II version 5046.

3.4.2.3. Single-crystal X-ray diffraction (SCXRD)

Single-crystal X-ray diffraction data were collected at 100 K in a Bruker-Nonius x8 ApexII X-ray diffractometer equipped with a CCD detector and using monochromatic $MoK_{\alpha1}$ radiation (λ = 0.71073 Å). For that experiment a suitable crystal was chosen and mounted on a glass fibber using instant glue. The crystal was cooled at a rate of 10K/min using a cold stream of nitrogen from a Kyroflex cryostream cooler. The data integration and reduction were performed using the Apex2 V.1.0-27 (Bruker Nonius, 2005) suite software. The intensity collected was corrected for Lorentz and polarization effects and for absorption by semiempirical methods on the basis of symmetry-equivalent data using SADABS (2004) of the suite software. The structure was solved by the dual-space algorithm implemented in SHELXT2014/5 program and were refined by least squares method on SHELXL2018/3.

3.4.2.4. Differential Scanning Calorimetry (DSC)

Differential scanning calorimetric (DSC) analysis measurement from 200 K to 390 K were carried out using a TA-Instruments Q2000 with a RCS 90 cooler, heated and cooled with a rate of 20 K min^{-1}, under nitrogen atmosphere, using around 20 mg of sample.

3.4.2.5. Thermogravimetric analysis (TGA)

Thermogravimetric analysis (TGA) was carried out in a simultaneous TGA-DTA analyzer SDT2960 with a rate of 10 K min^{-1} from 25 to 1000 K, under nitrogen atmosphere, using around 17 mg of sample.

3.4.2.6. Dielectric measurements

The complex dielectric permittivity ($\varepsilon_r = \varepsilon_r' - i\varepsilon_r''$) of the coldpress pelletized samples were measured as a function of frequency and temperature with a parallel-plate capacitor coupled to a Solartron 1260A Impedance/Gain-Phase Analyzer, capable of measuring in the frequency range from 10 mHz to 32 MHz using an amplitude of 2 V. The capacitor was mounted in a Janis SVT200T cryostat refrigerated with liquid nitrogen, and with a

Lakeshore 332 incorporated to control the temperature from 150 to 400 K. Data were collected upon heating.

Pelletized samples, made from cold-press non-oriented single crystals with an area of approximately 133 mm^2 and a thickness of approximately 1.3 mm, were prepared to fit into the capacitor, and gold was sputtered on their surfaces to ensure a good electrical contact with the electrodes.

All the dielectric measurements were carried out in a nitrogen atmosphere where several cycles of vacuum and nitrogen gas were performed to ensure that the sample environment was free of water.

3.4.2.7. Ultraviolet-visible (U-VIS) spectroscopy

Optical diffuse-reflectance measurements of powders were performed at room temperature using a Jasco V-650 UV-Visible double-beam spectrophotometer with single monochromators, operating from 200 to 800 nm. $BaSO_4$ was used as a non-absorbing reflectance reference.

3.4.2.8. Scanning electron microscopy (SEM) and Energy Dispersive X-Ray Spectroscopy (EDS)

The morphology of the samples was analysed using a JEOL JSM-7200F Schottky field emission scanning electron microscope (FE-SEM). Chemical analyses were carried out using JEOL JSM-7200F equipped with an Oxford Instruments X-Max detector for energy-dispersive X-ray spectroscopy (EDS).

3.4.2.9. Transmission Electron Microscopy (TEM)

The morphology and the microstructure of the samples were tested by transmission electron microscopy (TEM) in a JEOL TEM-1010 operating at 100kV and equipped with a Gatan Rio camera.

3.4.3. Results and discussion

3.4.3.1. Compositional and structural characterization

The doped-sample $[TPrA][Co_{0.5}Ni_{0.5}(dca)_3]$ have been synthesized as well as the parent hybrid perovskites, $[TPrA][Co(dca)_3]$ and $[TPrA][Ni(dca)_3]$, in order to study the crystal structure and various functional properties of the new Co:Ni = 1:1 material, and to compare it with the unsubstituted perovskites prepared in an analogous way. For this purpose the three systems have been prepared by adapting the method described in the literature[21,22] (see section 3.4.1). In that way, cubic-shaped single crystals of different colours depending on the Co:Ni ratio were obtained with sizes between 2 and 1.5 mm (see Figure 3-28).

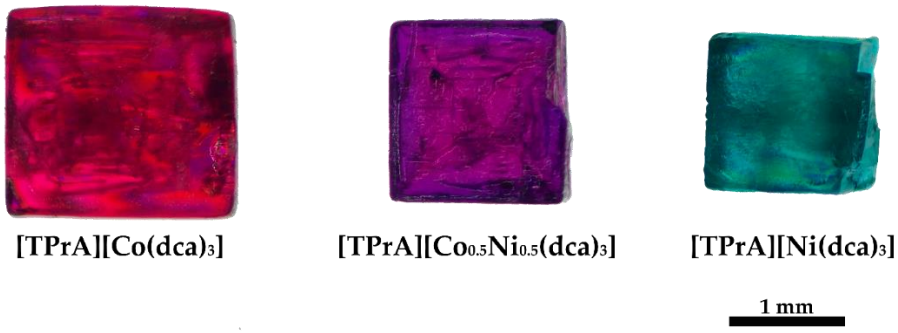

Figure 3-28. Cubic single-crystals obtained of $[TPrA][Co_xNi_{1-x}(dca)_3]$ where x = 1.0, 0.5, 0.0.

a) Energy Dispersive X-ray Spectroscopy (EDS) results

In order to corroborate the proportion of each metal in the doped sample, energy dispersive X-ray spectroscopy (EDS) analysis was performed (see Figure 3-29a). Figure 3-29 and 3-30 shows, respectively, EDS spectrum and mapping of such sample, nominally $[TPrA][Co_{0.5}Ni_{0.5}(dca)_3]$. The obtained data reveal the presence of both Ni and Co in similar proportions (48.8% of Co and 51.2% of Ni) with a homogeneous distribution on the microscale.

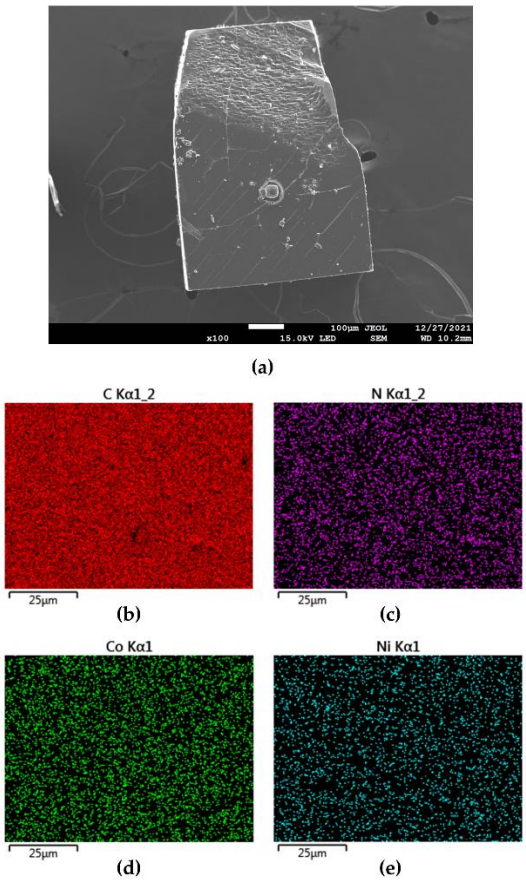

Figure 3-29. a) Scanning Electron Microscopy image of the [TPrA][$Co_{0.5}Ni_{0.5}(dca)_3$], X-ray map of b) carbon, c) nitrogen, d) cobalt and e) nickel.

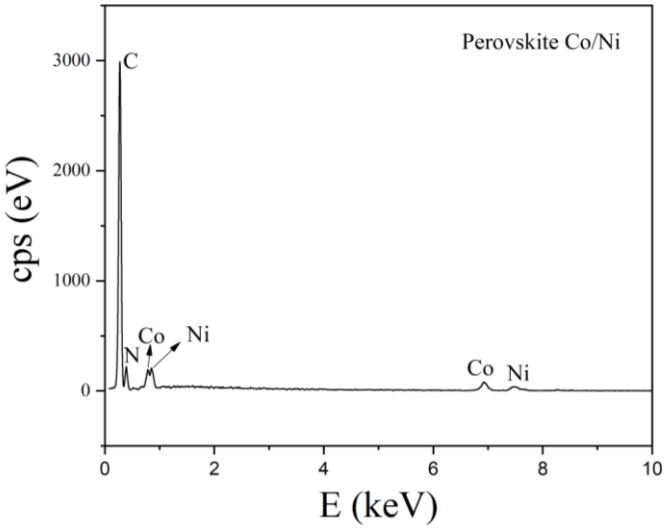

Figure 3-30. EDS spectrum of the [TPrA][$Co_{0.5}Ni_{0.5}(dca)_3$].

b) Powder X-ray diffraction

The X-ray diffraction patterns at room temperature (see Figure 3-31a) show that the doped sample has been obtained as a pure sample, and that it actually presents the same crystal structure as that already described for unsubstituted perovskites at the same temperature (from now on called "polymorph Ib", by analogy with the parent compounds).[23] Figure 3-31b shows a detail of the

most intense peak, in the 2θ region of 14-17º, where it can be clearly seen that: i) the maximum is not split in the compound with Co:Ni = 1:1 and ii) there is a regular displacement of the position of this maximum towards larger angles as the amount of nickel increases. This is an indication that, at the scale seen by PXRD, a solid solution is formed and no phase segregation is observed. Zooming in many other maxima shows analogous behaviour.

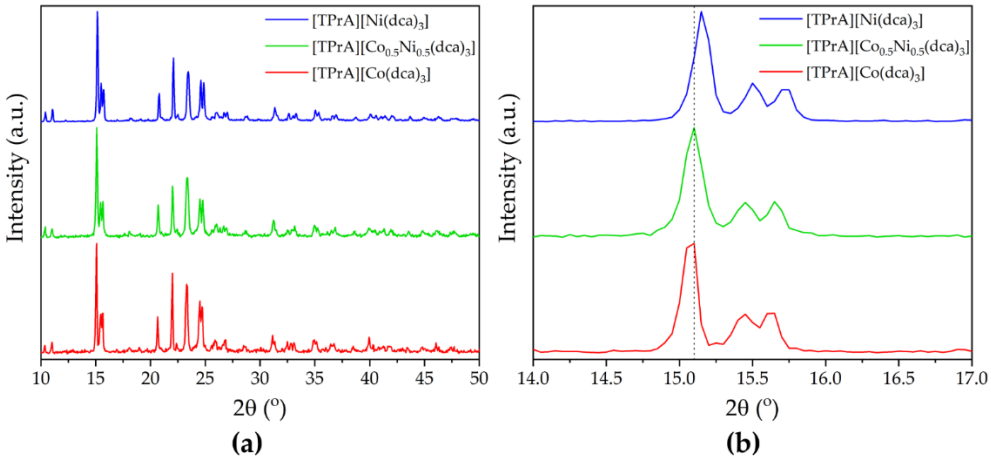

Figure 3-31. a) Powder X-ray diffraction patterns of $[TPrA][Co_xNi_{1-x}(dca)_3]$ where x = 1, 0.5, 0. b) Detail of a region of a), to see the shape and the shift of the peak as x changes.

Additionally, the obtained patterns were analyzed using a LeBail refinement (see Figures 3-32 and 3-33), which show a good agreement between the proposed model and the experimental patterns. It is worth to note that the $[TPrA][Co_{0.5}Ni_{0.5}(dca)_3]$ pattern could be satisfactorily refined as single phase without any evidence of phase segregation. It has orthorhombic symmetry with space group *Pnna* and lattice parameters a = 17.2330(17) Å, b = 23.0758(20) Å and c = 22.7800(19) Å. Figure 3-32 shows the evolution of the $[TPrA][Co_{1-x}Ni_x(dca)_3]$ lattice parameters and volume, obtained from the LeBail refinements, versus the Ni- content. It is worth to mention that the lattice parameters and volume clearly decrease upon Ni- doping, which can be related to the lower size of Ni^{2+} compared to Co^{2+} cations (0.69 Å versus 0.745 Å respectively).[25]

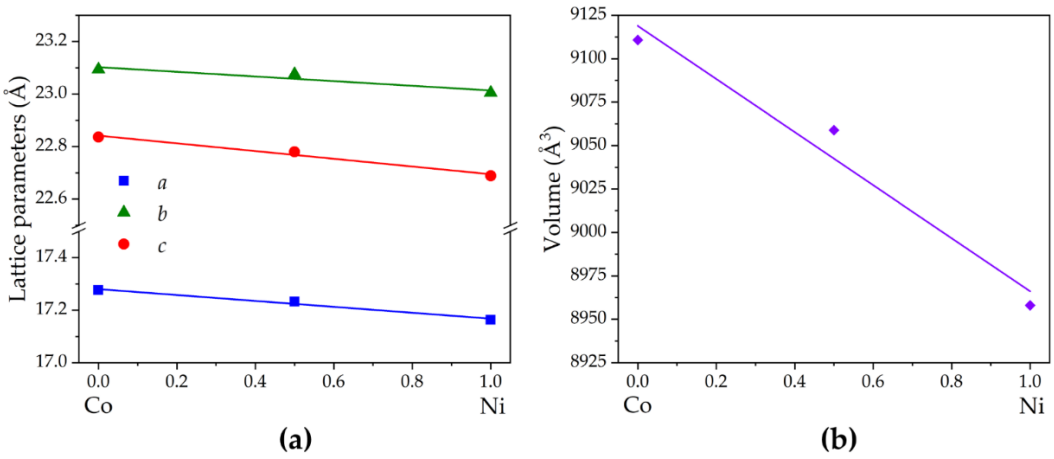

Figure 3-32. a) Lattice parameters and b) unit cell volume for $[TPrA][Co_xNi_{1-x}(dca)_3]$ where x = 1, 0.5, 0.

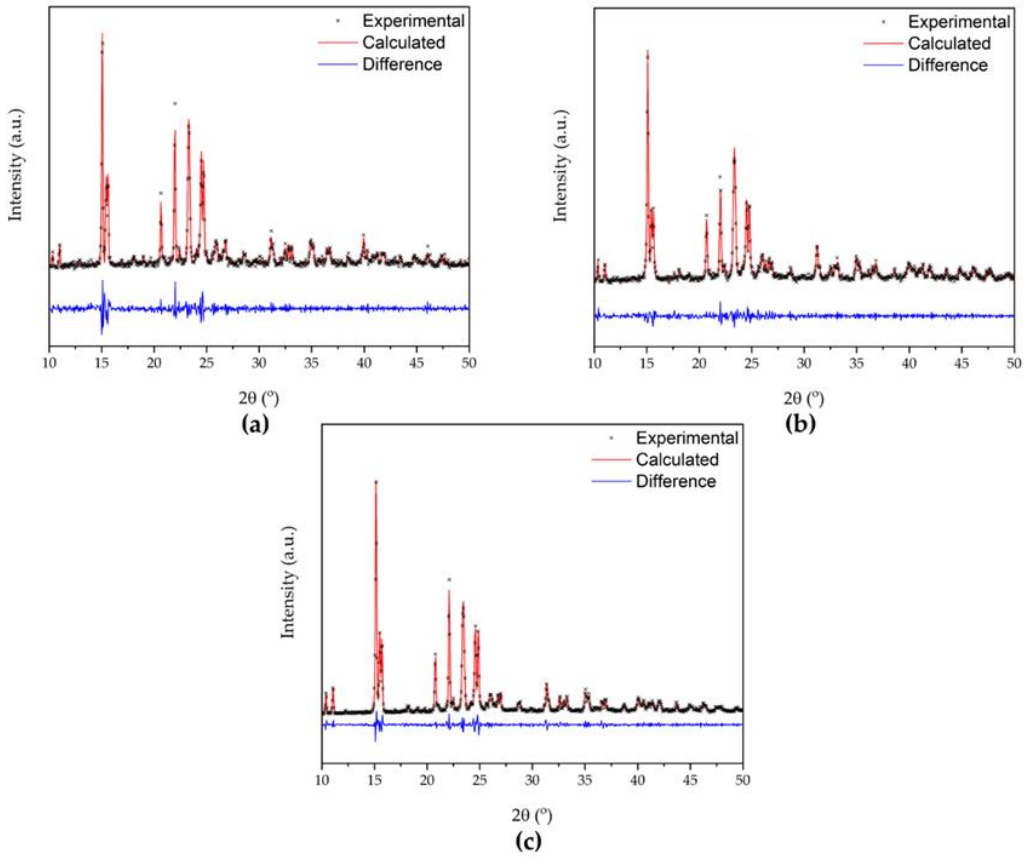

Figure 3-33. Le Bail refinements of the a) [TPrA][Co(dca)$_3$], b) [TPrA][Co$_{0.5}$Ni$_{0.5}$(dca)$_3$] and c) [TPrA][Ni(dca)$_3$].

c) Single crystal X-ray diffraction

To further analyze the crystal structure of [TPrA][Co$_{0.5}$Ni$_{0.5}$(dca)$_3$], it was performed single crystal X-ray diffraction at low temperature. The studies carried out at T = 100 K shown that [TPrA][Co$_{0.5}$Ni$_{0.5}$(dca)$_3$] crystallizes in a tetragonal symmetry with space group P$\bar{4}$2$_1$c (non-centrosymmetric) and cell parameters a = 16.065(1) Å and c = 17.055(1) Å (see Table A3-5 of *Annex II* for more details). It worth to note that this low temperature crystal structure is different to that obtained for this composition by PXRD at room temperature, and analogous to the low temperature crystal structure of the parent compounds.[23]

The asymmetric unit of this low temperature polymorph (from now on called "polymorph I", by analogy with the parent compounds), contains one independent metal cation, three dca anions and three TPrA cations. Both Co^{2+} and Ni^{2+} cations are randomly distributed in a single crystallographic site and connected to its six nearest neighbors, through six $\mu_{1,5}$-dca bridges, in a distorted octahedral environment, with six different M–N distances (see Table A3-6 of *Annex II*). The resulting [MN$_6$] octahedra are cooperatively rotated along the main crystallographic axes (tilt systems $a^-b^+c^-$ at Glazer notation). The metal cations and dca anions build a 3D framework with cuboctahedral cavities, which are occupied by TPrA cations. Additionally, this crystal structure exhibits a certain disorder in the N-amide atoms and C atoms of the dca anions, as well as in the C atom positions of half of the TPrA cations. The here obtained structural data for this mixed compound are summarized in Table A3-5 of *Annex* II and Figure 3-34. All those structural facts are in agreement with those previously reported in the literature for the parent compounds of Ni^{2+} and Co^{2+}. The values of the cell parameters fit between those of the parent hybrids and confirm the regular decrease of the unit cell size with in-creasing Ni:Co ratio, analogous to what was observed for the polymorph at room temperature.

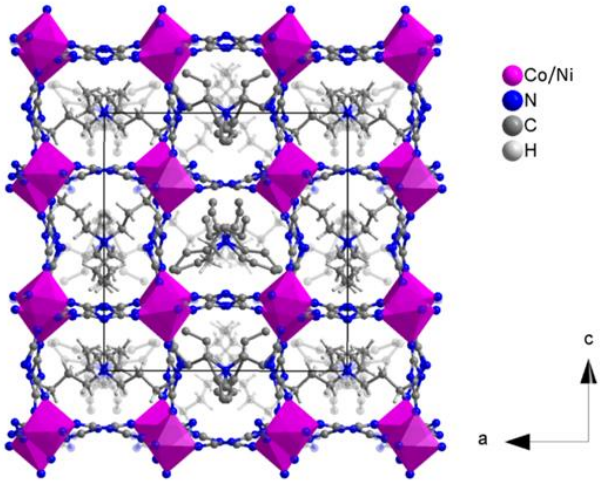

Figure 3-34. A polyhedral/ball-and stick representation of the crystal structure of $[TPrA][Co_{0.5}Ni_{0.5}(dca)_3]$ polymorph I (T = 100 K) along the b-axis.

3.4.3.2. Thermal properties

Given that the parent dicyanamide-perovskites, $[TPrA][Co(dca)_3]$ and $[TPrA][Ni(dca)_3]$ present multiple structural phase transitions in the 100-370 K interval, and those transitions are associated with enthalpy and entropy changes of interest for cooling applications,[23] differential scanning calorimetry (DSC) and thermogravimetric (TGA) analysis of $[TPrA][Co_{0.5}Ni_{0.5}(dca)_3]$ was performed in order check the thermal properties of the new solid solution.

As expected, DSC results (Figure 3-35) showed three phase transitions on heating and cooling for $[TPrA][Co_{0.5}Ni_{0.5}(dca)_3]$, that can be related to four different poly-morphs, named as I, Ia, Ib and II, in the order of the increasing temperature, analogous to the data reported for the parent compounds[23] (also compared in Figure 3-35, and in more detail in Figure 3-36). Assuming the analogy, the results suggest that the first endothermic peak, upon heating, corresponds to the transition from Polymorph I → Polymorph Ia, and is found at T_1 = 227.7 K with a total enthalpy change of 2.99 J g^{-1} and a total entropy change of 13.13 J K^{-1} kg^{-1} for the solid solution. Unfortunately, the corresponding peak on cooling cannot be found due to instrumental limitations to control the temperature in this region. The second transition, from Polymorph Ia → Polymorph Ib, can be seen at T_2 = 300.8 K on heating and 289.5 K on cooling, with enthalpies of 2.59 J g^{-1} and 2.24 J g^{-1} and entropies of 8.61 J K^{-1} kg^{-1} and 7.74 J K^{-1} kg^{-1}, respectively. The high temperature transition, from Polymorph Ib → Polymorph II, appears at T_3 = 347.4 K on heating and 347.3 K on cooling with enthalpy and entropy changes of 4.79 J g^{-1} and 4.74 J g^{-1} and 13.79 J K^{-1} kg^{-1} and 13.65 J K^{-1} kg^{-1}, respectively. Those values are compared with the reported for the parent compounds in Table 3-4, and also in Figure 3-37, where the transition temperatures are represented versus de Ni content. As it can be seen there and very interestingly: i) in the case of the first transition (from Polymorph I → Polymorph Ia) there is a clear metal content dependence on the transition temperature, the enthalpy and the entropy ii) the second transition (from Polymorph Ia → Polymorph Ib) is almost independent of the metal content; iii) in the case of the third transition (from Polymorph Ib → Poly-morph II) the transition temperature clearly depends on the metal content, while the enthalpy and entropy show a low dependence on this factor. In all cases, the values for the mixed sample are always between the values of the parent compounds, in line with the expected behavior for a solid solution.

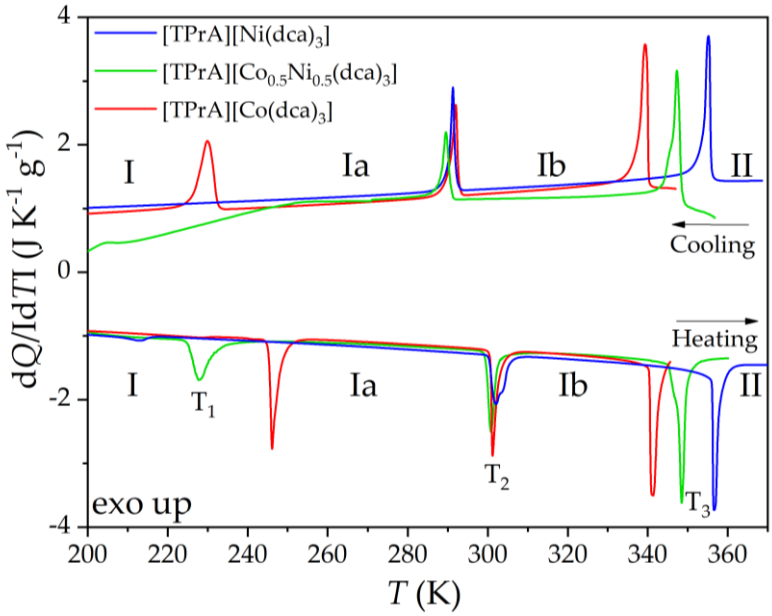

Figure 3-35. DSC curve of [TPrA][$Co_{0.5}Ni_{0.5}(dca)_3$] from 200 K to 360 K and comparison with the reported data for [TPrA][$Co(dca)_3$] and [TPrA][$Ni(dca)_3$] (Data obtained from reference).[23]

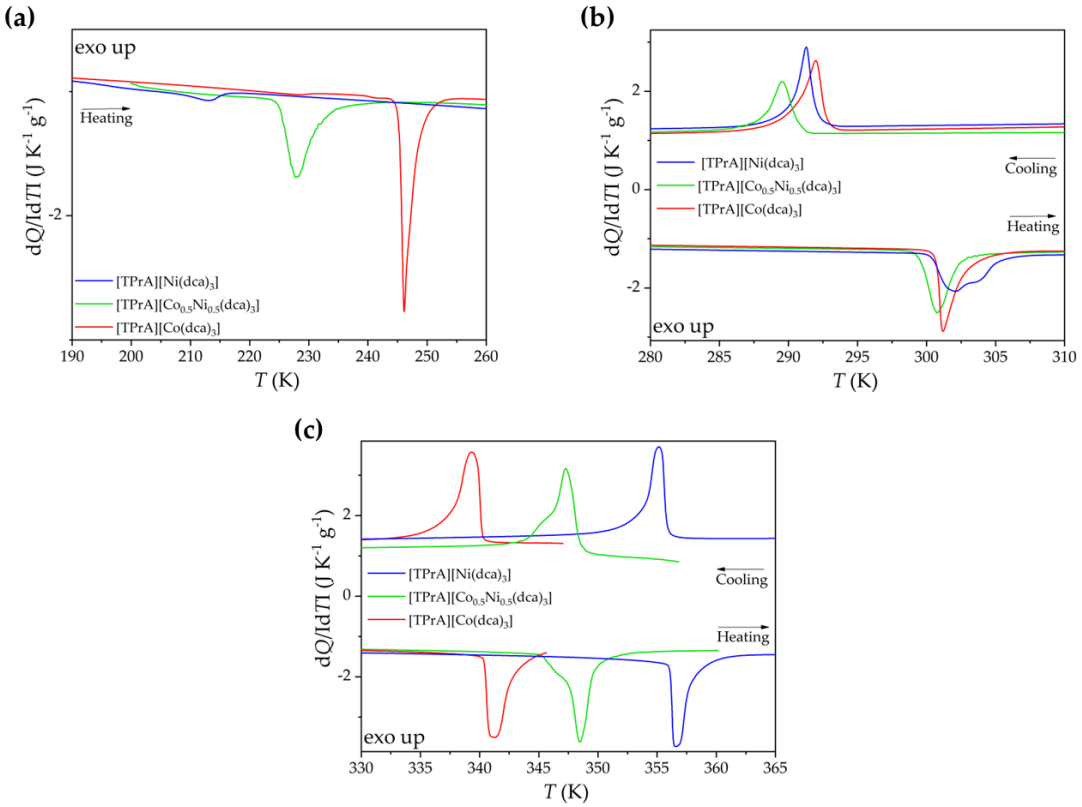

Figure 3-36. Detail of the DSC of the [TPrA][$Co(dca)_3$], [TPrA][$Co_{0.5}Ni_{0.5}(dca)_3$] and [TPrA][$Ni(dca)_3$] from a) 200 K to 260 K, b) 280 K to 310 K and c) 330 K to 365 K.

Table 3-4. Thermal parameters of [TPrA][$Co_{1-x}Ni_x(dca)_3$] (x = 0, 0.5 and 1).

Metal	T_1 (K)	ΔH_1 (J g^{-1})	ΔS_1 (J K^{-1} kg^{-1})	T_2 (K)	ΔH_2 (J g^{-1})	ΔS_2 (J K^{-1} kg^{-1})	T_3 (K)	ΔH_3 (J g^{-1})	ΔS_3 (J K^{-1} kg^{-1})	T_D (K)
Co	246^H	4.0^H	16.5^H	301^H	3.0^H	10.1^H	341^H	4.8^H	14.0^H	~510
	230^C	4.4^C	18.9^C	292^C	3.0^C	10.4^C	339^C	5.8^C	17.1^C	-
$Co_{0.5}Ni_{0.5}$	228^H	3.3^H	14.5^H	301^H	2.7^H	9.0^H	349^H	5.1^H	14.6^H	~540
	-	-	-	290^C	2.6^C	9.1^C	347^C	5.1^C	14.7^C	-
Ni	216^H	0.8^H	3.8^H	302^H	2.7^H	8.8^H	356^H	4.5^H	12.6^H	~560
	-	-	-	291^C	2.7^C	9.3^C	355^C	4.8^C	13.5^C	-

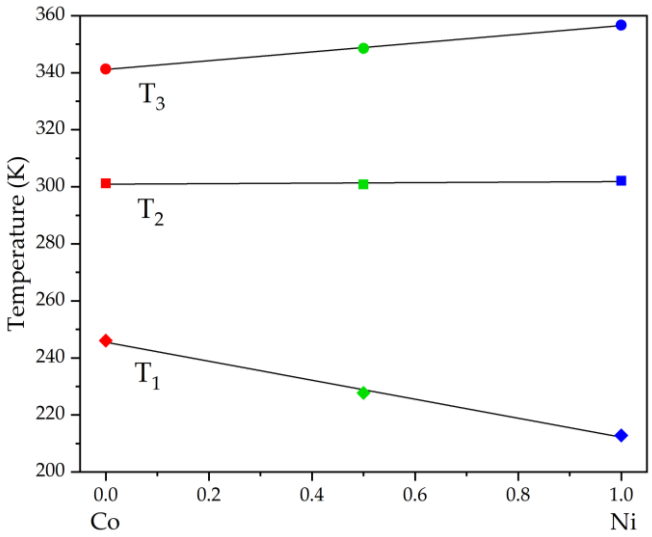

Figure 3-37. Dependence of the transition temperature observed by DSC (by heating) on the metal proportion, for the samples [TPrA][$Co(dca)_3$], [TPrA][$Co_{0.5}Ni_{0.5}(dca)_3$] and [TPrA][$Ni(dca)_3$].

Taking into account the Equation 3-4 for an order-disorder transition:

$$\Delta S = R\,ln(N) \qquad \textbf{Equation 3-4}$$

where R is the gas constant and *N* is the ratio of the number of configurations in the disordered and ordered system, so *N* was calculated as 2.1, 1.6 and 2.0 for the first, second and third transitions, respectively, of the solid solution. Such obtained values are consistent with the reported for the Co and Ni materials.[23]

Thermogravimetric analysis' curves (Figure 3-38) show that the thermal behaviour of the three compounds is also quite analogous at temperatures higher than 300 K, showing a temperature for the start of the decomposition of the solid solution (~540 K) in between the temperatures seen for the parent compounds (~510 K for Co and ~560 K for Ni), and quite similar steps for the complete decomposition.

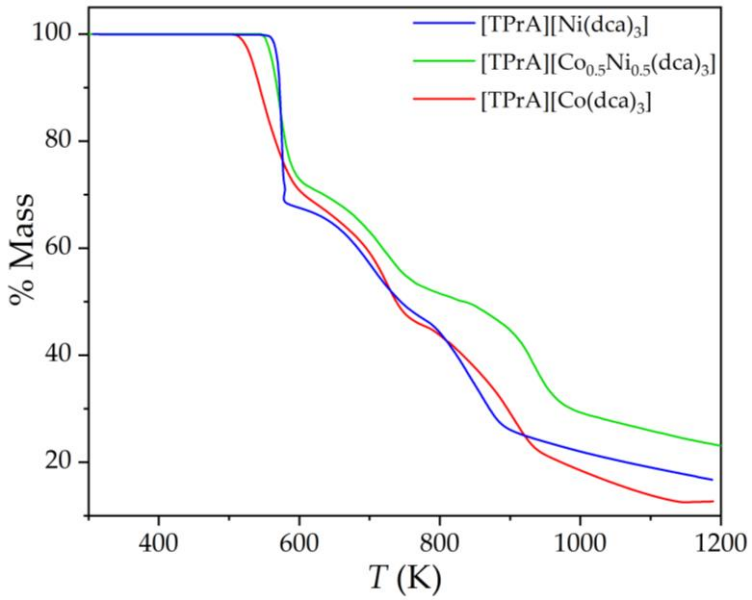

Figure 3-38. TGA curves of $[TPrA][Co_xNi_{1-x}(dca)_3]$ where x = 1, 0.5, 0 from 300 K to 1200 K.

3.4.3.3. Functional properties

a) Dielectric properties

Figure 3-39 shows the temperature dependence of the real part of the complex dielectric permittivity, ε_r', or dielectric constant, of the $[TPrA][Co_{0.5}Ni_{0.5}(dca)_3]$ compound, and the comparison with the parent compound.

The dielectric behavior of the solid solution seems to fit quite well between that of the parent compounds. Three maxima (or irregularities) on the dielectric constant are clearly observed for $[TPrA][Co_{0.5}Ni_{0.5}(dca)_3]$ at temperatures (T_1 = 233 K, T_2 = 306 K and T_3 = 358 K) close to the three solid-solid transitions identified by the differential scanning calorimetry over the heating. The first dielectric transition appears at 233 K. Otherwise, the second and third transitions, at 306 K and 358 K respectively, shows a step-like aspect, the most common in these types of materials.

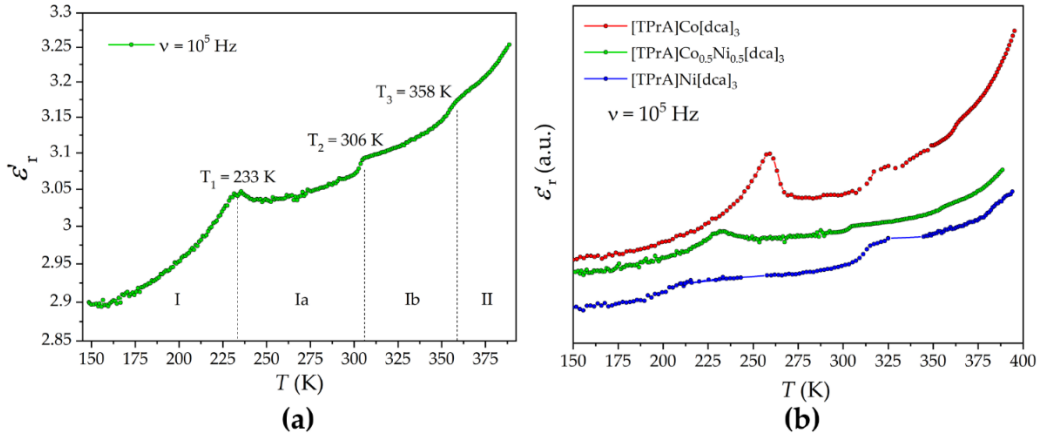

Figure 3-39. a) Dielectric constant of the $[TPrA][Co_{0.5}Ni_{0.5}(dca)_3]$ material over heating from 148 K to 390 K. b) Dielectric constant comparison between $[TPrA][Co_xNi_{1-x}(dca)_3]$ where x = 1, 0.5, 0.

b) Optical properties

Diffuse reflectance spectra were recorded for [TPrA][Co(dca)$_3$], [TPrA][Ni(dca)$_3$] and [TPrA][Co$_{0.5}$Ni$_{0.5}$(dca)$_3$] solid solution, from 250 to 800 nm and compared in Figure 3-40. Below 330 nm, intense bands are observed for all materials, due to matrix absorption. In the 330-800 range, characteristic d-d absorption bands from the metal ions al-low the optical characterization of the hybrids. Very interestingly, [TPrA][Co$_{0.5}$Ni$_{0.5}$(dca)$_3$] shows an absorption spectrum which is the combination (or the overlap) of the spectra of the parent compounds. For [TPrA][Co(dca)$_3$], three ab-sorption maximums are observed at 484, 523 and 613 nm, that were assigned to the transitions from the ground state $^4T^1(F)$ to the excited states $^4T^1(P)$, $^2T^2(G)$, ^2E, and $^2T^1(G)$.[26] The two first transitions produce intense, slightly overlapping bands, while the last two appear as a weak, overlapping shoulder, partially concealed by previous bands. For [TPrA][Ni(dca)$_3$], four distinct bands are recorded at 388, 458, 635 and 723 nm, and were assigned to the absorptions from ground state $^3A_{2g}(F)$ to the excited states $^3T_{1g}(P)$ and $^4T_{1g}(F)$.[26] They are both split due to symmetry loss. (See Table 3-5).

Such results open the possibility to modulate optical properties such as optical band gap just by adjusting the Ni:Co ratio of those solid solutions.[27]

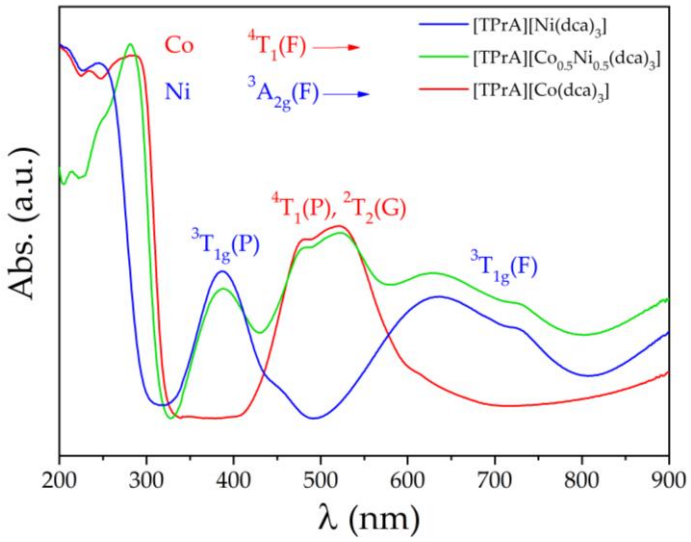

Figure 3-40. UV-Vis spectra of [TPrA][Co$_x$Ni$_{1-x}$(dca)$_3$] where x = 1, 0.5, 0 between 200 and 900 nm.

3.4.3.4. Precursor material for CNTs

After the calcination of [TPrA][Co$_{0.5}$Ni$_{0.5}$(dca)$_3$] at 900 °C under nitrogen atmosphere black ashes were obtained, which are easily attracted when approached to a magnet and indicate the presence of magnetic particles.

Figure 3-41 shows the powder X-ray diffraction patterns of the calcinated sample, compared with those obtained from the parent compounds. The most intense and sharply maxima are due to the crystalline structure of Ni/Co metals (COD data sheet 00-210-0649 and 00-900-8492, respectively).[28,29] As those maxima are not split in Ni:Co = 1:1 compound, and there is a regular dis-placement of the position of the maxima towards larger angles as the amount of nickel increases, meaning that, at least at the scale at which PXRD gives information, the obtained compound from the calcination of mixed cations perovskite is a Ni:Co alloy (or, in other words, a solid solution).

Additionally, the PXRD patterns show a small and wide peak at approximately 26º, which is the characteristic of (002) planes of graphite.

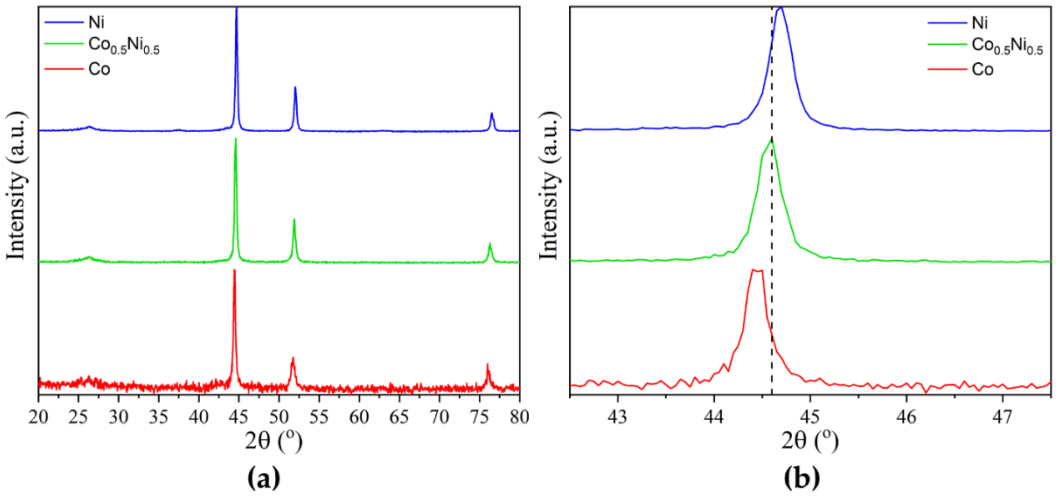

Figure 3-41. a) Powder X-ray diffraction patterns obtained after the calcination of the Co, Ni and mixed cations compounds. b) Detail in the region of the maximum intensity peak.

To deepen into the characterization of the calcinated sample, a study of the obtained ashes was carried out by different techniques of electron microscopy. The study by means of SEM and EDS (see Figure 3-42) show a homogeneous distribution of Co and Ni in the ashes, and an almost equal percentage of both metals (53% of Co and 47% of Ni). By means of TEM it was observed the presence of nanostructures in the form of carbon nanotubes with embedded metal nanoparticles (Figure 3-43).

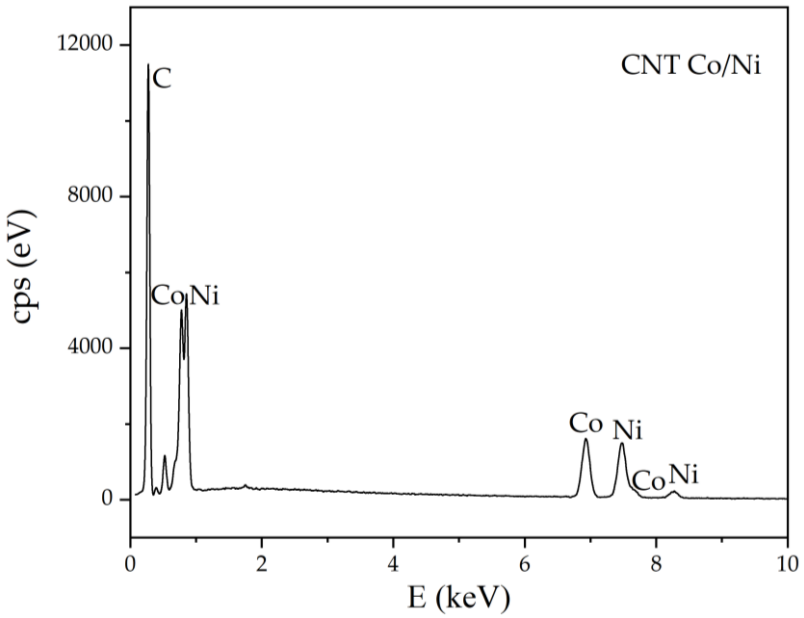

Figure 3-42. EDS spectrum of the CNTs obtained with the calcination of $[TPrA][Co_{0.5}Ni_{0.5}(dca)_3]$.

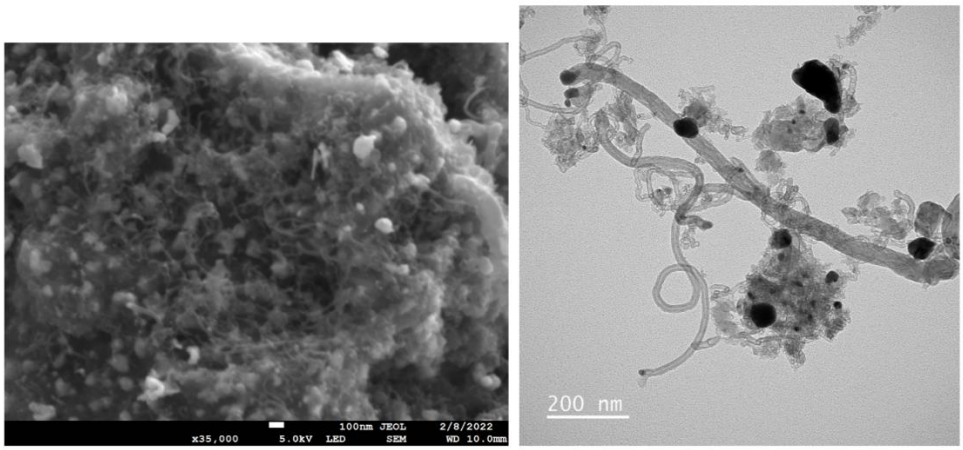

Figure 3-43. Images of CNTs obtained by the calcination of the solid-solution precursors in a) SEM and b) TEM.

Therefore, the simple calcination of the obtained mixed cation compound is an easy route for the preparation of nanostructured material with multiple and interesting applications.

3.4.4. Conclusions

Since the growth of interest on hybrid organic-inorganic perovskites (HOIPs) in the last years, these materials have been subjected to intensive study due to the enormous interest in their functional properties. An attractive option to obtain new compounds and modulate their properties is that of forming solid solutions, a strategy widely used in the case of classical inorganic-perovskites, but relatively unknown for HOIPs.

This work presents the first dicyanamide solid-solution of $[TPrA][Co_{0.5}Ni_{0.5}(dca)_3]$ and study its functional properties, caloric, thermal, dielectric and optical properties, comparing them with those of the parent undoped compounds $[TPrA][Co(dca)_3]$ and $[TPrA][Ni(dca)_3]$.

In the case of its caloric properties there is a linear trend in the three thermally induced solid-solid transitions temperatures as a function of Co:Ni proportion, while their associated enthalpy and entropy values remain similar. Also, the thermal stability of the three compounds seems to be modulated by the metal content, as the 100% Ni compound remains stable up to ~550 K, the 50:50% solid solution is stable up to ~530 K, while the 100% Co compound only up to ~510 K. The dielectric transitions associated to each of the structural phase transitions get similarly displaced. On the other hand, the absorption spectrum of $[TPrA][Co_{0.5}Ni_{0.5}(dca)_3]$ is the combination (or overlap) of the parent compounds of both full Ni and Co materials.

Therefore, this work confirms that traditional materials design strategies, such as solid solutions, used in classic perovskites are also applicable in emerging hybrid dicyanamide perovskites, which will help toward a more rational tunability of the transition temperature (being able to select the temperature of interest for barocaloric applications between others) and their other functional properties.

Finally, the results shown that the here prepared solid solution hybrid compound can be used as a precursor which, upon calcination, gives rise to CNTs with embedded Ni:Co alloy nanoparticles, a fast and much simpler synthetic route than other complex CVD or arc-discharge methods used to obtain such type of materials.

3.4.5. References

[1] W. Li, Z. Wang, F. Deschler, S. Gao, R. H. Friend, A. K. Cheetham, *Nat. Rev. Mater.* **2017**, *2*, 16099.

[2] B. Saparov, D. B. Mitzi, *Chem. Rev.* **2016**, *116*, 4558.

[3] P. Jain, N. S. Dalal, B. H. Toby, H. W. Kroto, A. K. Cheetham, *J. Am. Chem. Soc.* **2008**, *130*, 10450.

[4] P. Jain, V. Ramachandran, R. J. Clark, H. D. Zhou, B. H. Toby, N. S. Dalal, H. W. Kroto, A. K. Cheetham, *J. Am. Chem. Soc.* **2009**, *131*, 13625.

[5] M. Sánchez-Andújar, S. Presedo, S. Yáñez-Vilar, S. Castro-García, J. Shamir, M. a Señarís-Rodríguez, *Inorg. Chem.* **2010**, *49*, 1510.

[6] M. M. Lee, J. Teuscher, T. Miyasaka, T. N. Murakami, H. J. Snaith, *Science (80-.).* **2012**, *338*, 643.

[7] J. Burschka, N. Pellet, S.-J. Moon, R. Humphry-Baker, P. Gao, M. K. Nazeeruddin, M. Grätzel, *Nature* **2013**, *499*, 316.

[8] J. M. Bermúdez-García, M. Sánchez-Andújar, S. Castro-García, J. López-Beceiro, R. Artiaga, M. A. Señarís-Rodríguez, *Nat. Commun.* **2017**, *8*, 15715.

[9] J. Salgado-Beceiro, A. Nonato, R. X. Silva, A. García-Fernández, M. Sánchez-Andújar, S. Castro-García, E. Stern-Taulats, M. A. Señarís-Rodríguez, X. Moya, J. M. Bermúdez-García, *Mater. Adv.* **2020**, *1*, 3167-3170.

[10] J. Li, M. Barrio, D. J. Dunstan, R. Dixey, X. Lou, J. L. Tamarit, A. E. Phillips, P. Lloveras, *Adv. Funct. Mater.* **2021**, *31*, 2105154.

[11] F. S. Galasso, *Structure, Properties and Preparation of Perovskite-Type Compounds*, Oxford Pergamon Press, **1969**.

[12] C. N. R. Rao, *Chemistry of High Temperature Superconductors*, World Scientific, **1991**.

[13] C. N. R. Rao, B. Raveau, *Colossal Magnetoresistance, Charge Ordering and Related Properties of Manganese Oxides*, World Scientific, **1998**.

[14] O. J. Weber, B. Charles, M. T. Weller, *J. Mater. Chem. A* **2016**, *4*, 15375.

[15] S. Chen, R. Shang, B. W. Wang, Z. M. Wang, S. Gao, *Angew. Chemie - Int. Ed.* **2015**, *54*, 11093.

[16] Y. Wu, D. M. Halat, F. Wei, T. Binford, I. D. Seymour, M. W. Gaultois, S. Shaker, J. Wang, C. P. Grey, A. K. Cheetham, *Chem. - A Eur. J.* **2018**, *24*, 11309.

[17] E. A. Donlan, H. L. B. Boström, H. S. Geddes, E. M. Reynolds, A. L. Goodwin, *Chem. Commun.* **2017**, *53*, 11233.

[18] W. Li, A. Stroppa, Z.-M. Wang, S. Gao, *Hybrid Organic-Inorganic Perovskites*, Wiley **2020**.

[19] C. N. R. Rao, J. Gopalakrishnan, *New Directions in Solid State Chemistry*, Cambridge University Press, Cambridge, **1997**.

[20] J. García-Ben, L. N. McHugh, T. D. Bennett, J. M. Bermúdez-García, *Coord. Chem. Rev.* **2022**, *455*, 214337.

[21] J. M. Bermúdez-García, M. Sánchez-Andújar, S. Yáñez-Vilar, S. Castro-García, R. Artiaga, J. López-Beceiro, L. Botana, A. Alegría, M. A. Señarís-Rodríguez, *J. Mater.*

Chem. C **2016**, *4*, 4889.

[22] J. A. Schlueter, J. L. Manson, U. Geiser, *Inorg. Chem.* **2005**, *44*, 3194.

[23] J. M. Bermúdez-García, M. Sánchez-Andújar, et. al., *J. Mater. Chem. C* **2016**, *4*, 4889.

[24] J. M. Bermúdez-García, S. Yáñez-Vilar, A. García-Fernández, M. Sánchez-Andújar, S. Castro-García, J. Mira, J. A. Moreira, T. A. Centeno, M. A. Señarís-Rodríguez, *New J. Chem.* **2017**, *41*, 3124.

[25] R. D. Shannon, *Acta Cryst.* **1975**, *32*, 751.

[26] B. E. S. William B. White, Gregory J McCarthy, *Am. Mineral.* **1971**, *56*, 72.

[27] N. K. Kumawat, A. Dey, A. Kumar, S. P. Gopinathan, K. L. Narasimhan, D. Kabra, *ACS Appl. Mater. Interfaces* **2015**, *7*, 13119.

[28] J. E. Jørgensen, R. I. Smith, *Acta Crystallogr. Sect. B Struct. Sci.* **2006**, *62*, 987.

[29] R. W. G. Wyckoff, *Cryst. Struct.* **1963**, *1*, 7.

Chapter 4

New organometallic and hybrid organic-inorganic plastic crystals with enhanced barocaloric performance and simultaneous ‘cold-storage’

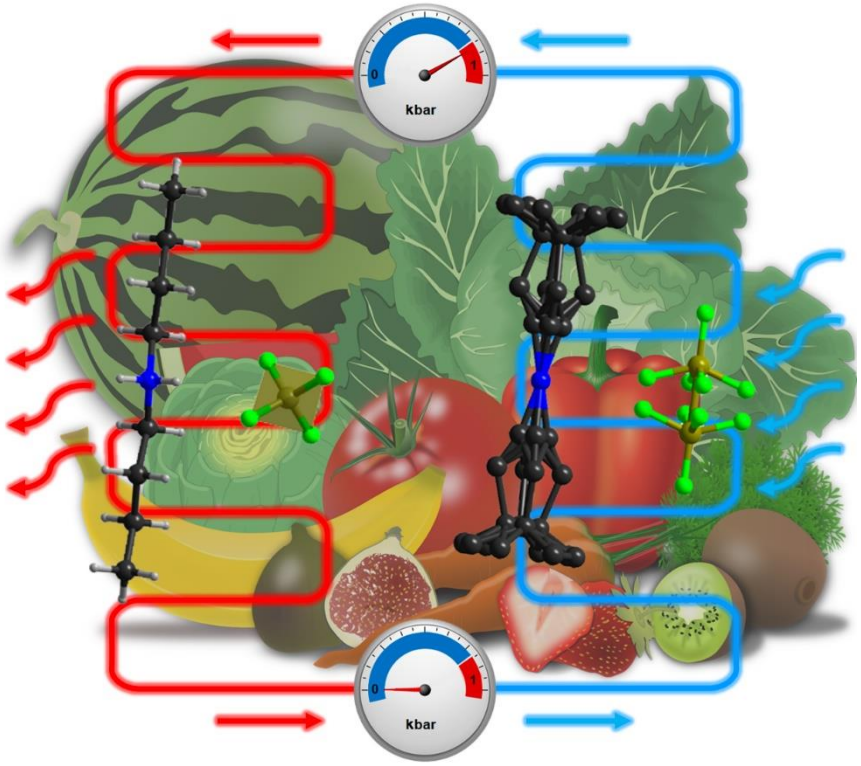

Chapter 4: New organometallic and hybrid organic-inorganic plastic crystals with enhanced barocaloric performance and simultaneous 'cold-storage'

Index

4.1. Introduction to plastic crystals **92**

4.2. Cyclopentadienyl organometallic-sandwich plastic crystals with ring-rotation induced barocaloric effects **97**

4.2.1 Introduction 97

4.2.2. Experimental 97

4.2.3. Results and discussion 98

4.2.4. Conclusions 111

4.2.5. References 112

4.3. Di-n-butylammonium tetrafluoroborate hybrid organic-inorganic material with thermal properties for multipurpose barocaloric refrigeration and 'cold-storage' **115**

4.3.1 Introduction 115

4.3.2. Experimental 116

4.3.3. Caloric properties 118

4.3.4. Structural characterization 125

4.3.5. Conclusions 137

4.3.6. References 138

4.1. Introduction to plastic crystals

Plastic crystals (PCs) are dense crystalline solids formed by molecules or ions with one or more orientational freedom transition (order-disorder transition). The material undergoes a transition from an ordered crystalline phase to another phase in which the molecules/ions gain rotational degrees of freedom while remaining fixed in the crystalline lattice (see Figure 4-1).[1]

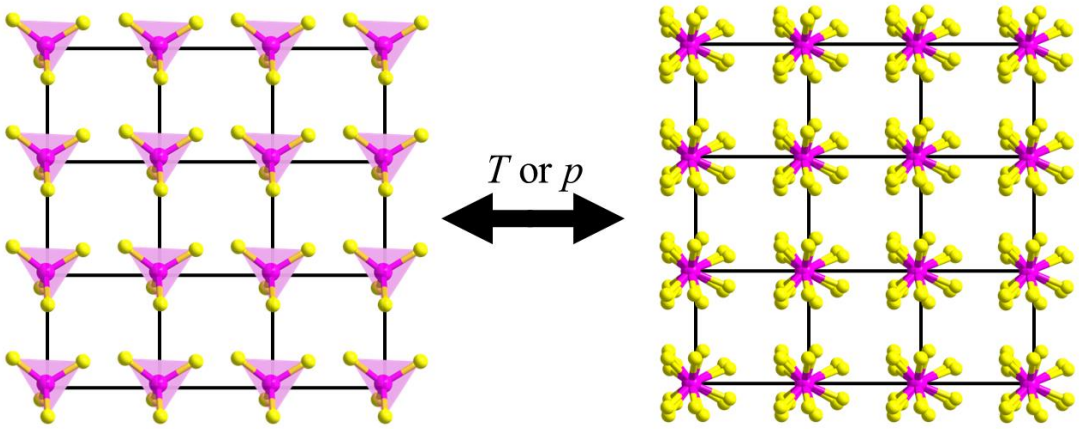

Figure 4-1. Scheme of the order-disorder transition of a PC after the application of temperature or pressure.

The material in the disordered phase exhibits plastic properties, despite its crystalline nature, giving rise to the name of the family. These properties are translated in the plasticity of their mechanic behaviour: upon the application of stress, irreversible deformations without fracture of the material are produced (see Figure 4-2). Furthermore, this order-disorder phase transition typically involves significant thermal changes, which further enhances the interest of PCs for applications related to energy, particularly in the thermal field.

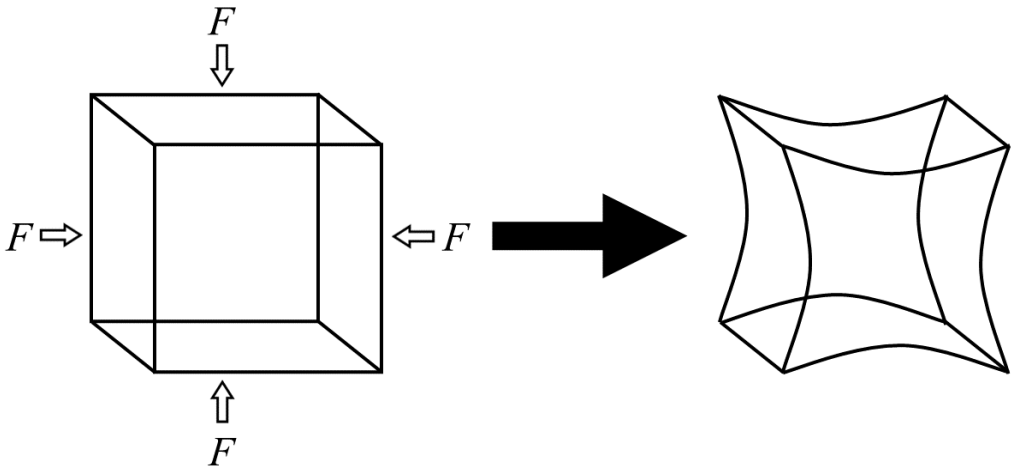

Figure 4-2. Scheme of the permanent deformation of a plastic crystal phase after applying some force.

PCs can be classified based on their composition, distinguishing between those formed by molecules and those composed of ions:

- **Molecular PCs**: are formed by non-charged species. Most of them are known as organic PCs such as neopentylglycol ($C_5H_{12}O_2$),[2] adamantane ($C_{10}H_{16}$) and derivates,[3–5] between others. Due to their properties, they show a lot of interest for different

applications as optoelectronics (optic fluorescence and waveguiding),[6–8] thermal storage[9] and more recently, caloric (in particular barocaloric) for cooling applications.[2–5]

- **Ionic PCs**: are formed by cations and anions. They can be organic or hybrid organic-inorganic plastic crystals if in addition to an organic part, they show inorganic components (metals coordinated or classical inorganic anions such as BF_4^-, PF_6^-, halides, NO_3^-, etc.).[10] These materials show a large number of applications, such as optics,[11] photon conductors,[12] magnetic,[13] electric,[14] thermal storage[15] and very recently barocaloric.[16]

The order-disorder transitions in these systems exhibit significant thermal changes, making them highly attractive for barocaloric and thermal energy-storage applications. However, the main limitations of barocaloric organic PCs are that they operate at very high temperatures (over 310 K) and under the application of very large pressures (over 1000 bar), which pose challenges for their practical use as barocaloric refrigerants.

The main objective of this chapter is to reduce the high pressures required for the effective functioning of PCs as refrigerants. To achieve this, this chapter will focus on studying hybrid ionic PCs, hoping that the combination of organic and inorganic species could minimize the working pressure. Therefore, this chapter aims to explore new organometallic and hybrid organic-inorganic compounds (namely cyclopentadienyl and long-chain alkylammonium derivatives) of interest for barocaloric effects at low pressure and temperature, and that can simultaneously present thermal energy storage for multipurpose applications.

The initial study will explore the barocaloric response of well-studied systems in other fields, such as organometallic sandwich-type salts. This study, detailed in the subchapter titled '*Cyclopentadienyl organometallic-sandwich plastic crystals with ring-rotation induced barocaloric effects*', focuses on compounds with the general formula $[Cp_2M][PF_6]$ ($Cp = C_5H_5$, M = Fe, Co).

Lastly, the second subchapter, titled '*Di-n-butylammonium tetrafluoroborate hybrid organic-inorganic material with thermal properties for multipurpose barocaloric refrigeration and 'cold-storage'',* explores the potential of hybrid ionic PCs for both barocaloric refrigeration and passive 'cold-storage'.

References

[1] L. A. K. Staveley, *Annu. Rev. Phys. Chem.* **1962**, *13*, 351.

[2] P. Lloveras, A. Aznar, M. Barrio, P. Negrier, C. Popescu, A. Planes, L. Mañosa, E. Stern-Taulats, A. Avramenko, N. D. Mathur, X. Moya, J. L. Tamarit, *Nat. Commun.* **2019**, *10*, 1.

[3] A. Aznar, P. Negrier, A. Planes, L. Mañosa, E. Stern-Taulats, X. Moya, M. Barrio, J. L. Tamarit, P. Lloveras, *Appl. Mater. Today* **2021**, *23*, 101023.

[4] A. Salvatori, P. Negrier, A. Aznar, M. Barrio, J. L. Tamarit, P. Lloveras, *APL Mater.* **2022**, *10*, *111117*.

[5] A. Aznar, P. Lloveras, M. M. Barrio, P. Negrier, A. Planes, L. L. Mañosa, N. D. Mathur, X. Moya, J. L. L. Tamarit, *J. Mater. Chem. A* **2020**, *8*, 639.

[6] M. Pope, C. Swenberg, *Electronic Processes in Organic Crystals and Polymers*,

[7] S. Hayashi, T. Koizumi, **2016**, *55*, 2701.

[8] L. Lan, H. Liu, X. Yu, X. Liu, H. Zhang, *Angew. Chemie - Int. Ed.* **2021**, *60*, 11283.

[9] A. Serrano, M. Duran, J. L. Dauvergne, S. Doppiu, E. P. Del Barrio, *Sol. Energy Mater. Sol. Cells* **2021**, *220*, 110848.

[10] J. M. Pringle, P. C. Howlett, D. R. MacFarlane, M. Forsyth, *J. Mater. Chem.* **2010**, *20*, 2056.

[11] S. Parola, B. Julián-López, L. D. Carlos, C. Sanchez, *Adv. Funct. Mater.* **2016**, *23*, 6506.

[12] M. Yoshizawa-Fujita, K. Fujita, M. Forsyth, D. R. MacFarlane, *Electrochem. Commun.* **2007**, *9*, 1202.

[13] H. L. Cai, Y. Zhang, D. W. Fu, W. Zhang, T. Liu, H. Yoshikawa, K. Awaga, R. G. Xiong, *J. Am. Chem. Soc.* **2012**, *134*, 18487.

[14] M. Wojciechowska, A. Gagor, A. Piecha-Bisiorek, R. Jakubas, A. Cizman, J. K. Zaręba, M. Nyk, P. Zieliński, W. Medycki, A. Bil, *Chem. Mater.* **2018**, *30*, 4597.

[15] J. Salgado-Beceiro, S. Castro-García, M. Sánchez-Andújar, F. Rivadulla, *J. Phys. Chem. C* **2018**, *122*, 27769.

[16] J. Salgado-Beceiro, J. M. Bermúdez-García, E. Stern-Taulats, J. García-Ben, S. Castro-García, M. Sánchez-Andújar, X. Moya, M. A. Señarís-Rodríguez, *ChemRxiv* **2021**, 17.

4.2. Cyclopentadienyl organometallic-sandwich plastic crystals with ring-rotation induced barocaloric effects

Part of this work is under review and pending to be published.

4.2.1. Introduction

Organometallic complexes which contain at least one metal-carbon bond, are a very large and important family of compounds, known since the XIX century,[1] that have played a critical role in catalysis and organic synthesis.[2] In addition, over last decades they have awakened the interest in new research fields due to their interesting applications in optics,[3] biomedicine,[4] molecular magnetic devices,[5] among others.

Within the broad diversity of organometallic compounds, metallocenium salts have attracted an special attention for crystal engineering and molecular motion in the solid state.[6] These compounds are complex 'sandwich' salts with general formula $[Cp_2M][X]$ (Cp: cyclopentadiene (C_5H_5) or functionalized Cp, M: transition metal cations and X: PF_6^-, Cl^-, BF_4^-, etc). They typically undergo multiple and fully reversible solid-solid phase transitions between ordered and totally/or partially disordered phases, due to the combination of an intramolecular structure flexibility (arising from the delocalized bonding interactions in the Cp_2M moieties) and an intermolecular flexibility (from the molecular crystals).[7,8] Interestingly, these phase transitions can be modified depending on the chemical components, such as metal cations and anions.[9] Moreover, these phase transitions frequently entail significant volume changes.[7,11] This characteristic is particularly intriguing for barocaloric applications and stands as a crucial parameter in the search for new barocaloric materials.

In this chapter, the potential of these metallocenium salts family was explored for solid-state barocaloric refrigeration. More specifically, this chapter focus on two hybrid ionic plastic crystals with general formula $[Cp_2M][PF_6]$ (compound **1**: M = Fe^{3+}, compound **2**: M = Co^{3+}), to study for the first time, this family as barocaloric materials. For this purpose, this chapter studies their sensitiveness to applied pressure, their isobaric and isothermal reversible entropy changes, their reversible adiabatic temperature changes and their operating temperature ranges.

These two metallocenium salts were previously characterized in detail by Braga *et al.*,[7,10] who have reported that both experience two fully reversible solid-solid phase transitions below and above room temperature. The first phase transition, transforming the low temperature phase I into the intermediate temperature phase II (both exhibiting a monoclinic symmetry and space group $P2_1/c$), is associated to a reorientation of the $[Cp_2M]^+$ cations. This change brings about a decrease in β together with a slight increase in the cell volume.[7,8,11]

Meanwhile the high temperature phase transition transforms the intermediate monoclinic phase II into the cubic (S.G: $Pm\bar{3}$) phase III, which provokes an order-disorder transformation. In the case of compound **1,** this leads to a complete orientational disorder of both cations and anions, resulting in a plastic crystal phase. Meanwhile, in the case of compound **2**, there is only orientational disorder in the $[Cp_2M]^+$ cations (with the $[PF_6]^-$ anions remaining ordered), which results in a high temperature semi-plastic crystal phase.[7,10]

4.2.2. Experimental

4.2.2.1. Materials

Commercially available reagent grade $[Cp_2Co][PF_6]$ (98% Sigma-Aldrich) was directly used for these studies.

Meanwhile ferrocenium hexafluorophosphate was prepared from $[Cp_2Fe]$ (98% Sigma-Aldrich), $FeCl_3 \cdot 6H_2O$ (97% Sigma-Aldrich) and $[NH_4][PF_6]$ (99.98% Sigma-Aldrich) according to a literature procedure.[12] For this purpose, ferrocene (3.35 mmol), dissolved in water/acetone (75/25; 15 ml), was mixed with $FeCl_3 \cdot 6H_2O$ (4.5 mmol) dissolved in water (10 ml), at room temperature. The mixture was stirred for 15 minutes and the obtained precipitate was removed by filtration. Subsequently, NH_4PF_6 (4.45 mol) was added to the solution. Blue crystals of $[Cp_2Fe][PF_6]$ were obtained after few days upon slow evaporation of the solvent at room temperature and they were collected by filtration and washed several times with water.

4.2.2.2. Thermal analysis

Variable-temperature differential scanning calorimetric (VT-TDSC) analysis at atmospheric pressure and heat capacity measurements were carried out using a TA-Instruments Q200, heated and cooled with a rate of 10 K min^{-1}, from 200 up to 380 K, under a nitrogen atmosphere, for both compounds. The C_p measurements were done following the literature dynamic method with a previous calibration of sapphire Eq 4-1:[13,14]

$$Cp_m = Cp_s \frac{D_m m_s}{m_m D_s} \qquad \textbf{Equation 4-1}$$

where C_{pm} is the heat capacity of each compound, Q_m the heat flow of the material, C_{ps} the heat capacity of the sapphire obtained from a tabulated table, m_s the mass of the sapphire, m_m the mass of the material and Q_s the heat flow of the sapphire.

Variable-pressure differential scanning calorimetry (VP-DSC) was performed with a Setaram mDSC7 EVO microcalorimeter equipped with a 65D Isco pressure pump that utilized nitrogen gas as pressure transmitting media. For the measurements, ~20 mg of sample was swept in temperature from 320 to 390 K in case of compound **1** and from 290 to 350 K in case of compound **2**, both at ±1.2 K min^{-1} at different isobaric pressures from atmospheric pressure to 1000 bar.

4.2.2.3. Variable-temperature synchrotron radiation powder X-ray diffraction

Variable temperature synchrotron powder X-ray diffraction (VT-SPXRD) patterns of compounds **1** and **2** were recorded at the I11 beamline of the Diamond Synchrotron (Oxford, UK) using a wavelength of 0.825955(3) Å. The wavelength was determined by refining the positions of six individual reflections of a NIST640D silicon standard at room temperature. The sample was enclosed in a glass capillary (inner diameter ϕ = 0.5 mm) and in continuous rotation during data collection to improve powder averaging. Patterns were collected using Mythen position sensitive detector while heating the sample from 170 to 335 K. The working temperature was set using a FMB Oxford hot-air blower. Le Bail refinement was carried out using the program GSAS-II.[15]

4.2.3. Results and discussion

4.2.3.1. Variable-temperature differential scanning calorimetry (VT-TDSC) at atmospheric pressure

According to the variable-temperature differential scanning calorimetric (VT-DSC) results, both compounds exhibit two reversible phase transitions, which occur between three consecutive polymorphs (see Figure 4-3). In the case of the compound **1**, the two endothermic peaks appear on heating at $T_{(I\rightarrow II)}$ ~212 K and $T_{(II\rightarrow III)}$ ~347 K and at $T_{(II\rightarrow I)}$ ~200 K and $T_{(III\rightarrow II)}$ ~344 K on cooling. Meanwhile, for compound **2**, the exothermic peaks are found at $T_{(I\rightarrow II)}$ ~253 K and $T_{(II\rightarrow III)}$ ~312 K on heating, and at $T_{(II\rightarrow I)}$ ~236 K and $T_{(III\rightarrow II)}$ ~309 K on cooling.

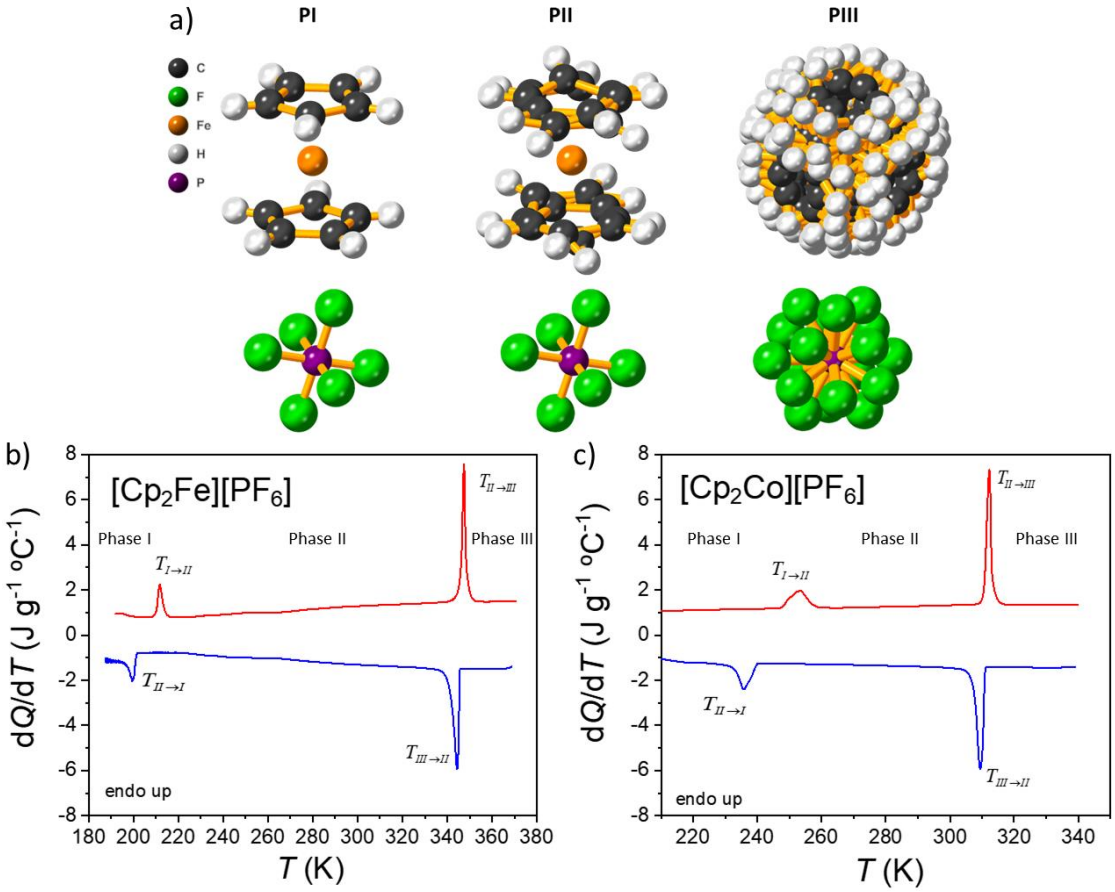

Figure 4-3 a) Illustrating example of the dynamic evolution of the $[Cp_2Fe]^+$ cations and the $[PF_6]^-$ anions across the thermally-induced phase transitions. *Note*: crystal structures represented from CIF files of reference.[7,11] VT-DSC curves on heating and cooling of b) compound **1** between 190 and 370 K and c) compound **2** between 210 and 340 K.

The associated thermally driven latent heat and entropy change associated to each of them, obtained from the integration of the area under the curve of the peaks, are summarized on Table 4-1 and are in good agreement with previous literature data.[7,10,11]

Table 4-1. Temperature, thermal hysteresis, enthalpy and entropy change values of the observed phase transitions for both materials on heating and cooling.

	Compound 1		Compound 2	
	I ↔ II	**II ↔ III**	**I ↔ II**	**II ↔ III**
$T_{t(h)}$ **(K)**	211.8	347.4	253.3	312.3
$T_{t(c)}$ **(K)**	199.5	344.4	235.8	309.5
$\lvert T_{t(h)} - T_{t(c)} \rvert$	12.3	3.0	17.5	2.8
$\Delta H_{(h)}$ **(kJ kg^{-1})**	3.95	13.20	4.79	10.68
$\Delta H_{(c)}$ **(kJ kg^{-1})**	3.98	13.87	5.23	11.61
$\Delta S_{(h)}$ **(J K^{-1} kg^{-1})**	18.64	38.00	18.95	34.21
$\Delta S_{(c)}$ **(J K^{-1} kg^{-1})**	19.91	40.55	22.27	37.54

Note: (h) = heating, (c) = cooling.

As it can be seen, in both compounds the higher temperature phase transition is more energetic and displays a lower thermal hysteresis on heating and cooling than the lower temperature one, so it will be the one of interest for our subsequent barocaloric characterization.

As for the differences observed between the behavior of both compounds, it should be noted that in **1** the II↔ III transition occurs at temperatures that are 35 degrees higher (on heating) than in **2**, and with an over 20% larger enthalpy change. This is probably related to two factors:

(i) In phase II of compound **1** the C-H---F-P interactions between the Cp-rings and the PF_6 anions are stronger than in compound **2**, according to the results of F. Grepioni *et al.*[10]

(ii) In the case of compound **1,** transforming the phase II into phase III implies the disordering of both cations and anions, which would require a high thermal energy. Meanwhile, in compound **2** only the cations get disordered.[10,27]

In this context, this chapter anticipates that with the adequate modification of the sandwich cation and/or the anion (to promote stronger or weaker interactions between them) the transition temperature and the ΔH can be modulated to obtain optimized properties.

Additionally, the heat capacity, C_p, of both materials have been measured for a temperature range close to the observed phase transitions (see Figure 4-4 which represents the heat capacity of both materials as a function of temperature). As a first general remark, it should be noted that their C_p values are relatively low, as also reported for other sandwich-type compounds.[18–22] In any case, compound **2** presents higher C_p than **1**: C_p (phase I) ~820 J ^{o}C^{-1} kg^{-1} (compound **1**) and ~1100 J ^{o}C^{-1} kg^{-1} (compound **2**); C_p (phase II) ~1260 J ^{o}C^{-1} kg^{-1} (compound **1**) and ~1355 J ^{o}C^{-1} kg^{-1} (compound **2**); C_p (phase III) ~1280 J ^{o}C^{-1} kg^{-1} (compound **1**) and ~1540 J ^{o}C^{-1} kg^{-1} (compound **2**), differences which could be related to the extra stability of compound **2**, with stronger intramolecular interactions.

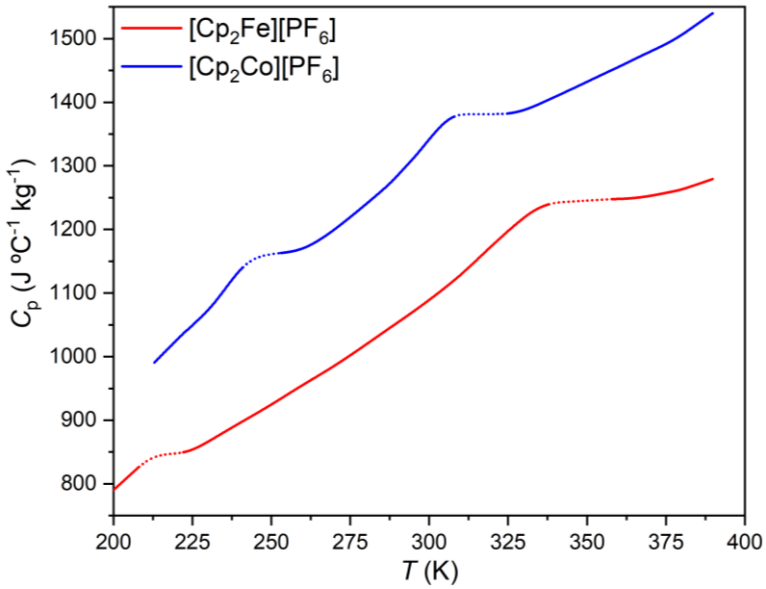

Figure 4-4. Heat capacity as function of temperature (heating) of compound **1** (red) and compound **2** (blue) between 200 and 400 K. *Note*: the dotted region represents the C_p estimation where phase transitions occur.

Such values are slightly lower than those shown by most of the reported barocaloric plastic crystals,[17–22] especially in the case of compound **1**, whose C_p is in fact very similar to that shown by fullerite (C_{60}).[16]

Regarding the thermogravimetric analysis, compound **2** presents higher thermal stability (with a decomposition temperature of T_d ~650 K) than compound **1** (with T_d ~450 K), see Figure 4-5. This could be related to the fact that, in compound **2**, the $[Cp_2Co]^+$ cation obeys the 18 e^- rule,[23] while the Fe-sandwich does not, resulting in more stable structure with stronger bonds and shorter M-C distances in the cation.[7,8,10]

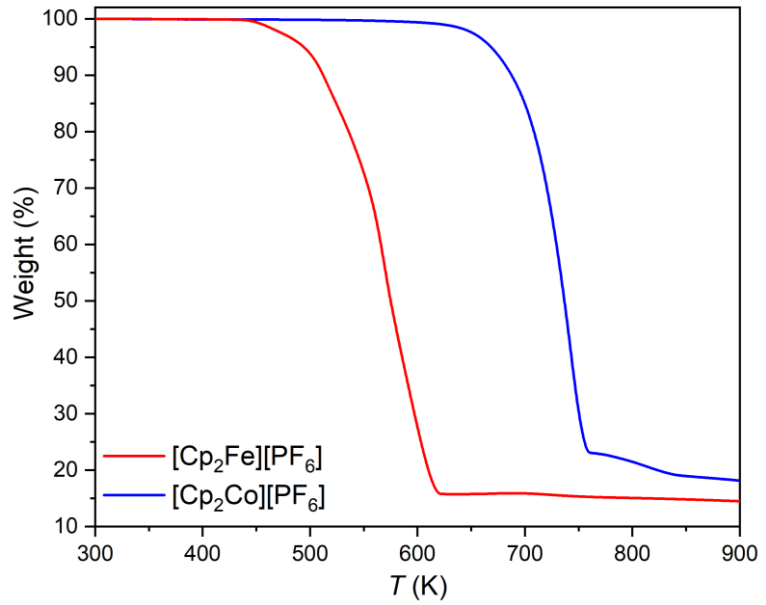

Figure 4-5. TGA in N_2 atmosphere of compound **1** (red) and compound **2** (blue) between 300 and 900 K.

4.2.3.2. Variable-temperature synchrotron powder X-ray diffraction and crystal structure at atmospheric pressure.

In order to calculate the different ΔV values across the phase transitions, VT-SPXRD analyses were performed. Here, the cell parameters were obtained by Le Bail refinement (see Figures 4-6 and 4-7). Accordingly, the obtained results show two sharp structural changes occurring at $T_{(I \rightarrow II)}$ ~211 K and $T_{(II \rightarrow III)}$ ~350 K for compound **1**, and at $T_{(I \rightarrow II)}$ ~258 K and $T_{(II \rightarrow III)}$ ~315 K for compound **2**. These values are completely in agreement with those observed by VT-DSC.

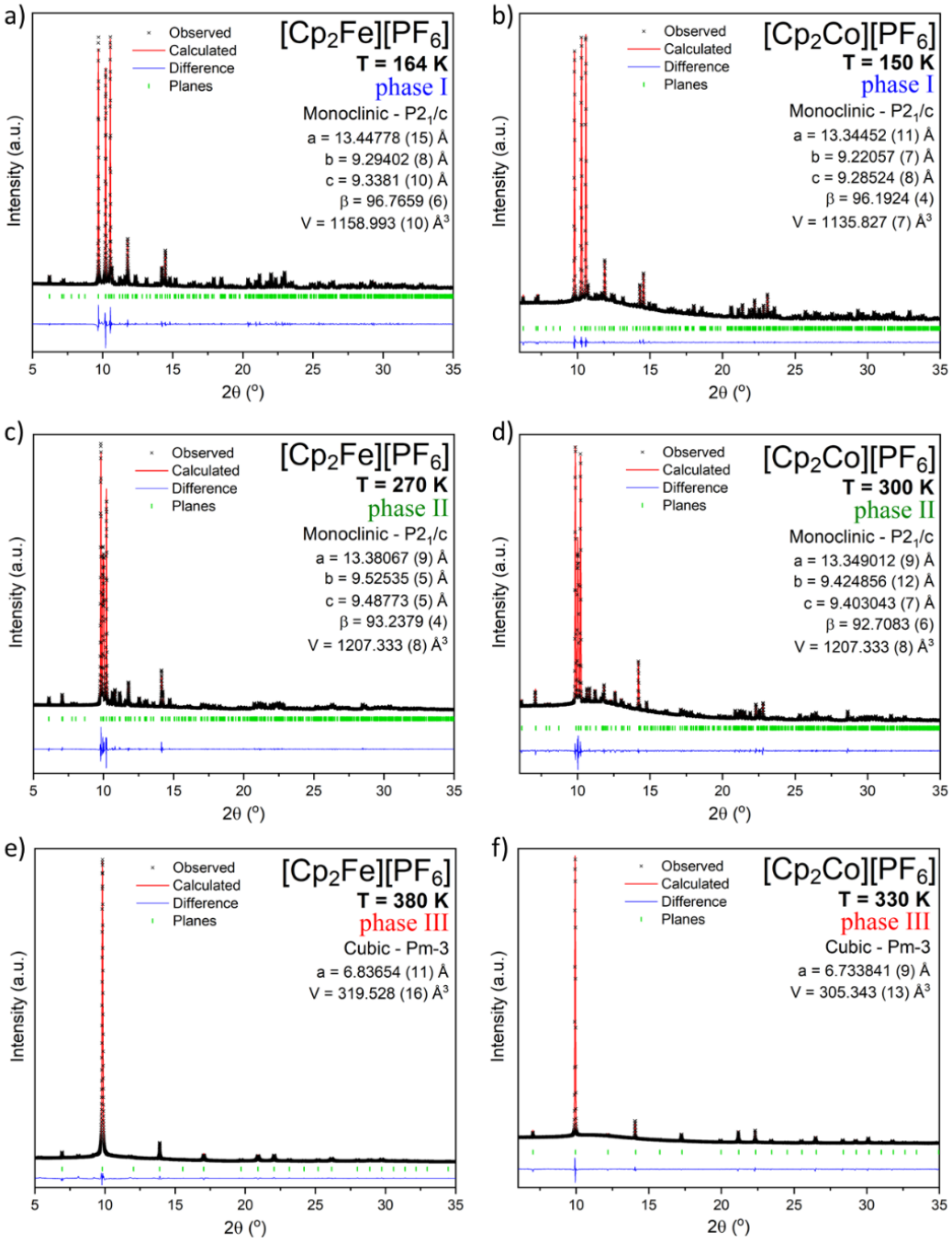

Figure 4-6. Le Bail refinements of all the phases of both compounds, a) and b) phase I, c) and d) phase II and e) and f) phase III of compound **1** and compound **2**, respectively.

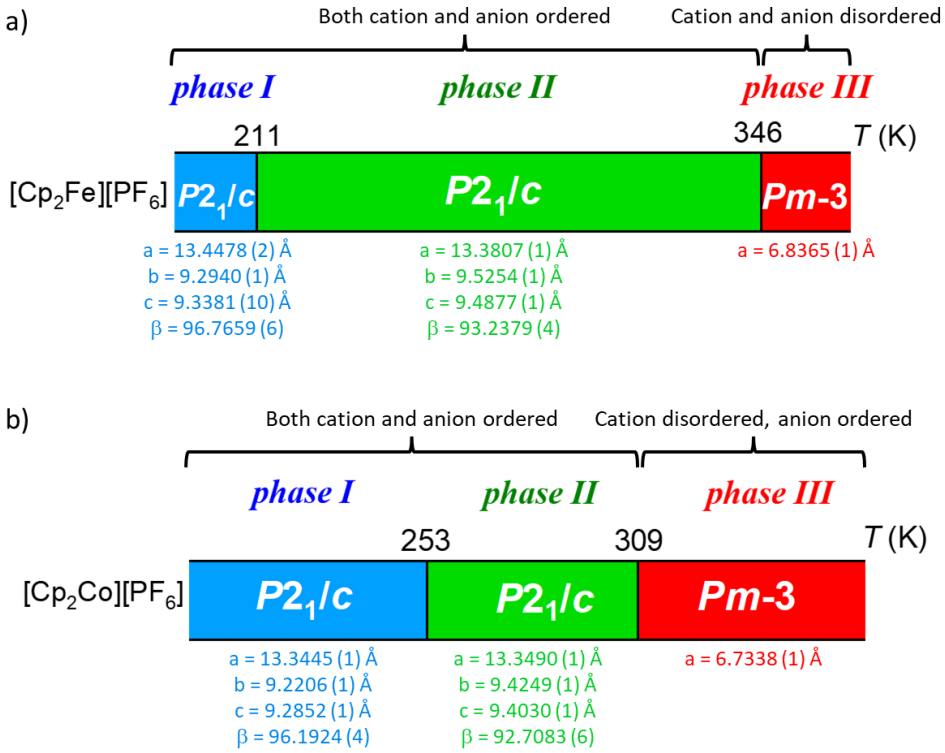

Figure 4-7. Structure information of the three phases of a) compound **1** and b) compound **2**.

Regarding the volume evolution over temperature (see Figure 4-8), both compounds exhibit a conventional positive thermal expansion upon heating and an abrupt volume change associated with each phase transition, effect which is larger in the case of the II-III phase transition: $\Delta V_{I \rightarrow II}$ ~1.22% (compound **1**) and ~1.27% (compound **2**), while $\Delta V_{II \rightarrow III}$ ~2.24% (compound **1**) and ~2.02% (compound **2**). Interestingly, the $\Delta V_{II \rightarrow III}$ is rather similar in both compounds, even if compound **1** shows disorder of both anions and cations, while in compound **2** presents disorder only in the cations.[7,11] Therefore, it can conclude that most of the observed volume increase is probably related to the disordering of the $[(C_5H_5)_2M]^+$ cations. This, in turn, is dependent on the intramolecular structural flexibility of these $[Cp_2M]^+$ cations, which show ease of rotation of each cyclopentadiene ring and a dynamic disorder of the sandwich in the crystal structure.[7,8,10,11]

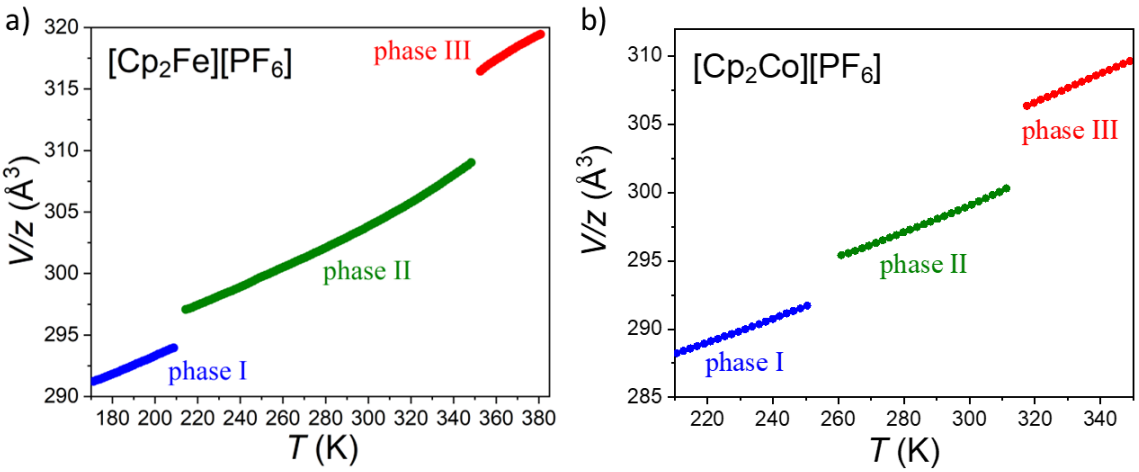

Figure 4-8. Thermal evolution of unit-cell volume per formula unit of a) compound **1** and b) compound **2**.

But it should also be noted that such metallocinium cations increase their rotational motion within the space defined by the PF_6^- anions, in which they are encapsulated in the CsCl-type structure.

On this basis, this chapter proposes that with modulation of the anion (looking for anisotropic shapes) much larger volume changes could be reached in the order-disorder transitions.

From the VT-SPXRD data and the previous VT-DSC results, this chapter focuses on the high-temperature phase transitions (which are more energetic and present higher volume changes) to estimate their barocaloric coefficient by indirect methods (see Equation 1-1 of *Chapter 1*, section 1.2.1.b). In that regard, they show values of dT_t/dp ~34.1 K kbar^{-1} and ~29.7 K kbar^{-1} for compound **1** and **2**, respectively.

4.2.3.3. Variable-pressure differential scanning calorimetry and barocaloric performance

The barocaloric performance of phase II ↔ phase III transition for both compounds **1** and **2** were estimated by variable-pressure differential scanning calorimetry (VP-DSC) following the quasi-direct methodology.[24] For that purpose, the samples were measured under heating-cooling cycles at different isobaric pressures (see Figure 4-9). In this context, VP-DSC measurements were performed from 1 bar to 1000 bar in the temperature region associated with the phase transition between phases II ↔ III. This transition was chosen because it is the one involving higher entropy and volume change values, so it is also expected to provide a higher BC response. As it can be seen in Figure 4-9 both compounds show a conventional barocaloric effect as the II ↔ III phase transition temperature increases with applied pressure

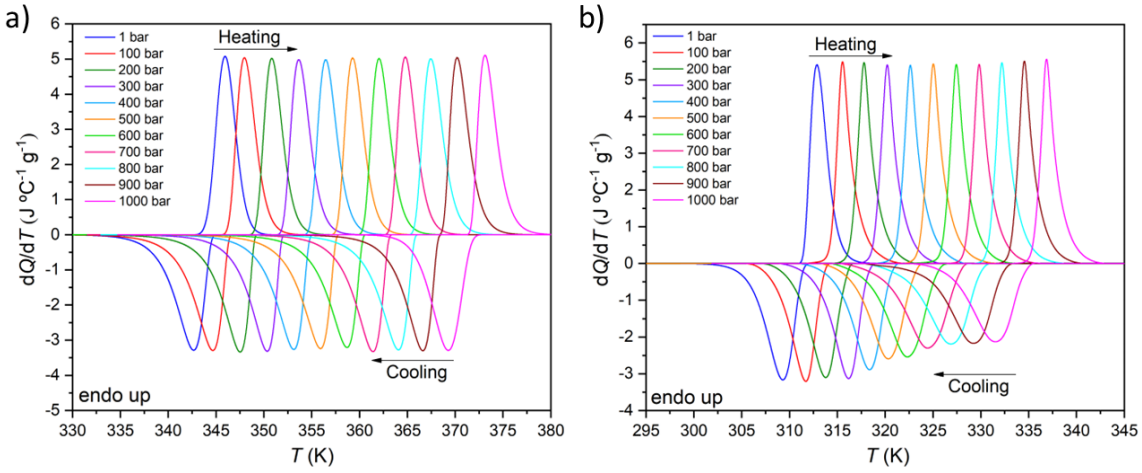

Figure 4-9. Heat flow, dQ/dT, as a function of temperature, under different applied pressures from 1 bar to 1000bar, of a) compound **1** and b) compound **2.**

Figure 4-10 shows the pressure dependence of the phase transition temperature, taken from the maximum of the peaks of Figure 4-9, on heating and cooling. In this context, the barocaloric tunability or the barocaloric coefficient (dT/dp)[25] of the phase transition was calculated from the slope of the linear region in Figure 4-10. The as obtained barocaloric tunability values, on heating, were ~27.6 K kbar^{-1} and ~24.0 K kbar^{-1}, for **1** and **2**, respectively, which have reasonable similarities to the previously obtained values by indirect method.

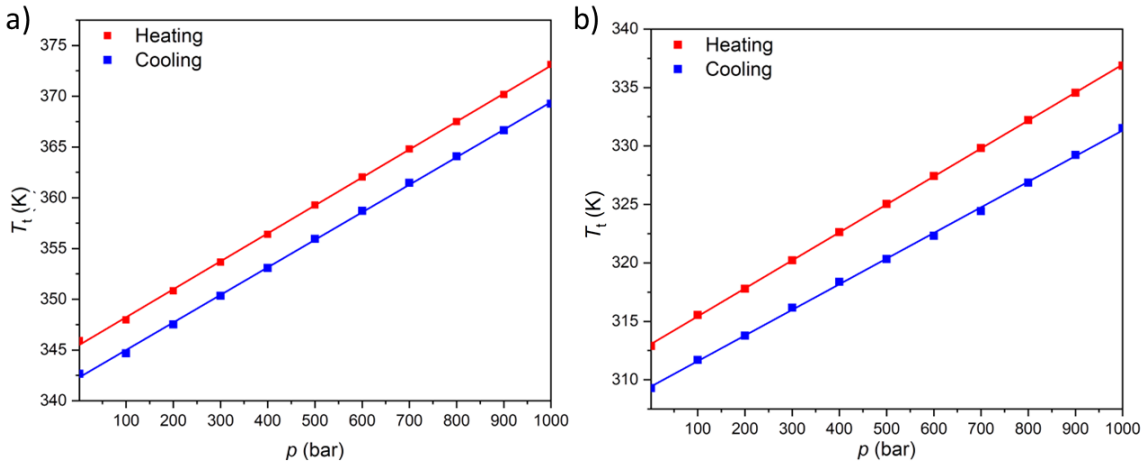

Figure 4-10. Pressure dependence of T_t for a) compound **1** and b) compound **2** on heating and cooling. *Note:* The scatter points show the maximum of the peak, and the shaded area is the temperature region in where the phase transition is taking place.

Additionally, Figure 4-11 shows the isobaric entropy changes (ΔS_{ib}) calculated following the Equation 1-2 (see *Chapter 1*, section 1.2.1.b). The values obtained at atmospheric pressure, $|\Delta S_{ib}|$ ~36.5 J K^{-1} kg^{-1} for **1** and ~36.7 J K^{-1} kg^{-1} for **2** (on average on heating and cooling), are in agreement with the obtained values by VT-DSC (see Table 4-1).

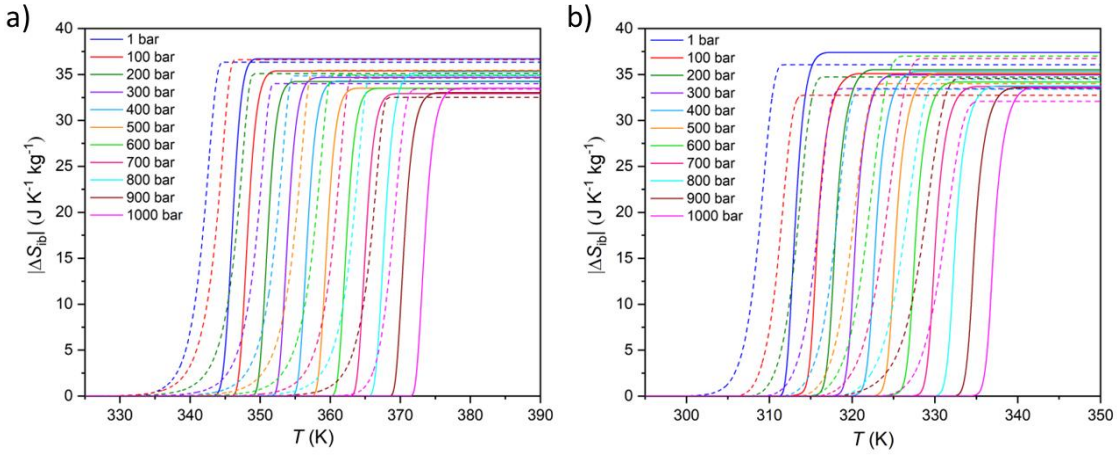

Figure 4-11. Isobaric entropy changes of the phase II ↔ phase III transition for applied pressures from 1 bar to 1000 bar for a) compound **1** and b) compound **2**. *Note:* the solid lines represent the heating curves while the dashed lines represent the cooling curves.

In order to calculate the BC performance for both compounds using the quasi-direct method, the ΔS_{ib} has been recalculated with the addition of the C_p contribution, following the Equation 1-3 (see *Chapter 1*, section 1.2.1.b).[26]

For these calculations it could be assume that the C_p of both materials at a given pressure is the same as at atmospheric pressure due to the Equation 4-2:[26]

$$\left(\frac{\partial C_p}{\partial p}\right)_T = -T\left(\frac{\partial^2 V}{\partial T^2}\right)_p \qquad \textbf{Equation 4-2}$$

where the second derivative of the volume as a function of the temperature is 0, since the system expands linearly with temperature (see Figure 4-8), so C_p is independent of the applied pressure.

Furthermore, there is an additional contribution to the entropy change (ΔS_{ad}) caused by the lattice contraction under pressure.[16,17] It can be calculated by the following Equation 4-3:

$$\Delta S_{ad}(p) = -\left[m^{-1}\left(\delta V/\delta T\right)_{p\ atm}\right](p - p\ atm) \qquad \textbf{Equation 4-3}$$

where m is the cell mass of the material, $\left(\delta V/\delta T\right)_{p\ atm}$ is the thermal expansion of unit cell volume (from Figure 4-9) and p is the pressure of measurement.

This approximation considers the thermal expansion independent from the applied pressure, which would be only valid for materials with relatively low compressibility. In the case of extremely compressible materials, this approximation can result into an overestimation of the barocaloric effects. In the same line, it should be noted that this additional entropy change would be additive to conventional barocaloric effects, but opposite to the inverse ones.

The as-calculated $|\Delta S_{ad}|$ show similar values for both compounds of around [17-19] J K^{-1} kg^{-1} at 1000 bar, which are a very significant contribution to the final barocaloric effects, as they represent around [33-36]% of the total entropy change at this pressure. It is worth noting that, due to the nature of both materials, they should not present an extremely low compressibility, leading to a possible slight overestimation in the previous $|\Delta S_{ad}|$ values.

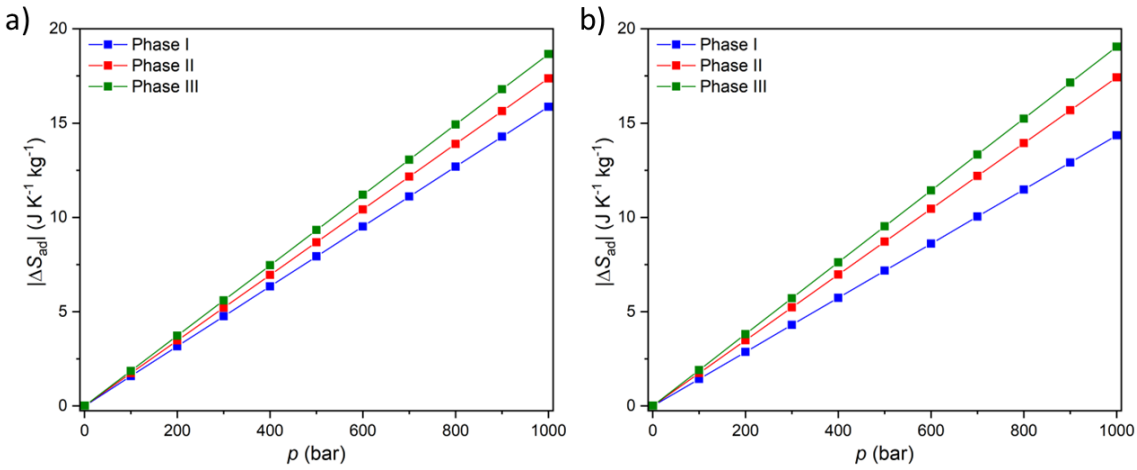

Figure 4-12. Entropy caused by volumetric thermal expansion of the II→III transition for a) compound **1** and b) compound **2**.

For this reason, each obtained $|\Delta S_{ad}|$ in Equation 4-2 of phase II for each pressure and compound is subtracted to the ΔS_{ib} curves previously calculated by Equation 1-3, as it was reported previously in the literature.[27] These new ΔS_{ib} obtained curves were represented in Figure 4-13.

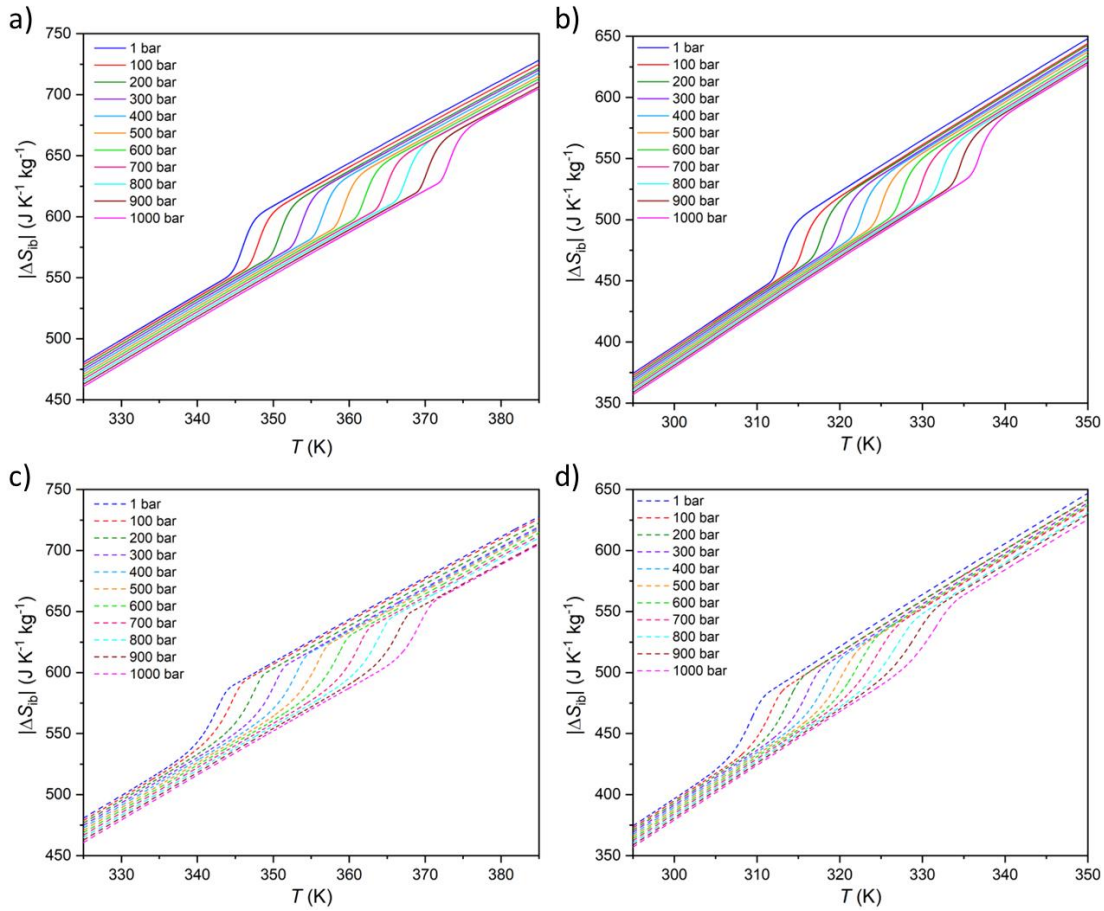

Figure 4-13. Thermally driven isobaric changes in entropy of compound **1** a) on heating and b) on cooling, and of compound **2** c) on heating and d) on cooling.

For practical applications, barocaloric cooling devices need to work in compression–decompression cycles. For this purpose, it is required to estimate the barocaloric effect of the materials in terms of pressure-driven isothermal entropy change (ΔS_{it}), which were calculated as the difference between ΔS_{ib} at two different pressures (applied pressure and atmospheric pressure) following the Equation 1-4 (see *Chapter 1*, section 1.2.1.b). If the selected ΔS_{ib} curves of the equation (two heating and two cooling curves) are subtracted as heating-heating and cooling-cooling, the resulting values are the irreversible isothermal entropy change ΔS_{it} (see Figure 4-14).

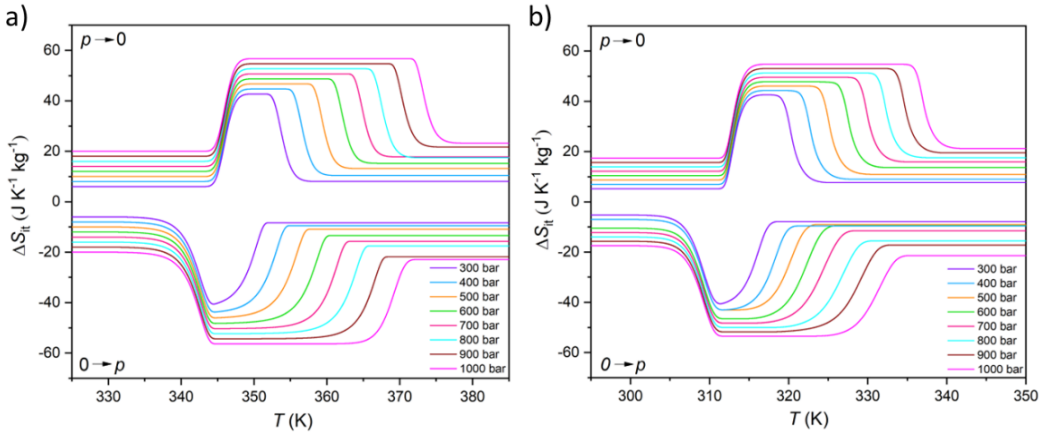

Figure 4-14. Irreversible pressure-driven isothermal entropy changes on applying ($0 \rightarrow p$) and removing ($p \rightarrow 0$) pressure of a) compound **1** and b) compound **2**.

On the other hand, the reversible isothermal entropy change (ΔS_{rev}) have been estimated using the same Equation 1-4 (see *Chapter 1*, section 1.2.1.b), but considering that ΔS_{ib} ($p \neq 1$, T) is the isobaric curve on cooling at $p \neq 1$ and ΔS_{ib} ($p = 1$, T) is the isobaric curve on heating at atmospheric pressure.

Figure 4-15 shows the ΔS_{rev} of both compounds, which display very similar maximum ΔS_{rev} values of ~56.7 J K^{-1} kg^{-1} in case of compound **1,** and ~54.8 J K^{-1} kg^{-1} in case of compound **2,** upon the application of 1000 bar. Also, it is worth noting that ΔS_{rev} values are about half of the maximum value at low pressures of 300 bar.

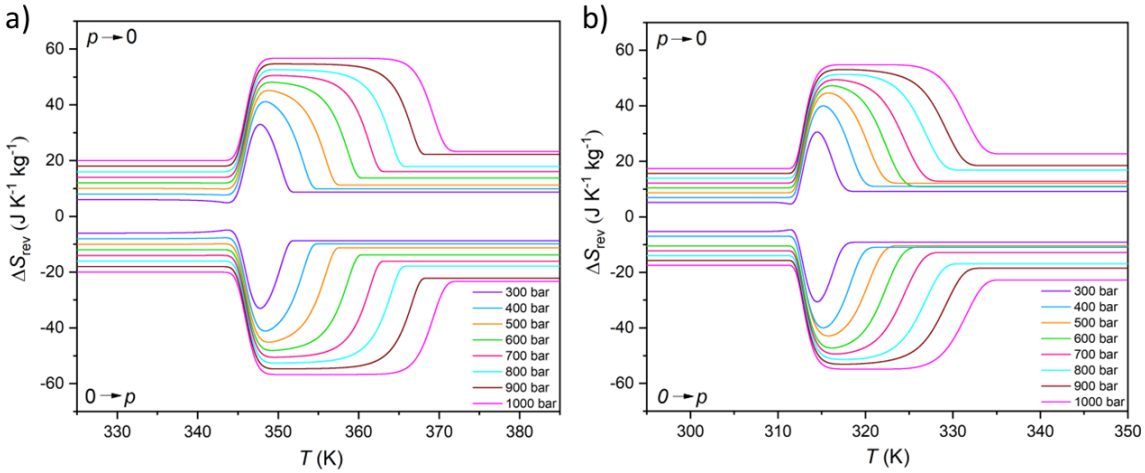

Figure 4-15. Reversible pressure-driven isothermal entropy changes on applying ($0 \rightarrow p$) and removing ($p \rightarrow 0$) pressure of a) compound **1** and b) compound **2**.

Moreover, the adiabatic temperature change (ΔT) have been obtained at different pressures are applied (see Figure 4-16). It was obtained following the Equation 4-4, which is similar a general case of Equation 1-5 of *Chapter 1*, section 1.2.1.b:

$$|\Delta T(S;p_{atm} \leftrightarrow p)| = |T(S;p) - T(S;p_{atm})| \qquad \textbf{Equation 4-4}$$

where $T(S;p)$ and $T(S;p_{atm})$ are each temperature of the cooling or heating (for $\Delta T > 0$ and $\Delta T < 0$, respectively) isobaric entropy change (see Figure 4-13) at high and room pressure, respectively.

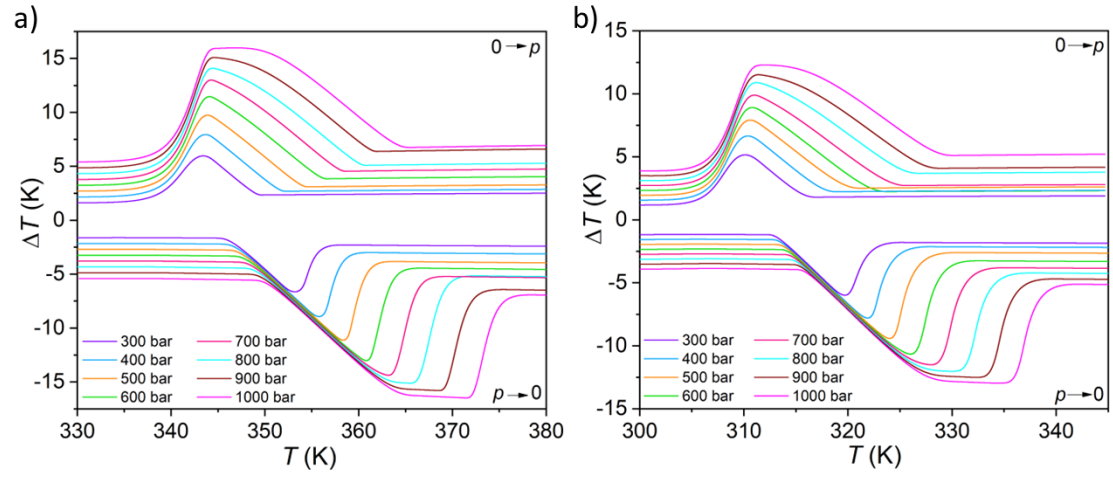

Figure 3-14. Irreversible adiabatic temperature changes on applying ($0 \rightarrow p$) and removing ($p \rightarrow 0$) pressure for a) compound **1** and b) compound **2**.

On the other hand, to take into account the thermal hysteresis of the first order transition, the cooling power have been also estimated as the reversible adiabatic temperature change, ΔT_{rev}. ΔT_{rev} was obtained following the Equation 1-5 of *Chapter 1*, section 1.2.1.b.

As shown in Figure 4-17, the compounds present ΔT_{rev} ~15.9 K (**1**) and ~12.0 K (**2**) on applying compression-decompression cycles of 1000 bar. In particular, the significant difference -in comparison with other BC parameters- in ΔT_{rev} of both materials, is probably due to the different C_p value of both compounds, see Figure 4-3. Interestingly, Table 4-2 present some selected materials which can work with similar pressures than compound **1** and compound **2** (around 1000 bar) and even with the low entropy changes showed by compound **1** and compound **2**, their adiabatic temperature changes are higher than the showed by most of plastic crystals reported with these pressures except chloride and bromide adamantane,[28] which show a slightly higher ΔT. In comparison with the rest materials which operate in this range of pressures, especially compound **1**, but also compound **2**, show relatively large values of ΔT_{rev}, higher than in most of the materials of other families (see Table 4-2).

This fact, which is a result of the cation flexibility and the low C_p of the compounds, allows a search of new materials with organometallic sandwich cations for barocaloric applications.

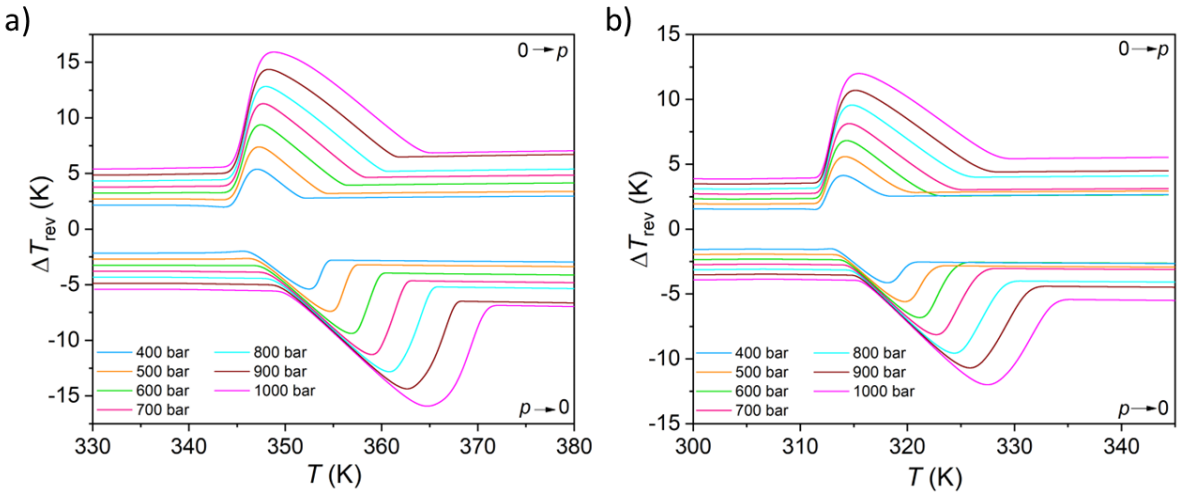

Figure 4-17. Reversible adiabatic temperature changes on applying ($0 \rightarrow p$) and removing ($p \rightarrow 0$) pressure for a) compound **1** and b) compound **2**.

Table 4-2. Barocaloric parameters of the selected barocaloric materials. *Note*: The materials were selected based on meeting both conditions: (i) exhibiting operating pressures lower than 2000 bar, and (ii) having reported reversible barocaloric effects. With these criteria in mind, certain materials such as metal alloys, neopentylglycol derivatives, and other relevant barocaloric materials were excluded from this comparison.

Material	T_t (K)	p (bar)	dT/dp (K kbar^{-1})	ΔS_{rev} (J K^{-1} kg^{-1})	ΔT_{rev} (K)	Reference
Plastic Crystals						
$[Cp_2Fe][PF_6]$	347	1000	27.6	56.7	15.9	This chapter
$[Cp_2Co][PF_6]$	312	1000	24	54.8	12.0	This chapter
C_{60}	257	1000	17	25	9.7	[29]
$C_{10}H_{15}Cl$	254	1000	27.4	153	16.1	[28]
$C_{10}H_{15}Br$	316	1000	35.5	134	19.6	[28]
1-Adamantanol	361	1600	17.9	175	11	[30]
2-Adamantanol	326	1850	21	100	8	[30]
2-Methyl-2-adamantanol	375	800	24.1	300	7	[30]
o-carborane	277	600	30	79	14*	[31]
m-carborane	286	600	34	71	-	[31]
p-carborane	308	600	31	97	-	[31]
Quinuclidinium perrhenate	344	1000	13.8	26	8	[32]
$[Me_4N][FeCl_4]$	384	900	40.0	81	21	[32]
Ammonium Salts						
$(NH_4)_2SnF_6$	110	1000	-15.7	-61	-11*	[33]
NH_4HSO_4	160	1000	-12.3	-60	-10	[34]
NH_4I	268	800	81	71	34*	[35]
FAI	345	1000	9.7	49.9	24*	[36]
$[DBA][BF_4]$	269	1000	28.9	254	17	Section 4.3
Hybrid Organic-Inorganic Materials						
$[Pr_4N][Mn(dca)_3]$	330	70	23.1	30.5	4.1*	[25]
[Pr4N][Cd(dca)$_3$]	385	70	38.2	11.5	-	[37]
$[C_{10}H_{21}NH_3]_2[MnCl_4]$	312	1000	25	241	12	[26]
$[C_9H_{19}NH_3]_2[MnCl_4]$	294	1000	17.2	212	10	[38]
$[C_9H_{19}NH_3]_2[CuBr_4]$	305	150	26.7	75	2.3	[16]
Polymers						
Acetoxy Silicone Rubber	250	1730	27	182	21	[39]
Vulcanized Natural Rubber	303	1730	6.07	17	10.5	[40]
Spin-Crossover Materials						
$[Fe(hyptrz)_3]A_2{\cdot}H_2O$	273	900	33.2	56	10	[41]
$Fe[HB(tz)_3]_2$	332	120	21.5	89	1.7	[42]
$[FeL_2][BF_4]_2$	257	430	15	68	4	[43]
$Fe_3(bntrz)_6(tcnset)_6$	318	1200	25.6	100	22	[44]
$[Fe(pzt)_6](PF_6)_2$	74	1000	29	46	27	[45]

Note: * = Adiabatic temperature change was calculated by indirect method ($\Delta T_{rev} = \Delta S * T_t / C_p$).

Finally, the operating temperature range or span temperature (T_{span}) of these compounds have been represented as a function of applied pressure and showing the different reversible isothermal entropy changes (Figure 4-18a and 4-18b) and the reversible adiabatic temperature changes (Figure 4-18c and 4-18d) that can be achieved. The obtained values can be compared with those reported by P. Lloveras *et al*. of the fullerene (C_{60})[29] due to their similar barocaloric parameters.

In this context, in the case of using fullerene under a pressure of 1000 bar the operating temperature range would be as large as 11 K, showing values of ΔS_{it} = 25 J K^{-1} kg^{-1} and ΔT_{rev} = 5 K. In the case of compound **1** and compound **2** under 1000 bar, they present a larger operating temperature range of 20 K and 17 K, respectively, with ΔS_{it} = 35 J K^{-1} kg^{-1} and ΔT_{rev} = 6 K.

In turn, the family of cyclopentadienyl organometallic compounds shows very promising barocaloric parameters, such as large barocaloric coefficient, adiabatic temperature change and operating temperature range, which encourage further exploration of related materials for barocaloric applications.

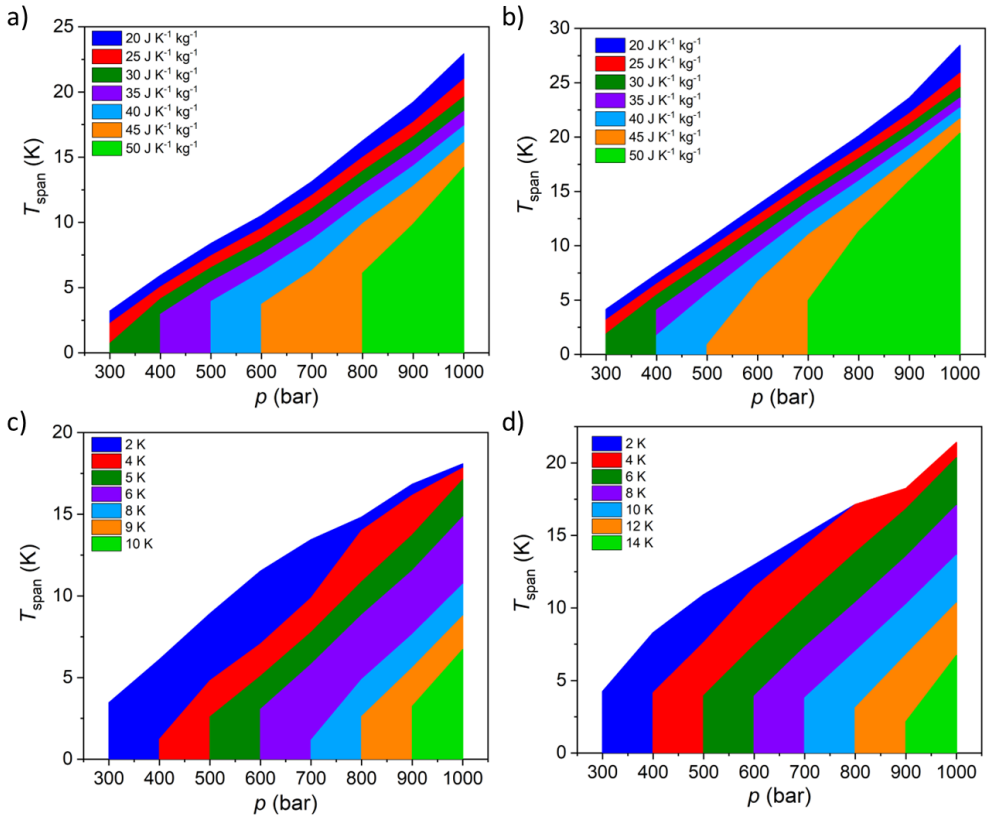

Figure 4-18. Temperature span as a function of applied pressure for different intervals of reversible isothermal entropy changes, for a) compound **1** and b) compound **2**. And temperature span as a function of the applied pressure for different intervals of reversible adiabatic temperature changes reversible adiabatic temperature changes for c) compound **1** and d) compound **2**.

4.2.4. Conclusions

This chapter report new properties and applications for relatively "old" and well-established materials, the metallocenium salts $[Cp_2M][PF_6]$ (M = Fe^{3+}, Co^{3+}). These salts present two solid-solid phase transitions, one of which occurs above room temperature, and it is sufficiently energetic to be of interest for barocaloric applications. These high-temperature transitions occur between a well-ordered crystalline phase and a plastic phase, where the cations and/or anions largely increase their dynamical disorder. The studied barocaloric properties show a moderate value of ΔS_{rev} ~55 J K^{-1} kg^{-1} at 1000 bar, overpassing the value of hybrid perovskites and the fullerene plastic crystal. Even more interestingly, these organometallic compounds exhibit very large barocaloric coefficients of dT_t/dp ~30 K $kbar^{-1}$, wide operating temperature ranges of $T_{span} \geq 15$ K at 1000 bar, and surprisingly large adiabatic temperature changes ΔT_{rev} of ~15 K, which can be attributed to the relatively low heat capacity found in both compounds.

From the structural point of view, these barocaloric properties are related to large volume changes from a wide intramolecular structural flexibility of the sandwich formed by the cyclopentadiene cycles of the metallocenium cations. Here, the π- C-M bonds have quite large flexibility in terms of angles and distances.[8,46,47] On the other hand, the low C_p is probably related to the sandwich system as all metallocenes derivatives and metalloceniums are known by showing low C_p values.[18–22] Furthermore, this chapter anticipates that giant barocaloric effects could be achieved in similar metallocenium salts by modifying the metal cations and/or the anions. With all that in mind, these encouraging results will promote the search for other innovative barocaloric materials within the family of metallocenium compounds.

4.2.5. References

[1] L. B. Hunt, *Platin. Met. Rev.* **1984**, *28*, 76.

[2] W. A. Herrmann, *Angew. Chemie - Int. Ed.* **2002**, *41*, 1290.

[3] H. S. Nalwa, *Appl. Organomet. Chem.* **1991**, *5*, 349.

[4] C. S. Allardyce, A. Dorcier, C. Scolaro, P. J. Dyson, *Appl. Organomet. Chem.* **2005**, *19*, 1.

[5] R. A. Layfield, *Organometallics* **2014**, *33*, 1084.

[6] D. Braga, G. Cojazzi, D. Paolucci, F. Grepioni, *Chem. Commun.* **2001**, 803.

[7] D. Braga, L. Scaccianoce, F. Grepioni, S. M. Draper, *Organometallics* **1996**, *15*, 4675.

[8] D. Braga, F. Grepioni, *Chem. Commun.* **1996**, *878*(11), 1783-1792.

[9] H. Kimata, T. Sakurai, H. Ohta, T. Mochida, *ChemistrySelect* **2019**, *4*, 1410.

[10] F. Grepioni, G. Cojazzi, S. M. Draper, N. Scully, D. Braga, *Organometallics* **1998**, *17*, 296.

[11] R. J. Webb, D. N. Hendrickson, M. D. Lowery, Y. Shiomi, M. Sorai, R. J. Wittebort, *Inorg. Chem.* **1992**, *31*, 5211.

[12] N. G. Connelly, W. E. Geiger, *Chem. Rev.* **1996**, *96*, 877.

[13] G. Ferrer, C. Barreneche, A. Solé, I. Martorell, L. F. Cabeza, *J. Energy Storage* **2017**, *11*, 1.

[14] American Society for Testing and Materials: E1269-11, *Standard Test Method for Determining Specific Heat Capacity by Differential Scanning Calorimetry* **2011**.

[15] B. H. Toby, R. B. Von Dreele, *J. Appl. Crystallogr.* **2013**, *46*, 544.

[16] J. Seo, R. D. McGillicuddy, A. H. Slavney, S. Zhang, R. Ukani, A. A. Yakovenko, S. L. Zheng, J. A. Mason, *Nat. Commun.* **2022**, *13*, 1.

[17] P. Lloveras, E. Stern-Taulats, M. Barrio, J. L. Tamarit, S. Crossley, W. Li, V. Pomjakushin, A. Planes, L. Mañosa, N. D. Mathur, X. Moya, *Nat. Commun*, **2015**, *6*, 8801.

[18] O. V. Krol, A. I. Druzhinina, R. M. Varushchenko, O. V. Dorofeeva, M. D. Reshetova, N. E. Borisova, *J. Chem. Thermodyn.* **2008**, *40*, 549.

[19] M. Sorai, Y. Shiomi, *Thermochim. Acta* **1986**, *109*, 29.

[20] R. B. Woodward, M. Rosenblum, in *Ring Rotational Barrier Ferrocene*, **1958**, 5543.

[21] L. G. Domracheva, N. V. Karyakin, M. S. Sheiman, G. V. Kamelova, V. N. Larina, O. N. Suvorova, G. A. Domrachev, *Russ. Chem. Bull.* **1999**, *48*, 1647.

[22] K. Elihn, K. Larsson, *Thin Solid Films* **2004**, *458*, 325.

[23] M. Bochmann, *Organometallics 1 - Complexes with Transitions Metal-Carbon σ-Bonds*, Oxford University Press, **1994**.

[24] X. Moya, S. Kar-Narayan, N. D. Mathur, *Nat. Mater.* **2014**, *13*, 439.

[25] J. M. Bermúdez-García, M. Sánchez-Andújar, S. Castro-García, J. López-Beceiro, R. Artiaga, M. A. Señarís-Rodríguez, *Nat. Commun.* **2017**, *8*, 15715.

[26] J. Li, M. Barrio, D. J. Dunstan, R. Dixey, X. Lou, J. L. Tamarit, A. E. Phillips, P. Lloveras, *Adv. Funct. Mater.* **2021**, *31*, 1.

[27] P. Lloveras, A. Aznar, M. Barrio, P. Negrier, C. Popescu, A. Planes, L. Mañosa, E. Stern-Taulats, A. Avramenko, N. D. Mathur, X. Moya, J. L. Tamarit, *Nat. Commun.* **2019**, *10*, 1.

[28] A. Aznar, P. Negrier, A. Planes, L. Mañosa, E. Stern-Taulats, X. Moya, M. Barrio, J. L. Tamarit, P. Lloveras, *Appl. Mater. Today* **2021**, *23*, 101023.

[29] J. Li, D. Dunstan, X. Lou, A. Planes, L. Mañosa, M. Barrio, J. L. Tamarit, P. Lloveras, *J. Mater. Chem. A* **2020**, *8*, 20354.

[30] A. Salvatori, P. Negrier, A. Aznar, M. Barrio, J. L. Tamarit, P. Lloveras, *APL Mat.* **2022**, *10*, 111117.

[31] K. Zhang, R. Song, J. Qi, Z. Zhang, Z. Zhang, C. Yu, K. Li, Z. Zhang, B. Li, *Adv. Funct. Mater.* **2022**, *32*, 2112622.

[32] A. Salvatori, D. Aguilà, G. Aromí, L. Mañosa, A. Planes, P. Lloveras, L. C. Pardo, M. Appel, G. F. Nataf, F. Giovannelli, M. Barrio, J. L. Tamarit, M. Romanini, *J. Mater. Chem. A* **2023**, 12140.

[33] I. N. Flerov, A. V. Kartashev, M. V. Gorev, E. V. Bogdanov, S. V. Mel'Nikova, M. S. Molokeev, E. I. Pogoreltsev, N. M. Laptash, *J. Fluor. Chem.* **2016**, *183*, 1.

[34] M. V. Gorev, E. A. Mikhaleva, I. N. Flerov, E. V. Bogdanov, *J. Alloys Compd.* **2019**, *806*, 1047.

[35] Q. Ren, J. Qi, D. Yu, Z. Zhang, R. Song, W. Song, B. Yuan, T. Wang, W. Ren, Z. Zhang, X. Tong, B. Li, *Nat. Commun.* **2022**, *13*, 1.

[36] C. Yu, J. Huang, J. Qi, P. Liu, D. Li, T. Yang, Z. Zhang, B. Li, *APL Mater.* **2022**, *10*, 11109.

[37] J. M. Bermúdez-García, S. Yáñez-Vilar, A. García-Fernández, M. Sánchez-Andújar, S. Castro-García, J. López-Beceiro, R. Artiaga, M. Dilshad, X. Moya, M. A. Señarís-Rodríguez, *J. Mater. Chem. C* **2018**, *6*, 9867.

[38] Y. Gao, H. Liu, F. Hu, H. Song, H. Zhang, J. Hao, X. Liu, Z. Yu, F. Shen, Y. Wang, H. Zhou, B. Wang, Z. Tian, Y. Lin, C. Zhang, Z. Yin, J. Wang, Y. Chen, Y. Li, Y. Song, Y. Shi, T. Zhao, J. Sun, Q. Huang, B. Shen, *NPG Asia Mater.* **2022**, *14*, 34.

[39] W. Imamura, É. O. Usuda, L. S. Paixão, N. M. Bom, A. M. Gomes, A. M. G. Carvalho, *Chinese J. Polym. Sci. (English Ed.)* **2020**, *38*, 999.

[40] E. O. Usuda, N. M. Bom, A. M. G. Carvalho, *Eur. Polym. J.* **2017**, *92*, 287.

[41] P. J. Von Ranke, B. P. Alho, R. M. Ribas, E. P. Nobrega, A. Caldas, V. S. R. De Sousa, M. V. Colaço, L. F. Marques, D. L. Rocco, P. O. Ribeiro, *Phys. Rev. B* **2018**, *98*, 2.

[42] J. Seo, J. D. Braun, V. M. Dev, J. A. Mason, *J. Am. Chem. Soc.* **2022**, *144*, 6493.

[43] S. P. Vallone, A. N. Tantillo, A. M. dos Santos, J. J. Molaison, R. Kulmaczewski, A. Chapoy, P. Ahmadi, M. A. Halcrow, K. G. Sandeman, *Adv. Mater.* **2019**, *31*, 1.

[44] M. Romanini, Y. Wang, G. Kübra, G. Ornelas, P. Lloveras, Y. Zhang, W. Zheng, M. Barrio, A. Aznar, A. Gràcia-Condal, B. Emre, O. Atakol, C. Popescu, H. Zhang, Y. Long, L. Balicas, J. L. Tamarit, A. Planes, M. Shatruk, L. Mañosa, *Adv. Mater.* **2021**, *33*, 2008076.

[45] P. J. von Ranke, B. P. Alho, P. O. Ribeiro, *J. Alloys Compd.* **2018**, *749*, 556.

[46] N. Sharma, J. K. Ajay, K. Venkatasubbaiah, U. Lourderaj, *Phys. Chem. Chem. Phys.* **2015**, *17*, 22204.

[47] M. Bühl, S. Grigoleit, *Organometallics* **2005**, *24*, 1516.

4.3. Di-n-butylammonium tetrafluoroborate hybrid organic-inorganic material with thermal properties for multipurpose barocaloric refrigeration and 'cold-storage'

Part of the work showed and discussed in this chapter has been published in the following article:

J. García-Ben, J.M. Bermúdez-García, R.J.C. Dixey, I. Delgado-Ferreiro, A.L. Llamas-Saiz, J. López Beceiro, R. Artiaga, A. García-Fernández, U.B. Cappel, B. Alonso, S. Castro-García, A.E. Phillips, M. Sánchez-Andújar, M.A, Señarís-Rodríguez, *J. Mater. Chem. A*, **2023**, Accepted Manuscript.

4.3.1. Introduction

Energy consumption in the refrigeration sector is expected to triple by the year 2050 due, among other things, to global warming. This would mean that, for the first time in history, more energy will be employed for cooling than for heating.

Food preservation is a particularly important aspect for maintaining the sustainable development and growth, since currently 46% of the total food production in the world requires refrigeration. Nevertheless, only half of it is properly refrigerated, which leads to around 13% of food losses every year.[1] Most perishable food must be preferably stored at chilled temperatures of between 272 and 287 K (-1 ºC and 14 ºC).[2,3]

To reach and/or maintain those temperatures two main technologies are normally used, namely, vapour-compression refrigeration and passive cold-storage technologies.

Some recent findings suggest that materials useful for passive thermal energy storage (including 'cold-storage') will exhibit some important limitations for barocaloric refrigeration. For example, 'cold-storage' materials require relatively large thermal hysteresis for separating the temperatures of heat storage and heat release. Meanwhile, barocaloric materials ideally present ultralow thermal hysteresis (of only a few degrees or even smaller), in order to minimize the pressure required for driving the transition in a reversible manner.[4,5] For instance, the plastic crystal neopentylglycol exhibits a large thermal hysteresis of around 15 ºC, which makes it suitable for thermal energy storage applications.[6,7] However, this large hysteresis makes necessary to apply a pressure of around 2500 bar in order to get reversible barocaloric effects in this neopentylglycol material.[8] On the contrary, the hybrid perovskite [TPrA][Mn(dca)$_3$] exhibits an ultralow thermal hysteresis of 0.9 ºC, which give rise to large and reversible barocaloric effects under the application of only 70 bar.[9] Nevertheless, this low thermal hysteresis prevent its use for any type of thermal energy storage.

This work shows that it is possible to find thermomaterials that combine moderate thermal hysteresis with a large pressure-responsiveness, which make them good candidates for multipurpose heating, cooling and thermal energy storage (or cold-storage in the specific case of this study). The study focused on the salt di-*n*-butylammonium tetrafluoroborate ([DBA][BF$_4$]). This compound, initially prepared by K. Syed Mohamed in 1988,[10] shows two solid-solid phase transitions in the region of interest for cold-storage and food preservation. These transitions, which were first studied by G. Zabinska in 1988, take place at T_{t1} ~268 K and at T_{t2} ~284 K, with an associated enthalpy change of ΔH_1 ~11.7 kJ mol^{-1} and ΔH_2 ~2.7 kJ mol^{-1}, respectively.[11] No further information about other thermal parameters (such as the thermal hysteresis or specific heat, for instance) or any structural information about the phase transitions has been reported.

For that reason, the thermal properties of this material were investigated in order to evaluate its interest for passive 'cold-storage', as well as for barocaloric heating and cooling, using differential

scanning calorimetry (DSC) at different pressures. Furthermore, a detailed structural characterization across the phase transitions was performed using single crystal X-ray diffraction (SC-XRD), variable-temperature synchrotron powder X-ray diffraction (VT-SPXRD) and solid-state nuclear magnetic resonance spectroscopy (SS-NMR), among others. Furthermore, this study will focus on the relationship between the structure and thermal properties, which will help the future design of multipurpose thermomaterials with enhanced properties.

4.3.2. Experimental

4.3.2.1. Synthesis

Commercially available reagent grades di-n-butylamine, (≥99% Sigma-Aldrich) and tetrafluoroboric acid solution, HBF_4, (48% wt.% in H_2O Sigma-Aldrich) were used as starting materials without further purification. The synthesis procedure was similar to that previously reported[11] with a slight modification on the recrystallization process. In a typical experiment, a solution of the amine (4.6 mmol) in water (10 ml) was prepared. Then, HBF_4 (4.6 mmol) was slowly added to the previous solution at room temperature and cooled using an ice-water bath. The solvent was removed using a rotary evaporator. The obtained polycrystalline and colorless powder was stored inside a vacuum desiccator. The obtained material was highly hygroscopic, remaining wet after the vacuum treatment. For that reason, the obtained powders were dispersed and recrystallized in *p*-xylene and, subsequently filtered and dried (Yield: 82%). This treatment appears to provide this material with a long-term protection (around few months) against water adsorption.

4.3.2.2. Elemental analysis (EA)

Elemental analysis (EA) was performed in an Elemental Analyzer ThermoQuest Flash EA 1112 using around 2 mg of sample (calc. %C: 44.27, %H: 9.29, %N: 6.45, found %C: 44.13, %H: 9.59, %N: 6.22).

4.3.2.3. Nuclear Magnetic Resonance (NMR)

Liquid-state ^{1}H-NMR spectra were recorded for samples dissolved in $CDCl_3$ (98.5% ACROS Organics) using a Bruker Advance 300 MHz equipped with a dual cryoprobe in the University of A Coruña. Chemical shifts were expressed as parts per million (ppm, δ) downfield of tetramethylsilane (TMS) (see Figure A4-1 of *Annex II*). The description of signals included: s = singlet, t = triplet and m = multiplet. All coupling constants were absolute values and were expressed in Hertz (Hz). δ 6.78 (s, 2H), 3.04 (t, J = 7.8 Hz, 4H), 1.72 (m, J = 7.5 Hz, 4H), 1.39 (m, J = 7.5 Hz, 4H), 0.94 (t, J = 7.2 Hz, 6H) ppm.

Solid-state ^{1}H single-pulse Magic Angle Spinning (MAS) spectra and ^{13}C Cross-Polarization Magic Angle Spinning (CPMAS) NMR were performed in a Bruker NEO 750 spectrometer (B_0 = 17.6 T) using 1.3 mm zirconia rotors spun at ν_{MAS} = 50 and 15 kHz respectively. Both experiments were carried out at 318 K in the University of Santiago de Compostela.

Variable temperature solid-state NMR MAS experiments were performed in a Varian-Agilent 600 WB spectrometer (B_0 = 14.1 T) using 3.2 mm zirconia rotors spun at different frequencies (ν_{MAS} = 5.5, 10 or 15 kHz) (located in the CNRS campus of Montpellier). ^{1}H single pulse spectra were recorded using π/2 flip angle pulses of 2.5 μs and recycling delays of 5 s. ^{1}H spin-echo spectra were recorded using MAS synchronized interpulse delays, and π/2 and π flip angle pulses of 2.5 and 5.0 μs respectively. Chemical shifts were referenced using adamantane (δ_{iso} = 1.8 ppm) as external reference. ^{11}B single pulse MAS spectra were recorded using π/10 flip angle pulses of 1 μs and recycling delays of 0.5 s. Chemical shifts were referenced using dry $NaBH_4$ (δ_{iso} = -42.1

ppm) as external reference. The temperatures were adjusted using chilled compressed air. The differences between *T* setpoints and sample temperatures are below 5 K. $Pb(NO_3)_2$ was used for the calibration of the sample temperatures following a previously published procedure.[12]

4.3.2.4. Thermal analysis

Thermogravimetric analysis (TGA) was carried out using TGA-DTA thermal analysis SDT2960 equipment of the Research Support Service of the University of A Coruña. The experiments were assembled at 10 K min^{-1} from 300 K to 800 K in a corundum crucible, under a flow of dry nitrogen, using around 25 mg of sample.

Variable-temperature differential scanning calorimetry (VT-DSC) in the lower-temperature range (115-150 K) at ambient pressure was performed in a Netzsch DSC 214 Polyma at KTH Royal - Institute of Technology. Meanwhile, VT-DSC in the higher-temperature range (250-310 K) at ambient pressure was carried out in using a TA-Instruments Q2000 coupled with a RCS 90 cooler in the Department of Naval and Industrial Engineering of the University of A Coruña. In both cases, around 10 mg of sample were tested under 10 K min^{-1} heating/cooling rate and under nitrogen atmosphere.

Heat capacity at ambient pressure, C_p, was calculated by the classic ASTM E1269 standard test method, by which the measured heat flow of the material is compared to sapphire reference according to Equation 4-1 of the previous subchapter.[13,14]

4.3.2.5. Variable temperature synchrotron powder X-ray diffraction (VT-SPXRD)

Patterns were recorded at the I11 beamline of the Diamond Light Source Synchrotron (Harwell, UK) using a wavelength of λ = 0.825955(3) Å. The wavelength was determined by Rietveld refinement of a NIST640D silicon standard at room temperature. The sample was enclosed in a glass capillary (inner diameter ϕ = 0.5 mm) and kept in continuous rotation during data collection to improve powder averaging. Patterns were collected using Mythen position sensitive detector while heating the sample from 170 K to 335 K. The working temperature was set using a FMB Oxford hot-air blower. Rietveld and Le Bail refinements were carried out using the program GSAS-II.[15]

4.3.2.6. Single crystal X-ray diffraction (SCXRD)

Single-crystal X-ray diffraction (SCXRD) experiments were carried out at two temperatures well above and below the observed DSC transitions. Two single-crystal data sets of the same crystal were collected at 100 K and 240 K in a Bruker D8 VENTURE Kappa X-ray diffractometer equipped with a PHOTON III detector and using monochromatic CuKα radiation (λ = 1.54178 Å) at the University of Santiago de Compostela. Several crystals among the best-looking ones in the crystallization batch were tested and one was selected for data collection. It was mounted on a MiTeGen MicroMount™ using Paratone® N (Hampton Research). The crystal temperature was changed and stabilized with a cold stream of nitrogen gas from an Oxford Cryosystem 800plus cooler. The data integration and reduction were performed using the APEX3 v2019.1-0 (Bruker AXS, 2019) software suite. The intensities collected were corrected for Lorentz and polarization effects and for absorption by semi-empirical methods based on symmetry-equivalent data using TWINABS 2012/1 of the software suite. The structures were solved by the novel dual-space algorithm implemented in SHELXT2018/2[16] program and were refined by least squares method on SHELXL2018/3.[17] As the presence of twinning in all data collected was clear from visual inspection of diffraction images, all datasets were indexed using CELL_NOW 2008/4. The four primary twin domains at both temperatures could be indexed, and the corresponding orientation matrices obtained, although the diffraction patterns displayed the presence of several additional domains with minor contribution. The integrations of the reflections were performed with SAINT

8.40B considering simultaneously the predictions given by the four orientation matrices corresponding to the twin domains found. The software used to treat the twinned data is included in the APEX3 suite.

The electron density maxima corresponding with the hydrogen atoms of the NH_2^+ group of the amine cation were clearly visible in the (Fo-Fc) Fourier map. The rest of the hydrogen atoms of the DBA cation were introduced at idealized positions. All hydrogen atoms were restrained during refinement using the riding model implemented in SHELXL2018/3.

Detailed experimental crystallographic data for phases IV (T = 100 K) and III (T = 240 K) of the [DBA][BF_4] compound are included in *Annex II*, Table A4-1 of *Annex II* and CCDC-2213758 (phase IV) and CCDC-2213757 (phase III) contain the supplementary crystallographic data for this study.

4.3.3. Caloric properties

4.3.3.1. Cold storage properties

To analyse the cold-storage properties of the material upon changes in the ambient temperature, VT-DSC at ambient pressure was performed. The results reveal that [DBA][BF_4] undergoes three reversible first-order phase transitions in the temperature range studied (115 - 310 K), see Figure 4-19 and Table 4-3. The first two transitions occur at T_{t1} ~ 282 K and T_{t2} ~ 269 K on heating, in agreement with previous reported.[11] These transitions exhibit a thermal hysteresis of 3 K and 6 K in the case of T_{t1} and T_{t2}, respectively. Furthermore, it was found a new phase transition at T_{t3} ~134 K with a thermal hysteresis of 5 K, which has not been previously reported.

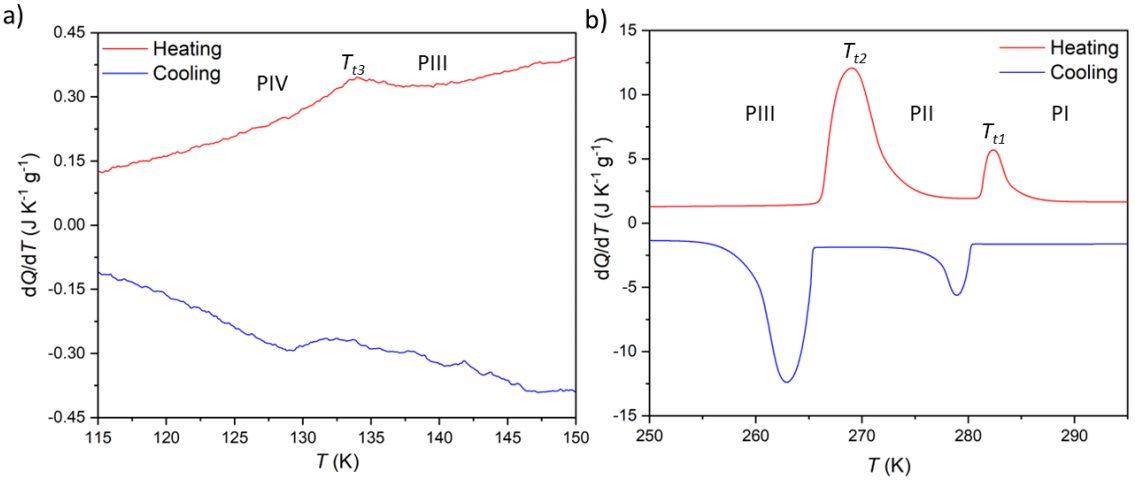

Figure 4-19. VT-DSC curves for the [DBA][BF_4] compound in the a) lower- and b) higher-temperature range.

These transitions occur between different phases (PI ↔ PII, PII ↔ PIII, and PIII ↔ PIV) as it will be further discussed in the following sections. Interestingly, it is observed that the two transitions occurring at higher temperature, exhibit very large latent heats of ΔH_1 ~13 kJ kg^{-1} and ΔH_2 ~58 kJ kg^{-1}. Even more interestingly, these two transitions are very close in temperature and appear in the range of 250-310 K, covering the temperature range adequate for food preservation and 'cold-storage'. Furthermore, even if the thermal hysteresis is still moderate for 'cold-storage', both transitions occur very close in temperature and can be combined for thermal energy storage applications. In that way, the heat absorbed by the combination of both transitions will be maximized for a charge temperature of ~290 K, meanwhile the stored heat would not be fully released until the temperature decreases back to ~250 K. This combined use of both close

transitions increases the separation between the full charge and discharge temperatures beyond the individual thermal hysteresis of both transitions.

Table 4-3. Thermodynamic parameters of observed phase transitions by DSC data for [DBA][BF_4] compound.

Transition	$T_{t(h)}$ (K)	$T_{t(c)}$ (K)	$\Delta H_{(h)}$ (kJ kg^{-1})	$\Delta H_{(c)}$ (kJ kg^{-1})	$\Delta S_{(h)}$ (J K^{-1} kg^{-1})	$\Delta S_{(c)}$ (J K^{-1} kg^{-1})
PI ↔ *PII*	282	279	12.7	13.7	45.0	49.1
PII ↔ *PIII*	269	263	58.3	56.6	216.7	215.2
PIII ↔ *PIV*	134	129	0.37	0.43	2.65	3.24

Note: (h) = heating, (c) = cooling.

With this in mind, the thermal storage capacity, E, of the material is calculated considering the latent heat of both combined transitions and the heat capacity heat throughout temperature range from 250 to 295 K, following Equation 1-6 of *Chapter 1*, section 1.2.2. using the C_p of the material between previous temperature range (see shaded area in Figure 4-20).[18] It is worth mentioning that, owing to the width and proximity of both transitions, using the C_p values only before and after the transitions would introduce a significant error. Therefore, in this case, the C_p value within the temperature range where both transitions occur will be estimated and used to calculate E.

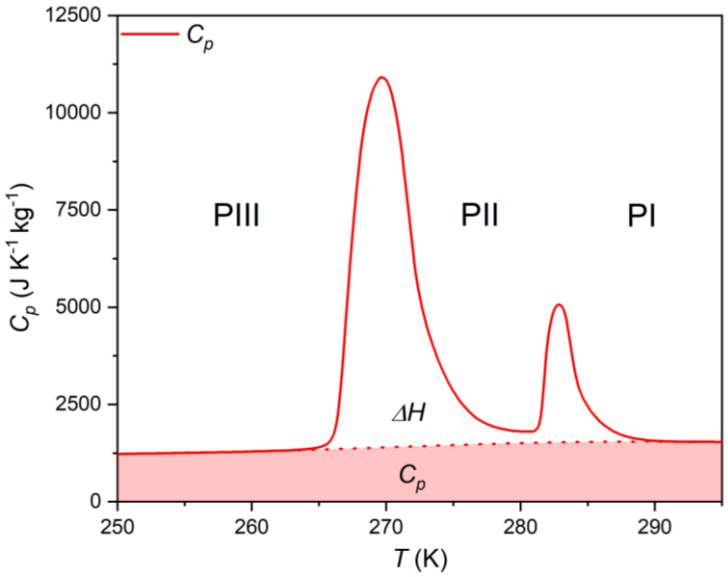

Figure 4-20. C_p measurements of the of [DBA][BF_4] material from 250 to 295 K on heating. *Note*: The dotted line shows the C_p estimation during the phase transitions, while the shaded area represents the TES capacity corresponding to C_p.

Accordingly, the sensible heat (the C_p contribution for calculating E) for the temperature range of 250-295 K (ΔH_{Cp}= 63.6 kJ kg^{-1}) combined with the latent heat (ΔH = 71.0 kJ kg^{-1}) gives a storage capacity as large as E = 134.6 kJ kg^{-1}. This sensible heat is very sensitive to the temperature range selected, even with a 45 K range, the sensible heat is still lower than the latent heat of the sample, showing the enormous input of this last one to E. In addition, the enthalpy change is close to many cold-storage materials reported in the literature (such as polyglycol E400 with ΔH = 99.6 kJ kg^{-1}, Isopropyl palmitate with ΔH = 95 kJ kg^{-1} or $K_2HPO_4 \cdot 6H_2O$ with ΔH = 109 kJ kg^{-1}) or even

commercially available (such as the compound TH31 with ΔH = 131 kJ kg^{-1}, ClimSel C7 with ΔH = 130 kJ kg^{-1} or MPCM(-30) with ΔH = 140 kJ kg^{-1}).[6]

According to TGA results, the [DBA][BF_4] compound remains thermally stable up to ~450 K, similar to other commercial PCMs, see Figure 4-21.

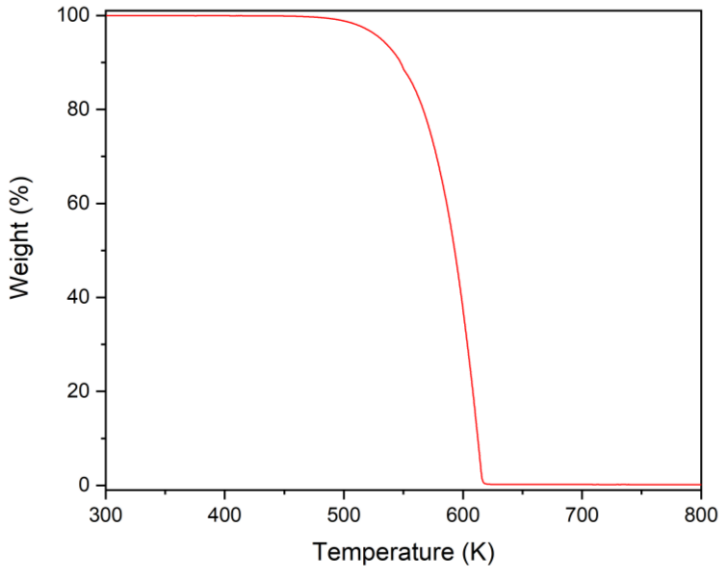

Figure 4-21. Thermogravimetric analysis of [DBA][BF_4] under N_2 atmosphere.

4.3.3.2. Barocaloric properties

To study the barocaloric properties of [DBA][BF_4], VP-DSC was used at various applied pressures from 1 to 1000 bar in the temperature range of 250-310 K, focusing on those transitions with larger thermal changes, T_{t1} and T_{t2} as previously discussed. Both transitions (between the PIII ↔ PII and PII ↔ PI, as it will be detailed in the following sections) exhibit conventional barocaloric effects, with an increase of the transition temperature upon pressurization, see Figure 4-22a.

Remarkably, this material has a particular behaviour predicted by M. V. Gorev *et al.*[19] where a triple-point between phases PI, PII and PIII can be observed in the temperature-pressure phase diagram (see Figure 4-22b). This is the first material reported with the merging transitions phenomenon where both transitions (PIII ↔ PII and PII ↔ PI) show direct barocaloric effects. In that way, both transitions are fully merged at 600 bar and a single transition is observed for $p \geq$ 600 bar, which involves a PIII ↔ PI phase transition.

The barocaloric tunability or the barocaloric coefficient (dT_t/dp) of each phase transition is calculated from the slope of the linear regions at Figure 4-22b. Due to the merging effect, three different barocaloric coefficients can be separated in heating and cooling. Below 600 bar, there are two barocaloric coefficients of dT_{t1}/dp ~5.5 K kbar^{-1} and dT_{t2}/dp ~29 K kbar^{-1} for the PII ↔ PI and PIII ↔ PII phase transition, respectively. This noticeable difference between the barocaloric coefficients is responsible for the phase transitions merging into a new single-phase transition for $p \geq$ 600 bar. This new PIII ↔ PI phase transition exhibits a new barocaloric coefficient of dT_{tm}/dp ~22.6 K kbar^{-1}.

The barocaloric coefficients of this material are comparable to the most pressure-responsive barocaloric materials to date,[20] such as [TPrA]Cd[dca]$_3$ (dT_t/dp ~38.2 K kbar^{-1})[21] and NH_4I[22] (dT_t/dp ~79 K kbar^{-1}).

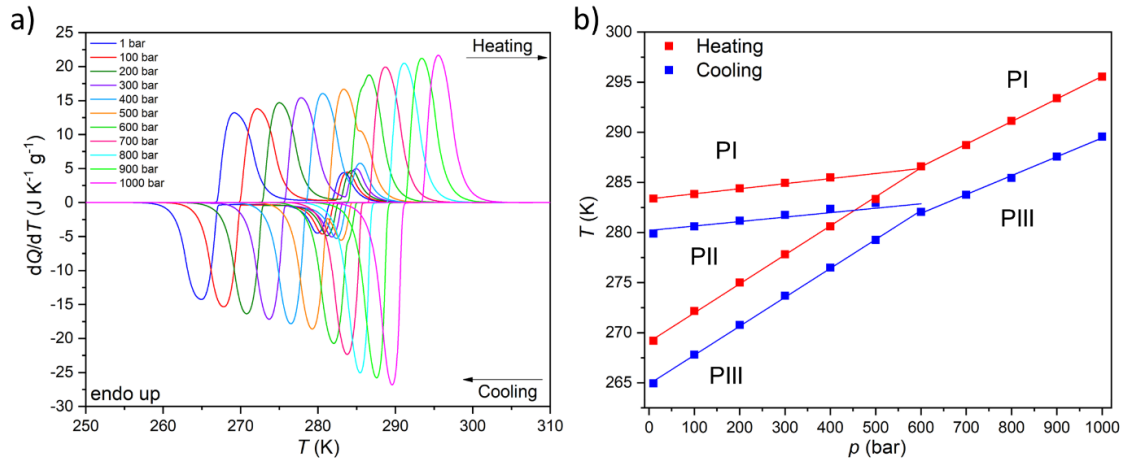

Figure 4-22. a) VP-DSC curves of [DBA][BF_4] in isobaric conditions from 1 bar to 1000 bar. b) Temperature of the maximum of each peak of the VP-DSC curves on cooling and heating as a function of the applied pressure.

The calculated latent heat and the entropy change of the transitions T_{t1} and T_{t2} are similar to the one previously described using VT-DSC at ambient pressure. Meanwhile, the values for the new PIII ↔ PI phase transition is approximately the sum of the values of ΔH and ΔS of the individual phase transition, reaching values of 75.0 J g^{-1} and 263.1 J K^{-1} kg^{-1} (see the structural characterization for more details).

In addition, the barocaloric effects of the [DBA][BF_4] compound were calculated in terms of isothermal entropy change, ΔS_{it}, by using quasi-direct methods.[23,24] For that purpose, first the isobaric entropy change (ΔS_{ib}) was estimated as a function of temperature following the Equation 1-3 of *Chapter 1*, section 1.2.1.b.

Figure 4-23 shows the obtained ΔS_{ib} versus temperature at different applied pressures on heating and cooling. For the pressure range of 1–400 bar, the ΔS_{ib} versus temperature curves exhibit a two step-like curve, in where the largest step is due the PIII ↔ PII phase transition with $|\Delta S_{ib}|$ ~ 211 J K^{-1} kg^{-1} (at 1 bar) and a small step is related to the PII ↔ PI phase transition with $|\Delta S_{ib}|$ ~ 36.0 J K^{-1} kg^{-1} (at 1 bar). For pressures above 400 bar, the ΔS_{ib} vs temperature curves exhibit a single and sharp increase of ΔS_{ib} due to the PIII ↔ PI phase transition with $|\Delta S_{ib}|$ ~ 254 J K^{-1} kg^{-1} (at 1000 bar).

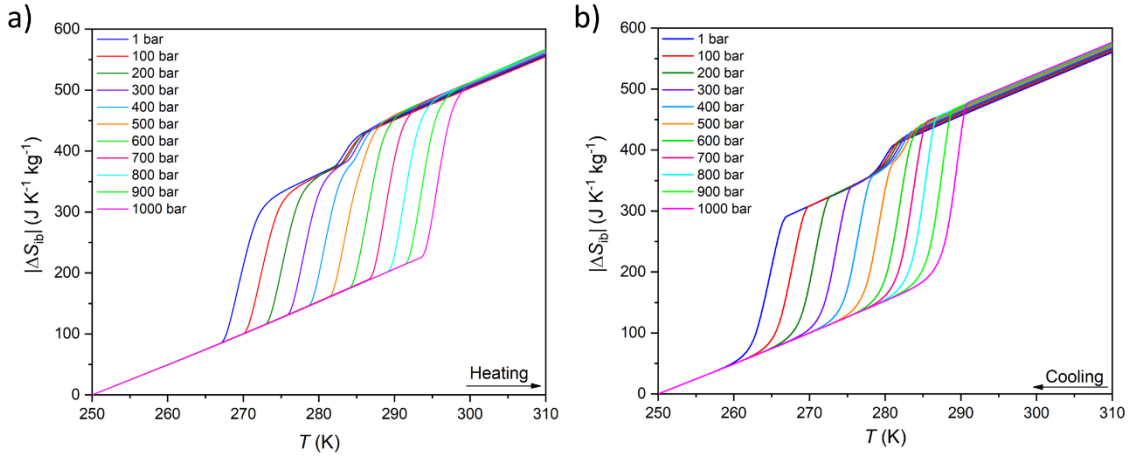

Figure 4-23. ΔS_{ib} curves at different pressures on (a) heating and (b) cooling for the [DBA][BF_4] compound.

Subsequently, the isothermal entropy change (ΔS_{it}) is calculated by difference following the Equation 1-4 (see *Chapter 1*, section 1.2.1.b). The resulting curve is the irreversible isothermal entropy change ΔS_{it} (see Figure 4-24a). Moreover, the adiabatic temperature change (ΔT) could be obtained at different pressures applied (see Figure 4-24b). It was obtained following the Equation 4-4 of previous subchapter:

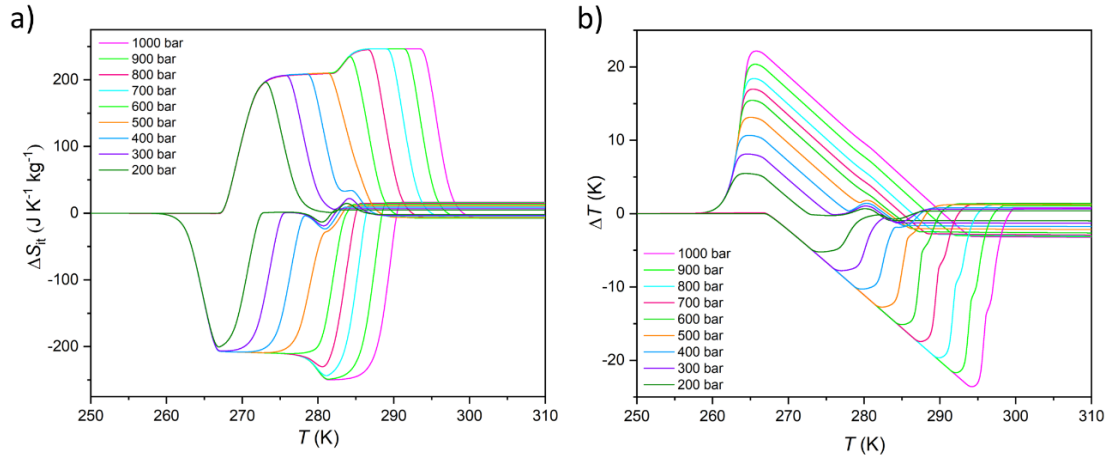

Figure 4-24. a) Pressure-driven isothermal entropy changes on applying ($0 \rightarrow p$) and removing ($p \rightarrow 0$) pressure. b) Reversible adiabatic temperature changes on applying ($0 \rightarrow p$) and removing ($p \rightarrow 0$) pressure at different pressures.

In Equation 1-4 of *Chapter 1*, section 1.2.1.b, after use the specific case of the cooling curve at $p > 1$ bar and the heating curve at $p = 1$, bar, it gives the isothermally reversible entropy change (ΔS_{rev}). Figures 4-25a shows the ΔS_{rev} curves from 200 bar to 1000 bar. Interestingly, a $\Delta S_{rev} >$ 200 J K^{-1} kg^{-1} is achieved for pressures higher than 500 bar and the largest value ΔS_{rev} ~237.7 J K^{-1} kg^{-1} is obtained at 1000 bar at $T = 285$ K (see Figure 4-26).

Furthermore, the reversible adiabatic temperature change (ΔT_{rev}) of the material can be estimated according to Equation 1-5 (see *Chapter 1*, section 1.2.1.b). As it is shown in Figure 4-25b, the largest ΔT_{rev} is about ~17 K at 1000 bar, a difference that is usable in cooling devices that work in sequential compression–decompression cycles.

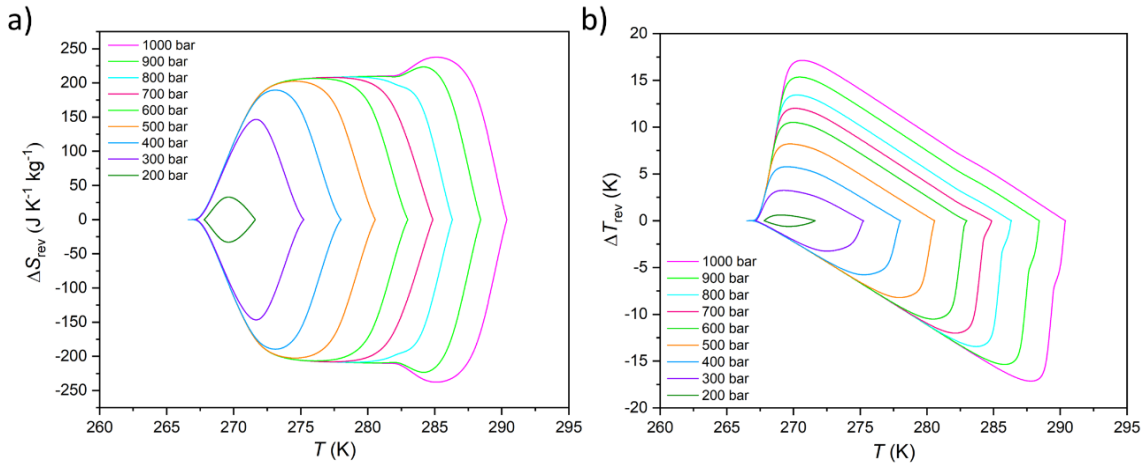

Figure 4-25. a) Pressure-driven reversible isothermal entropy changes on applying ($0 \rightarrow p$) and removing ($p \rightarrow 0$) pressure. b) Reversible adiabatic temperature changes on applying ($0 \rightarrow p$) and removing ($p \rightarrow 0$) pressure at different pressures.

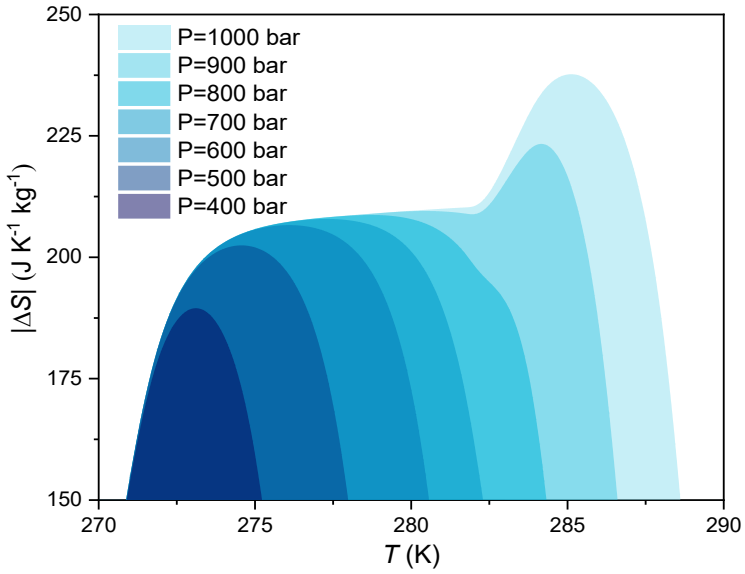

Figure 4-26. Maximum reversible isothermal entropy changes of the ($0 \rightarrow p$) curves at different pressures as a function of temperature.

Figure 4-27 shows the operating temperature range or span temperature (T_{span}) as a function of the applied pressure where a given interval of isothermal entropy change or reversible adiabatic temperature change values can be achieved. In both cases, T_{span} increases almost linearly with applied pressure. At p = 1000 bar, under isothermally reversible conditions, T_{span} = 13 K with reversible ΔS_{it} = 200 J K^{-1} kg^{-1}, while in the adiabatically reversible case, T_{span} = 10 K with reversible ΔT_{rev} = 10 K. This barocaloric performance is in a temperature range from 267 K to 290 K (-6 ºC to 17 ºC).

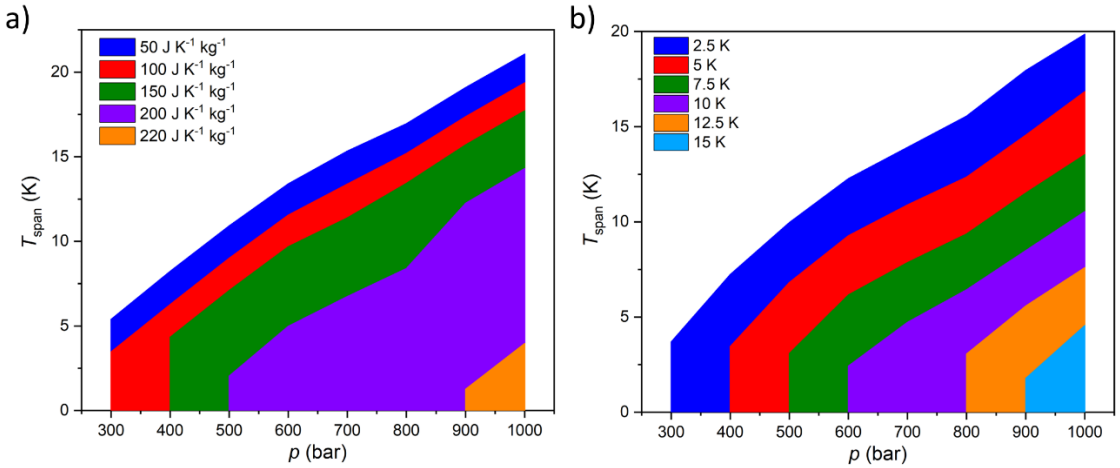

Figure 4-27. Temperature span as a function of applied pressure for fixed intervals of a) reversible isothermal entropy change and b) reversible adiabatic temperature changes for [DBA][BF_4].

The properties of the material presented in this section are quite promising for barocaloric cooling/heating applications: Its temperature transition is slightly below room temperature, an excellent range for refrigeration applications. The material presents a high sensitivity to applied pressures, showing a barocaloric coefficient of 28.9 K kbar^{-1} for PIII ↔ PII transition. This barocaloric tunability is higher than most of barocaloric coefficients reported up to date, and 22.6 K kbar^{-1} for PIII ↔ PI transition when both phase transitions merged. The material also presents

other excellent barocaloric parameters such as $\Delta S_{ib} > 250$ J K^{-1} kg^{-1}, $\Delta T_{rev} > 15$ K and a wide operational temperature.

As noted above, the active temperature range of this material corresponds well to the needs of food preservation. Relatively few barocaloric materials have previously been reported in this temperature range.[2,3]

Figure 4-28a shows the transition temperature and the entropy change of [DBA][BF_4] together with a selection of the best barocaloric materials reported to date. In this graphic it is only included pure barocaloric materials with solid-solid phase transitions showing colossal thermal changes of $\Delta S > 100$ J K^{-1} kg^{-1}. It is omitted other materials that exhibits barocaloric effects due to solid-liquid phase transitions (such as n-alkanes with $\Delta S > 700$ J K^{-1} kg^{-1})[25] or that are combined with simultaneous adsorption/desorption thermal changes (such as the breathing-caloric MIL-53 with $\Delta S > 300$ J K^{-1} kg^{-1}).[26]

Meanwhile Figure 4-28b shows the operating temperature range of the [DBA][BF_4] together with other barocaloric materials with large entropy changes (>100 J K^{-1} kg^{-1}) as a function of the applied pressure, where the most relevant materials are those which need less pressure to show large reversible thermal changes.

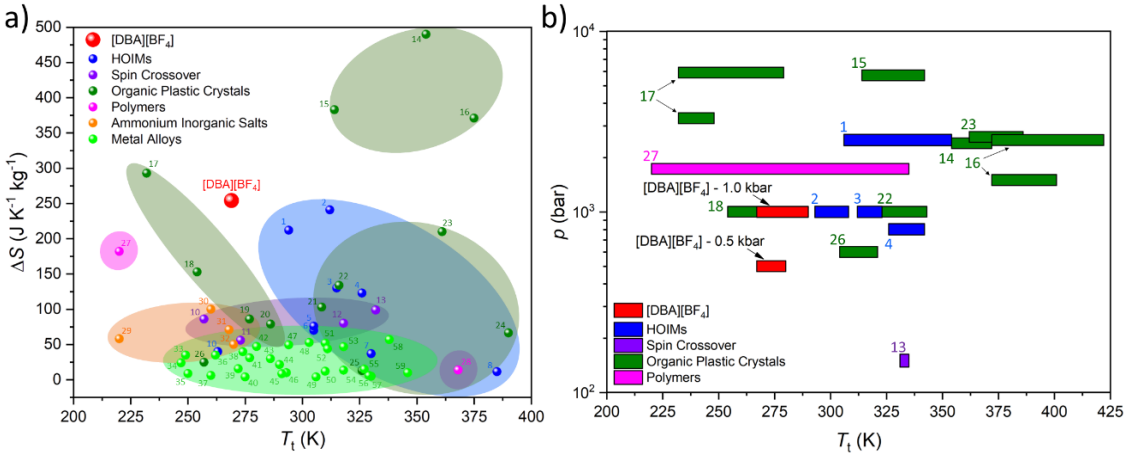

Figure 4-28. a) All barocaloric materials temperature transition (T_t) and entropy change (ΔS) comparison. b) Operating temperature range and the needed pressure of the largest entropy change materials (>100 J K^{-1} kg^{-1}). See more information of all materials represented in on Table A4-2 in *Annex II*.

4.3.4. Structural characterization

To fully understand the phase transitions and structural changes associated with the observed thermal changes, different complementary structural characterization was used to provide useful insights of the different phases.

In the case of the lower-temperature range, single crystal X-ray diffraction (SC-XRD) allowed the elucidation of the crystal structures of phases IV and III. Unfortunately, for $T > 265$ K the presence of twinning and strong diffuse scattering (characteristic of plastic crystal transitions) hindered resolving the crystal structure. Therefore, the structure of the higher temperature phases II and I were elucidated by using variable temperature synchrotron powder X-ray diffraction (VT-SPXRD) and solid-state ^{1}H-, ^{13}C- and ^{11}B-NMR.

4.3.4.1. Structural characterization of PIV and PIII by SC-XRD

a) Phase IV (T < 134 K)

According to single crystal X-ray diffraction the new PIV, here described for the first time, crystallizes in an orthorhombic symmetry, with space group *Ccce* and lattice parameters *a* = 7.3980(5) Å, *b* = 18.4562(11) Å and *c* = 16.8535(10) Å (at *T* = 100 K, see more details in Table A4-1 in *Annex II* and Figure 4-29*)*.

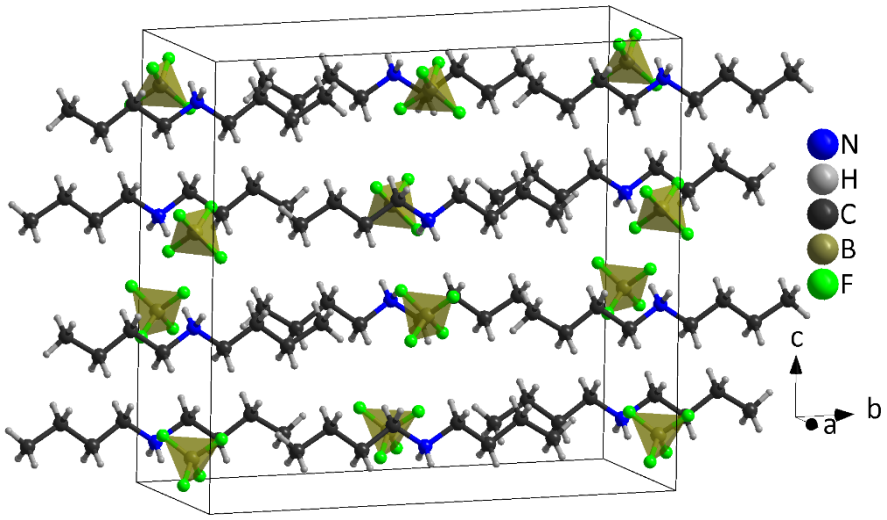

Figure 4-29. Structure of [DBA][BF_4] at 100 K, where the tetrahedra correspond to $[BF_4]^-$ anions, the chains to $[DBA]^+$ cations and the black cage represents the unit cell.

The asymmetric unit of phase IV consists of one half of $[DBA]^+$ and $[BF_4]^-$ ions, as both moieties are placed over a 2-fold symmetry axis. In the case of the $[BF_4]^-$ anions, the boron atoms are in a slightly distorted tetrahedral environment with two different B-F bond lengths (1.404(5) Å and 1.380(5) Å). Meanwhile, the $[DBA]^+$ cations show a perfect zig-zag configuration of the alkylammonium chains (see Figure 4-29*)*.

Concerning the molecular arrangement within the crystal structure, this compound displays a significantly distorted NaCl-type structure where the $[DBA]^+$ cations are surrounded by six $[BF_4]^-$ anions in a distorted octahedral environment, and vice versa (see Figure 4-30).

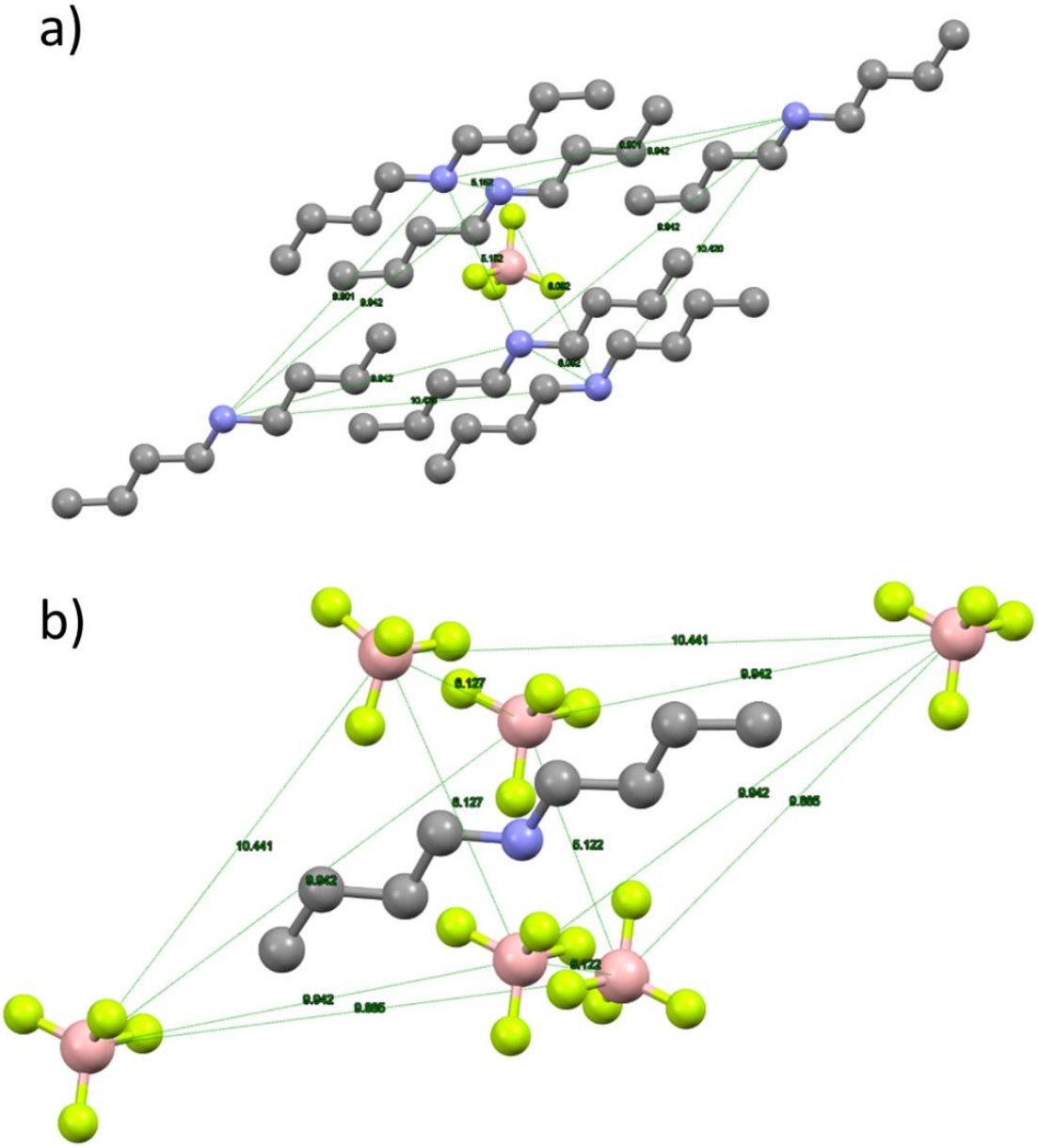

Figure 4-30. Coordination environment of a) BF_4^- and b) DBA^+ in phase IV at T = 100 K.

The interactions between the anionic and cationic components are electrostatic and via H-bonds. In this latter case, the donor atoms are the N-atoms of the amine groups and the acceptor atoms are the F-atoms of $[BF_4]^-$ anions (see Figure 4-31). That the distances between hydrogen and fluorine atoms are around 2.19 Å and 2.30 Å; the two fluorine atoms involved in the H-bonds are those with the longest B-F bond lengths (1.405(5) Å).

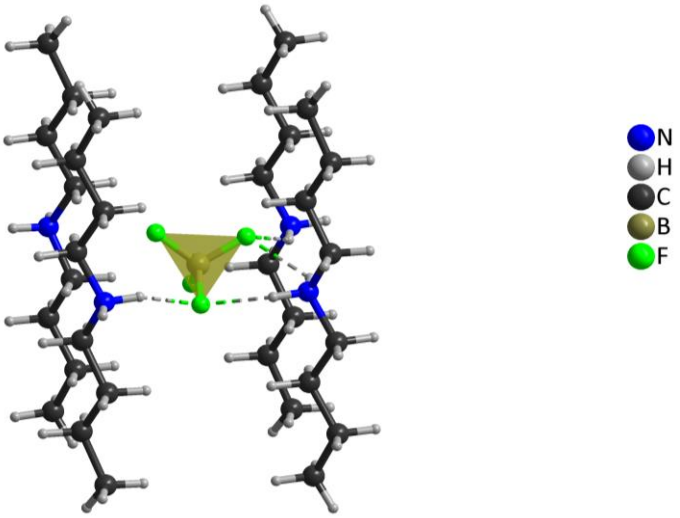

Figure 4-31. H-Bonds of each $[BF_4]^-$ molecule in phase IV at T = 100 K.

b) Phase III (134 K < T < 269 K)

According to SC-XRD phase III also crystallizes in an orthorhombic crystal system with space group *Cmme* and lattice parameters a = 7.5762(10) Å, b = 18.642(3) Å and c = 8.5564(12) Å at T = 240 K (see more details in Figure 4-32 and Table A4-1 of *Annex II*).

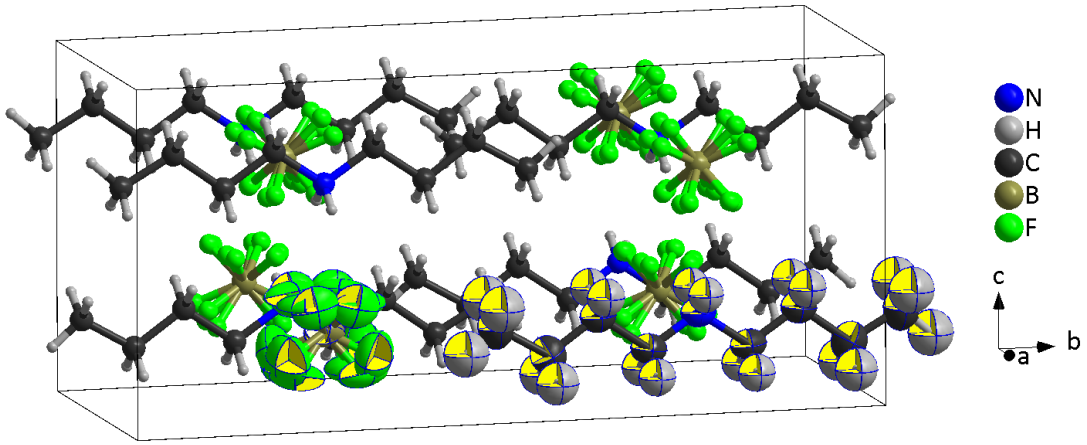

Figure 4-32. Crystal structure of [DBA][BF_4] at 240 K, where the $[BF_4]^-$ anions are represented in four different disordered orientations, the chains correspond to $[DBA]^+$ cations and the black cage represents the unit cell. *Note*: One $[DBA]^+$ and $[BF_4]^-$ species are shown as ORTEP drawing (ellipsoid probability at 50%).

The obtained crystal structure of this higher temperature phase III is very similar to that previously described for phase IV, although the local symmetry in the environment of both ions has increased from point group 2 (C2) to *mm*2 (C2v). The molecular geometry of both ions is compatible with this increased symmetry; however, while the DBA cations remain ordered, the $[BF_4]^-$ anions are now best represented by a fourfold disorder model. The two fluoride atoms involved in N-H···F hydrogen bonds display longer B-F bond distances (1.381(14) Å and 1.384(13) Å) compared to the other two (1.352(13) Å and 1.360(15) Å) that are the acceptors of weaker C-H···F interactions. The $[BF_4]^-$ anions remain recognisably tetrahedral on average, rather than appearing spherical as in the case of full orientational order; this could explain the small enthalpy and entropy changes experimentally observed for the transition between phases IV and III.

4.3.4.2. Structural characterization of phases I and II by VT-SPXRD and solid-state NMR, and further information on phase III

a) VT-SPXRD characterization

To characterize the high temperature crystalline phases and their phase transitions, variable temperature synchrotron powder X-ray diffraction (VT-SPXRD) experiments were carried out from 180 K to 320 K.

From the analysis of VT-SPXRD patterns (see Figure 4-33), two phase transitions can be clearly observed at T_{t1} ~280 K and T_{t2} ~260 K, between phases PI ↔ PII and PII ↔ PIII, respectively, consistent with the VT-DSC results. The data were initially modelled using the Le Bail method.

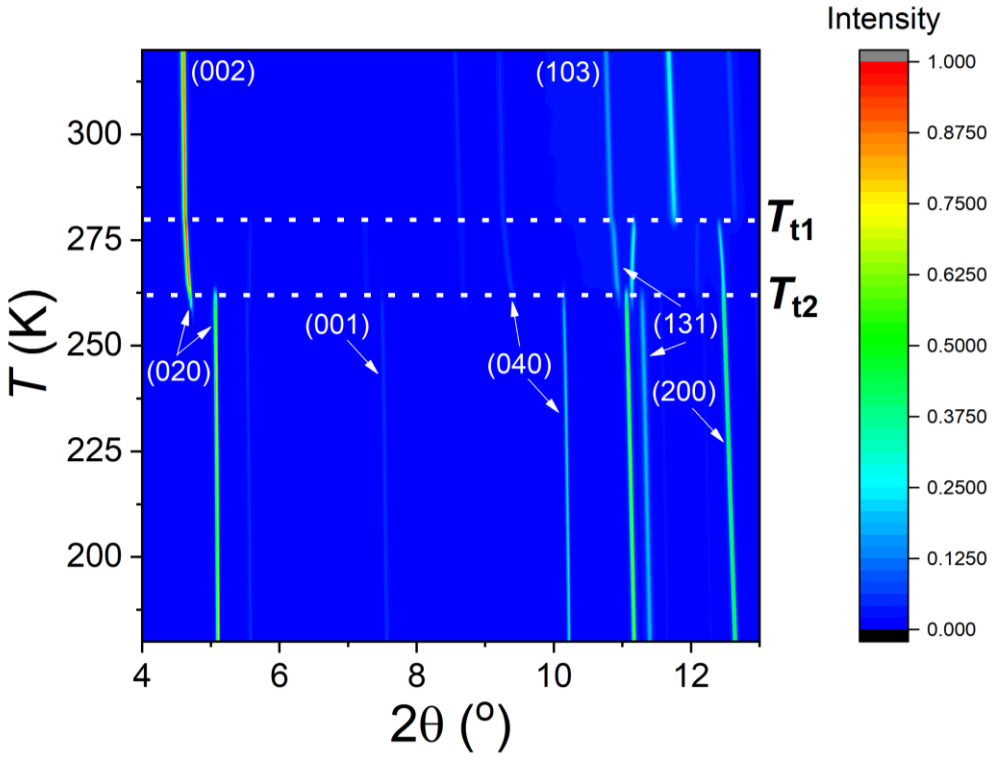

Figure 4-33. SPXRD patterns of [DBA][BF_4] as a function of temperature (180 K < T < 320 K).

The phase III data were well fitted by Le Bail refinement in the known orthorhombic cell with space group *Cmme* and lattice parameters a ~7.5 Å, b ~18.5 Å and c ~8.5 Å (Figure 4-34), in full agreement with our results obtained by SC-XRD.

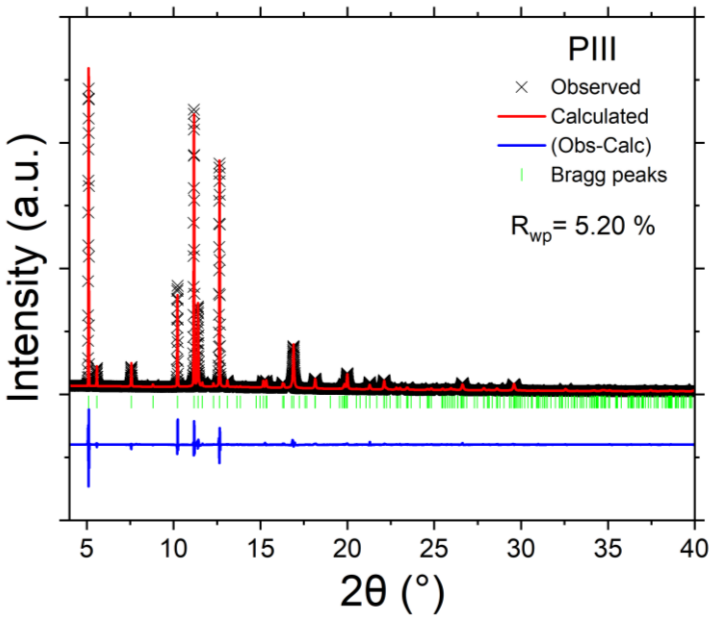

Figure 4-34. Le Bail refinement of phase III of [DBA][BF_4] at T = 180 K.

The data in the two phases I and II without single-crystal data were indexed by comparison with phase III. Phase II is well fitted in the same orthorhombic space group *Cmme* as phase III (Figure 4-35); while the *a* and *c* axes remain almost unchanged across the phase transition, there is a large increase of the *b* axis (from *b* ~18.5 Å to *b* ~20.3 Å) resulting in a very large volume increase of about 8.4%. Phase I has body-centred tetragonal symmetry with no further systematic absences, giving a good Le Bail refinement in space group *I*4/*mmm* with lattice parameters *a* ~5.7 Å and *c* ~20.5 Å (Figure 4-36). The basis vectors are related by:

$$(\mathbf{a} \quad \mathbf{b} \quad \mathbf{c})_o = (\mathbf{a} \quad \mathbf{b} \quad \mathbf{c})_t \begin{pmatrix} 1 & 0 & 1 \\ 1 & 0 & -1 \\ 0 & 1 & 0 \end{pmatrix}.$$

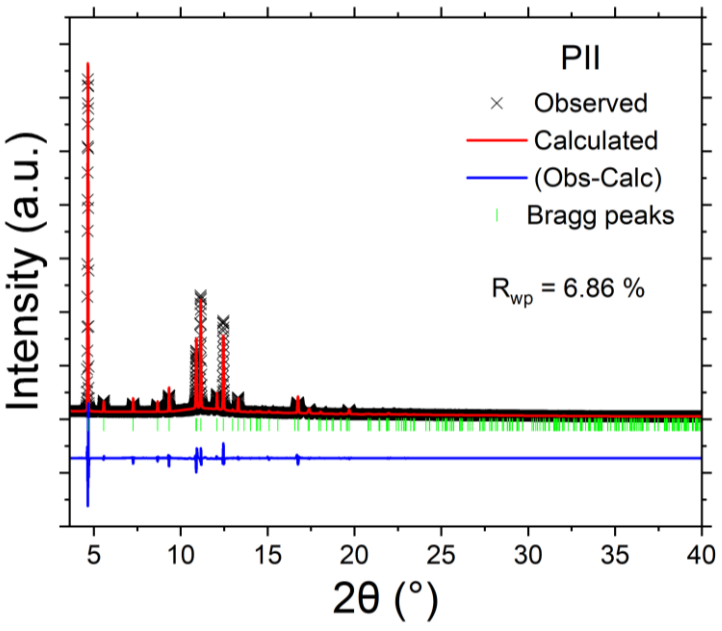

Figure 4-35. Le Bail refinement of phase II of [DBA][BF_4] at T = 270 K.

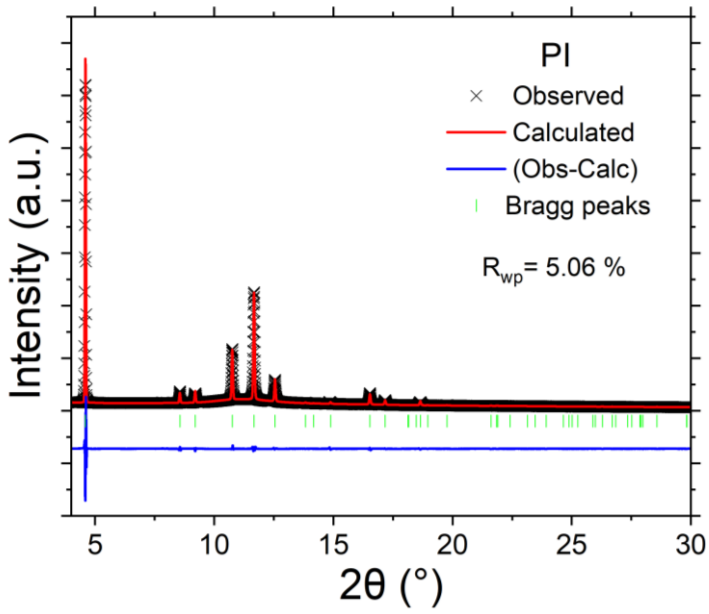

Figure 4-36. Le Bail refinement of phase I of [DBA][BF_4] at T = 320 K.

Once these unit cells had been established, tentative structural models for phases I and II were generated and refined by the Rietveld method. For phase II, the known crystal structure obtained from SC-XRD of phase III was used as the initial model. The obtained crystal structure and details of the refinement are summarized in Figure 4-37 and Table A4-3 of *Annex II*. The most noticeable feature of the crystal structure of this phase is the disorder of the terminal methyl group of the $[DBA]^+$ cations, which are split into two different positions (Figure 4-38), similar to other 2D perovskites.[23,27,28] This disorder means that it is no longer possible for adjacent butyl chains along the b direction to overlap as in phase III, and is thus responsible for the sudden increase in the *b* lattice parameter (Figure 4-39). In phase I, the disorder now affects the whole butyl chain. Moreover, the $[BF_4]^-$ ions sit slightly away from an inversion centre, so that the B-atom is now disordered between two sites in addition to the disorder of the F-atoms about the fourfold axis. Details of this refinement are given in Figure 4-38, Figure 4-40 and Table A4-4 of *Annex II*.

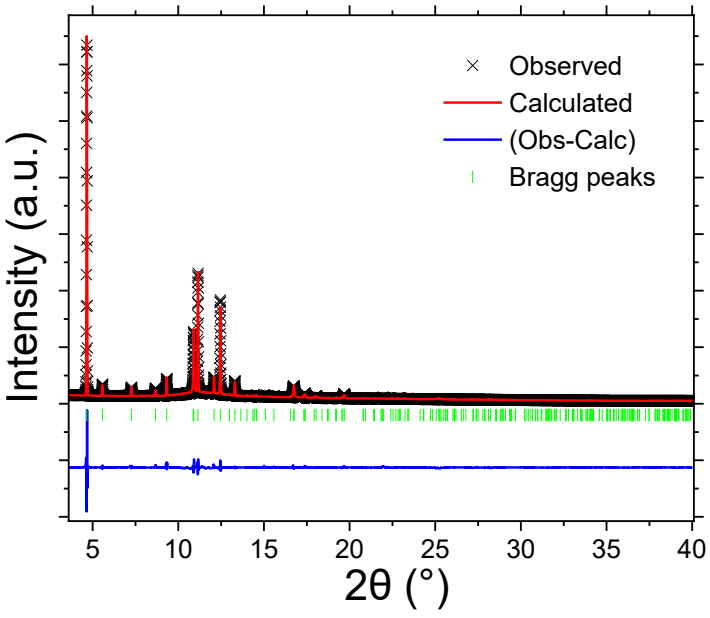

Figure 4-37. Rietveld refinement of phase II of [DBA][BF_4] at T = 270 K

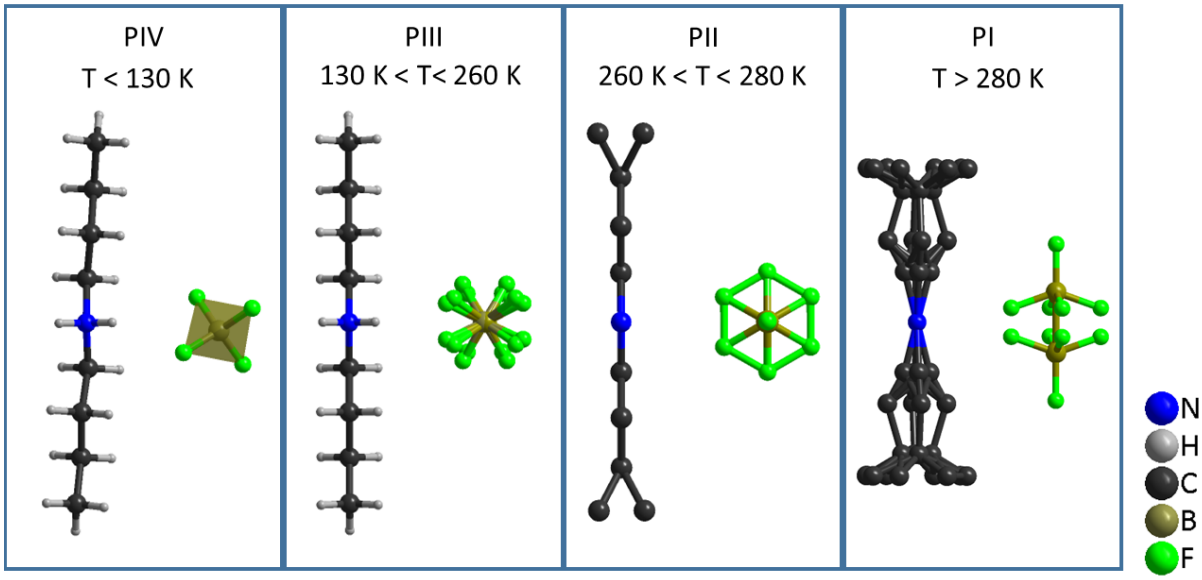

Figure 4-38. Scheme with the molecular configuration of ions for the different phases of [DBA][BF_4].

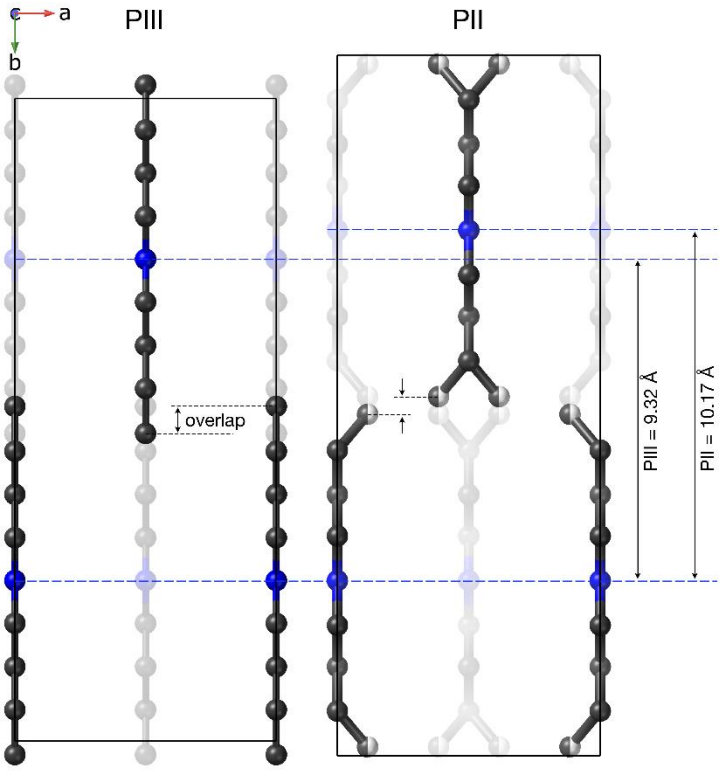

Figure 4-39. Distances differences along *b*-axis between PIII and PII.

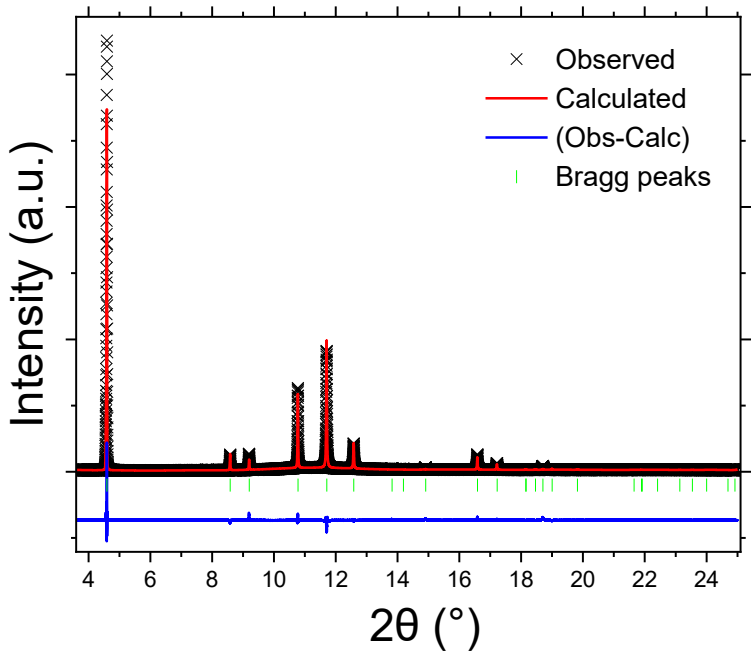

Figure 4-40. Rietveld refinement of phase I of [DBA][BF_4] at T = 300 K.

Figures 4-41a and 4-41b show the evolution of the lattice parameters and the volume as a function of temperature as obtained from the Le Bail refinement of the SPXRD patterns.

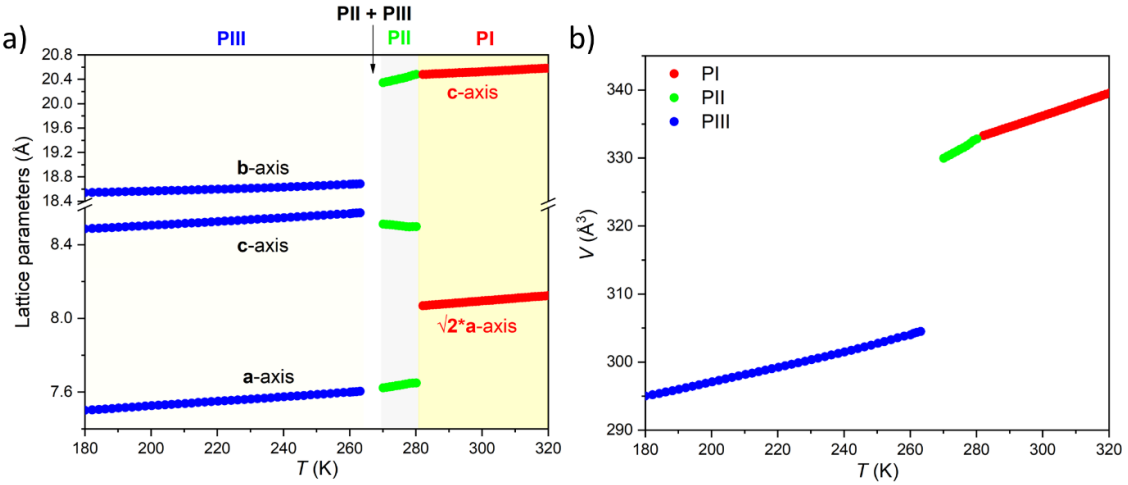

Figure 4-41. Evolution of a) the lattice parameters and b) the volume of PI, PII and PIII of [DBA][BF_4] as a function of temperature.

All phases exhibit conventional thermal expansion upon heating in all cell parameters, except phase II that exhibits negative thermal expansion along the *c*-axis.

The observed volume changes associated to both phase transitions seem to agree with the results observed by VT-DSC at ambient pressure. The larger ΔH and ΔS values observed for the phase transition between phases PIII ↔ PII seems to be related to the larger volume change across this transition. Meanwhile, the smaller volume change between phases PII ↔ PI will justify lower values of ΔH and ΔS.

From the VP-DSC results and the volume changes both barocaloric coefficients, dT_{t1}/dp and dT_{t2}/dp, can be estimated by using Clausius-Clapeyron (see Equation 1-1 of *Chapter 1*, section 1.2.1.b).[29] Here, the estimated coefficient by Clausius-Clapeyron equation is dT_{t2}/dp ~4.4 K kbar^{-1} and dT_{t1}/dp ~39.5 K kbar^{-1}, which are similar to those obtained in VP-DSC, dT_{t1}/dp ~5.5 K kbar^{-1} and dT_{t2}/dp ~29.0 K kbar^{-1}.

Furthermore, these volume changes together with the thermal changes obtained at ambient pressure anticipating that the [DBA][BF_4] compound can exhibit very large conventional barocaloric effects.

b) Solid-state Nuclear Magnetic Resonance of ^{1}H, ^{13}C and ^{11}B

^{1}H and $^{13}C\{^{1}H\}$ MAS spectra of [DBA][BF_4] have been recorded at high magnetic field (17.6 T) and fast MAS and show almost resolved peaks for $[DBA]^+$ (Figures 4-42 and A4-2 of *Annex II*, respectively). Under these conditions and at room temperature, the crystal phase corresponds to phase I. By decreasing MAS frequency and temperature important variations can be observed in the ^{1}H line-shapes of phases I, II and III (Figure 4-42b). These variations are related to a gradual broadening of the peaks when decreasing *T*. Transverse relaxation times T_2' were measured using a spin-echo pulse sequence (see Table 4-4). The main mechanisms of relaxation are here the dipolar couplings, notably between protons. The highest values obtained for phase I can therefore be explained by a higher degree of motion of the DBA^+ cation allowing for a decrease in the effective dipolar couplings. Also, this cation appears slightly more mobile in phase II compared to phase III, but the differences are smaller than with phase I. This gradual increase in $[DBA]^+$ mobility from phase III to phase I is consistent with the decrease in density and the increase in alkyl chain disorder that can be extracted from X-rays data.

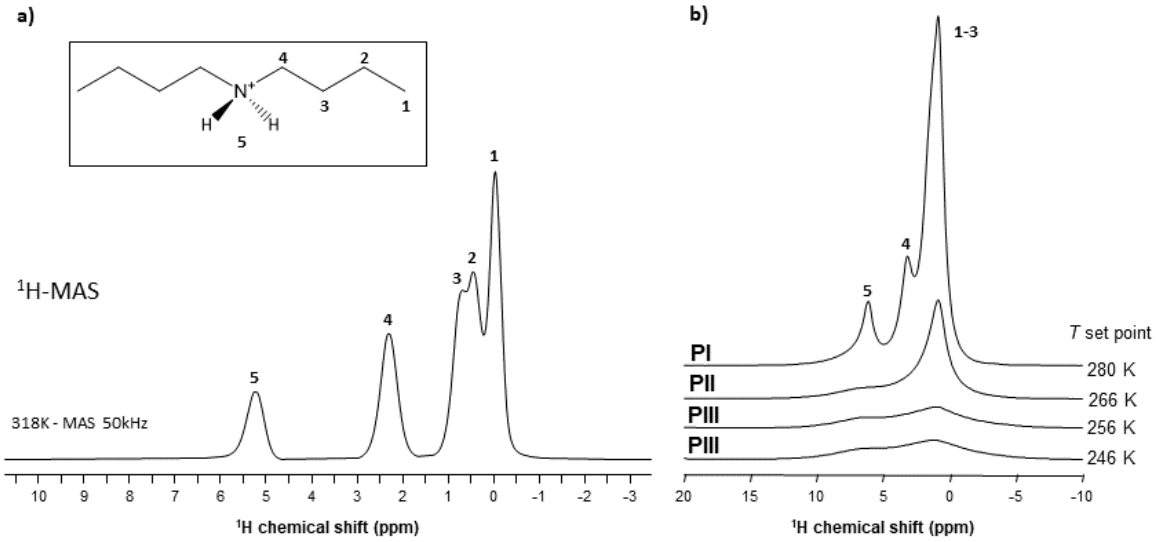

Figure 4-42. ^{1}H MAS NMR spectra: a) Fast MAS spectrum of phase I ($\nu_0 \equiv 750$ MHz, $\nu_{MAS} = 50$ kHz); b) MAS spectra of phases I, II and III obtained by decreasing T ($\nu_0 \equiv 600$ MHz, $\nu_{MAS} = 15$ kHz).

Table 4-4. ^{1}H spin-echo transverse relaxation times T_2'.

Phase	T_2' (ms) [a]			
	CH_3- (1)	**C-CH_2-C (2-3)**	**N-CH_2- (4)**	**-NH_2 (5)**
Phase I	0.66	0.50	0.65	0.78
Phase II	0.48	0.26		0.37
Phase III	0.2 – 0.3			0.3 – 0.4

a. Obtained using a spin-echo at ν_{MAS} = 15 kHz and T settled at: 278 K (PI), 263 K and 261 K (PII), 243 K (PIII).

As VT-SPXRD analysis and the solid-state ^{1}H single-pulse MAS spectra showed, the PIII ↔ PII phase transition shows larger disorder/mobility in the terminal -CH_3, while the PII ↔ PI phase transition presents larger disorder/mobility in the rest of the chain. In this context, it is reasonable to relate some of these results with the obtained in VT- and VP-DSC.

On one hand, the PIII ↔ PII phase transition shows a very large volume change due to the disorder of the terminal -CH_3 of both chains of $[DBA]^+$ cation (see Figures 4-38 and 4-42), while the PII ↔ PI phase transition, involving the rest of the chain, is less relevant in volume changes (see Figures 4-38 and 4-42). With that in mind, it could be expected that the new PIII ↔ PI phase transition would have a large dT_{tm}/dp, between dT_{t1}/dp and dT_{t2}/dp which agree with the experimental results. On the other hand, the new PIII ↔ PI phase transition involves order/disorder process affecting the four carbons of each chain, so its ΔH and ΔS should be similar to the addition of those corresponding to both, the PIII ↔ PII and the PII ↔ PI phase transitions, which is also what the experimental results of VP-DSC showed.

Information on the thermal behaviour of $[BF_4]^-$ might be gained from ^{11}B NMR spectroscopy. Figure 4-43 present a series of ^{11}B spectra obtained by increasing T. Clear discontinuities in the spinning sidebands (SSBs) patterns (Figure 4-43a) and in the isotropic chemical shifts (Figure 4-43b) are observed and assigned to the transitions between phases occurring in these ranges of temperature. Fitting the SSBs allowed to estimate the parameters of the ^{11}B quadrupolar couplings (coupling constant C_Q and asymmetry parameter η_Q) at each temperature. Their variations are plotted in Figure 4-44. The discontinuities observed for C_Q and η_Q coincide with those observed by X-ray diffraction (see Figure 4-38). They are again related to the transitions between phases. For phase III, the increase in T leads to a slight and gradual increase in C_Q before a sudden increase at the transition to phase II. Such increase in C_Q might be explained by a loss in the degree of symmetry of the electric field gradient due: to a deformation of $[BF_4]^-$ and/or to a hindrance of the orientational motion of the anion. For phase II, when the T is increased, it is observed a gradual decrease in C_Q and η_Q that becomes sudden at the transition to phase I. The change in η_Q is important (from 0.77 to 0.12 at the transition) and denotes either a strong reorganisation in the distribution of anions and cations or the appearance of new motions leading to a different time-averaged quadrupolar coupling tensor. This later argument bears consistency with the increase in motions detected by ^{1}H MAS NMR. In such a case, the small values of η_Q points to an almost axial motion, compatible with the refined structure of phase I (see Figure 4-38).

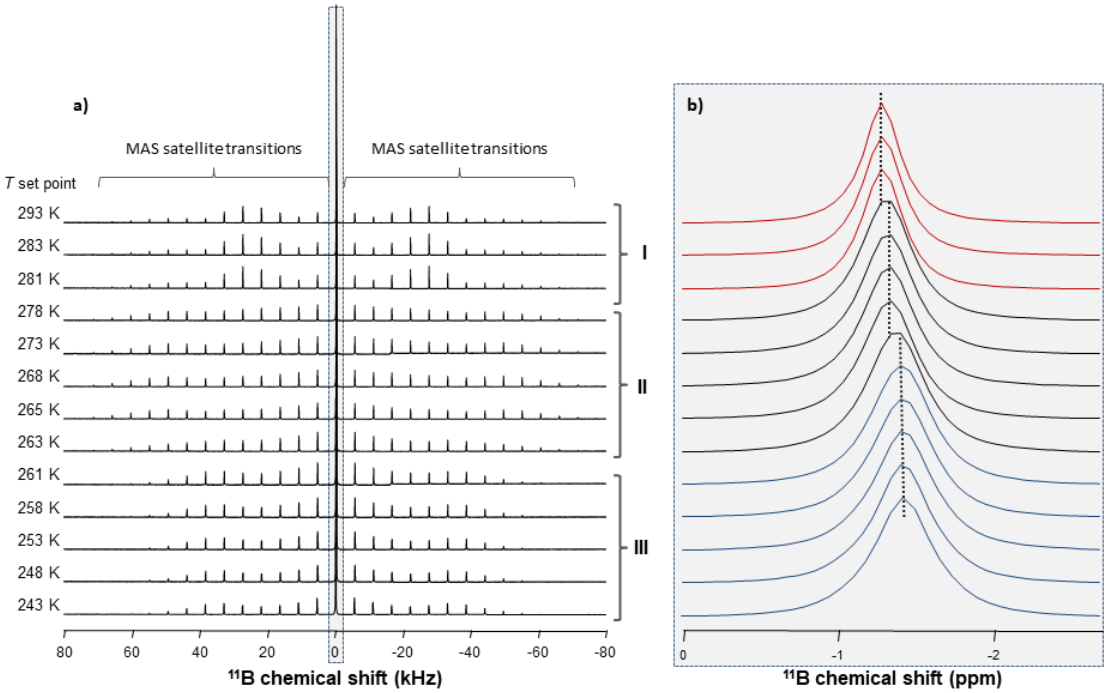

Figure 4-43. ^{11}B MAS spectra obtained at different T ($\nu_0 \equiv 193$ MHz, $\nu_{MAS} = 5.5$ kHz): a) full spectral window showing the MAS satellite transitions sidebands; b) zoom on the isotropic centreband.

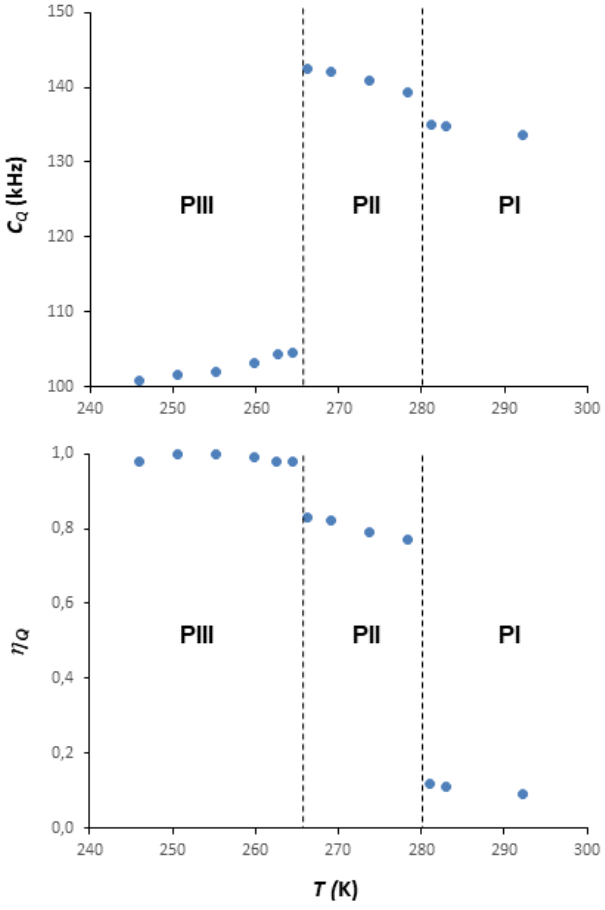

Figure 4-44. ^{11}B quadrupolar parameters as a function of sample temperature (upon heating).

In summary, all these structural studies have shown that the four phases, and the corresponding three phase transitions, of [DBA][BF_4] are related to the disorder increases (see Figure 4-38). At low temperature (T < 130 K), phase IV is the most stable phase and both cations and anions are fully ordered. In phase III, observed in the temperature range 130 K to 260 K, the $[DBA]^+$ cations remain ordered with a zig-zag conformation, but the $[BF_4]^-$ anions are slightly disordered. Phase II is stable in a small range of temperatures (260 - 280 K). In this phase the $[DBA]^+$ cations are partially disordered on the ending methyl group. Finally, phase I is stable for T > 280 K, with both $[DBA]^+$ cations and $[BF_4]^-$ anions disordered over multiple sites.

4.3.5. Conclusions

It has been able to obtain easily and by mild conditions the [DBA][BF_4] ionic compound, which is composed of lightweight atoms and has low density 1.25 g/cm^3 (from single crystal diffraction at 100 K). This material undergoes three order-disorder transitions, exhibiting four phases in the temperature range 100-300 K, of which the lowest-temperature phase IV is newly reported here. The PIV ↔ PIII phase transition has a low entropy change ~0.4 J K^{-1} kg^{-1} at T_{t3} ~130 K and it is associated with partial disorder of the $[BF_4]^-$ anions. On the other hand, the PIII ↔ PII phase transition exhibits a large entropy change ~205 J K^{-1} kg^{-1} at T_{t2} ~269 K and it is mainly due to order-disorder processes of the two-ending methyl group of the $[DBA]^+$ cations. The PII ↔ PI phase transition has a moderate entropy change ~38 J K^{-1} kg^{-1} at T_{t1} ~282 K mainly due to disorder of all carbon atoms of the $[DBA]^+$ cations. This material presents potential for cold-storage applications due to the fact that PIII ↔ PII and PII ↔ PI phase transitions show a total enthalpy change (~71.0 kJ kg^{-1}) similar to commercial materials, along with a moderate thermal hysteresis (3 K and 6 K for T_{t1} and T_{t2}, respectively). Furthermore, in addition to the transition temperature (T_{t1} and T_{t2}) and the large thermal changes (ΔS = 245 J K^{-1} kg^{-1}), the [DBA][BF_4] compound exhibits a large sensitive to pressure (dT_2/dp ~29 K kbar^{-1} and dT_m/dp ~22.6 K kbar^{-1}) allowing the material to have excellent barocaloric properties, including a large pressure-driven reversible isothermal entropy change (ΔS_{rev} > 200 J K^{-1} kg^{-1}) and a large reversible adiabatic temperature change (ΔT_{rev} ~17 K). Additionally, the material exhibits large barocaloric effects with a temperature span of 15 K, from 266 K to 281 K under the application of only 500 bar, which can be extended to 24K, from 266 K to 290 K, under the application of 1000 bar, resulting in an excellent material for barocaloric heating or refrigeration.

These results highlight that [DBA][BF_4] is not only a good candidate as solid-solid cold-storage material, but also as a new barocaloric material for cooling applications near 273 K, which make this new compound a very versatile multipurpose material for food preservation, either through passive cold-storage or active barocaloric refrigeration, opening the door to develop new multipurpose solid thermomaterials.

Finally, this study emphasises that relating the thermal properties to the structural transitions of the [DBA][BF_4], thanks to the combination of various characterization techniques, is essential to understand the structure-properties relationships that are necessary to design new thermomaterials.

4.3.6. References

[1] "The Role of Refrigeration in Worldwide nutrition (2020), 6th Informatory Note on Refrigeration and Food," can be found under https://iifir.org/en/fridoc/the-role-of-refrigeration-in-worldwide-nutrition-2020-142029, **2020**.

[2] S. J. James, C. James, *Chilling and Freezing*, Elsevier Inc., **2014**.

[3] B. H. Lado, A. E. Yousef, *Microbes Infect.* **2002**, *4*, 433.

[4] M. Masche, L. Ianniciello, J. Tušek, K. Engelbrecht, *Int. J. Refrig.* **2021**, *121*, 302.

[5] T. Hess, L. M. Maier, N. Bachmann, P. Corhan, O. Schäfer-Welsen, J. Wöllenstein, K. Bartholomé, *J. Appl. Phys.* **2020**, *127*, 075103.

[6] J. Font, J. Muntasell, J. Navarro, J.-L. Tamarit, J. Lloveras, *Sol. Energy Mater.* **1987**, *15*, 299.

[7] M. Barrio, J. Font, J. Muntasell, J. Navarro, J. L. Tamarit, *Sol. Energy Mater.* **1988**, *18*, 109.

[8] P. Lloveras, A. Aznar, M. Barrio, P. Negrier, C. Popescu, A. Planes, L. Mañosa, E. Stern-Taulats, A. Avramenko, N. D. Mathur, X. Moya, J. L. Tamarit, *Nat. Commun.* **2019**, *10*, 1.

[9] J. M. Bermúdez-García, M. Sánchez-Andújar, S. Castro-García, J. López-Beceiro, R. Artiaga, M. A. Señarís-Rodríguez, *Nat. Commun.* **2017**, *8*, 15715.

[10] S. K. Mohamed, D. K. Padma, *Indian J. Chem. A Inorganic, Phys. Theor. Anal. Chem.* **1988**, *27*, 759.

[11] G. Zabinska, P. Ferloni, M. Sanesi, *Thermochim. Acta* **1988**, *137*, 39.

[12] A. Bielecki, D. P. Burum, *J. Magn. Reson. Ser. A* **1995**, *116*, 215.

[13] G. Ferrer, C. Barreneche, A. Solé, I. Martorell, L. F. Cabeza, *J. Energy Storage* **2017**, *11*, 1.

[15] B. H. Toby, R. B. Von Dreele, *J. Appl. Crystallogr.* **2013**, *46*, 544.

[16] G. M. Sheldrick, *Acta Crystallogr. Sect. A Found. Crystallogr.* **2015**, *71*, 3.

[17] G. M. Sheldrick, *Acta Crystallogr. Sect. C Struct. Chem.* **2015**, *71*, 3.

[18] S. D. Sharma, K. Sagara, *Int. J. Green Energy* **2005**, *2*, 1.

[19] M. V. Gorev, E. V. Bogdanov, I. N. Flerov, *J. Phys. D. Appl. Phys.* **2017**, *50*, 384002.

[20] P. Lloveras, J.-L. Tamarit, *MRS Energy Sustain.* **2021**, *8*, 3.

[21] J. M. Bermúdez-García, S. Yáñez-Vilar, A. García-Fernández, M. Sánchez-Andújar, S. Castro-García, J. López-Beceiro, R. Artiaga, M. Dilshad, X. Moya, M. A. Señarís-Rodríguez, *J. Mater. Chem. C* **2018**, *6*, 9867.

[22] Q. Ren, J. Qi, D. Yu, Z. Zhang, R. Song, W. Song, B. Yuan, T. Wang, W. Ren, Z. Zhang, X. Tong, B. Li, *Nat. Commun.* **2022**, *13*, 1.

[23] J. Li, M. Barrio, D. J. Dunstan, R. Dixey, X. Lou, J. L. Tamarit, A. E. Phillips, P. Lloveras, *Adv. Funct. Mater.* **2021**, *31*, 1.

[24] X. Moya, N. D. Mathur, *Science* **2020**, *803*, 797.

[25] J. Lin, P. Tong, K. Zhang, K. Tao, W. Lu, X. Wang, X. Zhang, W. Song, Y. Sun, *Nat. Commun.* **2022**, *13*, 596.

[26] J. García-Ben, J. López-Beceiro, R. Artiaga, J. Salgado-Beceiro, I. Delgado-Ferreiro, Y. V. Kolen'ko, S. Castro-García, M. A. Señarís-Rodríguez, M. Sánchez-Andújar, J. M. Bermúdez-García, *Chem. Mater.* **2022**, *34*, 3323.

[27] L. Ricard, R. Cavagnat, M. Rey-Lafon, *J. Phys. Chem.* **1985**, *89*, 4887.

[28] Y. Abid, M. Kamoun, A. Daoud, F. Romain, *J. Raman Spectrosc.* **1990**, *21*, 709.

[29] X. Moya, S. Kar-Narayan, N. D. Mathur, *Nat. Mater.* **2014**, *13*, 439.

Chapter 5

Enhanced thermal changes through simultaneous combination of barocaloric effects and gas adsorption processes

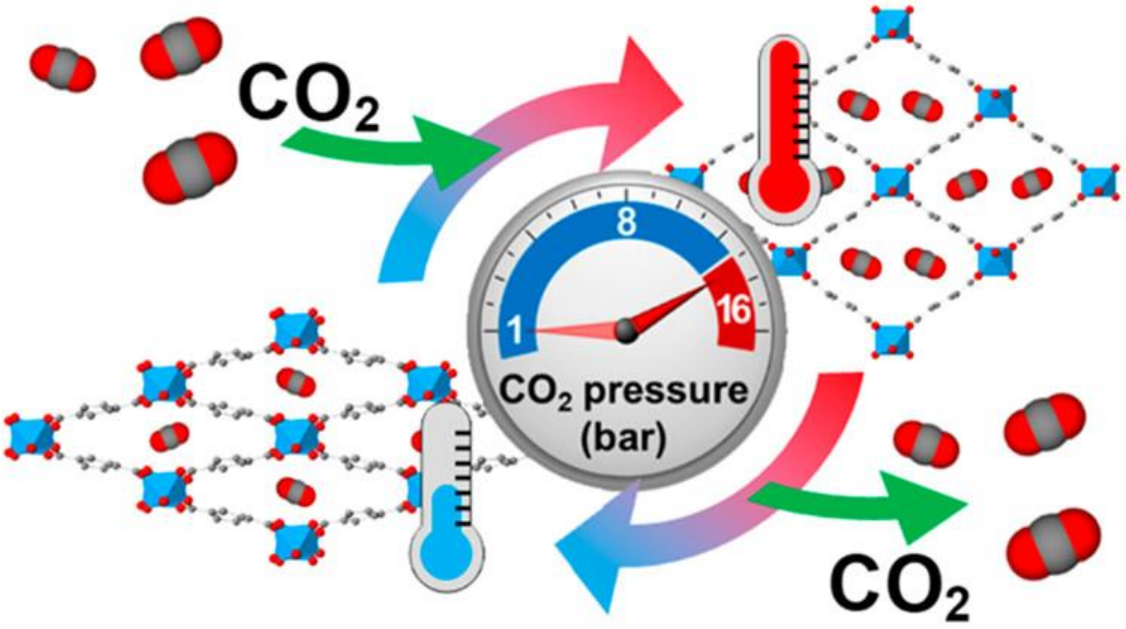

Chapter 5: Enhanced thermal changes through simultaneous combination of barocaloric effects and gas adsorption processes

Index

5.1. Introduction to flexible MOFs with solid-solid transitions **145**

5.2. Displaying the breathing-caloric effect: a new alternative based in the combination of barocaloric effect and adsorption cooling in MOFs **149**

5.2.1. Introduction 149

5.2.2. Experimental 151

5.2.3. Results and discussion 163

5.2.4. Conclusions 166

5.2.5. References 167

5.1. Introduction to flexible MOFs with solid-solid transitions

While HOIPs or the hybrid ionic PCs are considered dense HOIMs, metal-organic frameworks (MOFs) show structures with hollow cavities that classify them as porous HOIMs (see Figure 5-1).[1] Interestingly, the empty cavities of MOFs allow the easy exchange of guest molecules, as gases or solvents, through the application of external stimuli such as temperature, pressure, vacuum, humidity or dispersion in a solvent.[1] As mentioned in section 1.2.1.c of *Chapter 1*, MOFs are emerging porous materials used for cooling by adsorbing and desorbing gases or solvent molecules. Typically, these materials exhibit an exothermic change (heat release) upon adsorption of guest molecules, as new interactions are formed between the framework and the molecules. Conversely, an endothermic change (heat absorption) occurs during desorption.[2] The use of MOFs offers various advantages compared to other adsorbents like activated carbons or zeolites:

- The adsorption capacity of a family of porous materials is highly dependent on the specific material and adsorbate, but in general, MOFs tend to exhibit higher adsorption capacities compared to other porous materials.[3,4]
- The extensive variety of structures, metals, oxidation states, ligand's sizes, coordination number and shapes within the MOFs family, provides a wide range of possibilities for optimizing desired conditions.[5]
- MOFs also stand out among other porous materials for their exceptional chemical and, most importantly, mechanical resistance.[6,7]

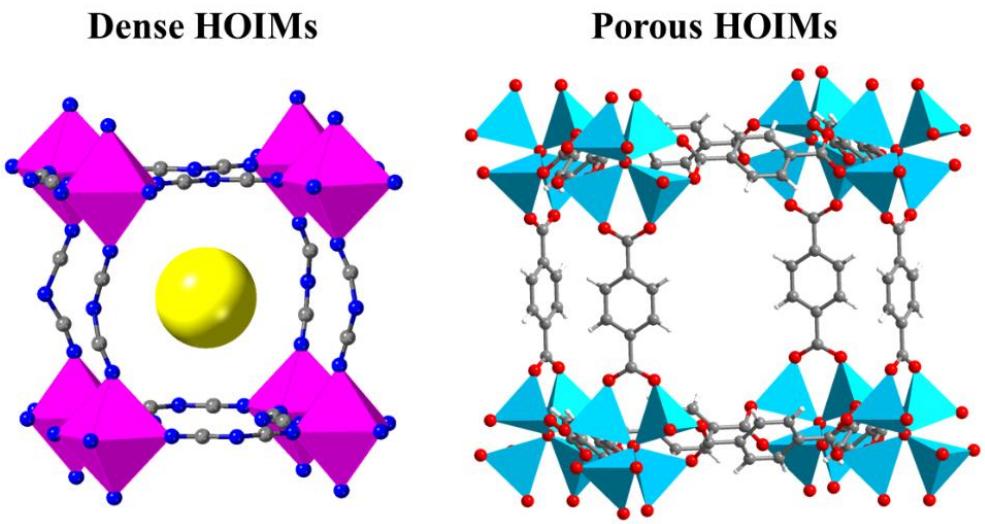

Figure 5-1. Examples of each porosity of HOIMs, on the left a general hybrid dicyanamide perovskite and on the right the MOF-5.

Many of the MOFs reported up to date display rigid structures, wherein the pore is fully accessible to guest molecules. However, there exist certain MOFs with flexible structures that undergo significant structural changes upon the application of specific stimuli such as temperature or pressure.[8] Most of these flexible MOFs exhibit reversible structural transitions, wherein the removal of the stimulus leads them to revert to their initial structure. These transitions are often accompanied by significant volumetric changes in the material, resulting in a substantial increase in its adsorption capacity. This can be attributed to either an enlargement of the pore size, complete or partial unblocking of the pore, or a combination of both phenomena. Based on the mechanism involved, the transitions of flexible MOFs (see Figure 5-2) can be classified as:[8]

- **Breathing**: is a reversible transition where the different parts of the MOF suffer a displacement or a rotation increasing or decreasing the unit cell of the structure (see Figure 5-2a). Typically, this transition comprises of two phases based on the pore size: a large pore (lp) phase and a narrow pore (np) phase.[9]
- **Swelling**: is very similar to breathing, but without any change in the shape or the space group of the unit cell, showing only an enlargement of the MOF's unit cell (see Figure 5-2b).[10]

- **Gate opening or linker rotation:** is a reversible process where the MOF changes from a phase with no adsorption in the cavity due to the block of the pore by the linkers and another phase where the linkers rotate, unblocking the pore and enabling the entry of guest molecules in it (see Figure 5-2c).[11]

- **Subnetwork displacement**: is a phase transition restricted to systems with more than one individual framework (frameworks not connected to each other). These structures can be three dimensional interpenetrated frameworks or two dimensional interdigitated or stacked frameworks (layers). These individual frameworks do not interact between them with strong chemical bonds (covalent or ionic) but show weak interactions (Van der Waals interactions). The subnetwork displacement mechanism is different depending on the framework's shape and morphology (see Figure 5-2d):

    - Catenated MOFs: it is very common that some 3D MOF structures present catenation (interpenetrated frameworks). In these cases, the pore of each individual framework is blocked by the neighbour framework. After the application of a stimulus (commonly pressure), the frameworks can be displaced in order to unblock de pore of each individual framework.[12]

    - Interdigitated layer: they are 2D MOFs with perpendicular ligands to the layers. These layers will move horizontally and vertically in order to generate space between them to allow the entry of guest molecules. The perpendicular ligands can interact with the layers, the ligands of the neighbour layers and the guest molecules. On one hand these interactions give robustness to the structure and could favour the adsorption (due to interactions with the guest molecules),[13] but on the other hand they will difficult the movement of the layers (principally the horizontal movement).[8]

    - Stacked layer: this phase transition also occurs in 2D MOFs, with a mechanism similar to the one explained previously. However, in this case, the MOF does not have perpendicular ligands, which facilitates the movement of the layers and the entry of guest molecules.

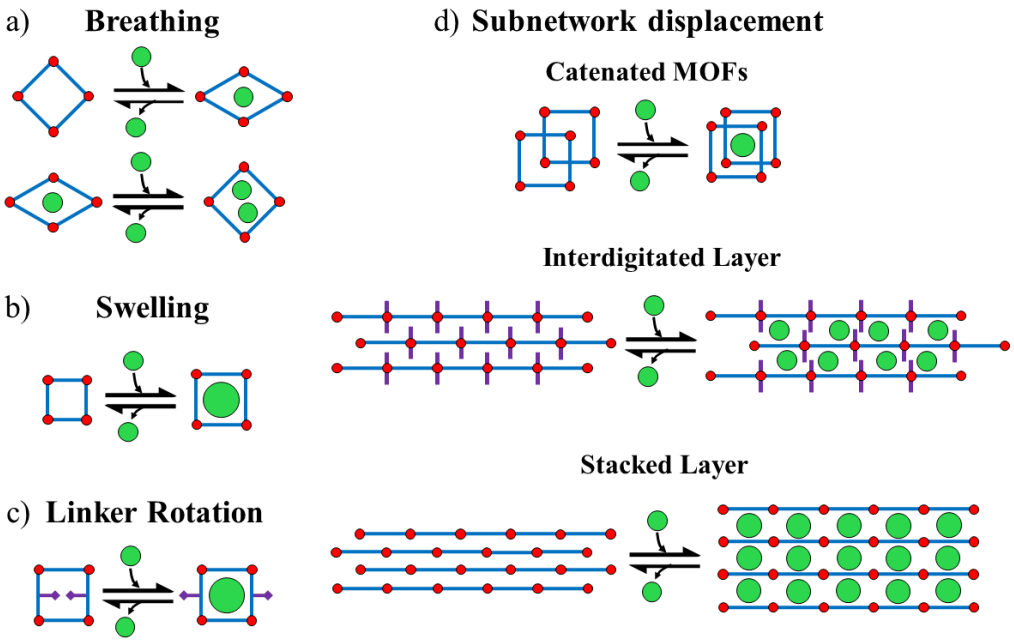

Figure 5-2. Different types of solid-solid phase transition in flexible MOFs depending on the structure: a) breathing, b) swelling, c) linker rotation and d) subnetwork displacement. *Note*: Figure adapted from reference.[8]

Generally, transitions in flexible MOFs typically occur following the application of very low pressures (< 30 bar) of certain gases, with CO_2 being a notable example (among others such as water, methanol, etc.).[5,14] CO_2 adds interest to this mechanism for two reasons. Firstly, it is a gas that is usually associated with high adsorption enthalpies due to the interactions it forms with the adsorbent, such as hydrogen bonding. Secondly, it is one of the most common residual gases, making it cheap, easily obtainable, and allowing for its reuse from other processes instead of releasing it to the atmosphere.

With this in mind, *Chapter 4* focuses on studying the enhancement of barocaloric effects through their combination with other thermal effects, specifically the combination of the barocaloric effect of these MOFs with the thermal response of gas adsorption (as observed in adsorption cooling).

Out of all the transitions and flexible MOFs, this chapter will focus on the MIL-53(Al) ($[Al(OH)(C_8H_4O_4)]$) with a breathing transition as the starting point for this new study based on its extensive literature. This literature provides valuable insights into various aspects such as the adsorption of several gases,[8,15] their adsorption's enthalpy changes (ΔH_{ad}),[2] the required pressure, and all crystallographic phases of the material.[9] However, the thermal response of the MIL-53(Al) breathing process (or any other MOF's transition) has not been previously studied for refrigeration, presenting a potential new application for this well-known MOF.

References

[1] Zhou, J. R. Long, O. M. Yaghi, *Chem. Rev.* **2012**, *112*, 673.

[2] S. Bourrelly, P. L. Llewellyn, C. Serre, F. Millange, T. Loiseau, G. Férey, *J. Am. Chem. Soc.* **2005**, *127*, 13519.

[3] Y. Yang, N. Burke, S. Ali, S. Huang, S. Lim, Y. Zhu, *RSC Adv.* **2017**, *7*, 12629.

[4] M. M. Hu, Z. Zhang, J. D. Atkinson, M. J. Rood, L. Song, Z. Zhang, *Chem. Eng. J.* **2019**, *360*, 89.

[5] J. R. Li, R. J. Kuppler, H. C. Zhou, *Chem. Soc. Rev.* **2009**, *38*, 1477.

[6] U. Mueller, M. Schubert, F. Teich, H. Puetter, K. Schierle-Arndt, J. Pastré, *J. Mater. Chem.* **2006**, *16*, 626.

[7] Q. Yang, V. Guillerm, F. Ragon, A. D. Wiersum, P. L. Llewellyn, C. Zhong, T. Devic, C. Serre, G. Maurin, *Chem. Commun.* **2012**, *48*, 9831.

[8] A. Schneemann, V. Bon, I. Schwedler, I. Senkovska, S. Kaskel, R. A. Fischer, *Chem. Soc. Rev.* **2014**, *43*, 6062.

[9] T. Loiseau, C. Serre, C. Huguenard, G. Fink, F. Taulelle, M. Henry, T. Bataille, G. Férey, *Chem. - A Eur. J.* **2004**, *10*, 1373.

[10] C. Mellot-Draznieks, C. Serre, S. Surblé, N. Audebrand, G. Férey, *J. Am. Chem. Soc.* **2005**, *127*, 16273.

[11] D. Fairen-Jimenez, S. A. Moggach, M. T. Wharmby, P. A. Wright, S. Parsons, T. Düren, *J. Am. Chem. Soc.* **2011**, *133*, 8900.

[12] P. M. Bhatt, E. Batisai, V. J. Smith, L. J. Barbour, *Chem. Commun.* **2016**, *52*, 11374.

[13] R. Kitaura, K. Seki, G. Akiyama, S. Kitagawa, *Angew. Chemie - Int. Ed.* **2003**, *42*, 428-431.

[14] K. Sumida, D. L. Rogow, J. A. Mason, T. M. McDonald, E. D. Bloch, Z. R. Herm, T. H. Bae, J. R. Long, *Chem. Rev.* **2012**, *112*, 724.

[15] S. Tomar, V. K. Singh, *Mater. Today Proc.* **2021**, *43*, 3291.

5.2. Displaying the 'breathing-caloric' effect: a new alternative based in the combination of barocaloric effect and adsorption cooling in MOFs

Part of this work showed and discussed here has been published in the following article:

J. García-Ben, J. López-Beceiro, R. Artiaga, J. Salgado-Beceiro, I. Delgado-Ferreiro, Y.V. Kolen'ko, S. Castro-García, M.A, Señarís-Rodríguez, M. Sánchez-Andújar, J.M. Bermúdez-García, *Chem. Mater.,* **2022**, *34*(7), 3323.

This work belongs to the Special Issue: *John Goodenough at 100*.

5.2.1. Introduction

The major challenge of barocaloric refrigeration is to find materials that comply with all three main requirements for commercial refrigeration: (i) very large thermal changes, (ii) under low operating pressures (similar to the current cooling systems), and (iii) in a wide operating temperature near room temperature. For example, recently discovered barocaloric organic plastic crystals exhibit unprecedentedly large thermal changes that can be comparable to those observed in commercial refrigerants.[1–3] However, they require very large operating pressures between 1000 and 2500 bar,[1–3] which are still far from the working pressure of conventional systems (p < 150 bar).

As was mentioned in *Chapter 1*, an hybrid organic-inorganic perovskite ([TPrA][Mn(dca)$_3$]) was recently reported as the first barocaloric materials working under 70 bar,[4,5] a pressure much closer to commercial needs. However, this compound exhibit noticeably smaller entropy changes than organic plastic crystals. Moreover, in most of barocaloric materials, the operating temperature range (temperature span) is still limited and should be improved.

In parallel and looking for alternatives to refrigeration based on compression/decompression, porous hybrid materials, specifically MOFs (metal-organic frameworks), have been explored for adsorption-driven heat pumps technologies taking advantage of their remarkable adsorption properties. In this case, and differently from the aforementioned barocaloric materials, the cooling effect is induced by the vaporization enthalpy upon ambient temperature change. Here, the enthalpy change is associated to the thermally induced release of an adsorbate (mainly water, but also other small molecules such as methanol, and/or CO_2) initially present in the cavities of the porous MOFs.[6–10]

Adsorption refrigeration shows remarkable advantages over vapour-compression and barocaloric cooling, such as the possibility of using residual heat as the driving stimuli for operating (instead of pressure), or avoiding the use of moving parts (such as the compressor) and their noise/vibrations, among others.[11] However, it also has important drawbacks, such as relatively low efficiency and complex technological designs that required high vacuum.[11]

Remarkably enough, and according to a very recent publication, porous MOFs with breathing transitions could also be of interest for refrigeration under pressure.[12] Breathing transitions are first-order solid to solid phase transitions that occur between two crystalline phases of MOFs with differences in their pores' size (the lower volume narrow-pore phase, np, and the larger volume large-pore phase, lp) transitions which take place upon uptake/release of gas, depending on the specific MOF.[13,14] This behaviour, resembles to the lungs breathing mechanism, which give rise to the aforementioned name. In view of the large volume changes which are associated to this type of phase transitions, such materials could exhibit potentially interesting pressure-induced thermal changes similar to solid state barocaloric refrigerants as indicated by D. Boldrin.[12]

For the present chapter, and to experimentally study such possibility, the literature on breathing-MOFs have been revised, identifying a material with a breathing transition near room temperature under pressures below 10 bar,[15–18] and which could be an ideal potential candidate to exhibit very large pressure-induced caloric effects for commercial refrigeration applications: the MIL-53(Al) compound.

From the chemical point of view, this compound exhibits the molecular formula Al(OH)[BDC].[G], where BDC = 1,4-benzenedicarboxylate $[C_6H_4(CO_2)_2]^{2-}$ anions; G = different guest molecules which can be adsorbed in the material's cavities, and can range from small gas molecules (H_2, CO_2) to even large dyes (methylene blue).[19,20] Meanwhile, from the structural point of view, the MIL-53(Al) framework topology is formed by unidimensional chains of corner-sharing $Al(BDC)_4(OH)_2$ octahedra linked by BDC ligands, which results in linear lozenge-shaped channels large enough to accommodate the guest molecules (see Figure 5-3).

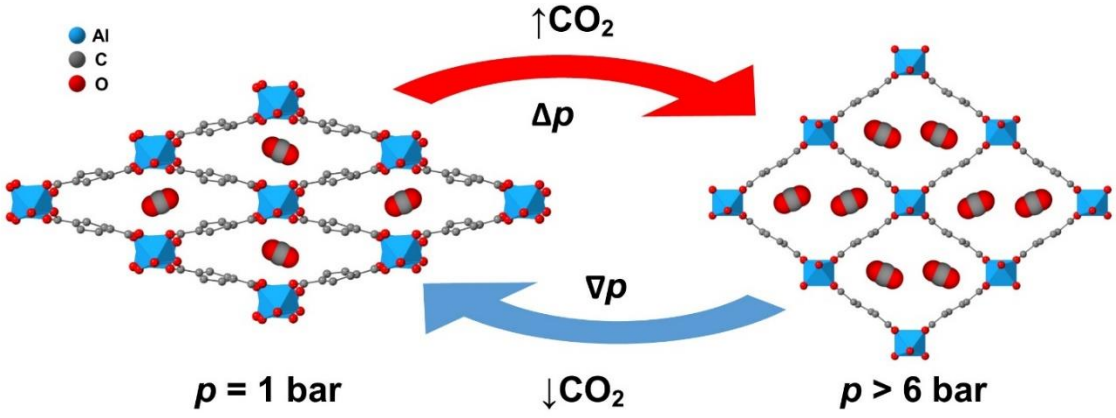

Figure 5-3. Representation of the np-phase (left) and lp-phase (right) of the MIL-53(Al) viewed along the axis of the unidimensional channels under compression and decompression with CO_2.[26] *Note:* CO_2 molecules have been randomly allocated for visualization purposes.

For this study, and in order to induce the breathing transition, CO_2 has been selected as the pressurized gas (see Figure 5-3), which not only induces structural changes from the np- to the lp-phase but also chemically interact with the framework creating/breaking hydrogen bonds upon adsorption/desorption.[17]

In this context, it should also be noted that CO_2 is a common refrigerant whose use is spreading within the commercial refrigeration sector due to its low Global Warming Potential (GWP). Even more, although CO_2 is undoubtedly one of the most well-known greenhouse gases, for the application of refrigeration it can be extracted from residual gases in industrial processes.[21] Additionally, the capture systems for extracting CO_2 from the atmosphere are growing more and more cost-effective.[22] In fact, one of the main strategies to keep CO_2 out of the atmosphere, besides minimizing its production, is to capture and reuse it in long-term industrial applications.[21] Therefore, the use of CO_2 in refrigeration does not contribute to global warming, but rather the opposite: its use in refrigeration would be a carbon neutral process. Moreover, this gas is chemically stable, non-toxic, non-flammable, widely available, and low cost.[23–26]

In the present experimental study, the thermodynamic response of the MIL-53(Al) breathing transition was studied in depth under different external stimuli (temperature and pressure), and its potential for refrigeration applications was analysed. As it will be showed, the obtained results reveal very large caloric effects induced by pressurization/depressurization cycles of CO_2, which are comparable in magnitude, and also in operating pressure and temperature, with commercial gases. These findings provide fundamental basis for an innovative caloric refrigeration mechanism (breathing-caloric effect, as will be properly defined below), and also open the door for future practical implementation of MOFs in new eco-friendly refrigeration technologies.

5.2.2. Experimental

5.2.2.1. Materials and synthesis

Commercially available analytical grade $Al(NO_3)_3.9H_2O$ (>98% ACS Reagent) and terephthalic acid (98% Sigma-Aldrich) were used as purchased without any further purification.

The MIL-53(Al) was synthesized following the literature conditions.[27] Specifically, the synthesis was carried out in a stainless-steel hydrothermal reactor containing a 50mL PTFE vessel. A deionized-water solution of 1.99 g (5.3 mmol) of $Al(NO_3)_3 \cdot 9H_2O$ and 1.38 g (8.3 mmol) of terephthalic acid was placed in the PTFE vessel. The hermetically closed reactor was heated and maintained at 493 K for 4 days. After this time, a white solid precipitate was obtained. This precipitate was filtered, washed with deionized water, and heated at 603 K for 3 days to remove the solvent-guest molecules from the material's cavities, following the reported procedure.[27]

5.2.2.2. Powder X-ray diffraction

The obtained material was characterized by powder X-ray diffraction (PXRD) using a Siemens D-5000 diffractometer with CuKα radiation at room temperature. The obtained patterns were compared with those simulated from reported single-crystal XRD.[27]

5.2.2.3. Fourier transform infrared spectroscopy

The infrared spectra of the solid product were analysed on powdered sample of MIL-53(Al) on a Thermo Scientific Nicolet is10 FT-IR spectrometer, in the range of 500 to 4000 cm^{-1}.

5.2.2.4. Transmission electron microscopy

The size and morphology of the samples was studied by transmission electron microscopy (TEM) using a JEOL 1010 microscope operating at 100 kV. For that purpose, the samples were suspended in isopropanol, and deposited onto copper grids.

5.2.2.5. BET characterization

Nitrogen adsorption/desorption isotherms were carried out using an ASAP 2020 Micromeritics equipment. For the degasification, the sample was dried at 423 K for 24 hours. The nitrogen adsorption/desorption isotherm was measured under nitrogen atmosphere at 77 K.

5.2.2.6. Calorimetry studies

Variable-temperature (VT) and variable-pressure (VP) differential scanning calorimetry (DSC) tests were performed in a TA Instruments pressure-cell mounted on a Q2000 MDSC (modulated differential scanning calorimeter). In a homemade upgrade of the calorimeter (see Figure 5-4), the gas-pressure in the input line is controlled by a Bronkhorst EL-PRESS P-802CV automatic regulator. Meanwhile, a Bronkhorst EL-FLOW Select F-201CV flux controller is placed at the output line.

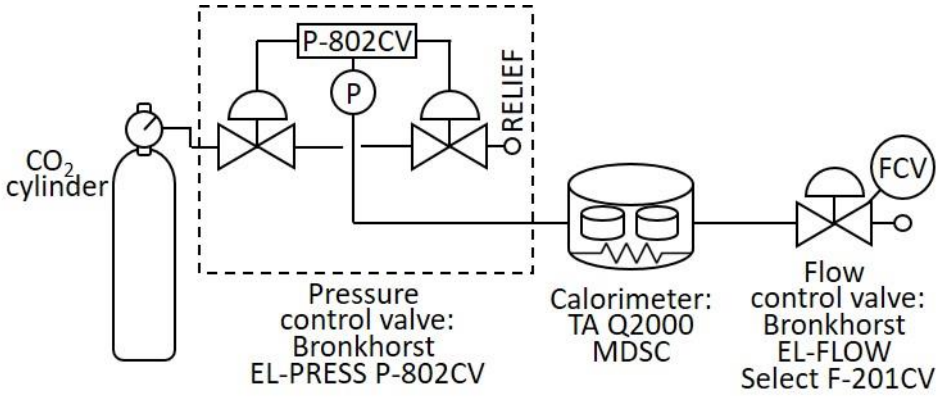

Figure 5-4. Scheme of the Q2000 MDSC customized with Bronkhorst EL-PRESS P-802CV pressure controller and Bronkhorst EL-FLOW Select F-201CV flow regulator, in the inlet and outlet, respectively.

Variable-temperature measurements were done only upon heating at 10 K min^{-1} between 310 K and 405 K at different constant pressures (1-5 bar). The absence of a cold source coupled with the pressure-cell hinder a controlled cooling ramp, and the quantitatively calorimetric analysis on cooling. Variable-pressure (VP) measurements were done under pressurization/depressurization ramps of CO_2 at different rates (0.6-1.6 bar min^{-1}) and different constant temperatures (298-333 K) and maintaining a constant flux of 50 ml min^{-1}. All the experiments were performed on a ~5 mg sample, previously dried inside the equipment under CO_2 at 473 K for 10 minutes. Baseline, enthalpy and temperature were calibrated according to manufacturer recommendations at 10 bar. The baseline of VT-DSC curves was corrected using a sapphire standard provided by the manufacturer in the experimental range. At the same time, the small effect of pressure on the temperature and enthalpy calibration was verified with Indium melting in the experimental range. The variation observed was, in all cases, less than 0.2 K and less than 1% of enthalpy (see Figure 5-5). In the case of VP-DSC experiments, the baseline was corrected by subtracting the calorimetric curves obtained by empty pans under CO_2 pressurization and depressurization in the experimental range. It should be also noted that before performing any DSC measurement on MIL-53(Al), any possible adsorbed moisture water was removed by drying the sample at 423 K in CO_2 atmosphere at ambient pressure (~1 bar).

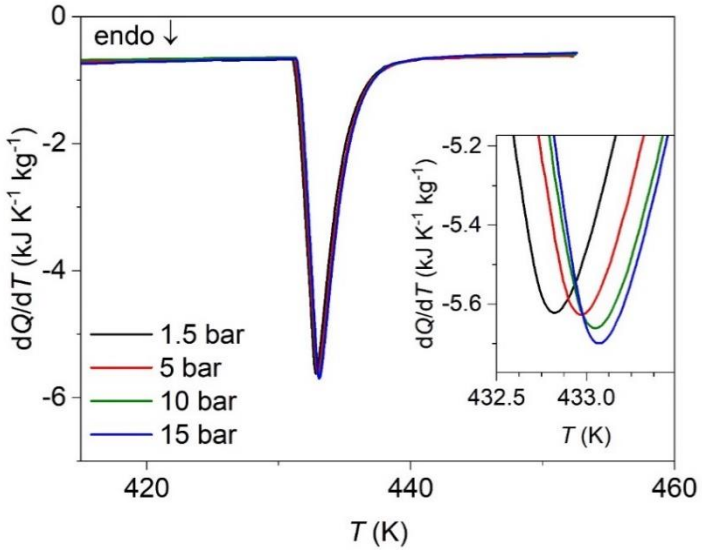

Figure 5-5. DSC curves of the Indium melting transition at different pressures for pressure calibration purposes following the manufacturer recommendations. *Inset*: zoom-in of the maximum of the peaks.

5.2.2.7. Thermal analysis

Thermogravimetric analysis (TGA) was carried out using TGA-DTA thermal analysis SDT2960 equipment. The experiment was set up with 5 mg of the prepared powder sample with a ramp of 10 K min^{-1} from 300 K to 1200 K, using an alumina crucible, and under a 100 mL min^{-1} flow of dry nitrogen.

5.2.3. Results and discussion

5.2.3.1. Basic characterization of the MIL-53 material

The purity of the prepared material has been confirmed by powder X-ray diffraction and FT-IR spectroscopy (see Figure 5-6 and Figure 5-7). The slight discrepancy in the intensity of some peaks of the experimental PXRD pattern compared to that simulated from reported single crystal XRD can be attributed to preferred orientations in the sample favoured by the shape of the particles, rhomboid platelets with a size of 1.1 μm and a dispersion of ±0.4 μm according to TEM (see Figure 5-8).

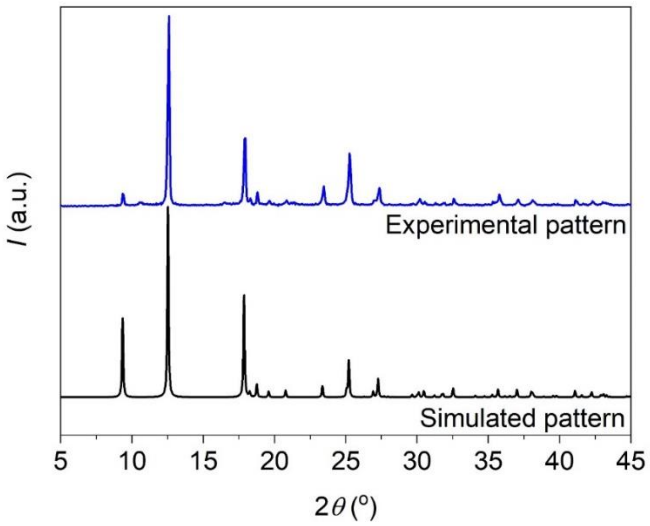

Figure 5-6. PXRD pattern at ambient conditions of temperature and pressure for the MIL-53(Al) compared with that simulated from reported single crystal XRD data.[27]

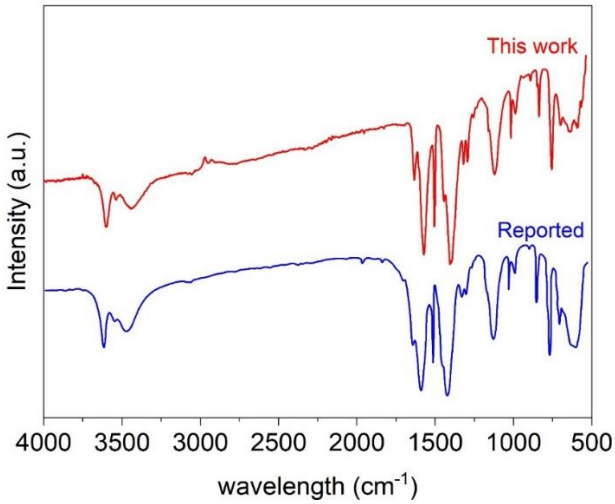

Figure 5-7. FT-IR spectra of the MIL-53(Al) sample synthesized in this work compared with the spectra reported in the literature under the same conditions.[27]

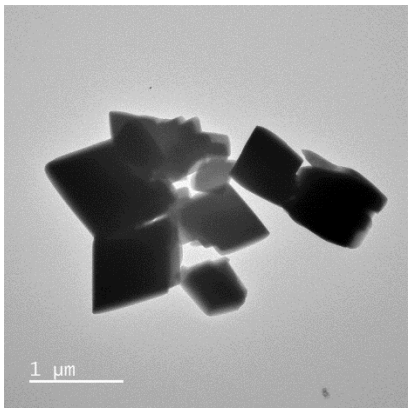

Figure 5-8. TEM micrograph showing the morphology of the MIL-53(Al) sample.

In addition, according to TGA data (see Figure 5-9) the obtained sample captures water from the environment (~8% in weight), that is eliminated when heating it above 373 K. As for the porosity of the obtained material, according to BET analysis it shows a surface area of ~1400 m^2 g^{-1} (see Figure 5-10), which is in good agreement with the literature considering the reported porosity dispersion depending on the sample (see comparison of this experimental data with those reported in Figure 5-10).[28,29]

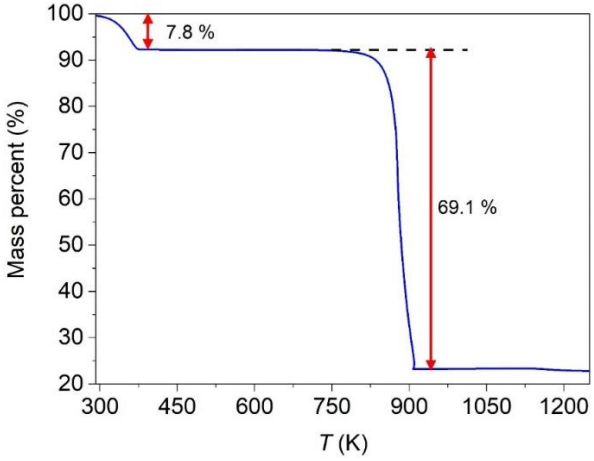

Figure 5-9. TGA water desorption and decomposition curve for the MIL-53(Al) sample under nitrogen atmosphere.

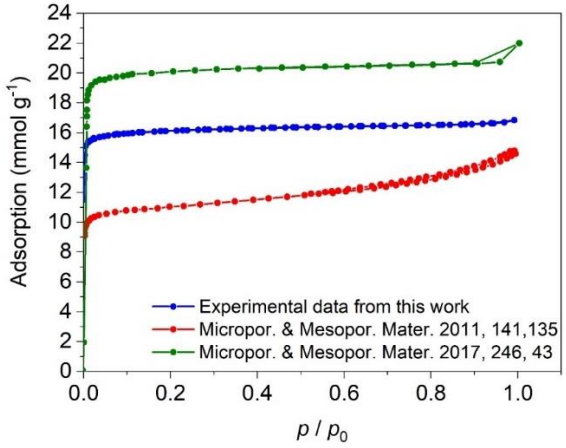

Figure 5-10. N_2-BET adsorption/desorption isotherms at 77 K.

5.2.3.2. Thermodynamic response of the breathing transition under different external stimuli: temperature and pressure.

To deepen into the thermodynamic response of the MIL-53(Al) breathing transition and explore its potential for refrigeration, the response of this material was studied under different external stimuli (such as temperature and isostatic pressure) under CO_2 atmosphere by VP-DSC.

In all those experiments, the starting conditions were room temperature and 1 bar of CO_2, under which the MIL-53(Al) material is in the np-phase with several CO_2 molecules inside the cavities.[15,16] Therefore, the applied external stimuli (temperature and/or pressure) will provoke a reversible breathing transition between np- and lp-phase (see Figure 5-3).

a) Temperature influence under different isobaric conditions

For studying the influence of temperature on the breathing transition, variable-temperature (VT) DSC studies were performed under different CO_2 isobaric conditions (p = [1.5-5] bar). Figure 5-11 shows the obtained DSC curves, which reveal the endothermic peak associated to the first-order transition from the np-phase to the lp-phase at different pressures. Very interestingly, and as it can be seen there, the transition temperature markedly shifts towards higher temperatures as the CO_2 pressure increases. Actually, such displacement is as large as dT_t/dp ~7.5 K bar-1 for $p <$ 3 bar and 3.3 K bar^{-1} for p > 3 bar (see Figure 5-11 left inset), a value that is two orders of magnitude larger than in any reported barocaloric material.[30]

On the other hand, the latent heat associated to the breathing transition is seen to largely decrease for CO_2 pressures above 3 bar, almost disappearing at 5 bar (see Figure 5-11 right inset). According to the literature, such latent heat consists of two major contributions, one associated with the CO_2 adsorption and another with lattice effects.[15–18] Both effects occur at the same time, therefore, it is challenging to identify the thermal changes of each individual process.

In this context, molecular dynamics simulations indicate that the lattice effect from np-phase to lp-phase is endothermic with an enthalpy change value of ΔH ~43 kJ kg^{-1}.[17] Therefore, for $p < 3$ bar, it can assume that the main contribution of the here observed thermally-induced phase transition corresponds to the structural transition from np-phase to lp-phase alone (lattice effect). To rationalize the results observed at higher pressures, where the value of ΔH decreases sharply, CO_2 adsorption (exothermic process) is suggested that will be favoured in this interval.

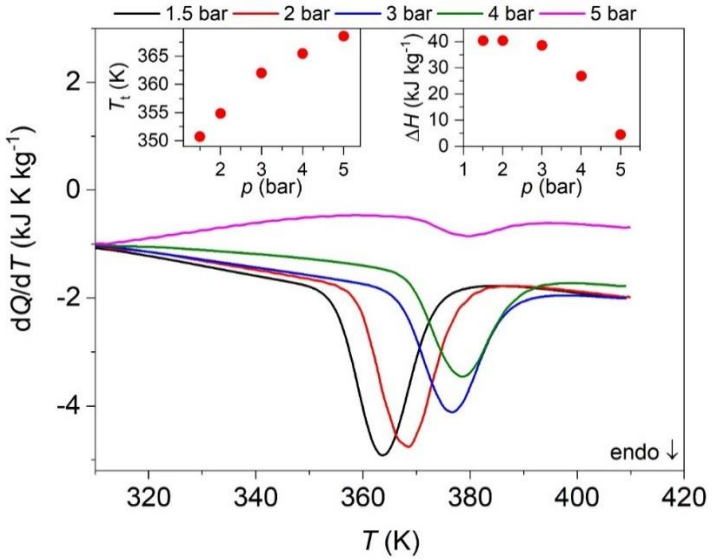

Figure 5-11. VT-DSC curve on heating ramps (10 K min^{-1}) under different CO_2 isobaric conditions (p = [1.5-5] bar). *Left inset:* pressure dependence of the transition temperature. *Right inset:* pressure dependence of the latent heat.

In any case, the transition temperature is undoubtedly related to the structural transition between the np-phase and the lp-phase. Actually, these data help completing the *p*-*T* phase diagram previously reported in the literature[15] as shown in Figure 5-12, where the simulated profile previously calculated from adsorption isotherms data, together with a few previous experimental points in the low temperature region, is now completed in the high temperature range by the here obtained data (blue points).

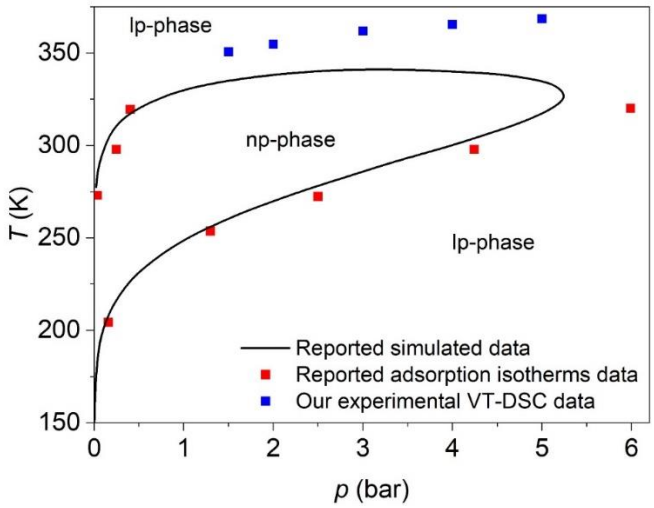

Figure 5-12. Pressure-temperature phase diagram of MIL-53(Al) under CO_2 atmosphere, where the solid black line presents the reported simulated profile calculated by adsorption isotherms data, the red points indicate the reported experimental points obtained by adsorption isotherms, both taken from reference,[15] and the blue points represent the experimental data obtained by VT-DSC in the present work.

b) Pressure influence under different isothermal conditions

To study the influence of pressure on the breathing transition, variable-pressure VP-DSC analysis was carried out under different isothermal conditions. These studies are very useful to better characterize the potential refrigeration capability of a material, given that traditional cooling devices operate under pressurization/depressurization cycles. However, due to the complexity of such experiments and the specific equipment required they remain very scarce in the literature.

For this purpose, a point-by-point pressure adsorption calorimetric analysis[31] was first performed increasing the CO_2 pressure in steps of 0.5 bar from 1.5 to 16 bar under isothermal conditions at ~300 K, and registering the heat flow (see Figure 5-13). As shown there, each step of pressure increase generates a sharp, lambda shape peak with a small narrow width of ~2 minutes at the base, where the enthalpy change is directly related to the area under the peaks.

As for the origin of the changes in enthalpy upon compression, in view of their endothermic nature in all cases it can conclude that CO_2 adsorption is the prevalent contribution in the observed behaviour. On this basis and taking into account the variation of ΔH upon compression for the different pressures values, the observed behaviour can be rationalized as: From ambient pressure up to 5.5 bar, ΔH decreases upon pressurization (from 3.6 kJ kg^{-1} at 1.5 bar down to 1.4 kJ kg^{-1} at 5.5 bar) due to the progressive saturation of the MIL-53(Al) pores in the np-phase. Second, when increasing the CO_2 pressure from 5.5 bar up to 7.5 bar, the structural transition from np-phase to the lp-phase takes place (breathing transition). This provokes an increase of the ΔH value (with a maximum of ΔH ~16.5 kJ kg^{-1} at 7.5 bar), which can be related to the enhanced adsorption capacity of the induced lp-phase. And third, from 7.5 up to 16 bar, the value of ΔH keep decreasing due to a further saturation of the lp-phase pores. It should be noted that the here reported experimental data are fully in agreement with the experimental and theoretical data reported in the literature.[15,16,18]

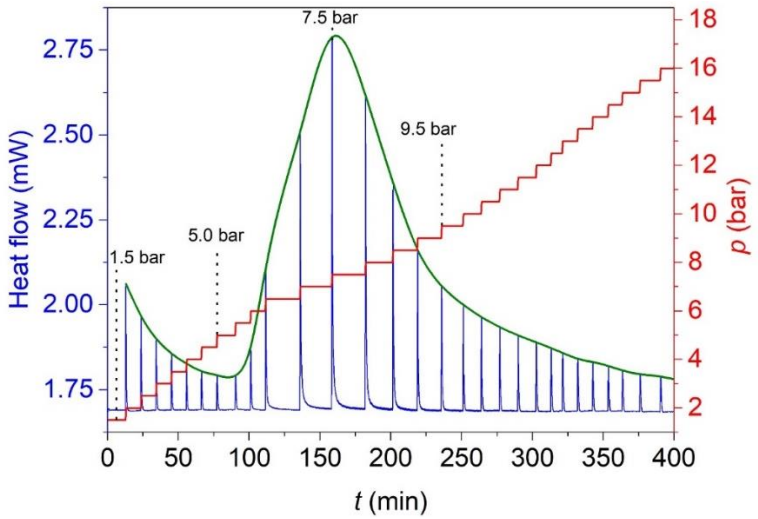

Figure 5-13. Pressure and heat flow signals obtained during CO_2 adsorption on MIL-53(Al) at 300 K using a point-by-point procedure of gas introduction.

From these point-by-point calorimetric data at 300 K (see Figure 5-13), the total enthalpy change of the complete pressurization process (from 1.5 to 16 bar) can be estimated as the sum of the enthalpy change of each one of these steps. The measure shows a value of $\Delta H_{(1.5\rightarrow16\ bar)}$ ~106.8 kJ kg^{-1}, and this would be the maximum ΔH value at p ~16 bar allowing the material to reach the thermodynamic equilibrium over a time of 400 minutes.

However, for practical applications the compression cycle must be much faster. For that reason, continuous isothermal calorimetry experiments on pressurization and depressurization from 1.5 bar to 16 bar were also carried out at different temperatures, and at different pressurization/depressurization rates. The obtained results indicate that while temperature highly affects the thermal behaviour of the sample (see Figure 5-14), the effect of pressurization rates is almost negligible (see Figure 5-15). Moreover, they also show that the thermal behaviour for a given temperature is reproducible along time under pressurization cycles maintaining quasi-isothermal conditions (see Figure 5-16). It should be noted that all experiments have been performed on the same sample, which has maintained its stability and thermal behaviour.

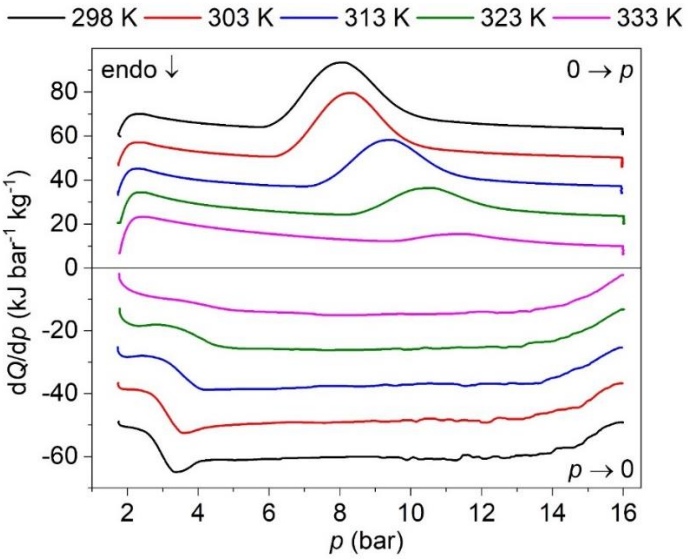

Figure 5-14. Heat flow dQ/dp on cycles of applying (0 → p) and removing (p → 0) CO_2-pressure at different temperatures (from 298 K to 333 K) at the same rate of dp/dt ~1.6 bar min^{-1}. *Note:* curves have been vertically shifted for facilitating visualization.

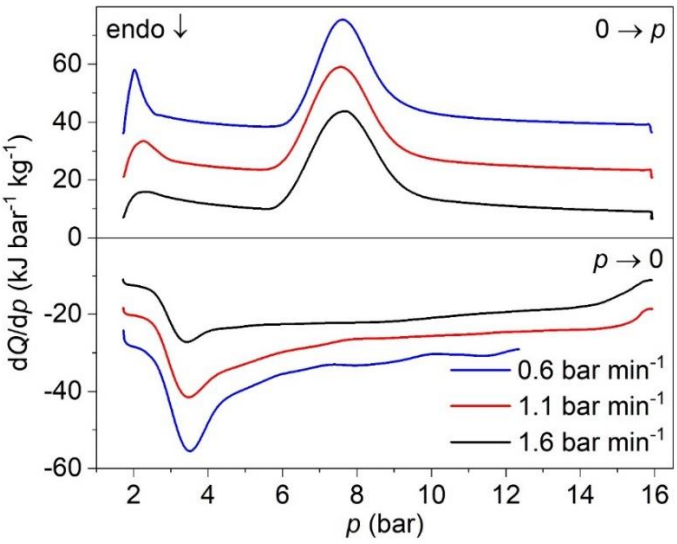

Figure 5-15. Heat flow dQ/dp on cycles of applying (0 → p) and removing (p → 0) CO_2-pressure at different dp/dt rates (from 0.6 bar min^{-1} to 1.6 bar min^{-1}) at the same temperature, T = 298 K. *Note:* curves have been vertically shifted for facilitating visualization.

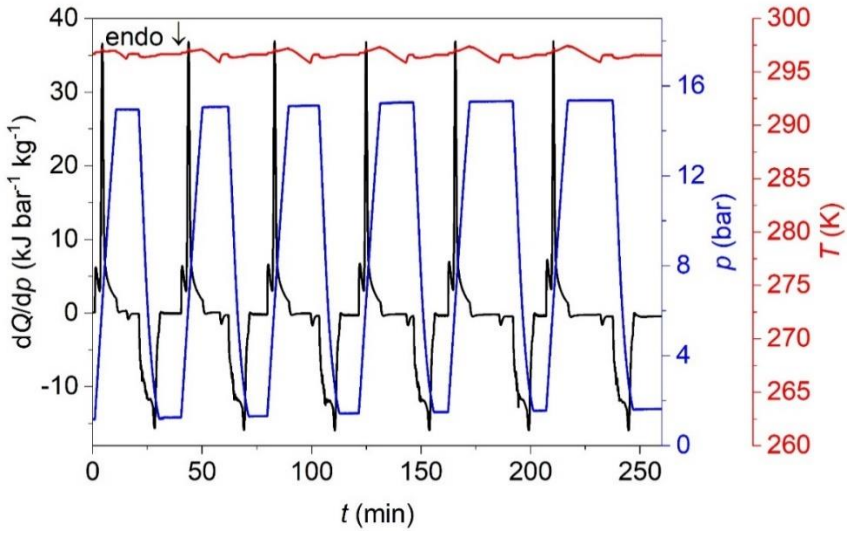

Figure 5-16. Heat flow on 6 cycles of applying (0 → p) and removing (p → 0) CO_2-pressure under quasi-isothermal conditions at 298 K and at a rate of dp/dt ~1.6 bar min^{-1}. *Note:* there is a noticeable change of temperature on the isobaric region due to the equipment temperature stabilization when stopping the pressure increase. This change is reflected in a small endothermic peak on the heat flow curve in the isobaric region that falls out (and does not affect to) the pressure-induced breathing-caloric effect region.

Moreover, and as shown in Figure 5-14 and Figure 5-15, in these experiments the MIL-53(Al) is seen to exhibit two exothermic peaks on pressurization. At room temperature (T ~298 K), the first peak appears at 2.2 bar with an enthalpy change of ΔH ~10.9 kJ kg^{-1}, whose position is independent from temperature, and it is reversible on depressurization without showing any hysteresis. This peak can be related to the CO_2 adsorption/desorption in the np-phase, which accordingly to reported isotherms occur at such pressure without any pressurization/depressurization hysteresis.[15]

Meanwhile, a second exothermic peak appears at 8.1 bar upon pressurization at room temperature (T ~298 K) with a value of ΔH ~81.8 kJ kg^{-1}, and it is reversible with a pressure hysteresis of 4.5 bar^{-1}. This pressure hysteresis remains constant upon the application of several cycles (see Figure 5-16), and is in agreement with the hysteresis observed in the reported CO_2 BET curves for the breathing transition.[15] Even more remarkably, this hysteresis is noticeably lower than in hybrid barocaloric materials, where the hysteresis for the pressure-induced structural transition can reach values of up-to 380 bar.[32]

Furthermore, this second peak gets shifted towards higher pressures when increasing the temperature up to T ~333 K, at the expense of progressively reducing its enthalpy change. In that regard, this peak can be related to the CO_2 adsorption/desorption arising from the breathing transition between the np-phase and the lp-phase, where the large increase of CO_2 uptake capacity of the lp-phase provokes this broad and large peak.[15] Therefore, it can be concluded that the breathing transition is responsible for the large thermal transition occurring at p ~8.1 bar. In this latter thermal transition, and as previously discussed, two thermal processes coexist which are opposite in sign, namely the CO_2 adsorption/desorption and the solid-solid structural transition. In turn, since the resulting peak is exothermic on pressurization, the CO_2 adsorption should be the dominant contribution. However, it would not happen without the presence of the structural transition, which upon occurring suddenly increases the adsorption capacity of the material.

On the other hand, considering the whole CO_2 pressurization on to MIL-53(Al) from 1.5 to 16 bar, the total enthalpy change reaches a value of ΔH ~92.7 kJ kg^{-1}, which is consistent with the total enthalpy change obtained from the point-by-point calorimetric experiments described in the previous section (ΔH ~106.8 kJ kg^{-1}), even if is slightly lower because here the pressure is applied at a faster rate without giving enough time for complete thermodynamic equilibrium. In any case the fact that most of ΔH is achieved, even under short cycle times, is a very favourable result, especially for practical applications.

5.2.3.3. Analysis of breathing-caloric effects for potential refrigeration applications

The breathing transition of MIL-53(Al) has been previously explored for gas storage[13] and mechanical energy storage[33,34] applications, among others. However, this is the first time that the breathing mechanism is experimentally studied for caloric cooling and/or heating effects, in turn differ from the well-stablished magneto-, electro-, elasto- and barocaloric effects.[35]

Actually, the here observed pressure-induced caloric effects show more resemblances with barocaloric effects than with the others since in both a pressurizing fluid applies an isostatic pressure (as external stimulus) to the material that induces structural transitions and large thermal changes. However, there are also important differences that make necessary to coin a new term for the caloric effects observed in these breathing transitions as: (i) the pressurizing fluid in barocalorics does not chemically interact with them, while the pressurizing gas gets adsorbed in MOF's cavities during the breathing transitions creating new chemical bonds; (ii) the pressurizing fluid in barocalorics always favours the lower volume phase, while the pressurizing gas generally favours the larger volume phase (lp-phase) in breathing MOFs; and (iii) the barocaloric effects arise only from the crystalline structural changes, while the caloric effects in breathing MOFs arise from a combination of crystalline structural changes and CO_2 adsorption.

Therefore, and since all these singularities have their origin in the breathing nature of the solid-solid phase transition, it is introduced the term 'breathing-caloric' to refer to this noticeably different solid-state caloric effect.

In this context, to analyse the breathing-caloric effects for potential refrigeration applications, the caloric effect was calculated in terms of isothermal entropy change, which exhibits very large (colossal) values of up to ΔS ~311.0 J K^{-1} kg^{-1} at 298 K. This pressure-induced breathing-caloric effect is very superior to most of pressure-induced barocaloric effects reported in the literature.[4,12,30,35–41] And even more remarkably, the breathing-caloric effect is fully reversible

under the application of very low pressures (p = 16 bar,) in contrast to the p > 1000 bar required for most barocalorics.[12,30,35,37–40] Accordingly, the caloric strength of the material, defined as the isothermal entropy change per unit of pressure, $\Delta S/\Delta p$ ~19.4 x 10^3 J K^{-1} kg^{-1} $kbar^{-1}$, is the largest strength reported up to date (see below).

Also, these studies reveal that the operating temperature range (T_{span}) extends from 333 K down to (at least) 298 K (detection limit of the equipment used), as observed in Figure 5-14. Interestingly, when decreasing the temperature, the critical pressure for the breathing transition (measured at the maximum of the second peak) decreases from 11.6 bar at 333 K down to 8.1 bar at 298 K, which would imply a lower energy consumption to refrigerate at lower temperatures (see Figure 5-17a). Therefore, the required pressure is in the range of commercial gas refrigerants for vapour-compression technologies (for instance, $p(CO_2)$ ~64 bar and p(R134a) ~6 bar)[42] and is much lower than in the case of traditional solid barocalorics.[4,12,30,35–41] In view of these results, MIL-53(Al) shows a temperature span of, at least, 35 K for p = 16 bar, which widely overpass the span of most barocaloric materials.[4,12,30,35–41]

Furthermore, it was also observed that ΔH and ΔS of the whole process increases when decreasing temperature, from ΔH ~49.9 kJ kg^{-1} and ΔS ~149.8 J K^{-1} kg^{-1} at 333 K (upper limit of the operating range) up to ΔH ~92.7 kJ kg^{-1} ΔS ~311.0 J K^{-1} kg^{-1} at 298 K. These results suggest that the caloric refrigeration of this material will be even larger below room temperature (see Figure 5-17b and 5-17c). In that regard, BET isotherms data suggest that MIL-53(Al) can present breathing mechanisms down to 254 K,[15] which will be the lower limit of the temperature span. Additionally, it is also anticipate that it would be possible to further enhance the caloric response by modulating the particle size, shape and aggregation of the MIL-53(Al) sample, since these factors have been already demonstrated to affect the gas adsorption capacity.[43]

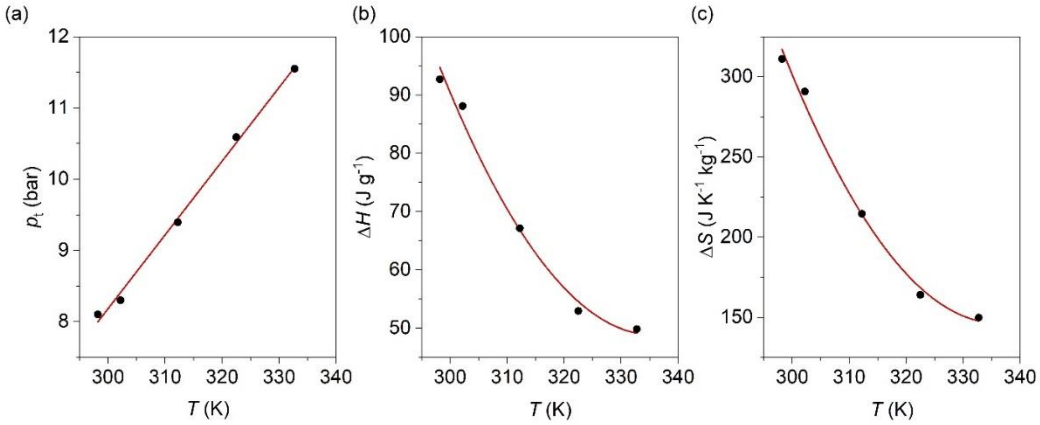

Figure 5-17. a) Variation of transition pressure, p_t, of the breathing transition as a function of operating temperature. b) Variation of ΔH as a function of operating temperature. c) Variation of ΔS as a function of operating temperature. *Note:* data represented from the pressurization curves.

In the following paragraphs, the performance of the here reported breathing-caloric effect of MIL-53(Al) is compared with that of selected barocalorics and of very well-known gas refrigerants: the F-gas R-134a and stand-alone CO_2.[42] Figure 5-18 shows the Ashby plot of isothermal entropy change (ΔS) as a function of the required working pressure (p), and temperature span (T_{span}) of these refrigerants. As it can be observed, the values of ΔS and p for the MIL-53(Al) are very close to the commercial refrigerant gases, while the rest of barocaloric materials are still far away in terms of thermal changes and/or operating pressure. Interestingly, the barocaloric strength ($\Delta S/\Delta p$) of MIL-53(Al) widely overpass that of the best barocaloric materials and it is 200% superior to that of the CO_2 gas refrigerant, which at 298 K shows a value of ΔS ~400 J K^{-1} kg^{-1} and requires p ~64 bar to operate (see Figure 5-19).[42] It should be also noted that at temperatures higher than 298 K, the CO_2 refrigerant needs even higher pressures.

Additionally, the T_{span} of MIL-53(Al) is also superior to that of the best reported barocalorics,[12,30,35,37–40] and perfectly matches with that of low-temperature CO_2 systems.[23–26,42] Therefore, MIL-53(Al) would be an ideal complementary refrigerant that would operate above 298 K requiring lower pressure than stand-alone CO_2. In that way, a combined CO_2/MIL-53(Al) HVAC system could make use of the cooling capacities of both refrigerants expanding the operating temperature range (T_{span}) and reducing the required working pressure.

Overall, the caloric strength of MIL-53(Al) is superior to that of solid barocalorics and CO_2 gas refrigerant. Furthermore, the operating pressure is similar to that of gas refrigerants and significantly lower than that of barocalorics, which offers a wider temperature span in addition to less energy consumption.

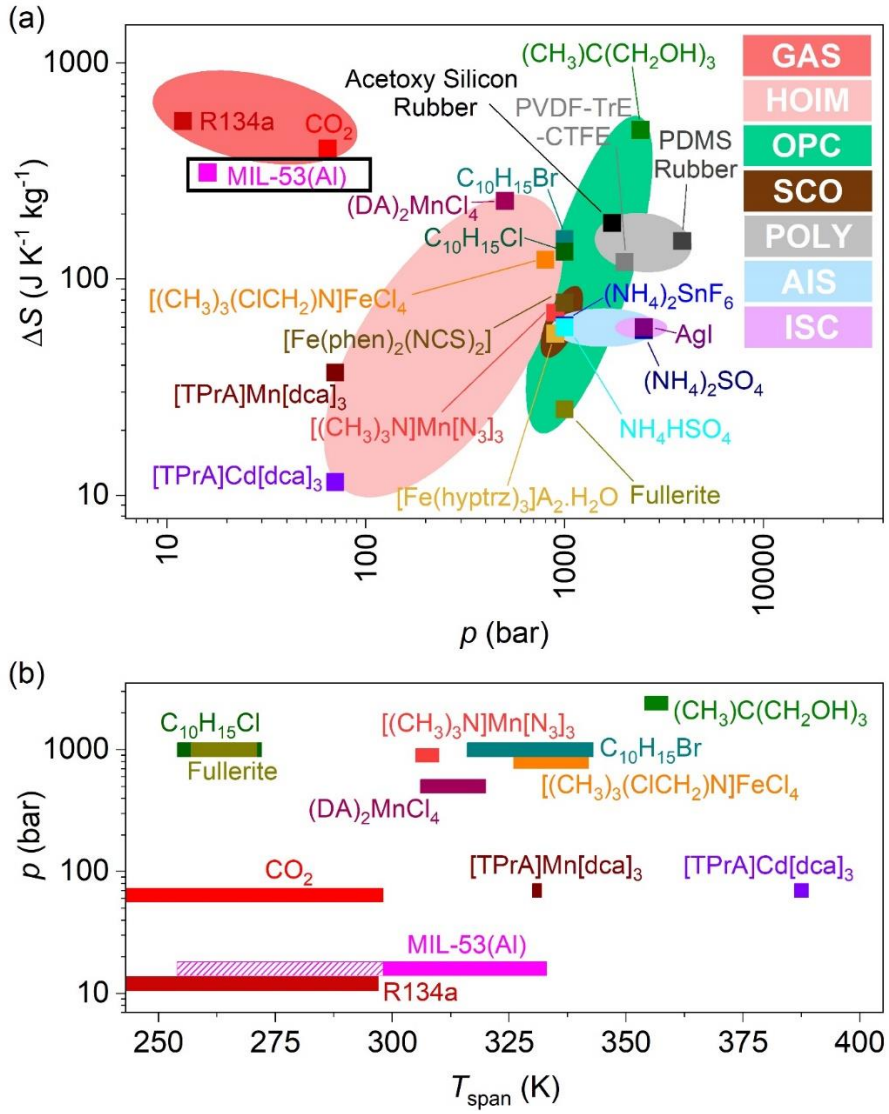

Figure 5-18. a) Ashby plot of ΔS vs. p for MIL-53(Al) and different refrigerants.[4,12,30,35-37,39–42,45] b) Comparison of the operating temperature range (T_{span}) of the best refrigerants selected from a). *Note:* In Figure 5-18a: GAS = gas refrigerants, HOIMs = hybrid organic-inorganic materials, OPC = organic plastic crystals, SCO = spin crossover materials, POLY = polymers, AIS = ammonium inorganic salts, ISC = ionic superconductors. In Figure 5-18b, the pink striped area indicates the T_{span} below RT for MIL-53(Al) estimated from reported BET isotherms.[15]

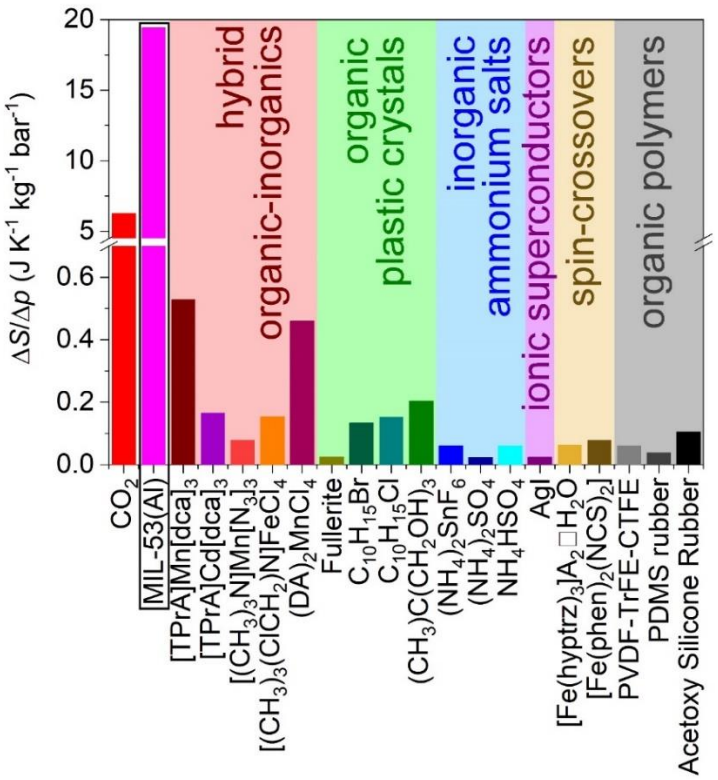

Figure 5-19. Comparison of caloric strength ($\Delta S/\Delta p$) of the MIL-53(Al) hybrid material with that of the CO_2 gas refrigerant and of the best barocaloric materials reported up-to date.

It worth to note that the here reported breathing-caloric effect keeps similarities with three current refrigeration technologies, namely, vapour-compression, barocaloric and adsorption cooling. The breathing-caloric effect is similar to vapour-compression and barocaloric refrigeration in that all of them work under pressurization/depressurization cycles that trigger a phase transition. However, these technologies differ in the origin of the generated thermal changes. In the breathing-caloric effect, the main thermal change is originated from an adsorption process, which keeps resemblance with adsorption cooling technologies. Meanwhile, thermal change of vapour-compression and barocaloric refrigerants is mainly due a volume change associated with a first-order phase transition. In the here shown breathing-caloric material, the thermal change from the structural transition is opposite in sign to the thermal change from the adsorption mechanism, and this latter is responsible for the observed caloric effect. However, this works anticipates that both lattice and adsorption processes can also be additive, enhancing even further the resulting breathing-caloric effect. For example, the phase diagram (Figure 5-12) of MIL-53(Al) shows a phase transition from the lp- to the np-phase below ambient pressure and at room temperature. This phase transition involves a decrease of volume and an adsorption process upon compression from very low pressure and very remarkably, both processes should be additive (both exothermic processes). Unfortunately, the DSC equipment used is not able to perform measurements under low pressure to confirm this hypothesis.

In any case, and very interestingly, the breathing-caloric effect combine the advantages of both barocaloric and adsorption cooling technologies. For example, the thermal changes are as large as in the case of adsorption technologies, but they are fully reversible upon pressurization/depressurization cycles on a solid-state material, without the need of thermal treatments to desorb the adsorbate and regenerate the adsorbent. This is a clear advantage for designing new refrigeration technologies based on pressurization/depressurization cycles making use the breathing transitions, not only in MIL-53(Al) but also in any other material with this type of singular phase transitions.

In that regard, for illustration purposes, Figure 5-20 shows a tentative refrigeration/heating cycle based on the ideal Brayton cycle that is often used to depict caloric effects in solid-state materials.[46] In the case of MIL-53(Al), this cycle would consist of four stages. In the first stage (1→2), there is an adiabatic pressurization of the material using CO_2, where the MIL-53(Al) adsorbs CO2 and increases its temperature. In the second stage (2→3), the MIL-53(Al) is kept under constant pressure (isobaric conditions) and releases heat (Q^-) to the environment (which can be used for heating applications of just discarded as residual heat). In turn, the MOF decreases its temperature. In a third stage (3→4), there is an adiabatic depressurization where the MIL-53(Al) desorbs the previously captured CO_2 molecules and decreases further its temperature. And finally, in the last stage (4→1), the MIL-53(Al) is kept depressurized (isobaric conditions) and it absorbs heat (Q^+) from the surroundings (which could be used to cool down a fridge chamber or a room in the case of an air conditioning system).

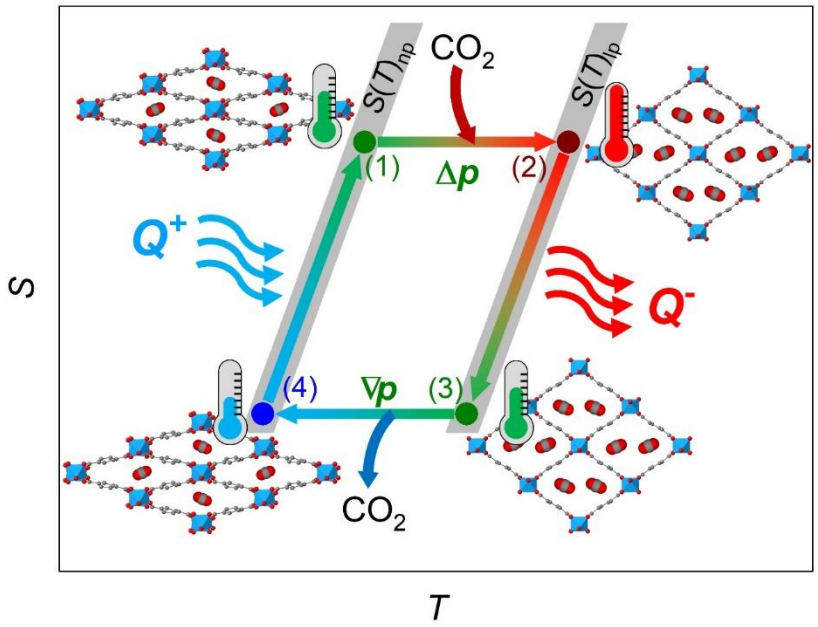

Figure 5-20. Ideal Brayton cycle that illustrates a possible cooling/heating mechanism of the MIL-53(Al) breathing-caloric effect. The cycle consists of four stages: (1→2) temperature increase of the material under adiabatic pressurization, (2→3) heat release (Q^-) under isobaric conditions, (3→4) further temperature decrease of the material under adiabatic depressurization, and (4→1) heat absorption (Q^+) from the surroundings under isobaric conditions. *Note*: the heat released in (2→3) can be used for heating applications or just discarded as residual heat, meanwhile the heat absorbed in (4→1) is useful to cool down a fridge chamber and/or a room in the case of an air conditioning system.

5.2.4. Conclusions

Since its discovery, the MIL-53 family has been subjected to an intensive study due to its enormous structural flexibility during adsorption-desorption of guest molecules, which induces the well-known breathing transition between two phases: the so-called narrow-pore phase and the large-pore phase. Very interestingly, it has experimentally observed that the breathing transition of MIL-53(Al) material exhibits colossal thermal changes of ΔS ~311 J K^{-1} kg^{-1} and ΔH ~93 kJ kg^{-1} at room temperature (298 K) and under only 16 bar of CO_2 gas. Therefore, this material with a breathing transition is very promising for refrigeration applications, owing to its colossal thermal changes, its extremely low operating pressure and its wide temperature span. Moreover, these findings open up a new path towards eco-friendly refrigeration technologies, here coined as 'breathing-caloric'. Very remarkably, this new refrigeration technology combines characteristics of the vapour-compression technology with those of the adsorption and barocaloric technologies. For example, the breathing-caloric technology requires a gas compressor as the

current vapour-compression refrigeration, the thermal changes are mainly due to adsorption-desorption processes as the adsorption cooling technology, and it requires the presence of a solid-solid phase transition as the barocaloric technology. In any case, this innovative breathing-caloric refrigeration mechanism offers very large thermal changes (in the range of vapour-compression and adsorption refrigeration) under compression/decompression cycles (typical of vapour-compression and barocaloric refrigeration). At the same time, this mechanism requires significantly low operating pressures (even lower than vapour-compression and barocaloric refrigeration) and do not require thermal-induced regeneration as typical adsorption materials do. Accordingly, the MIL-53(Al) material exhibits interesting physical-chemical properties very suitable for practical applications in refrigeration. In that regard, it is suggested that the practical implementation of breathing-calorics could be straightforward given that they present engineering requirements similar to existing cooling technologies.

Finally, this chapter anticipates that MIL-53(Al) is not an isolated example, but these breathing-caloric or similar effects will appear in more flexible MOFs and other porous materials with breathing or other similar transitions. It is expected that the here obtained results encourage the search of new materials with breathing-caloric effect. In addition, this new breathing-caloric technology could be added to the list of emerging technologies that aim to achieve a more efficient and eco-friendly refrigeration.

5.2.5. References

[1] B. Li, Y. Kawakita, S. Ohira-Kawamura, T. Sugahara, H. Wang, J. Wang, Y. Chen, S. I. Kawaguchi, S. Kawaguchi, K. Ohara, K. Li, D. Yu, R. Mole, T. Hattori, T. Kikuchi, S. ichiro Yano, Z. Zhang, Z. Zhang, W. Ren, S. Lin, O. Sakata, K. Nakajima, Z. Zhang, *Nature* **2019**, *567*, 506.

[2] P. Lloveras, A. Aznar, M. Barrio, P. Negrier, C. Popescu, A. Planes, L. Mañosa, E. Stern-Taulats, A. Avramenko, N. D. Mathur, X. Moya, J. L. Tamarit, *Nat. Commun.* **2019**, *10*, 1.

[3] A. Aznar, P. Lloveras, M. Barrio, P. Negrier, A. Planes, L. Mañosa, N. Mathur, X. Moya, J. L. Tamarit, *J. Mater. Chem. A* **2020**, *8*, 639.

[4] J. M. Bermúdez-García, M. Sánchez-Andújar, S. Castro-García, J. López-Beceiro, R. Artiaga, M. A. Señarís-Rodríguez, *Nat. Commun.* **2017**, *8*, 15715.

[5] J. García-Ben, L. N. McHugh, T. D. Bennett, J. M. Bermúdez-García, *Coord. Chem. Rev.* **2022**, *455*, 214337.

[6] M. F. De Lange, K. J. F. M. Verouden, T. J. H. Vlugt, J. Gascon, F. Kapteijn, *Chem. Rev.* **2015**, *115*, 12205.

[7] B. B. Saha, K. Uddin, A. Pal, K. Thu, *JMST Adv.* **2019**, *1*, 161.

[8] G. Férey, C. Serre, *Chem. Soc. Rev.* **2009**, *38*, 1380.

[9] S. K. Henninger, H. A. Habib, C. Janiak, *J. Am. Chem. Soc.* **2009**, *131*, 2776.

[10] J. Ehrenmann, S. K. Henninger, C. Janiak, *Eur. J. Inorg. Chem.* **2011**, 471.

[11] H. Demir, M. Mobedi, S. Ülkü, *Renew. Sustain. Energy Rev.* **2008**, *12*, 2381.

[12] D. Boldrin, *Appl. Phys. Lett.* **2021**, *118*(17), 170502.

[13] M. Alhamami, H. Doan, C. H. Cheng, *Materials (Basel)* **2014**, *7*, 3198.

[14] C. R. Murdock, B. C. Hughes, Z. Lu, D. M. Jenkins, *Coord. Chem. Rev.* **2014**, *119*, 258–259.

[15] A. Boutin, F.-X. Coudert, M.-A. Springuel-Huet, A. V Neimark, G. Férey, A. H. Fuchs, *J. Phys. Chem. C* **2010**, *114*, 22237.

[16] N. A. Ramsahye, G. Maurin, S. Bourrelly, P. L. Llewellyn, T. Loiseau, C. Serre, G. Férey, *Chem. Commun.* **2007**, 3261.

[17] E. Stavitski, E. A. Pidko, S. Couck, T. Remy, E. J. M. Hensen, B. M. Weckhuysen, J. Denayer, J. Gascon, F. Kapteijn, *Langmuir* **2011**, *27*, 3970.

[18] S. Bourrelly, P. L. Llewellyn, C. Serre, F. Millange, T. Loiseau, G. Férey, *J. Am. Chem. Soc.* **2005**, *127*, 13519.

[19] A. Schneemann, V. Bon, I. Schwedler, I. Senkovska, S. Kaskel, R. A. Fischer, *Chem. Soc. Rev.* **2014**, *43*, 6062.

[20] S. Tomar, V. K. Singh, *Mater. Today Proc.* **2021**, *43*, 3291.

[21] B. Metz, O. Davidson, H. Coninck, M. Loos, L. Meyer, *Carbon Dioxide Capture and Storage*, Cambridge University Press, **2005**.

[22] D. W. Keith, *Science (80-.).* **2009**, *325*, 1654.

[23] S. Dilshad, A. R. Kalair, N. Khan, *Int. J. Energy Res.* **2020**, *44*, 1408.

[24] E. Bellos, C. Tzivanidis, *Energy Convers. Manag. X* **2019**, *1*, 100002.

[25] P. Bansal, *Appl. Therm. Eng.* **2012**, *41*, 18.

[26] Emerson, *Clim. Technol.* **2015**, *6*, 44.

[27] T. Loiseau, C. Serre, C. Huguenard, G. Fink, F. Taulelle, M. Henry, T. Bataille, G. Férey, *Chem. - A Eur. J.* **2004**, *10*, 1373.

[28] X. D. Do, V. T. Hoang, S. Kaliaguine, *Microporous Mesoporous Mater.* **2011**, *141*, 135.

[29] F. Martínez, G. Orcajo, D. Briones, P. Leo, G. Calleja, *Microporous Mesoporous Mater.* **2017**, *246*, 43.

[30] P. Lloveras, J.-L. Tamarit, *MRS Energy Sustain.* **2021**, *8*, 3.

[31] P. L. Llewellyn, G. Maurin, *Comptes Rendus Chim.* **2005**, *8*, 283.

[32] J. Salgado-Beceiro, A. Nonato, R. X. Silva, A. García-Fernández, M. Sánchez-Andújar, S. Castro-García, E. Stern-Taulats, M. A. Señarís-Rodríguez, X. Moya, J. M. Bermúdez-García, *Mater. Adv.* **2020**, *1*, 3167-3170.

[33] P. G. Yot, L. Vanduyfhuys, E. Alvarez, J. Rodriguez, J. P. Itié, P. Fabry, N. Guillou, T. Devic, I. Beurroies, P. L. Llewellyn, V. Van Speybroeck, C. Serre, G. Maurin, *Chem. Sci.* **2016**, *7*, 446.

[34] J. Rodriguez, I. Beurroies, T. Loiseau, R. Denoyel, P. L. Llewellyn, *Angew. Chemie - Int. Ed.* **2015**, *54*, 4626.

[35] X. Moya, S. Kar-Narayan, N. D. Mathur, *Nat. Mater.* **2014**, *13*, 439.

[36] J. Li, M. Barrio, D. J. Dunstan, R. Dixey, X. Lou, J. L. Tamarit, A. E. Phillips, P. Lloveras, *Adv. Funct. Mater.* **2021**, *31*, 1.

[37] X. Moya, N. D. Mathur, *Science* **2020**, *803*, 797.

[38] L. Mañosa, A. Planes, *Adv. Mater.* **2017**, *29*, 1603607.

[39] C. Cazorla, *Appl. Phys. Rev.* **2019**, *6*(4), 041316.

[40] J. Salgado-Beceiro, J. M. Bermúdez-García, E. Stern-Taulats, J. García-Ben, S. Castro-García, M. Sánchez-Andújar, X. Moya, M. A. Señarís-Rodríguez, *ChemRxiv* **2021**, 17.

[41] J. M. Bermúdez-García, S. Yáñez-Vilar, A. García-Fernández, M. Sánchez-Andújar, S. Castro-García, J. López-Beceiro, R. Artiaga, M. Dilshad, X. Moya, M. A. Señarís-Rodríguez, *J. Mater. Chem. C* **2018**, *6*, 9867.

[42] M. O. McLinden, *Thermophysical Properties of Refrigerants. ASHRAE Handbook: Fundamentals*, ASHRAE, Atlanta, **2021**.

[43] H. Embrechts, H. Embrechts, M. Kriesten, M. Ermer, W. Peukert, W. Peukert, M. Hartmann, M. Hartmann, M. Distaso, M. Distaso, *Cryst. Growth Des.* **2020**, *20*, 3641.

[44] M. M. Vopson, *J. Phys. D. Appl. Phys.* **2013**, *46,* 345304.

Chapter 6

General conclusions

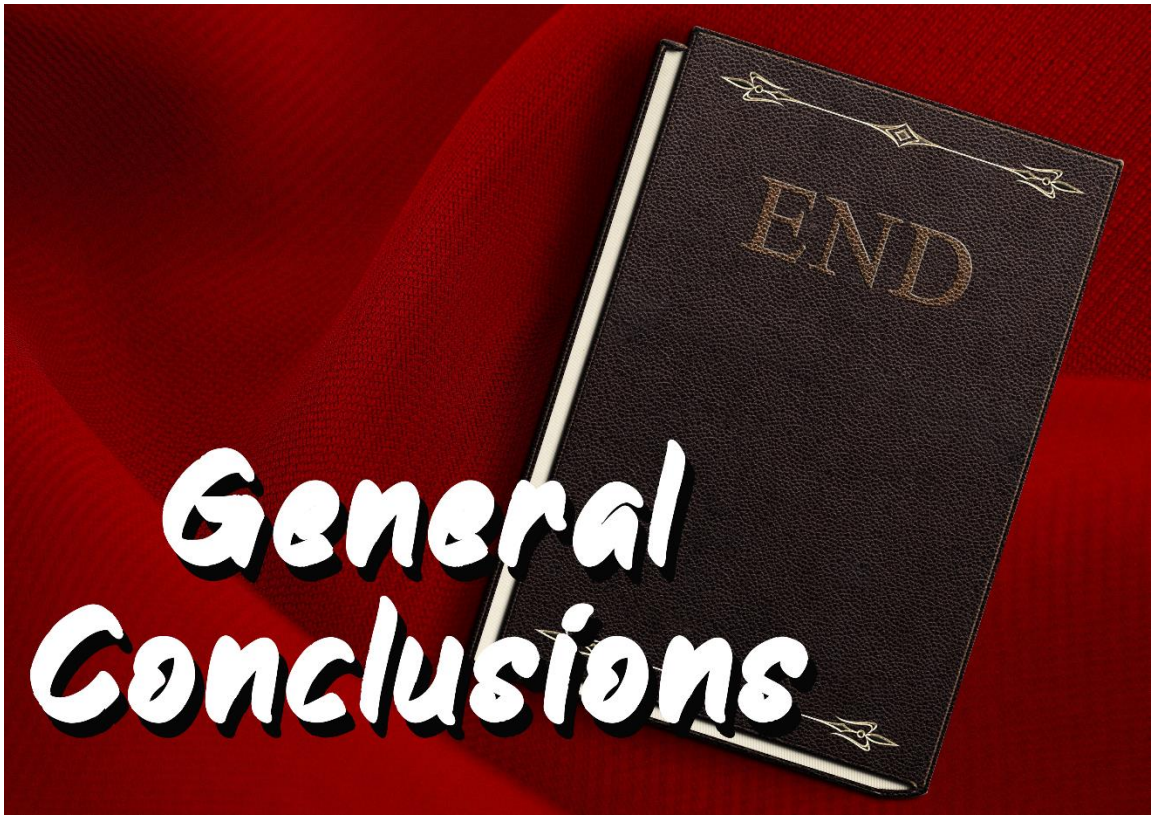

Chapter 6: General Conclusions

This *PhD Thesis* has been focused on the search of hybrid organic-inorganic materials with thermal changes originated from pressure-induced solid-solid phase transitions, as an eco-friendly alternative for active barocaloric refrigeration and/or passive 'cold-storage'. In order to accomplish this, three major families of hybrid materials were thoroughly studied: (i) hybrid dicyanamide perovskites, (ii) hybrid ionic plastic crystals, and (iii) metal-organic frameworks.

In the case of hybrid dicyanamide perovskites, this *PhD Thesis* has identified and explored new tools to help towards the design of future compounds with enhanced barocaloric properties. In that regard, this research has discovered new structural distortions across the solid-solid phase transitions, such as extreme octahedral tilting, cavity sharing of guest cations within consecutive pseudo-cubooctahedral cavities, π···π stacking, among others, which could largely contribute to the thermal changes in the pursue of enhanced barocaloric effects. Furthermore, a more accurate approach for the calculation of the tolerance factor was proposed, which will be a very useful tool to predict the formation of new dicyanamide-based compounds with perovskite-like structure. In addition, this *PhD* work also demonstrates the possibility of tuning the transition temperature of barocaloric dicyanamide-perovskites through the preparation of solid solutions, which will help to adapt these compounds to the desired operating temperature, as well as to modify other functional properties such as dielectric and optical properties.

Regarding hybrid ionic plastic crystals, this research has identified two new families of barocaloric compounds, namely, 'sandwich' type organometallic ionic salts, $[Cp_2M][PF_6]$ (Cp = $C_5H_5^-$, M = Fe^{3+}, Co^{3+}) and the long-chain alkylammonium $[DBA][BF_4]$ (DBA = $(C_4H_9)_2NH_2^+$) compound. The $[Cp_2M][PF_6]$ materials exhibit reasonably large thermal changes ($\Delta S > 30$ J K^{-1} kg^{-1}) that arise from the rotation of the organic Cp rings across, which also exhibit a very large sensitivity towards the pressure according to the very large barocaloric coefficients ($dT/dp = 27.6$ K kbar^{-1} for Fe and 24 K kbar^{-1} for Co). Meanwhile, the $[DBA][BF_4]$ compound has shown large thermal changes below room temperature, covering a wide temperature range suitable for food preservation – an unusual range for solid-state refrigeration. Moreover, this latter compound exhibits a unique behavior that enables its use as a thermomaterial in both passive 'cold-storage' and active barocaloric refrigeration. On one hand, it the thermal storage capacity of commercially available compounds. On the other hand, the material not only demonstrates a remarkable caloric effect ($\Delta S > 200$ J K^{-1} kg^{-1} and $T_{span} > 10$ K) but also achieves it with the application of only 500 bar, significantly reducing the operational pressure compared to other reported plastic crystals. The key to these exhibited properties lies in the two linear dibutyl chains, as their disorder leads to the highly promising solid-solid transition.

Finally, the utilization of a flexible MOF, such as MIL-53(Al), revealed a remarkable phenomenon named as 'breathing-caloric' effect, which was reported for the first time within this *PhD Thesis*. In this case, the effect exhibits thermal changes comparable to some refrigerant gases ($\Delta S > 300$ J K^{-1} kg^{-1}) and can be achieved at low pressures ($p \sim 16$ bar of CO_2), overcoming the major limitations of most barocaloric materials for commercial implementation. These changes result from the combination of the solid-solid structural phase transition and the adsorption of CO_2 gas. This alternative approach holds great promise for new refrigeration technology due to its wide range of working temperatures (both above and below room temperature), low pressures, reduced environmental impact, and simplified systems, overcoming the limitations of vapor compression, barocaloric, and adsorption cooling technologies.

In summary, this *PhD Thesis* offers a significant progress in the field of refrigeration and 'cold-storage'. It has successfully achieved all the proposed objectives, leading to the exploration and reporting of new materials with enormous potential in the refrigeration sector. It should be highlighted that this *PhD Thesis* covers studies of barocaloric effects and cold-storage, as well as shows pioneer studies on the 'breathing-caloric' effects discovered along this research. Therefore, the here presented results will serve the scientific community to keep advancing in the field of solid-state refrigeration towards more efficient, safe and eco-friendly technologies.

Annexes

Spanish summary, crystallographic data, NMR, IP protections, science communications, collaborations and research visits

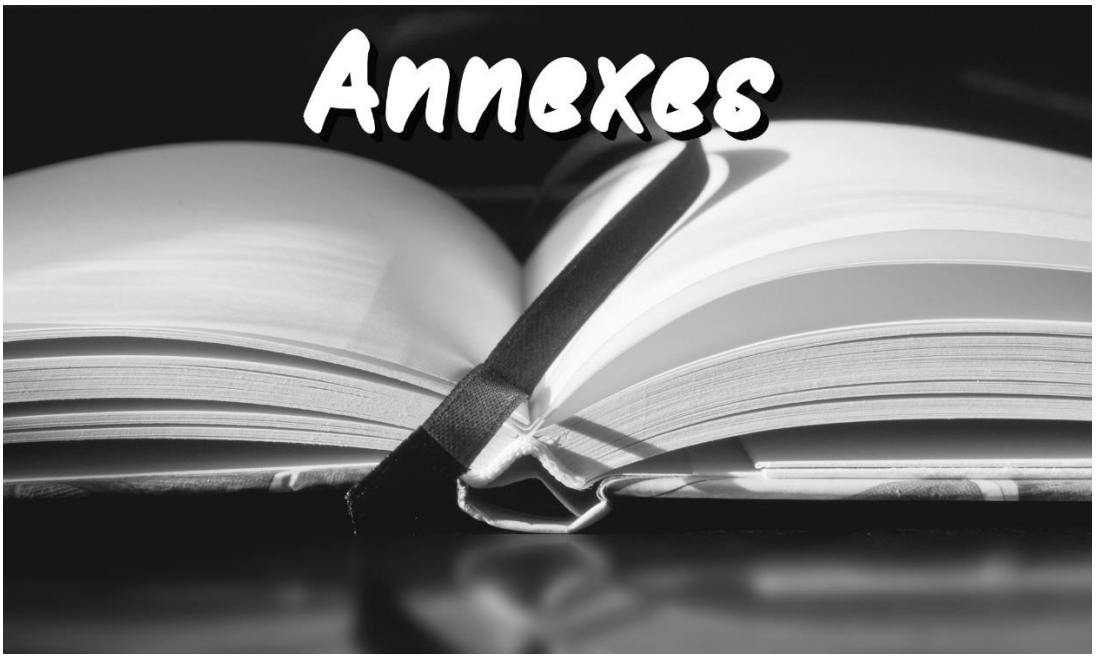

Annex I: Spanish summary

Resumen en español

Nuestra sociedad aún vive una enorme dependencia de las energías no renovables. La creciente demanda de energía y la lenta adaptación del mundo a las alternativas renovables se traducen en el preocupante cambio climático que está experimentando nuestro planeta.

En este contexto, la refrigeración es una de las fuerzas impulsoras de nuestra sociedad, siendo esta uno de los sectores principales que contribuyen a la creciente demanda energética, tanto a nivel doméstico (neveras, congeladores, aires acondicionados, etc.) como a industrial (industria alimentaria, química, médico-farmacéutica, textil, naval, automovilística, ocio, etc.). Pese a esta gran importancia, la refrigeración sigue profundamente arraigada a una tecnología antigua, asociada a una baja eficiencia energética y conectada a problemas relacionados con el clima, como el calentamiento global.

Según la Agencia Internacional de Energía (AIE), las tecnologías de refrigeración (como neveras, congeladores y sistemas de climatización) ya representan más del 20% del consumo energético mundial. Además, se espera que esta enorme demanda aumente en los próximos años debido al alarmante crecimiento del calentamiento global, ya que se estima que la temperatura del planeta se incremente entre 1.5 y 2 °C para el año 2050. Además, las tecnologías de refrigeración son responsables de aproximadamente el 7% de las emisiones totales de gases de efecto invernadero. Estas emisiones se dividen en directas e indirectas. Por un lado, las directas, representan el 2% de las emisiones totales de gases contaminantes y son causadas por fugas de los gases refrigerantes o por el manejo inadecuado de los residuos relacionados con la refrigeración (como dispositivos, refrigerantes, etc). Por otro lado, las emisiones indirectas contribuyen aproximadamente un 5% del total y ocurren debido al consumo de energía de estas tecnologías. Esto finaliza en un ciclo vicioso, ya que el aumento que se espera en el consumo energético dedicado a la refrigeración en las próximas décadas, estará ligado a mayores emisiones de gases de efecto invernadero, resultando en una mayor necesidad de energía dedicada a la refrigeración.

Una alternativa emergente es el uso de termomateriales como refrigerantes. Estos materiales sólidos poseen una transición de fase sólido-sólido reversible que puede ser inducida por un estímulo externo (temperatura, presión, campo eléctrico y/o magnético, etc.). Dentro de esta lista, los materiales barocalóricos son una familia de termomateriales con una amplia proyección para la refrigeración. Estos muestran una transición de una fase sólida a otra fase sólida bajo la aplicación de presión externa.

Durante los últimos años, ha habido dos avances significativos en el campo de los materiales barocalóricos: (i) la reducción drástica de la presión de trabajo desde más de 1000 bar hasta menos de 70 bar observada en perovskitas híbridas de dicianamina, y (ii) el enorme aumento de los efectos barocalóricos desde alrededor de 10 J K^{-1} kg^{-1} hasta más de 250 J K^{-1} kg^{-1} en el caso de los cristales plásticos orgánicos. Sin embargo, estos dos parámetros parecen ser difíciles de combinar, por lo que, el principal desafío de la refrigeración barocalórica es encontrar materiales con transiciones de fase sólido-sólido que puedan mostrar cambios térmicos lo suficientemente grandes con una presión de trabajo aceptable.

Por esa razón, esta *Tesis Doctoral* tiene tres objetivos principales:

(1) **Comprender y optimizar la estructura y las transiciones de fase sólido-sólido en perovskitas híbridas de dicianamina:** Una de las principales limitaciones de las perovskitas híbridas de dicianamina para aplicaciones barocalóricas es que presentan efectos barocalóricos relativamente bajos en términos de cambios de entropía (ΔS = [11.5-40] J K^{-1} kg^{-1}). Para lograr este objetivo, será necesario estudiar a fondo la estructura de las perovskitas híbridas de dicianamina y proporcionar nuevas estrategias químicas para la ingeniería de materiales.

(2) **Explorar nuevas familias orgánicometálicas e híbridas orgánico-inorgánicas con transiciones de cristal plástico para refrigeración barocalórica y 'almacenamiento de frío':** Los cristales plásticos orgánicos son muy conocidos por su capacidad de almacenamiento de energía térmica y, más recientemente, también por presentar efectos barocalóricos colosales. Sin embargo, ambas propiedades térmicas a menudo son mutuamente excluyentes. Además, una de las principales limitaciones de los cristales plásticos orgánicos barocalóricos (principalmente glicoles o derivados de adamantanos) es que operan a temperaturas muy altas (por encima de 310 K) y bajo la aplicación de presiones muy altas (por encima de 1000 bar). Este objetivo busca encontrar nuevas familias de cristales plásticos híbridos iónicos que puedan funcionar a temperaturas más bajas y que puedan reducir la presión de trabajo observada en los cristales plásticos orgánicos.

(3) **Mejorar los efectos barocalóricos mediante la combinación con otros efectos térmicos:** Los materiales barocalóricos en general se postulan como una alternativa prometedora para la refrigeración ecológica. No obstante, en comparación con los gases de refrigeración comerciales, estos materiales barocalóricos aun presentan importantes desventajas como cambios térmicos notablemente más bajos, rangos de temperatura operacionales más reducidos y/o presiones de trabajo más altas. El objetivo principal de este punto es reducir o eliminar estas desventajas mediante la combinación de la tecnología barocalórica y otros efectos térmicos como el usado en la refrigeración por adsorción.

Teniendo en cuenta estos objetivos, esta *Tesis Doctoral* se organiza en los siguientes capítulos:

El **Capítulo 1** ofrece una introducción a los desafíos energéticos, climáticos y socioeconómicos que la refrigeración debe abordar para realizar la transición hacia una tecnología más respetuosa con el medio ambiente y más favorable energéticamente. Se aborda el estado actual de algunas de las tecnologías de refrigeración, tanto activas (compresión de vapor, refrigeración barocalórica y refrigeración por adsorción) como pasivas ('almacenamiento de frío'), centrándose no sólo en el estado del arte, sino también en los problemas y ventajas que acarrean cada una de ellas.

El **Capítulo 2** aborda los objetivos previamente mencionados.

El **Capítulo 3** se centra en el estudio de perovskitas híbridas de dicianamina debido a su enorme potencial en la refrigeración barocalórica por la gran sensibilidad a la presión que han mostrado los termomateriales de esta familia. Las diferentes distorsiones que presentan las estructuras de esta familia son la razón principal de la mayoría de las transiciones sólido-sólido que poseen, por lo que la primera parte de este capítulo trató de recopilar dichas distorsiones en las diferentes estructuras conocidas de estas pervoskitas. Se identificaron, por una parte, las distorsiones ya conocidas en perovskitas inorgánicas clásicas, pero también otras distorsiones típicas solo en las perovskitas híbridas orgánico-inorgánicas (HOIPs). Además, en este apartado se identificaron nuevas distorsiones no reportadas anteriormente en otras HOIPs. Por último, se concluyó que, debido al interés de grandes cambios térmicos para aplicaciones barocalóricas, las distorsiones que se deberían priorizar son: el desorden configuracional, interacciones del catión A con la estructura o con otros cationes A, inclinación extrema de los octaedros o compartición de cavidades.

El siguiente apartado del **Capítulo 3** se enfocó en la búsqueda de herramientas que ayuden al diseño de futuras estructuras de esta familia. Para ello se reanalizó el factor de tolerancia reformulado por Kieslich para pervoskitas híbridas, el cual establece un modo de calcular el volumen que ocupan los cationes orgánicos A en la cavidad de la estructura que se ajusta muy bien para cationes pequeños como los tetrametilamonios, pero con cationes más voluminosos, como los usados en perovskitas híbridas de dicianamina, sobreestima el volumen real del catión. Debido a esto, en este apartado propuso una nueva forma de calcular dichos volúmenes, usando la densidad electrónica isosuperficial de "promolécula". Con esta nueva alternativa y teniendo en cuenta la globularidad, se consiguieron recalcular los volúmenes de dichos cationes los cuales se

ajustaron mucho mejor, obteniendo valores de factor de tolerancia dentro del rango esperable. De esta forma, se confirmó la veracidad de este nuevo ajuste en todas las perovskitas híbridas de dicianamina, y se verificó su efectividad seleccionando cinco nuevos cationes A para formar nuevas estructuras tipo perovskita con aniones dicianamina y cationes manganeso. Estos cationes A se distribuyen en: dos cationes demasiados pequeños para formar la estructura deseada, dos con tamaño adecuado y uno demasiado grande. Tal como predijo la nueva aproximación, los dos pequeños y el catión grande no formaron la estructura deseada, mientras que los cationes con el tamaño adecuado sí. Por consiguiente, esta revisión del factor de tolerancia es una poderosa herramienta que ayudará a diseñar nuevas estructuras de esta prometedora familia de materiales.

El último apartado del **Capítulo 3** se centró en el último punto a tratar para el entendimiento y optimización de las perovskitas de dicianamina: la capacidad de modulación de sus propiedades. Para ello se preparó la primera disolución sólida de esta pequeña familia, variando en proporciones iguales los cationes B de una misma estructura ([TPrA][M(dca)$_3$] dónde TPrA = tetrapropilamonio y M = Co, Ni). Los resultados fueron positivos, siendo capaces de modificar la temperatura de transición además de otras propiedades funcionales como dieléctricas y ópticas. De esta forma se cumplió el primer objetivo de esta tesis, tras estudiar a fondo la estructura y distorsiones de esta familia y conseguir nuevas herramientas para diseñar y modular sus propiedades con el fin de optimizar la estructura y las transiciones de fase.

Los cristales plásticos son materiales bien conocidos que han sido estudiados en el campo barocalórico mostrando en general grandes cambios térmicos. Desgraciadamente, estos termomateriales necesitan presiones de trabajo demasiado elevadas para mostrar dichos cambios térmicos. Debido a esto, el **Capítulo 4** estudió tres cristales plásticos híbridos con el fin de buscar posibles nuevos refrigerantes sólidos con cambios térmicos similares a los cristales plásticos ya conocidos, pero con menor presión de trabajo. Por una parte, se analizó la respuesta barocalórica de dos sales iónicas organometálicas tipo sándwich ([Cp$_2$M][PF$_6$] dónde M = Fe, Co). Estos compuestos se caracterizan por tener un catión tipo 'sandwich', los cuales poseen dos anillos aromáticos alrededor del metal que presentan gran movilidad lo que los hace interesantes para estudiar su respuesta frente a la presión. Las medidas mostraron una alta sensibilidad de las transiciones de estos materiales frente a la presión, obteniendo resultados muy prometedores pese al pequeño cambio térmico mostrado en comparación a otros cristales plásticos. Estos estudios barocalóricos han sido los primeros que se han realizado en especies organometálicas con esta disposición tipo 'sandwich', y los resultados obtenidos fueron tan positivos que podrían promocionar el futuro estudio de materiales de la misma familia o similares en el campo barocalórico.

Además, el siguiente apartado del **Capítulo 4**, examinó un material prometedor ([DBA][BF$_4$] donde DBA = dibutilamonio) para su uso en refrigeración pasiva de 'almacenamiento de frío' y barocalórica. Este material está formado por un catión orgánico, un amonio, el cual presenta dos cadenas lineares alquílicas, y un anión inorgánico clásico, el tetrafluoroborato. El [DBA][BF$_4$] mostró un gran potencial para la refrigeración pasiva, pese a poseer transiciones sólido-sólido en lugar de sólido-líquido, igualando o incluso superando la capacidad de almacenamiento de energía térmica de compuestos comerciales. Además, los resultados barocalóricos fueron excepcionales, presentando un enorme cambio térmico con una gigantesca sensibilidad frente a la presión. Tanto es así, que con solo la aplicación de 500 bar ya se conseguían unos resultados excelentes (ΔS > 200 J K^{-1} kg^{-1} y T_{span} > 10 K), mientras que la mayoría de los materiales barocalóricos con cambios térmicos similares precisan de presiones por encima de 1000 bar. También cabe destacar que la temperatura de trabajo de este material es perfecta para la conservación de alimentos (tanto en refrigeración pasiva como activa), región donde hay un vacío importante de materiales barocalóricos, ya que todos los termomateriales que se pueden usar en este rango de temperaturas presentan muy poca sensibilidad a la presión, o carecen de cambios térmicos relevantes. Por último, para el futuro diseño termomateriales para su uso en refrigeración pasiva y activa barocalórica, se intentó entender la razón de por qué el [DBA][BF$_4$] tenía unas características tan prometedoras. Para ello, se realizó una exhaustiva caracterización del material combinando técnicas como rayos X de monocristal, rayos X de polvo de sincrotrón y resonancia magnética

nuclear en estado sólido de ^{1}H y ^{11}B. En estos estudios se determinó que la clave de las propiedades mostradas de este material eran las dos cadenas lineales de dibutilo, las cuales se desordenan provocando la transición sólido-sólido tan prometedora. Estos resultados podrán ayudar al futuro diseño y búsqueda de nuevos termomateriales tanto para almacenamiento de energía térmica como para refrigeración barocalórica.

En conclusión, el **Capítulo 4** ha estudiado tres nuevos cristales plásticos híbridos con resultados muy positivos, cumpliendo con creces el objetivo principal del capítulo. Así, se ha mostrado la gran perspectiva de una nueva familia en el campo barocalórico como los materiales organometálicos tipo 'sandwich'. Y, además, no solo se ha encontrado un material con propiedades barocalóricas excelentes que se podrá con enorme potencial como refrigerante, si no que, a mayores, se han sentado las bases para buscar futuros termomateriales con características similares.

Para concluir, el **Capítulo 5** abordó la búsqueda de mejorar los efectos barocalóricos mediante la combinación con otros efectos térmicos como los utilizados en enfriamiento por adsorción. Este objetivo se cumplió superando todas las expectativas iniciales. Para ello, se evaluó la respuesta térmica de una red metal-orgánica (MOF) flexible —material híbrido orgánico-inorgánico poroso—, el MIL-53(Al) (con fórmula molecular $[Al(OH)(C_8H_4O_4)]$), bajo la aplicación de pequeñas presiones de CO_2. Este material presenta un aumento en el tamaño del poro tras la aplicación de dicha presión ('breathing-effect'), conllevando así un significante aumento en la adsorción del gas. Al medir la respuesta térmica de este proceso, se descubrió el enorme cambio térmico que mostraba el material, tanto en la presurización, como en la despresurización. Este respuesta térmica, por primera vez reportada en este capítulo, se nombró como efecto 'respiro-calórico' e implicó el nacimiento de un nuevo campo con gran potencial para aplicaciones de refrigeración más ecológico que la actual compresión de vapor, basado en la combinación de la tecnología barocalórica con el enfriamiento por adsorción. El efecto 'respiro-calórico' del MIL-53(Al) mostró cambios térmicos similares a algunos gases refrigerantes ($\Delta S > 300$ J K^{-1} kg^{-1}), presiones de trabajo muy bajas, menores incluso a algunos sistemas actuales ($p \sim 16$ bar de CO_2) y un gran rango de temperatura de trabajo (superiores e inferiores a temperatura ambiente, siendo esto óptimo para su uso en refrigeración). Pero cabe destacar, que el MIL-53(Al) no es un caso aislado, y se espera que muchos otros MOFs flexibles muestren propiedades similares o incluso mejores. Con esto en mente, estos resultados pueden promocionar la búsqueda de nuevos MOFs flexibles u otros materiales porosos que puedan presentar efectos similares, para su uso en este nuevo campo que puede solucionar muchos de los problemas actuales de la refrigeración (ya que supondrían sistemas sencillos, muy poco contaminantes, presiones de trabajo muy pequeñas y rango de temperaturas operacionales muy amplio).

El **Capítulo 6** presenta las conclusiones generales del trabajo presentado en esta *Tesis Doctoral*, las cuales resumen los hallazgos clave y los resultados de la investigación realizada.

En este anexo, el **Anexo I**, se resume en castellano de toda la presente *Tesis Doctoral*.

En el **Anexo II** se encuentran todos los datos cristalográficos y resultados de la resonancia magnética nuclear (RMN) convencional que respaldan la discusión de los diferentes capítulos.

El **Anexo III** incluye información sobre la protección de la propiedad intelectual y las comunicaciones científicas relacionadas con la investigación realizada en esta *Tesis Doctoral*. Se incluyen patentes, publicaciones, comunicaciones y participaciones en congresos científicos. Este anexo destaca los esfuerzos realizados para proteger la propiedad intelectual y difundir los hallazgos de la investigación.

En el **Anexo IV** se detallan las colaboraciones nacionales e internacionales establecidas durante el desarrollo de la investigación. Se incluye información sobre visitas de investigación, colaboraciones con otras instituciones y esfuerzos conjuntos con investigadores de diferentes países. Este anexo resalta la naturaleza colaborativa de la investigación y su impacto en la promoción de la cooperación científica a nivel internacional.

En resumen, esta *Tesis Doctoral* ha mostrado un gran avance en el campo de la refrigeración, y ha cumplido todos los objetivos propuestos. Cabe destacar que se han estudiado y reportado nuevos materiales con enorme potencial como refrigerantes tanto en el campo barocalórico como en el nuevo campo del efecto 'respiro-calórico'. Pero además y más importante, se han sentado las bases para: el diseño y modulación de propiedades de perovskitas de dicianamina, la preparación de nuevos cristales plásticos híbridos prometedores para la refrigeración barocalórica y la búsqueda de nuevos MOFs flexibles u otros materiales porosos con efectos similares al efecto 'respiro-calórico' para su uso en este campo muy prometedor y emergente.

Annex II: Crystallographic data and conventional NMR

3.3. Revisiting the tolerance factor, a useful tool for designing novel hybrid dicyanamide perovskites

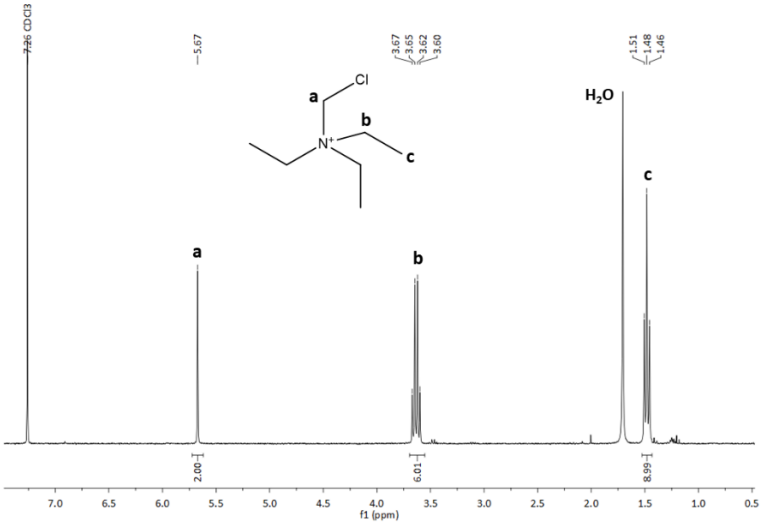

Figure A3-1. ^{1}H-NMR in $CDCl_3$ of $[Et_3(CH_2Cl)N]Cl$.

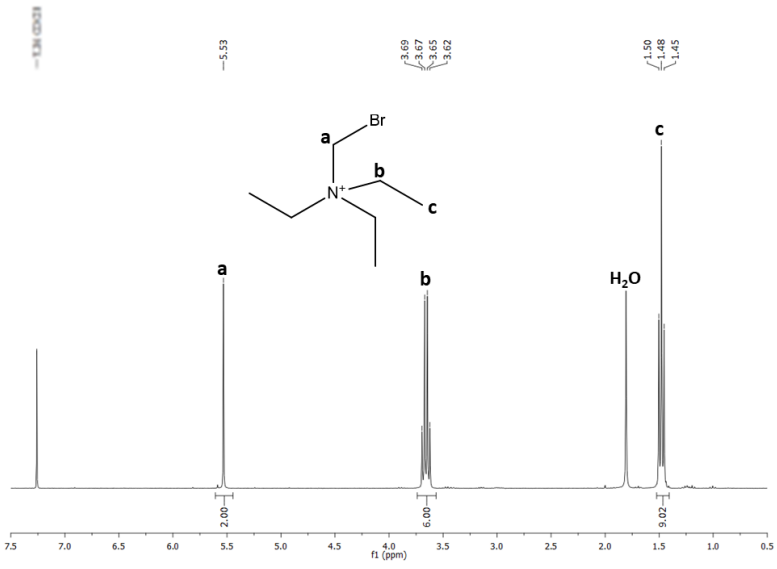

Figure A3-2. ^{1}H-NMR in $CDCl_3$ of $[Et_3(CH_2Br)N]Br$.

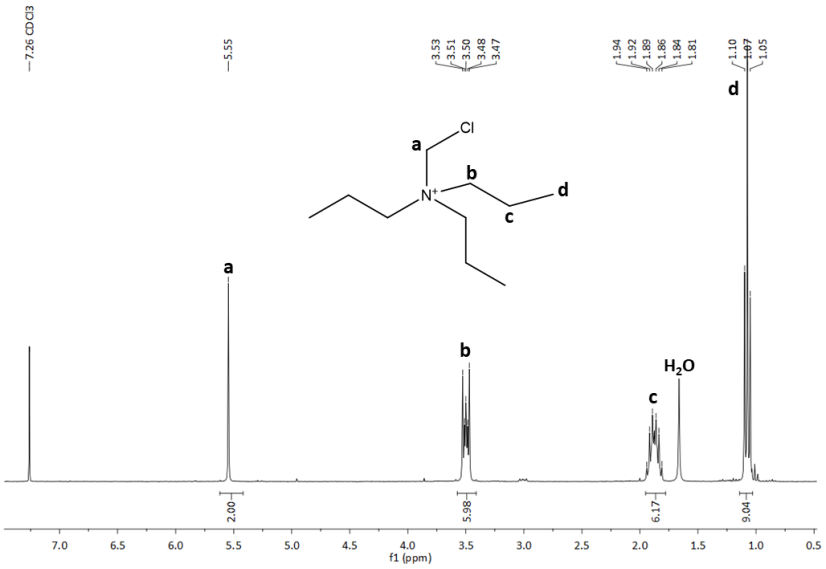

Figure A3-3. ^{1}H-NMR in $CDCl_3$ of $[Pr_3(CH_2Cl)N]Cl$.

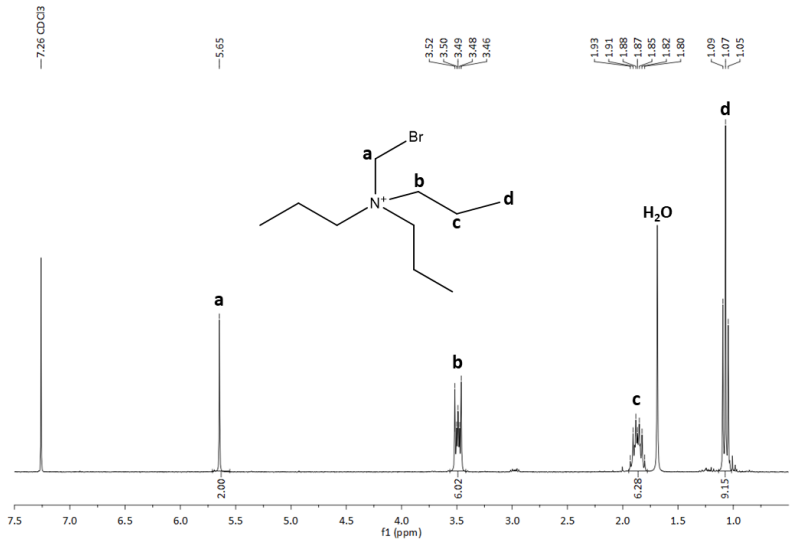

Figure A3-4. ^{1}H-NMR in $CDCl_3$ of $[Pr_3(CH_2Br)N]Br$.

Table A3-1. Crystal data and structure refinement for $[Pr_3(CH_2X)N][Mn(dca)_3]$ (X = Cl, Br) compounds obtained by single crystal X-ray diffraction.

CCDC number	2182322	2182325
Empirical formula	$C_{32}H_{46}Cl_2Mn_2N_{20}$	$C_{32}H_{46}Br_2Mn_2N_{20}$
Formula weight	891.67	980.59
Temperature/K	100.0	100.0
Crystal system	monoclinic	monoclinic
Space group	$P2_1/n$	$P2_1/n$
a/Å	16.0853(4)	16.1458(11)
b/Å	16.2405(5)	16.2630(13)
c/Å	16.4503(5)	16.4926(13)
α/°	90	90
β/°	97.6480(10)	96.469(3)
γ/°	90	90
Volume/Å^3	4259.1(2)	4303.0(6)
Z	4	4
ρ_{calc}g/cm^3	1.391	1.514
μ/mm^{-1}	0.769	2.494
F(000)	1848.0	1992.0
Crystal size/mm^3	0.233 × 0.183 × 0.133	0.183 × 0.124 × 0.051
Radiation	MoKα (λ = 0.71073)	MoKα (λ = 0.71073)
2Θ range for data collection/°	3.804 to 72.742	3.748 to 66.362
Index ranges	$-20 \leq h \leq 26$, $-27 \leq k \leq 27$, $-27 \leq l \leq 27$	$-19 \leq h \leq 24$, $-25 \leq k \leq 25$, $-25 \leq l \leq 25$
Reflections collected	274281	215321
Independent reflections	20562 [R_{int} = 0.0426, R_{sigma} = 0.0229]	16443 [R_{int} = 0.0583, R_{sigma} = 0.0275]
Data/restraints/parameters	20562/0/512	16443/0/511
Goodness-of-fit on F^2	1.028	1.047
Final R indexes [I>=2σ (I)]	R_1 = 0.0303, wR_2 = 0.0711	R_1 = 0.0302, wR_2 = 0.0676
Final R indexes [all data]	R_1 = 0.0445, wR_2 = 0.0769	R_1 = 0.0441, wR_2 = 0.0727
Largest diff. peak/hole / e Å^{-3}	0.89/-0.71	0.94/-0.79

Table A3-2. Crystal data and structure refinement for $[Et_3(CH_2Cl)N][Mn(dca)_3]\cdot H_2O$ compound obtained by single crystal X-ray diffraction.

CCDC number	2182323
Empirical formula	$C_{12}Cl_2MnN_{10}O$
Formula weight	426.06
Temperature/K	150.0
Crystal system	Monoclinic
Space group	C2/m
a/Å	14.9722(3)
b/Å	17.2255(3)
c/Å	7.4663(2)
α/°	90
β/°	102.7240(10)
γ/°	90
Volume/Å^3	1878.30(7)
Z	4
ρ_{calc}g/cm^3	1.507
μ/mm^{-1}	1.010
F(000)	836.0
Crystal size/mm^3	0.247 × 0.173 × 0.13
Radiation	MoKα (λ = 0.71073)
2Θ range for data collection/°	5.578 to 61.066
Index ranges	$-21 \le h \le 21$, $-24 \le k \le 24$, $-10 \le l \le 10$
Reflections collected	17055
Independent reflections	2931 [R_{int} = 0.0333, R_{sigma} = 0.0232]
Data/restraints/parameters	2931/0/147
Goodness-of-fit on F^2	1.078
Final R indexes [I>=2σ (I)]	R_1 = 0.0568, wR_2 = 0.1707
Final R indexes [all data]	R_1 = 0.0675, wR_2 = 0.1826
Largest diff. peak/hole / e Å^{-3}	0.72/-0.73

Table A3-3. Crystal data and structure refinement for $[Et_3(CH_2Br)N][Mn(dca)_3]\cdot H_2O$ compound obtained by Rietveld refinement of the synchrotron radiation X-ray powder diffraction pattern.

Temperature/K	295
Crystal system	Monoclinic
Space group	*C*2/*m*
a/Å	15.2521(8)
b/Å	17.2552(3)
c/Å	7.5481(3)
α/°	90
β/°	100.867(2)
γ/°	90
Z	4
$R_{F,}$ GOF, wR	12.72%, 5.63, 2.04%

Atom code	Atom	x	y	z	Occ.	U
Mn1	Mn	0.75	0.25	1	1	0.007
Br1a	Br	0.8981	0.5	1.2675	0.5	0.073
Br1b	Br	0.8458	0.5	0.74811	0.5	0.165
N1	N	1	0.5	1	1	0.023
N2	N	0.5	0.5	0.5	1	0.032
Br2	Br	0.6294	0.3970	0.4481	0.5	0.197
N4e2	N	0.8328	0.2732	0.8109	1	0.036
N3e	N	0.7022	0.3653	0.9993	1	0.039
N3c	N	0.6568	0.5	1.094	1	0.046
N4e	N	0.8482	0.2674	0.2075	1	0.041
N4c	N	0.9021	0.3164	0.5339	1	0.044
C4ce2	C	0.8515	0.2921	0.6757	1	0.030
C4ce	C	0.6930	0.4293	1.0364	1	0.027
C3	C	0.8688	0.2933	0.3495	1	0.032
O	O	1	0.1663	1	1	0.137
C1a	C	0.957	0.4473	1.1252	0.75	0.044
C1b	C	0.9295	0.5533	0.88983	0.75	0.044
C2a	C	0.5774	0.4496	0.6007	0.75	0.053
C2b	C	0.5303	0.5532	0.3571	0.75	0.063

Table A3-4. Crystal data and structure refinement for $[Bu_4P][Mn(dca)_3]$ compound obtained by single crystal X-ray diffraction.

CCDC number	2182324
Empirical formula	$C_{22}H_{14.5}MnN_9P$
Formula weight	490.84
Temperature/K	296.25
Crystal system	orthorhombic
Space group	$P2_12_12$
a/Å	16.268(6)
b/Å	16.323(6)
c/Å	21.550(7)
α/°	90
β/°	90
γ/°	90
Volume/Å^3	5722(4)
Z	8
ρ_{calc}g/cm^3	1.139
μ/mm^{-1}	0.541
F(000)	1996.0
Crystal size/mm^3	0.243 × 0.123 × 0.136
Radiation	MoKα (λ = 0.71073)
2Θ range for data collection/°	4.53 to 52.64
Index ranges	$-19 \leq h \leq 20$, $-20 \leq k \leq 20$, $-24 \leq l \leq 26$
Reflections collected	61176
Independent reflections	11623 [R_{int} = 0.0857, R_{sigma} = 0.0643]
Data/restraints/parameters	11623/6/592
Goodness-of-fit on F^2	1.029
Final R indexes [I>=2σ (I)]	R_1 = 0.0746, wR_2 = 0.1915
Final R indexes [all data]	R_1 = 0.1291, wR_2 = 0.2221
Largest diff. peak/hole / e Å^{-3}	0.38/-0.51
Flack parameter	0.075(18)

3.4. Modulation of functional properties of hybrid dicyanamide perovskites by solid solution preparation

Table A3-5. Crystal data and structure refinement for $[TPrA][Co_{0.5}Ni_{0.5}(dca)_3]$.

Empirical formula	$C_{36}H_{28}CoN_{20}Ni$
Formula weight	73.06
Temperature/K	100
Crystal system	tetragonal
Space group	$P\text{-}42_1c$
a/Å	16.0652(12)
b/Å	16.0652(12)
c/Å	17.0550(12)
α/°	90
β/°	90
γ/°	90
Volume/Å^3	4401.7(7)
Z	4
ρ_{calc}g/cm^3	1.295
μ/mm^{-1}	0.855
F(000)	1756.0
Crystal size/mm^3	0.485 × 0.236 × 0.19
Radiation	MoKα (λ = 0.71073)
2Θ range for data collection/°	2.388 to 52.766
Index ranges	$-20 \leq h \leq 20$, $-20 \leq k \leq 18$, $-21 \leq l \leq 21$
Reflections collected	65896
Independent reflections	4494 [R_{int} = 0.0430, R_{sigma} = 0.0189]
Data/restraints/parameters	4494/11/285
Goodness-of-fit on F^2	1.337
Final R indexes [I>=2σ (I)]	R_1 = 0.0750, wR_2 = 0.1798
Final R indexes [all data]	R_1 = 0.0759, wR_2 = 0.1823
Largest diff. peak/hole / e Å^{-3}	0.69/-1.19
Flack parameter	0.008(4)

Table A3-6. Bond lengths of M-N.

	Bond length (Å)
M-N1	2.12 (1)
M-N4	2.12(1)
M-N7	2.13(1)
M-N8	2.07(1)
M-N11	2.12(1)
M-N12	2.06(1)

4.3. Di-n-butylammonium tetrafluoroborate hybrid organic-inorganic material with thermal properties for multipurpose barocaloric refrigeration and cold-storage

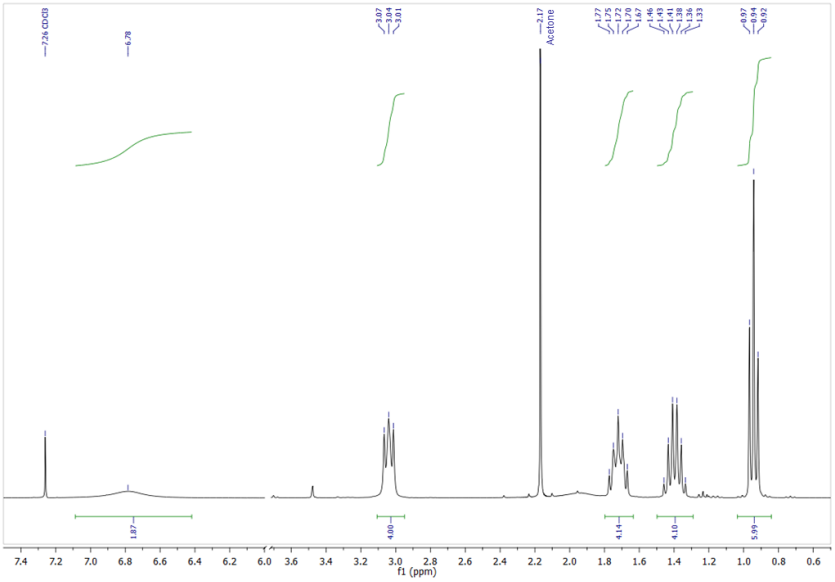

Figure A4-1. Liquid ^{1}H-NMR of [DBA][BF_4] in $CDCl_3$.

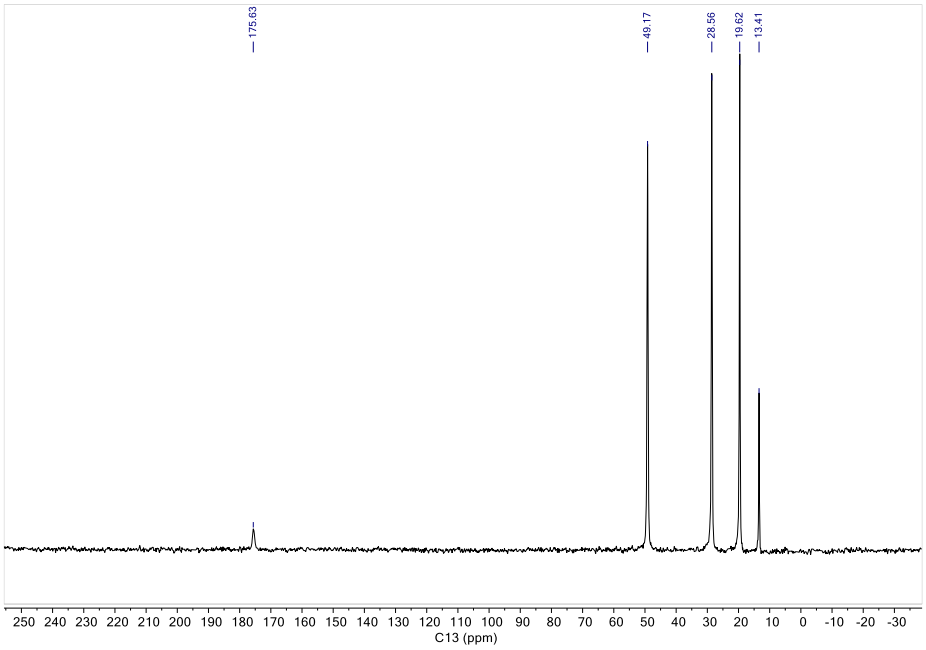

Figure A4-2. $^{13}\{^{1}H\}$ CP-MAS spectra of phase I of [DBA][BF_4] at T = 318 K.

Table A4-1. Data collection, cell and refinement parameters from the single crystal X-ray diffraction studies carried out at $T = 100$ K and $T = 240$ K for phases IV and III of [DBA][BF_4].

Empirical formula	**$C_8H_{20}N{\cdot}BF_4$**	**$C_8H_{20}N{\cdot}BF_4$**
Formula weight	217.06	217.06
Temperature	100.0(1) K	240.0(1) K
Wavelength	1.54178 Å	1.54178 Å
Crystal system	Orthorhombic	Orthorhombic
Space group	*Ccce*	*Cmme*
Unit cell dimensions	a = 7.3980(5) Å b = 18.4562(11) Å c = 16.8535(10) Å	a = 7.5762(10) Å b = 18.642(3) Å c = 8.5564(12) Å
Volume	2301.2(2) $Å^3$	1208.5(3) $Å^3$
Z	8	4
Density (calculated)	1.253 Mg/m^3	1.193 Mg/m^3
Absorption coefficient	1.02 mm^{-1}	0.97 mm^{-1}
F(000)	928	464
Crystal size	0.32 x 0.22x 0.08 mm^3	0.32 x 0.22x 0.08 mm^3
Theta range for data collection	5.3 to 67.8°	5.2 to 65.0°.
Index ranges	0<=h<=8 0<=k<=22 0<=l<=20	0<=h<=8 0<=k<=21 0<=l<=10
Reflections collected	50094	13977
Completeness (theta max.)	98.7 % (67.76º)	97.2 % (65.04º)
Refinement method	Full-matrix least-squares on F^2	Full-matrix least-squares on F^2
Data / restraints / parameters	1100 / 0 / 69	629 / 96 / 77
Goodness-of-fit on F^2	1.14	1.55
Final R indices [I>2sigma(I)]	R1 = 0.1091 wR2 = 0.3093	R1 = 0.1248 wR2 = 0.2748
R indices (all data)	R1 = 0.1310 wR2 = 0.3378	R1 = 0.1695 wR2 = 0.3096
Largest diff. peak and hole	0.61 and -0.32 $e.Å^{-3}$	0.48 and -0.28 $e.Å^{-3}$

Table A4-2. All the barocaloric materials represented in Figure 4-28. *Note:* HOIM = Hybrid Organic-Inorganic Material, SP = Spin Crossover compound, OPC = Organic Plastic Crystal, POL = Polymer, AIS = Ammonium Inorganic Salt and MA = Metal Alloy. *Note₂:* 24 and 25 are the same compound due to it has 2 phase transitions.

Number	Family	Material	Number	Family	Material
1	HOIM	$(C_{10}H_{21}NH_3)_2MnCl_4$	31	AIS	NH_4I
2	HOIM	$(C_9H_{19}NH_3)_2MnCl_4$	32	AIS	$(NH_4)_2MoO_2F_4$
3	HOIM	$(Me_3S)FeCl_4$	33	MA	$Ni_{50}Mn_{31.5}Ti_{18.5}$
4	HOIM	$(Me_3(ClMe)N)FeCl_4$	34	MA	$MnNiSi_{0.59}FeCoGe_{0.41}$
5	HOIM	$(C_9H_{19}NH_3)_2CuBr_4$	35	MA	$LaFe_{11.33}Co_{0.47}Si_{1.2}$
6	HOIM	$[Me_4N][Mn(N_3)_3]$	36	MA	Mn_3NiN
7	HOIM	$[Pr_4N][Mn(N(CN)_2)_3]$	37	MA	$Gd_2Si_5Ge_5$
8	HOIM	$[Pr_4N][Cd(N(CN)_2)_3]$	38	MA	$Ni_{0.95}Fe_{0.05}S$
9	HOIM	$[Me_2NH_2][Mg(HCOO)_3]$	39	MA	$Ni_{44.6}Co_{5.5}Mn_{35.5}In_{14.4}$
10	SC	$[FeL_2][BF_4]_2$	40	MA	$Ni_{2.00}Mn_{1.32}In_{0.68}$
11	SC	$[Fe(hyptrz)_3]A_2{\cdot}H_2O$	41	MA	$Co_{50}Fe_{2.5}V_{31.5}Ga_{16}$
12	SC	$Fe_3(bntrz)_6(tcnset)_6$	42	MA	$MnNiSi_{0.60}FeCoGe_{0.40}$
13	SC	$Fe[HB(tz)_3]_2$	43	MA	$MnCoGeB_{0.03}$
14	OPC	$(CH_3)C(CH_2OH)_3$	44	MA	Mn_3GaN
15	OPC	$(CH_3)_2C(CH_2OH)_2$	45	MA	$Ni_{35.5}Co_{14.5}Mn_{35}Ti_{15}$
16	OPC	$C_{11}H_{18}O$	46	MA	$Ni_{49.26}Mn_{36.08}In_{14.66}$
17	OPC	$(CH_3)_3C(CH_2OH)$	47	MA	$Ni_{0.875}Fe_{0.125}S$
18	OPC	$C_{10}H_{15}Cl$	48	MA	$Ni_{0.85}Fe_{0.15}S$
19	OPC	*o*-$C_2B_7H_{12}$	49	MA	$Ni_{1.99}Mn_{1.34}In_{0.67}$
20	OPC	*m*-$C_2B_7H_{12}$	50	MA	$Fe_{49}Rh_{51}$
21	OPC	*p*-$C_2B_7H_{12}$	51	MA	$MnCoGe_{0.99}In_{0.01}$
22	OPC	$C_{10}H_{15}Br$	52	MA	$MnNiSi_{0.61}FeCoGe_{0.39}$
23	OPC	1- $C_{10}H_{15}O$	53	MA	$Ni_{0.825}Fe_{0.175}S$
24	OPC	2- $C_{10}H_{15}O$	54	MA	$Ni_{58.3}Mn_{17.1}Ga_{24.6}$
25	OPC	2- $C_{10}H_{15}O$	55	MA	$Ni_{42.3}Co_{7.9}Mn_{38.8}Sn_{11.0}$
26	OPC	C_{60}	56	MA	$Ni_{1.99}Mn_{1.37}In_{0.64}$
27	POL	Acetoxy Silicone Rubber	57	MA	$Ni_{2.05}Mn_{1.30}In_{0.65}$
28	POL	PVDF-TrFE-CTFE	58	MA	$MnNiSi_{0.62}FeCoGe_{0.38}$
29	AIS	NH_4HSO_4	59	MA	$Ni_{2.02}Mn_{1.36}In_{0.62}$
30	AIS	$(NH_4)_2NbOF_5$			

Table A4-3. Atom distances and Rietveld refinement parameters of phase II.

Unit cell: a = 7.62273, b = 20.34391, c = 8.51112

Final refinement: wR = 5.92% on 9126 observations in this histogram

Other residuals: R = 3.45%, R-bkg = 8.29%, wR-bkg = 5.92% $wRmin$ = 0.41%

Atom name	x	y	z	Occ.	Uiso
N1	0	0.75	0.27243	1	0.11078
C2	0	0.68191	0.20262	1	0.10748
C3	0	0.64166	0.29171	1	0.11633
C4	0	0.58008	0.18323	1	0.1233
C5	0.08897	0.51155	0.29982	0.5	0.23804
B1_1	0.495	0.7494	0.2854	0.25	0.17123
F1_1	0.49964	0.68345	0.16725	0.25	0.17313
F2_1	0.33725	0.78389	0.32159	0.25	0.30528
F3_1	0.57343	0.71161	0.42633	0.25	0.34777
F4_1	0.5873	0.79578	0.24478	0.25	0.1503

Table A4-4. Atom distances and Rietveld refinement parameters of phase I.

Unit Cell: a = 5.73161, b = 5.73161, c = 20.61450

Final refinement: wR = 8.98% on 21501 observations in this histogram

Other residuals: R = 6.70%, R-bkg = 8.25%, wR-bkg = 8.98% $wRmin$ = 3.48%

Atom name	x	y	z	Occ.	Uiso
B	0	0	0.47	0.5	0.30668
F1	0	0	0.41	0.5	0.31835
F2	0.18501	0	0.5	0.25	0.39494
N4	0	0	0	1	0.92652
C1	0.95817	0.04183	0.0851	0.125	0.58818
C2	0.95552	0.04448	0.12233	0.125	0.30176
C3	0.91324	0.08676	0.19077	0.125	0.4033
C4	0.82974	0.17026	0.22989	0.125	0.40361

Annex III: IP protection and science communication (patents, publications, communications)

Patents

Title: **Proceso y dispositivo de refrigeración/calefacción basados en compuestos híbridos orgánico-inorgánicos moleculares**.

Application number: **P202130565**

Publication number: **P2931216**

Presentation date: **17/06/2021**

Granting date: **05/05/2023**

Authors: J.M. Bermúdez García, J. Salgado Beceiro, **J. García Ben**, M. Sánchez Andújar, S. Castro García, M.A. Señarís Rodríguez, E. Stern Taultats, X. E. Moya Raposo.

Title: **Proceso y dispositivo de refrigeración/calefacción basados en MOFs inducido por modificaciones de presión**.

Application number: **P202130753**

Presentation date: **02/08/2021**

Authors: J.M. Bermúdez García, M.A. Señarís Rodríguez, M. Sánchez Andújar, S. Castro García, **J. García Ben**, J. López Beceiro, R.P. Artiaga Díaz.

Publications

Title: **Simple and Low-Cost Footstep Energy-Recover Barocaloric Heating and Cooling. Device**

Authors: **J. García Ben**, I. Delgado Ferreiro, J. Salgado Beceiro, J.M. Bermúdez García.

Reference: *Materials*, **2021**, *14*(20), 5947.

DOI: **https://doi.org/10.3390/ma14205947**

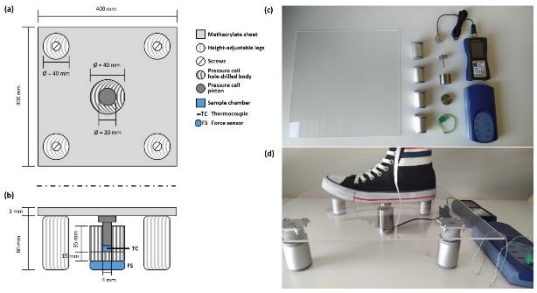

Title: **Dicyanamide-perovskites at the edge of dense hybrid organic–inorganic materials.**

Authors: **J. García Ben**, L.N. McHugh, T.D. Bennett, J.M. Bermúdez García.

Reference: *Coord. Chem. Rev.*, **2022**, *455*, 214337.

DOI: **https://doi.org/10.1016/j.ccr.2021.214337**

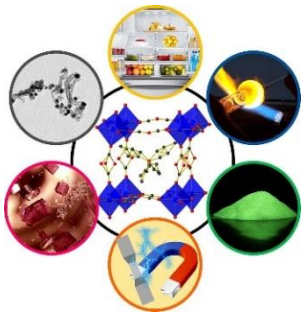

Title: **Structural, Thermal and Functional Properties of a Hybrid Dicyanamide-Perovskite Solid Solution**

Authors: **J. García-Ben**, J. Salgado Beceiro, I. Delgado Ferreiro, P. Dafonte Rodríguez, J. López Beceiro, R. Artiaga, S. Castro García, M. Sánchez Andújar, J.M. Bermúdez García, M.A. Señarís Rodríguez.

Reference: *Crystals*, **2022**, *12*(6), 860.

DOI: **https://doi.org/10.3390/cryst12060860**

Title: **Discovery of Colossal Breathing-Caloric Effect under Low Applied Pressure in the Hybrid Organic–Inorganic MIL-53(Al) Material.**

Authors: **J. García Ben**, J. López Beceiro, R. Artiaga, J. Salgado Beceiro, I. Delgado Ferreiro, Y.V. Kolen'ko, S. Castro García, M.A. Señarís Rodríguez, M. Sánchez Andújar, J.M. Bermúdez García.

Reference: *Chem. Mater.*, **2022**, *34*(7), 3323.

DOI: **https://doi.org/10.1021/acs.chemmater.2c00137**

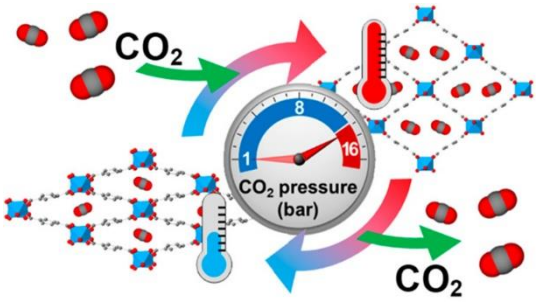

Title: **Narrowing the tolerance factor limits for hybrid organic-inorganic dicyanamide-perovskites.**

Authors: **J. García Ben**, A. García Fernández, P. Dafonte Rodríguez, I. Delgado Ferreiro, U.B. Cappel, S. Castro García, M. Sánchez Andújar, J.M. Bermúdez García, M.A. Señarís Rodríguez.

Reference: *J. Solid State Chem.*, **2022**, *316*, 123635.

DOI: **https://doi.org/10.1016/j.jssc.2022.123635**

Title: **Structure and thermal properties relationships in the thermomaterial di-n-butylammonium tetrafluoroborate for multipurpose cooling and cold-storage.**

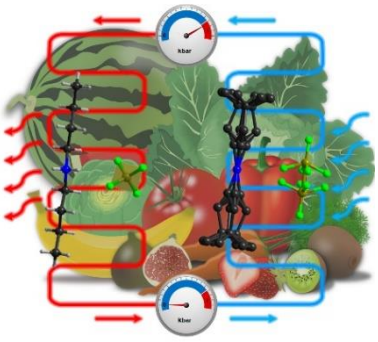

Authors: **J. García Ben**, J.M. Bermúdez García, R.J.C. Dixey, A.L. Llamas Saiz, J. López Beceiro, R. Artiaga, A. García-Fernández, U.B. Cappel, B. Alonso, S. Castro García, A.E. Phillips, M. Sánchez Andújar and M.A. Señarís Rodríguez.

Reference: *J. Mater. Chem. A*, **2023**, Accepted Manuscript. Chosen as *Hot Paper* by the journal.

DOI: **https://doi.org/10.1039/D3TA04063A**

Title: **Photoluminescent and vapochromic properties of the Mn(II)-doped $(C_6H_{11}NH_3)_2PbBr_4$ layered organic–inorganic hybrid perovskite**

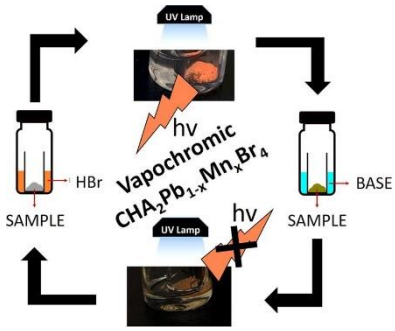

Authors: A. Cuquejo Cid, A. García Fernández, **J. García-Ben**, M.A. Señarís Rodríguez, S. Castro García, M. Sánchez Andújar, D. Vázquez García.

Reference: *Polyhedron*, **2021**, *193*(1), 114840.

DOI: **https://doi.org/10.1016/j.poly.2020.114840**

Title: **Hybrid ionic plastic crystals in the race for enhanced low-pressure barocaloric materials.**

Authors: J. Salgado Beceiro, J.M. Bermúdez García, E. Stern Taulats, **J. García Ben**, S. Castro García, M. Sánchez Andújar, X. Moya, M.A. Señarís-Rodríguez.

Reference: *ChemRxiv*, **2021** (pre-print).

DOI: **https://doi.org/10.33774/chemrxiv-2021-c4hx5**

Title: **Empowering CO_2 eco-refrigeration with MOF-508b: colossal breathing-caloric-like effects and proof-of-concept.**

Authors: M. Gelpi[§], **J. García-Ben**[§], S. Rodríguez-Hermida, J. López-Beceiro, R. Artiaga, Á. Baaliña, M. Romero-Gómez, J. Romero-Gómez, S. Zaragoza, J. Salgado-Beceiro, J. Walker, C. McMonagle, S. Castro-García, M. Sánchez-Andújar, J.M. Bermúdez García, M.A. Señarís-Rodríguez.

[§]*These authors have equally contributed to this work.*

Submitted: 21/06/2023.

Title: **Structural and Physico-Chemical Characterization of Hybrid Materials Based on Globular Quinuclidinum Cations Derivatives and Tetrachloridocobaltate(II) Anions**

Authors: C. Belloso-Casuso, I. de Pedro, L. Canadillas-Delgado, G. Beobide, M. Sánchez-Andújar, **J. García-Ben**, J. Walker, J. Rodríguez Fernández, O. Fabelo.

Submitted: 28/07/2023.

Title: **Covalent Organic Frameworks as Catalyst Support: A Case Study of Thermal, Hydrothermal, and Mechanical Pressure Stability of β-Ketoenamine-linked TpBD-Me_2**

Authors: L.P.L. Gonçalves, **J. García-Ben**, K. Strutynski, L. Rodríguez-Lorenzo, J.P.S. Sousa, O.S.G.P. Soares, M.F.R. Pereira, M. Melle-Franco, Y.V. Kolen'ko, L.M. Salonen.

Submitted: 29/07/2023.

Title: **Organometallic-sandwich compounds $[Cp_2M][PF_6]$ (M: Fe, Co) with barocaloric properties**

Authors: **J. García-Ben**, I. Delgado-Ferreiro, R.J.C. Dixey, S. Castro-García, J. López-Beceiro, R. Artiaga, M. Sánchez-Andújar, A.E. Phillipsb, J.M. Bermúdez-García*, M.A. Señarís-Rodríguez.

In preparation.

Communications

Oral communication: **A new organic plastic crystal with multiple solid-solid phase transitions for "cold storage".**

Authors: **J. García Ben**, J. Salgado Beceiro, I. Delgado Ferreiro, A.L. Llamas Saiz, J. López Beceiro, R. Artiaga, A. García Fernández, U.B. Cappel, B. Alonso, S. Castro García, M. Sánchez Andújar, M.A. Señarís Rodríguez, J.M. Bermúdez García.

Event: *EMRS Fall 2021*, Warsaw (Poland), 20th – 23rd September 2021.

Oral communication: **Multifunctional hybrid organic-inorganic compounds: an emerging family for eco-friendly refrigeration and heating.**

Authors: J.M. Bermúdez García, J. Salgado Beceiro, **J. García-Ben**, I. Delgado Ferreiro, M. Sánchez Andújar, S. Castro García, M.A. Señarís Rodríguez.

Event: *EMRS Fall 2021*, Warsaw (Poland), 20th – 23rd September 2021.

Oral communication: **Polar Ionic Plastic Crystals for Multi-Energy Storage Applications.**

Authors: J. Salgado Beceiro, J. Walker, A. García Fernández, J.M. Bermúdez García, **J. García Ben**, I. Delgado Ferreiro, S. Castro-García, M. Sánchez Andújar, U.B Cappel, M. Einarsrud, M.A. Señarís Rodríguez.

Event: *EMRS Fall 2021*, Warsaw (Poland), 20th – 23rd September 2021.

Poster communication: **New organic-inorganic halometallates [A][$FeCl_4$] plastic crystals for electric and solar thermal energy storage.**

Authors: I. Delgado Ferreiro, J. Salgado Beceiro, **J. García Ben**, S. Castro García, M.A. Señarís Rodríguez, M. Sánchez Andújar, J.M. Bermúdez García.

Event: *EMRS Fall 2021*, Warsaw (Poland), 20th – 23rd September 2021.

Written communication: **Blended learning methods for modern teaching of crystal chemistry in science bachelor degrees.**

Authors: **J. García Ben**, I. Delgado Ferreiro, J.M. Bermúdez García,

Event: Congreso de Innovación docente, *CUICIID 2021*, Madrid, 6th – 8th October 2021.

Oral communication: **Metalocinios: nuevas aplicaciones en refrigeración barocalórica.**

Authors: **J. García Ben**, M.A. Señarís Rodríguez, S. Castro García, M. Sánchez Andújar, R.J C. Dixey, A. Phillips, J.M. Bermúdez García.

Event: *QIES2022*, Sevilla (España), 30th January – 2nd February 2022.

Poster communication: **Hybrid organic-inorganic dicyanamide perovskites: A new playground for structural distortions.**

Authors: **J. García Ben**, M.A. Señarís Rodríguez, S. Castro García, M. Sánchez Andújar, L.N. McHughy, T.D. Bennett, J.M. Bermúdez García.

Event: *QIES2022*, Sevilla (España), 30th January – 2nd February 2022.

Oral communication: **New organic-inorganic halometallates [A][$FeCl_4$] plastic crystals for electric and solar thermal energy storage.**

Authors: I. Delgado Ferreiro, **J. García Ben**, M.A. Señarís Rodríguez, S. Castro García, M. Sánchez Andújar, J.M. Bermúdez García.

Event: *QIES2022*, Sevilla (España), 30th January – 2nd February 2022.

Poster communication: **Unusual reverse barocaloric effect in organic-inorganic hybrid perovskite [$(CH_3)_3NOH]_2[KCo(CN)_6$].**

Authors: I. Delgado Ferreiro, **J. García Ben**, M.A. Señarís Rodríguez, S. Castro García, M. Sánchez Andújar, P. Loveras, J.M. Bermúdez García.

Event: *QIES2022*, Sevilla (España), 30th January – 2nd February 2022.

Oral communication: **Nuevos materiales (multi)funcionales basados en perosvkitas híbridas orgánicas-inorgánicas.**

Authors: J.M. Bermúdez García, J. Salgado Ferreiro, **J. García Ben**, I. Delgado Ferreiro, S. Castro García, M. Sánchez Andújar, M.A. Señarís Rodríguez.

Event: *QIES2022*, Sevilla (España), 30th January – 2nd February 2022.

Poster communication: **Modulation of functional properties in the emerging dicyanamide hybrid perovskites by using traditional solid solution strategies.**

Authors: J.M. Bermúdez García, **J. García Ben**, I. Delgado Ferreiro, J. Salgado Ferreiro S. Castro García, M. Sánchez Andújar, M.A. Señarís Rodríguez.

Event: *QIES2022*, Sevilla (España), 30th January – 2nd February 2022.

Poster communication: **A tolerance factor adaptation to dicyanamide perovskites.**

Authors: **J. García Ben**, S. Castro García, M. Sánchez Andújar, J.M. Bermúdez García, M.A. Señarís Rodríguez.

Event: *RSEQ Bienal meeting 2022*, Granada (España), 27th – 30th June 2022.

Poster communication: **$[(CH_3)_3NOH]_2MnCl_4$, a novel plastic crystal with phase transition and multifunctional properties.**

Authors: I. Delgado Ferreiro, **J García Ben**, J. López Beceiro, R. Artiaga, S. Castro Garcia, M.A. Señarís Rodríguez, M. Sánchez Andújar, J.M. Bermúdez García.

Event: *RSEQ Bienal meeting 2022*, Granada (España), 27th – 30th June 2022.

Oral communication: **Hybrid organic-inorganic thermomaterials for barocaloric refrigeration and solar energy storage.**

Authors: **J. García Ben**, I. Delgado Ferreiro, J. Salgado Beceiro, J. López Beceiro, R. Artiaga, S. Castro García, M. Sánchez Andújar, M.A. Señarís Rodríguez, J.M. Bermúdez García.

Event: *RSEQ Bienal meeting 2022*, Granada (España), 27th – 30th June 2022.

Annex IV: National and international collaborations and research visits

Group | Department: ***Nanochemistry Research Group***

Institution | Country: International Iberian Nanotechnology Laboratory (**INL**), Braga, **Portugal**.

Activity: 3-months research stay under the supervision of Dr. Yury V. Kolen'ko.

Group | Department: ***Phillips Group***

Institution | Country: Queen Mary University of London (**QMUL**), London, **United Kingdom**.

Activity: 3-months research stay under the supervision of Dr. Anthony Phillips.

Group | Department: ***Department of Chemistry of Graduate School of Science***

Institution | Country: Kobe University, Kobe, **Japan**.

Activity: 1.5-months research stay under the supervision of Prof. Tomoyuki Mochida.

Group | Department: ***Department of Materials Science & Metallurgy***

Institution | Country: Cambridge University, Cambridge**, United Kingdom.**

Activity: Patent collaboration with Dr. Xavier Moya.

Group | Department: ***Institut Charles Gerhardt Montpellier*** (ICGM)

Institution | Country: Université de Montpellier, Montpellier, **France**.

Activity: Measurements of solid-state NMR with the collaboration of Dr. Bruno Alonso.

Group | Department: ***Propiedades térmicas y reológicas*** (PROTERM)

Institution | Country: Universidade da Coruña (**UDC**), A Coruña, **Spain**.

Activity: Measurements of DSC with collaboration of Dr. Jorge López Beceiro and Dr. Ramón Pedro Artiaga Díaz.

Group | Department: ***Network of Infrastructures to Support Research and Technological Development*** (RIAIDT)

Institution | Country: Universidade de Santiago de Compostela (**USC**), Santiago de Compostela, **Spain**.

Activity: Measurements and analysis of single crystal x-ray diffraction data

---

Group | Department: ***I11 Beamline***

Institution | Country: Diamond Light Source, Oxford, **United Kingdom.**

Activity: Synchrotron powder X-ray diffraction at variable temperature measurements of plastic crystals.

Group | Department: ***BM01 Beamline***

Institution | Country: European Synchrotron Radiation Facility (**ESRF**), Grenoble, **France**.

Activity: Synchrotron powder X-ray diffraction at variable temperature and pressure measurements under the collaboration of Dr. Julian Walker and Dr. Charlie McMonagle.

Group | Department: ***Functional Materials and Materials Chemistry*** (FACET)

Institution | Country: Norges Teknisk-Naturvitenskaplige Universitet (**NTNU**) of Trondheim, **Norway.**

Activity: Collaboration in studies with Dr. Julian Walker.

Group | Department: ***Division of Applied Physical Chemistry***

Institution | Country: KTH - Royal Institute of Technology of Stockholm, **Sweden**.

Activity: Collaboration in studies with Dr. Alberto García Fernández and Dra. Ute B. Cappel.